Commissioning and Characterization of the first DSSC ladder X-ray camera prototype for the European XFEL

Dissertation
zur Erlangung des Doktorgrades

an der Fakultät für Mathematik, Informatik und Naturwissenschaften

Fachbereich Physik
der Universität Hamburg

vorgelegt von

Mattia Donato

geboren
am 23.01.1986 in

Levanto
(La Spezia, Ligurien, Italien).

Hamburg
2018

Gutachter/innen der Dissertation: Prof. Dr. Erika Garutti
(Assessors of the Disseration):   Dr. Monica Turcato

Zusammensetzung der Prüfungskommission: Prof. Dr. Robin Santra
(Composition of the Examination Committee):   Prof. Dr. Erika Garutti
     Prof. Dr. Heinz Graafsma
     Prof. Dr. Henry N. Chapman
     Dr. Monica Turcato

Vorsitzende/r der Prüfungskommission: Prof. Dr. Robin Santra
(Chair of the Examination Committee):

Datum der Disputation: 11.12.2018
(Date of the Disputation):

Vorsitzender Fach-Promotionsausschusses PHYSIK: Prof. Dr. Wolfgang Hansen
(Chairman of the Physics Subject Doctoral Committee):

Leiter des Fachbereichs PHYSIK: Prof. Dr. Michael Potthoff
(Head of the Department of Physic):

Dekan der Fakultät MIN: Prof. Dr. Heinrich Graener
(Dean of the MIN Faculty):

Abstract:

The European X-Rays Free-Electron Laser (XFEL.EU) is a new X-ray facility built in the Hamburg metropolitan area. It is the most largest and brilliant coherent X-ray source ever built. The machine is able to provide to the end-stations trains of 2700 X-ray pulses with 222ns (4.5 MHz) separation time between each other; the trains are repeated every 0.1 s. In order to perform scientific experiments using the X-rays provided by the machine, the XFEL.EU commissioned three new detector projects able to match the characteristic XFEL.EU time structure and to implement the high demanding requirements defined by the scientific community.

One of these three projects is the DSSC (DEPFET Sensor with Signal Compression) detector project. The DSSC is the imaging detector prepared for soft X-ray instruments at XFEL.EU. It is a one-million pixel camera able to acquire up to 800 consecutive images in a train, with a 4.5 MHz frame rate. The DSSC is designed to reach a single photon sensitivity at 1 keV together with a high dynamic range. To reach these requirements, the detector was originally designed to use the non-linear DEPFET sensors, which implement an internal signal compression. However, in its first version the DSSC uses more conventional mini silicon drift detector (Mini-SDD) pixel arrays. The signal compression can be realized in the first amplification stage of the front-end electronics. The DSSC 1M pixel camera is composed of 16 units, each called a DSSC ladder.

The goal of the work of this thesis was to integrate, bring into operation and perform the first characterization of the DSSC ladder systems implementing two different types of sensors, DEPFET and Mini-SDD. A DSSC ladder equipped with DEPFET sensors was tested with pulsed visible light, emulating the XFEL.EU timing structure. A DSSC ladder equipped with Mini-SDD sensors was tested in a dedicated vacuum setup at the soft X-ray beamline P04 at Petra III, DESY. In both cases, the detectors were successfully brought into operation, measurements were performed and the detector was characterized. However, due to the performances of the first version of the full-size ASIC, the detector could not reach the target specification defined for operation at XFEL.EU. This is expected to be improved with the second version of the ASIC.

Zusammenfassung:

Der Europäische Freie-Elektronen-Röntgenlaser (XFEL.EU) ist eine neue Forschungseinrichtung zur Erzeugung von Röntgenstrahlung in Hamburg und Schleswig-Holstein. Es ist die größte und leuchtstärkste, kohärente Röntgenquelle der Welt. Die Anlage versorgt die angeschlossenen Experimente mit einer Abfolge (Train) von bis zu 2700 Röntgenblitzen mit einer zeitlichen Trennung von 222ns (4.5MHz); die Trains wiederholen sich alle 0.1s. Um die Möglichkeiten der von der Anlage zur Verfügung gestellten Röntgenstrahlung vollständig ausschöpfen zu können, initiierte das XFEL.EU die Entwicklung dreier neuartiger Röntgendetektoren.

Eines dieser drei Projekte ist das DSSC (DEPFET Sensor mit Signalkompression) Detektorprojekt. Der DSSC ist ein bildgebender Detektor für Experimente mit weicher Röntgenstrahlung am XFEL.EU. Insgesamt verfügt der Detektor über eine Million Pixel und ist in der Lage während eines Trains 800 aufeinanderfolgende Bilder mit einer Bildrate von 4.5MHz aufzuzeichnen. Der DSSC soll sowohl bei einer Photonenenergie von 1keV Einzelphotonen auflösen können als auch einen hohen dynamischen Bereich zur Verfügung stellen. Zur Umsetzung dieser Anforderungen sollte der Detektor ursprünglich mit nicht-linearen DEPFET Sensoren ausgestattet werden, welche durch ihr Funktionsprinzip eine interne Signalkomprimierung erreichen. In seiner ersten Version verwendet der DSSC jedoch zunächst eine Matrix von Siliziumdriftdetektoren (Mini-SDD). Die Signalkompression wird dabei in der ersten Verstärkerstufe der Front-End Elektronik realisiert. Der vollständige Detektor umfasst 16 individuelle Baugruppen, die sogenannten DSSC Ladders.

Das Ziel dieser Disseration ist die Integration, Inbetriebnahme und Charakterisierung des DSSC Ladder Systems mit beiden Sensortypen. Dazu wurde eine mit einem DEPFET Sensor bestückte DSSC Ladder mittels eines gepulsten, optischen Lasers getestet. Eine weitere, mit einem SDD Sensor ausgerüstete DSSC Ladder wurde einer Vakuum-Umgebung am Strahlrohr P04 des PETRAIII Synchrotons (DESY) getestet. In beiden Fällen konnten die DSSC Ladders erfolgreich in Berieb genommen, für Messungen verwendet und charakterisiert werden. Bei den Tests zeigte sich, dass die Leistung der ersten Version der in der Front-End Elektronik verbauten ASICs hinter den Zielvorgaben des XFEL.EU zurückbleibt. Eine zweite, verbesserte Version des ASICs soll den Zielvorgaben künftig gerecht werden.

Contents

Introduction

The X-ray radiation was discovered in 1895 by Wilhelm Röntgen. From the very beginning, the applications of X-rays involved imaging techniques. The famous "Röntgen's wife's hand with ring" image was the first radiography, obtained a few months after then X-ray discovery [1]. The discovery of Röntgen allowed for the first time to inspect bodies and objects in a non-destructive way [2], opening the way for countless medical and industrial applications.

About twenty years later, Max von Laue discovered the diffraction of X-rays on crystal by using a novel technique involving X-rays and imaging techniques. Von Laue won the Nobel Prize in 1914 [3], opening the way to crystallography and to the usage of X-rays in the study of the physics of matter.

The more and stringent requirements for X-rays in medical, industrial and scientific applications push the improvement of the quality of X-rays sources. Nowadays, the one of the state-of-the-art X-rays source is the European XFEL (XFEL.EU) [4], a facility inaugurated on September 1st, 2017, which after the commissioning period is expected to become the most brilliant coherent X-ray source ever built [5]. In parallel to the improvement of X-ray sources, the X-ray detection techniques made considerable progresses. The demands and performances in terms of low-noise, high dynamic-range and extremely high frame rate makes the imaging-detector projects developed for the XFEL.EU the state-of-art in terms X-ray of detection.

The goal of the work described in this thesis was to build-up, bring into operation, and characterize the first prototype of the DSSC detector [6]. Starting from the testing of the single electronics and data-acquisition components, the first prototype was built in two different versions, featuring sensors different in technology. The first two prototypes were use to prove the functionality of the whole system, and after that, to perform the first calibration a large-size DSSC prototype, using either visible light or photons from a synchrotron beamline. This thesis is divided into five chapters.

The first chapter is an introduction on the production, detection and interactions of X-rays with matter. An historical overview is presented starting from the discovery of X-rays up to their use nowadays. In this chapter, both old and modern techniques used to produce X-rays are described. Then, an overview on the interactions of X-rays with matter is presented. It includes also a description of diffraction phenomena of X-ray scattering on crystals. The last part of this chapter explains the basic technique used for the detection of X-rays with semiconductor devices (the PN-junction).

The second chapter describes the European XFEL (XFEL.EU) facility. The main components of the beamlines and the features of the end-stations (instruments) are described. An overview on the three detector projects developed for XFEL.EU is also presented.

The third chapter describes the DEPFET Sensor with Signal Compression (DSSC) detector [6]. The two possible sensor types used to build the DSSC detectors, DEPFET, and MiniSDDs, are described, together with the different building blocks of the electronics and data acquisition systems. This chapter includes also the description of the vacuum test-stand used to test and bring into operation the first large-size prototype of the DSSC detector.

The fourth describes the first tests performed with the DSSC ladder, namely, the smallest unit of the detector which contains all the electronics components representative of the final system. In particular, the fourth chapter shows the first measurement performed with the first DSSC ladder equipped with a 64 x 64 pixels DEPFET sensor.

The fifth chapter shows the results of the first measurements performed with the DSSC ladder equipped with a full-size Mini-SDD sensor (512 x 128 pixels). The measurements were performed at a synchrotron beamline.

1 X-rays: production, interactions and principles of detection

1.1 X-rays history and definition

The X-ray radiation was first defined with such a name by Röntgen in 1895, [2]. In that period, discharge tubes – called Crookes tubes from the scientist who developed them – were used for producing and studying the so-called cathodic rays. The discharge tubes are evacuated glass bulb containing a gas at extremely low pressure, where a very high voltage (1-100 kV) is applied between anode and cathode. In the tube under high voltage, luminescent rays are produced out of the cathode, called for this reason *cathodic rays*. Röntgen was studying the cathodic rays when he observed for the first time an unknown type of radiation. This type of radiation could generate luminescence on a fluorescent screen even if the screen was outside the the tube and far from it, [2]. This radiation was therefore generated inside the Crookes tube but it could pass through its surface. To be sure that this effect was not caused by any light reflection in the laboratory, Röntgen shielded the Crookes tube with dark paper. He observed that the luminescence was visible on the screen also when the tube was shielded. Therefore, the paper was transparent to the new radiation, thus he started to study the transparency to these rays of many different thicknesses and different materials. Röntgen called this unknown type of radiation X-rays. He observed also that this new type of radiation could impress a photographic plate. This allowed him to produce, by holding his wife's hand between the tube and the photographic plate, the first radiography. This implies the discovery that the soft tissues of the human body are almost transparent to X-rays radiation, while the bones are opaque. This started a revolution, because for the first time the human body in the medical field could be inspected without surgery. For the X-ray discovery, Wilhelm Conrad Röntgen won the Nobel prize in 1901 [1].

After Röntgen's discovery, many experiments were performed to understand the nature of X-rays. The observations showed that it was not possible to deviate X-rays by a magnetic field, giving indication that the radiation was neutral in charge. Moreover it was highly likely that this type of radiation was similar to light, but there was no evidence of refraction of the X-rays, thus it was not possible to assume that the radiation could consist of transverse waves as the light. The turning point on the understanding of the nature of the X-rays was given by Max von Laue, [7]. For the first time, illuminating a crystal with a thin X-ray beam, a pattern of spots was observed on a photographic film

positioned around the crystal. Laue understood that this pattern was the result of an interference phenomenon. The discovery of X-ray diffraction on crystals proofed that the X-ray radiation was identical to light but with a much shorter wavelength. Moreover, the discovery of Laue gave the start to direct measurements of the distance between atoms in a crystal. By using diffraction on a crystal it was possible to perform measurements of X-ray spectroscopy. Max von Laue was awarded with the Nobel price in 1914 [3].

Nowadays, the X-ray radiation is defined as the part of the electromagnetic spectrum covering an energy range between 100 eV and 100 keV. The scientific community usually divides this range in two subsets: soft X-rays and hard X-rays, see Table 1.1.

This distinction is bases on the fact that air is transparent to hard X-rays, while the soft X-ray are strongly attenuated in air. For this reason the soft X-ray experiments need to be performed in a vacuum environment, nowadays ultra-high vacuum (UHV).

	Soft X-ray		Hard X-ray
Energy	0.1 keV – 5 keV		5 keV – 100 keV
Wavelength	12 nm – 0.25 nm		0.25 nm – 0.12 nm

Table 1.1: Definition of hard and soft-X-rays.

Although in nature different kinds of X-ray sources exist (mainly radionuclide decays and astrophysical phenomena), X-rays are artificially produced with different techniques. Also the first source used by Röntgen was an artificial source. Nowadays, due to the high demands on quality and intensity of X-ray from the scientific community, big facilities dedicated to X-rays production are built. The next sections give an overview about X-ray production, starting from the radiation of an accelerated charge, introducing X-ray tubes and finally describing the basic principle of X-ray production in big facilities.

1.2 X-ray tubes

The first X-ray source used by Röntgen, and which lead to the discovery of the X-rays, was a Crookes tube. The working principle of this vacuum X-ray device is similar to the modern one: electrons are extracted from a cathode, accelerated via electric field and finally hit a target located at a certain distance.

In order to extract the electrons from the cathode it is possible to use different methods. Here the cold cathode and the hot cathode methods will be described. Figure 1.1 shows the difference between the two techniques.

In a tube with a cold cathode, like the Crookes tube, the residual gas in the tube gets ionized due to the high voltage applied between the cathode and the anode. Typical values of voltage range from a few kV to 100 kV. The ions (positively charged) are attracted by the cathode (negatively charged), and by hitting the metal they deposit energy to its surface. If during this process the energy acquired by the electrons of the metal is higher
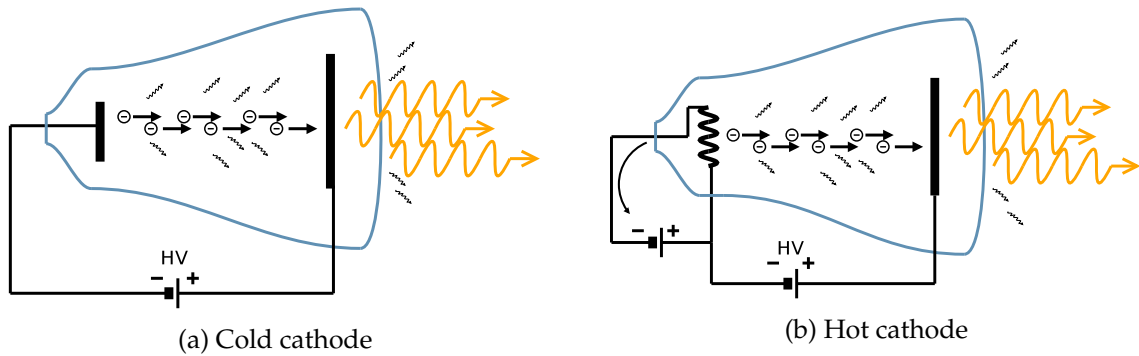
(a) Cold cathode   (b) Hot cathode

Figure 1.1: A sketch of cathodic tubes, (a) is a cold cathode tube, and (b) is a hot cathode tube. In both cases the electrons are accelerated by the high voltage applied between the cathode and the anode. The hot cathode tube has a filament, a resistor heated up by a current. In both sketches, the orange arrows represent the X-rays, and the black small arrows represent optical light.

than the minimal energy (workfunction) needed to remove an electrom from the solid to a point immediately outside the surface, electrons will be knocked out from the metal surface, see also Section 1.5.1. These electrons are in turn attracted by the anode and constitute the cathodic rays.

The hot cathode is a method used for improving the efficiency of electron extraction from the cathode. In a hot cathode, the cathode is heated to emit electrons, this phenomenon is called thermionic emission [9]. Electrons are emitted as the thermal energy exceeds the workfunction of the material, which is in general a filament. In this way, much more electrons than in a cold cathode are emitted from the same surface area.

Once electrons are extracted from the cathode, the high voltage field accelerates them towards the direction of the anode. X-rays are generated by the quick deceleration of the electrons on the anode. The high-energy electrons can also excite electron bounds in the inner shell of the atom. The reassessment can cause emission of photons. The radiation emitted by the electrons while decelerating is known in literature with the german word *Bremsstrahlung* [10] (literally *brake radiation*). The Bremsstrahlung radiation presents a continuum spectrum. An example is shown in Figure 1.2.

1.3 Radiation of an accelerated charge

The artificial sources of X-rays exploit the fact that, as any electrically charged particle, accelerated electrons generate electromagnetic radiation. In classical electrodynamics, the total emitted power of an accelerated charge is given by the Larmor equation, [11]. A short description is given below, a rigorous derivation and the details can be found in Classical Electrodynamics books, [11].

The Larmor equation for the non-relativist case, for a particle with charge q, mass m and acceleration a, reads:
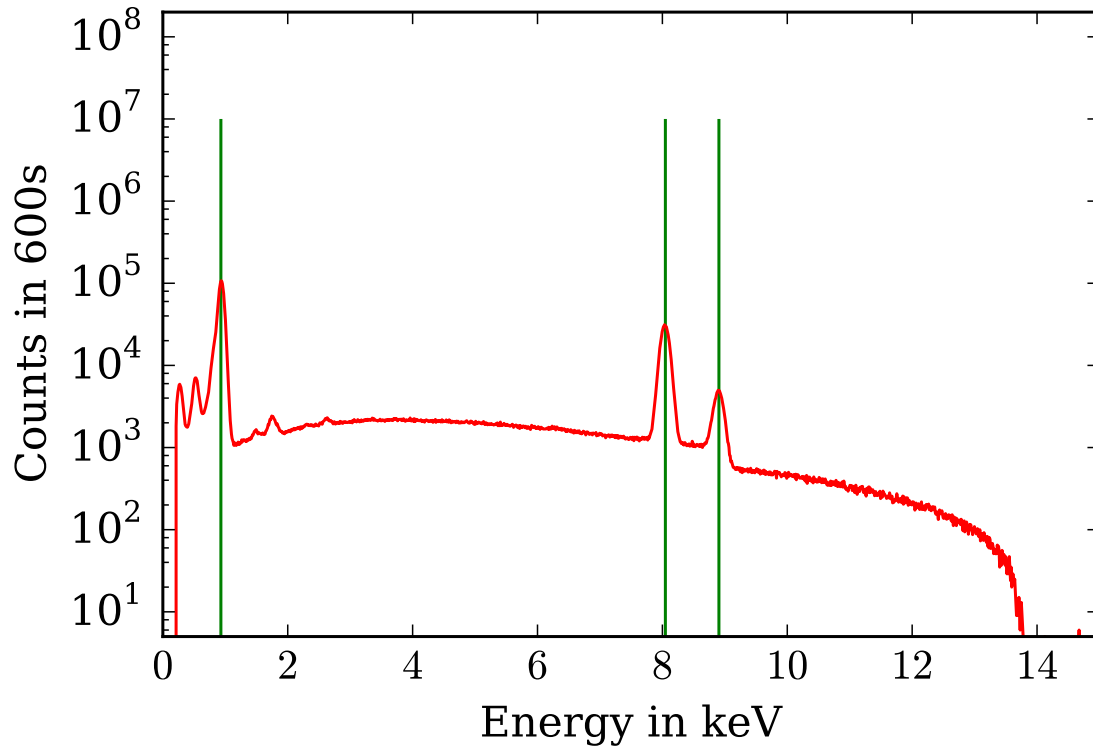
Figure 1.2: An energy spectrum generated with PANTER, a X-ray tube device used for test and calibration of the XFEL.EU detectors, [8]. The target of the tube is selectable and in this case was copper. In the plots are visible, the characteristic peaks of the copper $Cu(K_\alpha) = 8.0\,\text{keV}$, $Cu(K_\beta) = 8.9\,\text{keV}$, $Cu(L_{\alpha,\beta}) = 0.9\,\text{keV}$ and the continuum background, which is the bremstrahlung radiation. The maximum energy of the bremstrahlung is determined by the voltage used, in the X-ray tube. Courtesy of N. Raab, Detector Group, European XFEL.

$$P = \frac{2}{3} \frac{q^2}{4\pi\varepsilon_0 c^3} |a|^2 . \tag{1.1}$$

In the relativistic case, Equation 1.1 becomes:

$$P = \frac{2}{3} \frac{q^2}{4\pi\varepsilon_0 c} \gamma^6 \left[(\dot{\beta})^2 - (\beta \times \dot{\beta})^2 \right] , \tag{1.2}$$

where $\beta = v/c$ and $\gamma = \frac{1}{\sqrt{1-\beta^2}}$.

This equation can also be written by splitting the acceleration vector into its parallel and perpendicular components to the speed, $(v \cdot \dot{v} = v \cdot a_\parallel)$ and $(v \times \dot{v} = v \cdot a_\perp)$, [12]. In this way the formula can be written as:

$$P = \frac{2}{3} \frac{q^2}{4\pi\varepsilon_0 c^3} \gamma^4 \left[a_\perp^2 + \gamma^2 a_\parallel^2 \right] . \tag{1.3}$$

Equation 1.3 in non-relativistic case ($\gamma \to 1$) can be written as Equation 1.1.

In the case of linear motion,

$$a_\parallel = a , \\ a_\perp = 0 , \tag{1.4}$$

$$P = \frac{2}{3} \frac{q^2}{4\pi\varepsilon_0 c^3} \gamma^6 a_\parallel^2 . \tag{1.5}$$

In the case of circular motion, the acceleration is perpendicular to the speed:

$$a_\parallel = 0 , \\ a_\perp = \frac{v^2}{R} . \tag{1.6}$$

Therefore, Equation 1.3 becomes:

$$P = \frac{2}{3} \frac{q^2}{4\pi\varepsilon_0 c^3} \gamma^4 \left(\frac{v^2}{R} \right)^2 = \frac{2}{3} \frac{q^2}{4\pi\varepsilon_0} c\gamma^4 \frac{\beta^4}{R^2} = \frac{2}{3} \frac{q^2 c}{4\pi\varepsilon_0} \left(\frac{E}{mc^2} \right)^4 \frac{\beta^4}{R^2} . \tag{1.7}$$

which for relativistic speed, $\beta \to 1$, can be written as:

$$P \simeq \frac{2}{3} \frac{q^2 c}{4\pi\varepsilon_0} \left(\frac{E}{mc^2} \right)^4 \frac{1}{R^2} . \tag{1.8}$$

Therefore the emitted power of a charged particle moving in a circular trajectory scales with $\sim 1/R^2$.

Thus, the larger the radius of curvature is, the lower power is emitted. At the limit of linear uniform trajectory no radiation is emitted. Viceversa, the smaller the radius of curvature, the higher the emitted radiation. The radiation of a particle in a circular trajectory is commonly called synchrotron radiation.

Equation 1.3 plays an important role in the description of the production of X-rays, for example in synchrotron and applications involving undulators.

1.4 X-ray production in big facilities

In big facilities such as synchrotrons or free-electron lasers, X-rays are produced from electrons of high energy passing through an undulator system, [13]. The working principle of these devices is described in this section.
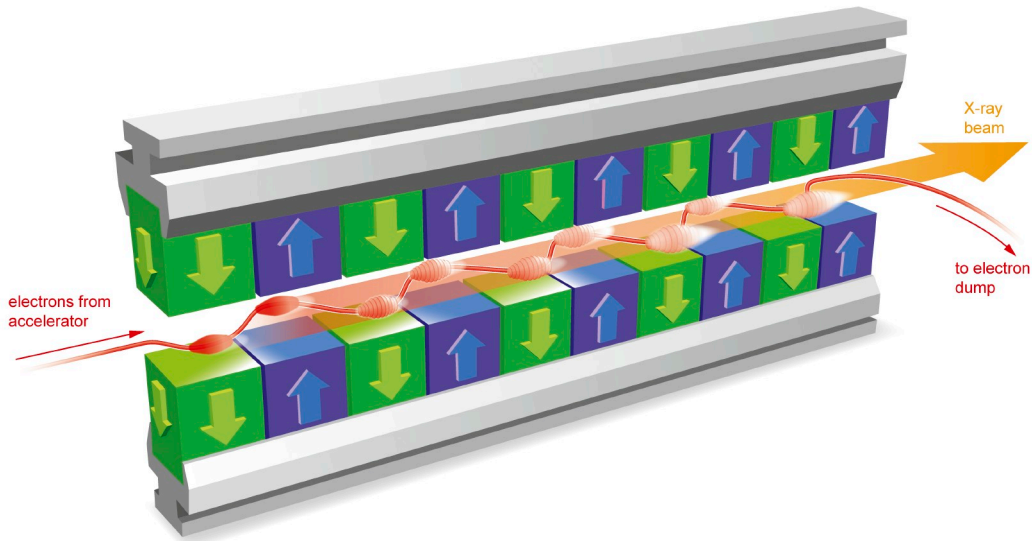

Figure 1.3: A 3D scheme of an undulator. Copyright European XFEL, [5].

The undulators are composed by two rows of magnets, hold by arms which set the distance between the two rows. The magnets are positioned with an alternate polarity so that the magnetic field is oscillating along the undulator, see Figure 1.3. The electrons, previously accelerated by a synchrotron or linac, pass through the undulator system. The alternate magnetic field accelerates them transversally, driving them into a sinusoidal trajectory. The acceleration of electrons produces photons. Figure 1.3 shows a 3D sketch about the undulator working principle.

The magnetic field of an undulator can be approximated as having a sinusoidal intensity:

$$|\boldsymbol{B}| = B_y(z)\hat{\boldsymbol{u}}_y = B_0 sin\left(\frac{2\pi}{\lambda_u}\right) , \qquad (1.9)$$

where B_0 is the maximum intensity of the magnetic field, $\hat{\boldsymbol{u}}_y$ is the unit vector along the y-axis. λ_u is the distance along the undulator between two magnets with the same polarity (period legth). Figure 1.4 shows a sketch of the model used with the axis.

The electrons enter in the undulator after having been accelerated by the synchrotron or a linac to a relativistic speed so $v \simeq c$. According to the Lorentz law, the force generated by a magnetic field on a charge of a given speed is perpendicular to the velocity, so the acceleration of the electron can be written as:

$$|\boldsymbol{a}| = a_\perp \hat{\boldsymbol{u}}_\perp = \frac{eBc}{\gamma m_e} \,, \tag{1.10}$$

where B is the magnitude of the component of the mangnetic field perpendicular to the velocity of the electron; m_e is the electron mass; and $\hat{\boldsymbol{u}}_\perp$ is the unit vector perpendicular to the velocity $\boldsymbol{v}$; the Lorentz factor $\gamma = \frac{1}{\sqrt{1-\beta^2}}$, where $\boldsymbol{\beta} = \boldsymbol{v}/c$.
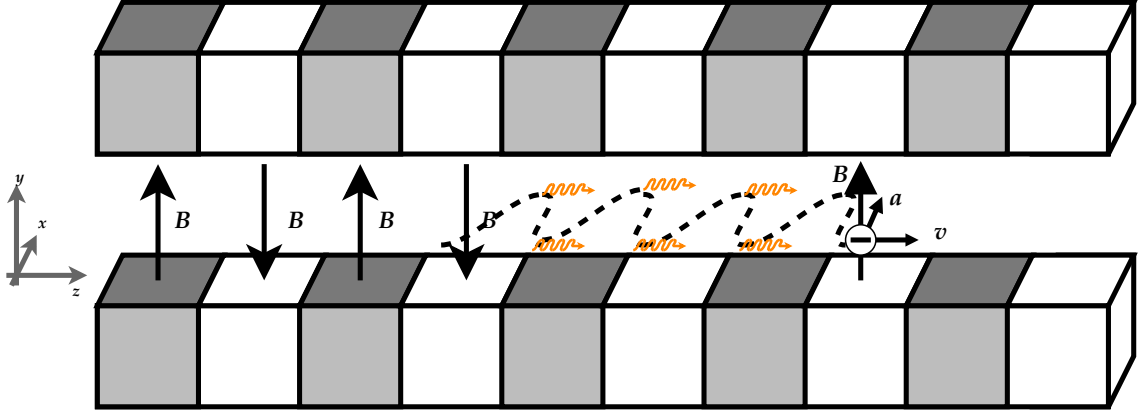

Figure 1.4: Sketch showing an undulator. The arrows indicate the direction of the magnetic field; the dashed line is the electron trajectory and the photon are drawn as orange waves.

According to Larmor's Equation (Equation 1.3), the total power emitted by an accelerating electron is given by

$$P = \frac{2}{3} \frac{e^2}{4\pi\varepsilon_0 c^3} \gamma^4 \left[a_\perp^2 + \gamma^2 a_\parallel \right] \,, \tag{1.11}$$

which, by including the acceleration as expressed in Equation 1.10, becomes

$$P = \frac{2}{3} \frac{e^4 \gamma^2}{4\pi\varepsilon_0 c m_e^2} B^2 \,. \tag{1.12}$$

Thus, the average emitted power is

$$<P> = \frac{2}{3} \frac{e^4 \gamma^2}{4\pi\varepsilon_0 c m_e^2} <B^2> \,. \tag{1.13}$$

From the assumption of Equation 1.9, the average $<B^2>$ can be written as

$$<B^2> = \frac{B_0^2}{2} \,, \tag{1.14}$$

Therefore, including 1.14 into 1.15, the average total emitted power can be written as

$$<P> = \frac{2}{6} \frac{e^4 \gamma^2}{4\pi\varepsilon_0 c m_e^2} B_0^2 \,. \tag{1.15}$$

Equation 1.15 represents the average power emitted by a single electron passing through a ideal undulator. This type of radiation is called *spontaneous undulator emission*, [13].

An important parameter used to describe an undulator is the *K*-parameter, which is defined as

$$K = \frac{eB_0\lambda_u}{2\pi m_e c} = 0.934\, B_0[T]\, \lambda_u[cm]\,, \tag{1.16}$$

where B_0 is the maximum intensity of the magnetic field and λ_u is the period length of the undulator, as defined in Equation 1.9.

By knowning the K parameter, the central wavelength of the produced X-ray radiation can be extracted [13] as

$$\lambda_{ph} = \frac{\lambda_u}{2\gamma^2}\left(1 + \frac{K^2}{2}\right)\,, \tag{1.17}$$

By using the definition of the *K*-parameter (Equation 1.16) the average emitted power can be rewritten as

$$<P> = \frac{e^2 c \pi^2 \gamma^2}{3\varepsilon_0 \lambda_u^2}K^2\,. \tag{1.18}$$

The undulators are built typically with a fixed array of magnets at a given distance between them, so λ_u is typically a fixed parameter. On the other hand, it is possible to control and to set the distance between the arms holding the magnet arrays, which defines the intensity of B_0. So by modifying the arm position it is possible to tune the *K*-parameter, of the undulator and therefore to change the energy of the emitted radiation.

The power emitted by a beam composed by N_e electrons passing through an undulator scales as [14]

$$P \propto N_e + N_e^2|\mathcal{B}|^2 \tag{1.19}$$

where the bunching factor $\mathcal{B}$ is defined as [14]

$$\mathcal{B} = \frac{1}{N_e}\sum^{N_e} e^{i\Theta_n}\,, \tag{1.20}$$

where $\Theta_n = 2\pi\left(\frac{z_n - ct}{\lambda_{ph}} + \frac{z_n}{\lambda_u}\right)$. z_n is the position of the n-th electron, λ_{ph} emitted photon wavelength and λ_u is the length of a period of the undulator. Θ_n represents the difference of between the electromagnetic-wave phase and the electron-oscillation phase.

Ideally, $|\mathcal{B}| = 1$ when all electrons are located in a single position, or positioned in micro-bunches with a distance of λ_{ph}. In this case the electrons emits coherently, and the main contribution to the emitted power is given by the quadratic part of formula 1.19. Therefore, in the case of $|\mathcal{B}| = 1$, the power emitted by a bunch of electron scales as $P \sim N_e^2$, as if the electrons bunched together would behave as a single charge.

The opposite case $|\mathcal{B}| \to 0$ happens the electron spatial distribution is quasi-flat. In this case the quadratic part of Formula 1.19 becomes negligible, so the emitted power of a bunch of electrons with $|\mathcal{B}| \to 0$ scales as $P \sim N_e$.

The photon production, the distribution of the electrons and their energy distribution

are influence each other along the undulator [14]. In particular this process features a positive feedback loop, happening by the following steps:

1. the bunching of the electrons creates coherent radiation;

2. the coherent radiation induces an energy modulation in the electron bunch;

3. the energy modulation induces the bunching of the electron;

and the loop closes in 1. Due to this process,the bunching, the energy modulation and the emitted power P increase exponentially along the undulator length up to saturation. Figure 1.5 shows electron distribution, from a random distribution up to the formation of micro bunches.

In the X-ray free electron lasers as XFEL.EU, the photons generated by spontaneous emission in the first part of the undulator are used to modulate the distribution of the electrons downstream. The photons generated at the beginning of the FEL are used to seed the beam more downstream. This is process is called *self-amplified spontanous emission* (SASE), [13].
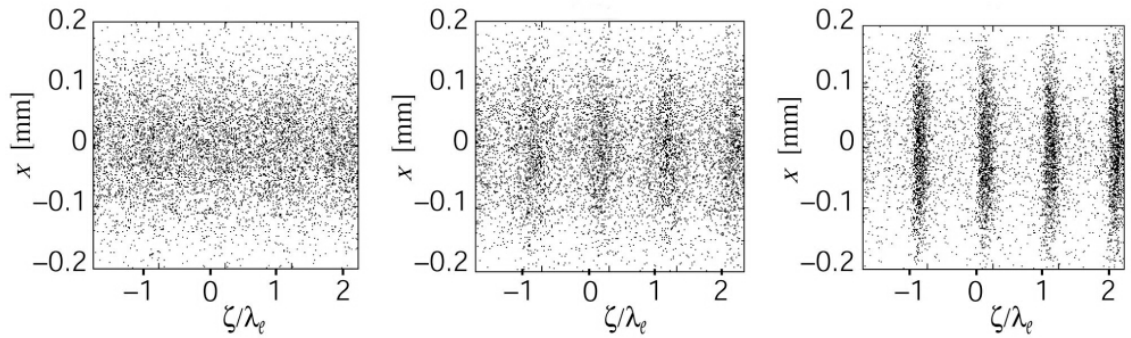
Figure 1.5: The micro-bunching formation: from a random distribution to the microbunching. The x-axis ζ/λ_e represents the ratio between the distance in λ_e units, where $\lambda_e = \lambda_{ph}$. Copyright HASYLAB DESY, [15].

In a 1-dimensional free electron laser model, the FEL equations [14] can be expressed as a function of the parameter ρ, the efficiency parameter, defined as

$$\rho = \left(\frac{K \Omega_P \lambda_u}{4 \cdot 2\pi c} \right)^{2/3} , \tag{1.21}$$

where K is the *K*-parameter of the FEL defined in Equation 1.16; λ_u is the length of the undulator period and Ω_P is the plasma frequency defined as

$$\Omega_P = \left(\frac{4\pi r_e c^2 n_e}{\gamma^3} \right)^{1/2} , \tag{1.22}$$

where r_e is the classical electron radius and n_e is the electron bunch density.

The efficiency parameter ρ can be used to approximate the saturation power

Figure 1.6: Energy emitted by the electron beam at a given position in the undulator. In the first part of the curve the low-gain regime is visible; then the exponential growth given by high-gain mode and then the saturation regime. Copyright HASYLAB DESY, source [15].
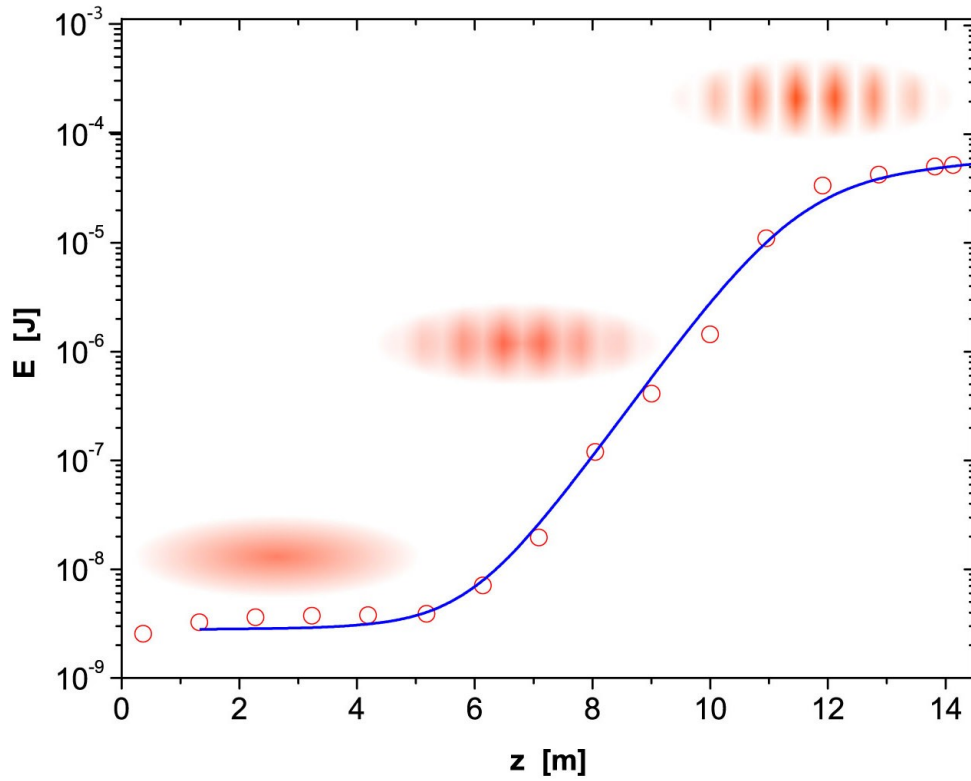
$$P_S \simeq \rho\, P_{beam} = \rho E_{beam}\, I_{beam}/e\,, \tag{1.23}$$

where E_{beam} is the electron beam energy, I_{beam} the electron beam current and e the electron charge.

The emitted power along an undulator increases exponentially. The parameter defining the exponential growth is the gain length L_G, which in a 1-dimensional model is approximated as [14]

$$L_G = \frac{\lambda_u}{4\pi\sqrt{3}\,\rho}\,. \tag{1.24}$$

In the first part, the undulator works in the low-gain regime. The initial distribution of the electrons is given by the injector and the process of acceleration. The injector – depending on the facility – can be either a thermionic cathode or a photocathode. In both cases, the space and energy distribution of the electron beam is broad. For this reason at the beginning of the undulator the emission features low intensity, a broad energy

spectrum and a broad angle of emission, too. Despite the low intensity, the photons produced by emission in the initial part of the undulator act on the electron beam, increasing its energy and space modulation. When the distance of the undulator is long enough, the free electron laser operates in the high-gain regime and the power emission can be approximated by an exponential equation as [14]

$$P(z) = P_0 e^{z/L_G} \, , \tag{1.25}$$

where z is the distance from the beginning of the undulator and P_0 is the emitted power at the beginning of the undulator. The growth stops at saturation, when the emitted power is P_S.

The exponential behavior of the energy emitted by an electron beam along the undulator is shown in Figure 1.6. At short distance, it is visible the low-gain regime, then the exponential behavior appears and finally the saturation regime kicks in.

1.5 Interaction of X-rays with matter

Photon interaction with matter proceeds via different processes depending on the energy of the incoming photon. Since the binding energy of the nucleons in an atom is about $\sim$ 1MeV, the minimum photon energy required for interacting with the nucleons is of the order of 1MeV. Therefore, at lower energy, as in the case of X-rays, only the electrons of the atom are involved in the interaction with the photons, [16].

This section describes the way X-ray photons interact with electrons in matter. The cross section values provided by NIST [17] [18] show that the most important contribution to the photon absorption cross section in the X-ray energy range is given by:

- Photoelectric absorption,

- Coherent scattering,

- Incoherent scattering.

As an example, the absorption cross-section of a photon hitting on silicon and the different subprocesses contributing to the cross section are shown in Figure 1.7.

1.5.1 Photoelectric absorption

In an isolated atom, the energy states allowed to be occupied by electrons are discrete, [19]. To excite an electron from an energy level E_B to an energy level E_A, a photon with an energy equal to the gap, $E_\gamma = \Delta E_{A-B} = E_A - E_B$, is needed. The process is schematically described in Figure 1.8.

The vacuum energy level is defined as the energy level where the electron can be considered free from the binding. The minimum energy needed to extract an electron from an atom is called commonly *workfunction*, [19].
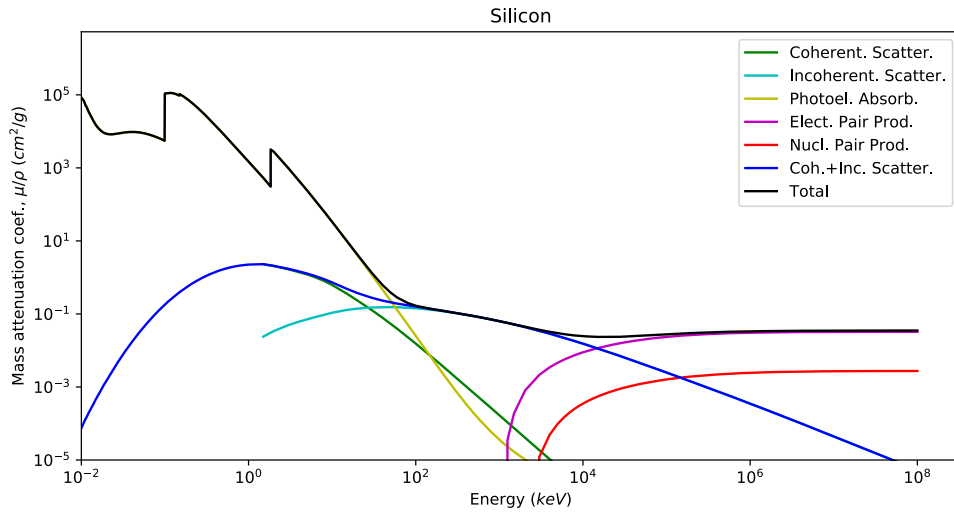
Figure 1.7: The mass attenuation coefficient for silicon. From 10^{-2} keV up to 1 keV data source NIST XCOM database [18]; from 1 keV up to 10^8 keV data source NIST FFAST database [17]. The different contributions to the cross section are shown in different colors.

The photoelectric absorption occurs when a photon, of high enough energy, knocks out an electron bound in the atom (or molecule). The incoming photon is completely absorbed and an electron is emitted from its energy shell. Defining the vacuum level as $E_{vacuum} = E_0 = 0$, the energy of the emitted electron is:

$$E_{e^-} = E_\gamma - |E_{level}| . \tag{1.26}$$

For X-ray photons, the cross section of interaction with matter is dominated by photoelectric absorption. The emitted electron typically interacts with other atoms in the material exciting their electrons. As such, this process is fundamental for the X-ray detection, see Section 1.7.
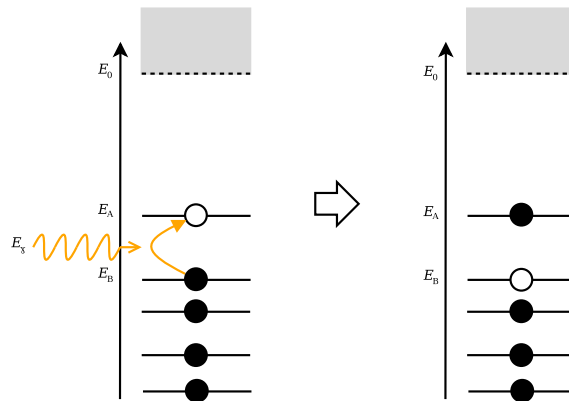

Figure 1.8: Photon absorption. A photon of energy E_γ is absorbed by an electron of the energy level E_B, which then jump to the energy level $E_A = E_B + E_\gamma$.
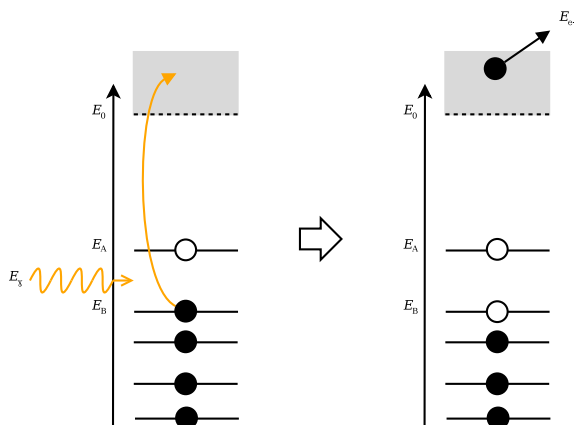
Figure 1.9: Photoelectric emission due to photon absorption. A photon of energy E_γ is absorbed by an electron at the energy level E_{level}. The electron gets enough energy to be freed from the material. The energy of the emitted electrons is $E_{e^-} = E_\gamma - |E_{level}|$.

1.5.2 Coherent scattering

The coherent scattering occurs when the incoming and the outgoing photon have the same energy and the phase relation, between the incoming and the outgoing photon is conserved. Since the relation between the phase of the incoming and outgoing photon is fixed, it is possible to observe diffraction [20]; a description of the diffraction process is given in Section 1.6. The coherent scattering includes Thomson scattering, Rayleigh scattering and other phenomena, such as the resonant elastic scattering explained Section 1.5.4.

The **Thomson scattering** [16] occurs when a low energy photon scatters on a free electron. The cross-section of this process is relevant (different from zero) only if the energy of the incoming photon is lower than the mass (energy at rest) of the particle it scatters onto. In case of scattering on an electron the energy threshold is $E_\gamma \leq 510$ keV. In this scattering, there is no energy transfer but only a change in the photon direction.

The **Rayleigh scattering** [21] is a process which occurs when a photon interacts with a whole cloud of electrons of an atom (or an object) whose dimensions are negligible in comparison to the photon wavelength. As in the Thomson scattering, the photon is deviated but maintains the same energy and phase.

1.5.3 Incoherent scattering

The **incoherent scattering** occurs when the phase relation between the incoming and outgoing photon is not conserved, for instance when the outgoing photon does not have the same energy as the incoming photon. A typical case is the **Compton scattering** [16], an elastic scattering between a photon and a free electron. An electron bound in an atom can be considered free when the binding energy is negligible in comparison to the energy of the incoming photon. In the Compton scattering a part of the energy of the photon

is transferred to the electron which recoils; the rest of the energy is given to the outgoing photon. Other cases of incoherent scattering will be described in the next Section.

1.5.4 Electronic transitions in matter

When a photon of energy $E_\gamma = E_{A-B}$ excites an electron to an energy level E_A, the electron can decade spontaneously back to a lower energy state by emitting a photon. This phenomenon is called **spontaneous emission**, [21]. If the lower energy state is the same the electron was originally occupying, the emitted photon has the same energy of the incoming photon. This process is schematically represented in Figure 1.10.
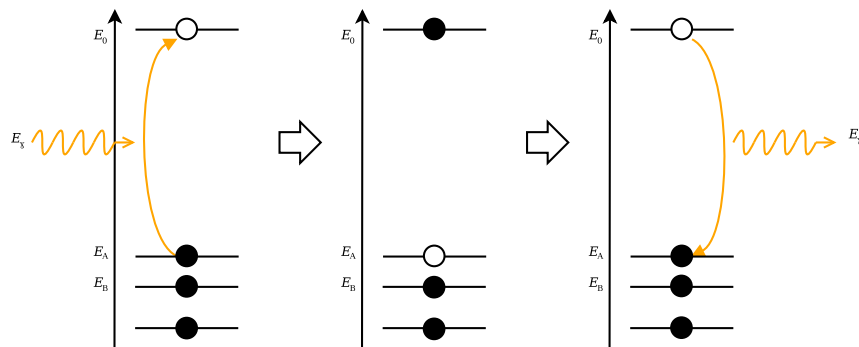
Figure 1.10: Spontaneous emission. A photon interacts with an electron at the energy level E_B. The electron is excited to the energy level E_A. It can then decay back to the level E_B emitting a photon of energy E_γ.

When a photon with high enough energy kicks out an electron from a deep shell, a cascade of decays can occur. Radiative decays are associated with the emission of photons. In structures like crystals or molecules, also non-radiative decays can occur; in this case, the decay is mediated by a phonon exchange in the structure.
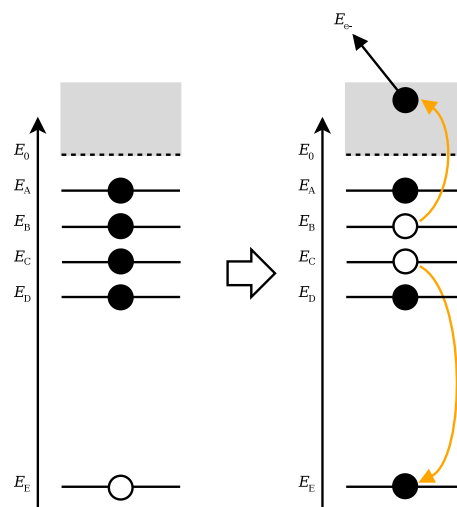
Figure 1.11: Auger electrons emission. An electron energy level E_C decays to a level E_E. The decay is not radiative and the energy is transferred to an electron E_B which is emitted.

A special case of spontaneous decay is given by the Auger effect, shows in Figure 1.11. In most of the cases, when an electron from a inner shell decays into a deep-inner shell, it releases energy as photons. But in the case of Auger effect, the energy is transferred to an electron of a higher shell, which is emitted. The emitted electron is called **Auger electron** [16].

In contrast to the spontaneous emission, a phenomenon exits called **stimulated emission**, [21]. It occurs when a photon with energy $E_\gamma = \Delta E_{A-B}$ interacts with an electron, which is already in the excited state of energy E_A. In this case an electron is stimulated to decay to the lower state E_B, by emitting a further photon which has the same energy, phase and direction of the incoming photon, see Figure 1.12.
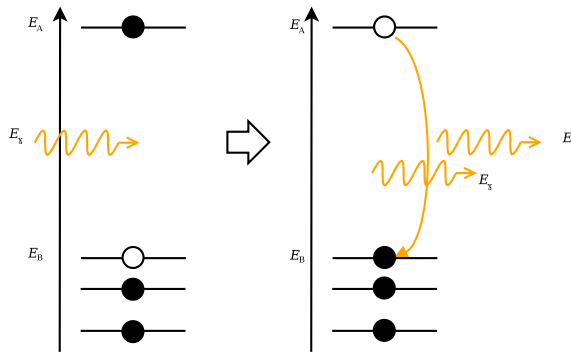
Figure 1.12: Stimulated emission. A photon of with energy E_{A-B} stimulates the decay of the electron from A to B emitting another photon with same energy, phase and direction of E_{A-B}.

1.6 Diffraction and Fourier Transform

In this section, the link between diffraction, Fourier transform [22] and reciprocal lattice [19] is introduced and described.

In general, a function $f(x)$, where x is a vector in the real space, can be transformed into a function $\hat{f}(\omega)$, where ω is a vector in the frequency space using the Fourier transform ($\mathcal{F}$). Viceversa, by applying $\hat{f}(\omega)$ the inverse Fourier transform ($\mathcal{F}^{-1}$) is possible to recover the original function $f(x)$.

The direct Fourier transform is defined as

$$\hat{f}(\omega) = \mathcal{F}\left[f(r)\right], \tag{1.27}$$

$$\hat{f}(\omega) = \int_V f(r)e^{-i\omega r} dV, \tag{1.28}$$

where dV represent the volume element, and V the volume in the real space where f is defined. The inverse Fourier transform becomes

$$f(\boldsymbol{r}) = \mathcal{F}^{-1}\left[\hat{f}(\boldsymbol{\omega})\right] \tag{1.29}$$

$$f(\boldsymbol{r}) = \frac{1}{V_\omega} \int_{V_\omega} \hat{f}(\boldsymbol{\omega}) e^{i\boldsymbol{\omega} \boldsymbol{r}} dV_\omega, \tag{1.30}$$

where dV_ω represents the volume element, and V_ω the volume in the frequency space where $\hat{f}$ is defined.

In order to show the link between the Fourier transform and the diffraction process, a simple model is used. The model is shown in Figure 1.13. An incoming light wave, assumed an ideal plane wave, scatter on a target. The target is an object composed by identical atoms located each at a position indicated by the vector $\vec{r}_N$. It is assumed that each atom of the target has a single free electron on which the photon scatters in an ideal elastic and coherent way.
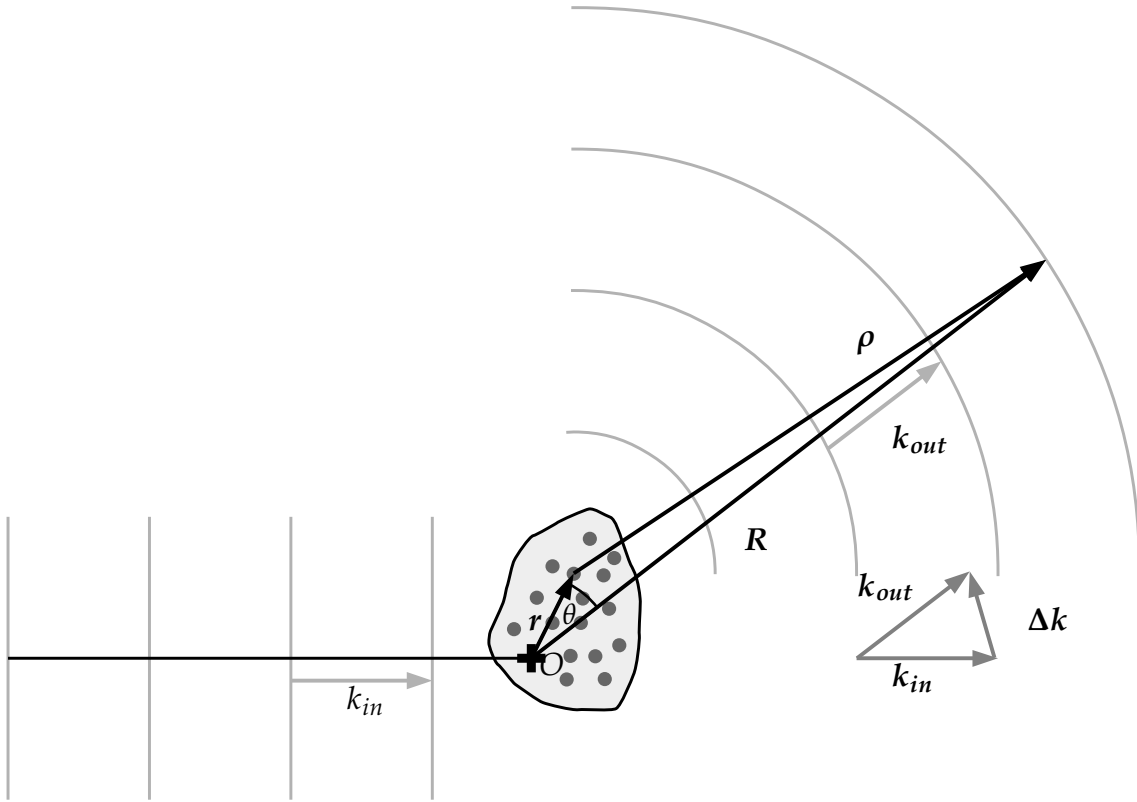
Figure 1.13: A simple model of the diffraction. $\boldsymbol{k}_{in}$ is the incoming wavevector, $\boldsymbol{k}_{out}$ is the outcoming wavevector, $\boldsymbol{\Delta k}$ is the transfer momentum, $\boldsymbol{r}$ is the position of the atom, $\boldsymbol{R}$ is the position of the observer, $\boldsymbol{\rho}$ is the position of the observer with respect to the atom position.

The electric field of the incoming light wave can be described with the following formula:

$$\boldsymbol{E}_{in}(\boldsymbol{r}, t) = \boldsymbol{E}_0 e^{-i(\boldsymbol{k}\cdot\boldsymbol{r} - \omega t + \phi)}, \tag{1.31}$$

where E_0 is the intensity of electric field; r is the vector defining the position with respect to the origin of the axis; k is the wave-vector having the direction of the wave and $\omega = vk$, where v is the speed of light in the mean ($v = c/n_{diffraction}$, where c is the speed of light and $n_{diffraction}$ is the diffraction index of the mean); ϕ represents the initial phase of the light wave.

The wave-vector magnitude is

$$k = \frac{2\pi}{\lambda} = \frac{E_{photon}}{\hbar c}, \qquad (1.32)$$

where λ is the wavelength, $\hbar$ is the reduced Planck constant and E_{photon} is the energy of the photon.

Due to the assumption of elastic scattering, the incoming photon has the same energy of the outgoing photon,

$$|k_{in}| = |k_{out}| = k. \qquad (1.33)$$

Due to the assumption of coherent scattering, the relation between the phase of the incoming and outgoing photon is fixed. For this reason the phase ϕ will be omitted in the formulas. Moreover, in order to simplify the calculation, also the temporal part ωt and the polarization of the wave will be neglected. Under this assumption, the Equation 1.31 reduces to:

$$E_{in}(r, t) \propto e^{-ik_{in} \cdot r}. \qquad (1.34)$$

The incoming photon interacts with the electrons in the atoms and it scatters in a coherent way emitting a spherical wave. The electric field of the emitted spherical wave is expressed as:

$$E_{dif}(\rho, t) \propto \frac{e^{k_{out}\rho}}{\rho} \propto e^{k_{out}\rho}, \qquad (1.35)$$

where ρ is the distance vector from the atom to the observation point.

For each single atom the emitted outgoing wave is

$$E_{out}(r, t) \propto E_{dif}(\rho, t) E_{in}(r, t), \qquad (1.36)$$

that is

$$E \propto e^{-ik_{in} \cdot r} e^{k_{out}\rho}. \qquad (1.37)$$

In order to write Equation 1.36 in the coordinate of the observer, the vector R is introduced. It defines the position of the observer with respect to the axis origin. In order to simplify the calculations, it is assumed also that the observer is *far away* from the sample, namely, the dimensions of the target are negligible in comparison to the distance between

the target and the observer, $R \gg r$. This approximation allows considering $\rho \parallel R$. Thus, due to these geometry assumptions,

$$\rho = R - r \cos \theta, \tag{1.38}$$

so the Equation 1.37 can be rewritten as

$$E \propto e^{-ik_{in} \cdot r} e^{ik_{out} R} e^{-ik_{out} r \cos \theta}. \tag{1.39}$$

The $e^{ik_{out} R}$ factor does not play a role in the interference phenomenon as it is a constant factor.

As the scalar product between two vectors is defined as

$$r \cdot k_{out} = k_{out} r \cdot cos\theta, \tag{1.40}$$

Equation 1.39 becomes

$$E \propto e^{-ik_{in} \cdot r} e^{ik_{out} \cdot r}. \tag{1.41}$$

Defining the transferred wavevector as

$$\Delta k \equiv k_{out} - k_{in}, \tag{1.42}$$

Equation 1.41 becomes

$$E_{out}(\Delta k) \propto e^{-i\Delta k \cdot r}, \tag{1.43}$$

Due to the superimposition principle [20], considering all the atoms in the target the resulting outgoing wave light can be expressed as

$$E_{out}^{tot}(\Delta k) \propto \sum_{N_{el}} e^{-i\Delta k \cdot r_N}. \tag{1.44}$$

This formula can be extended to the continuum, by introducing the electronic density, $n_{el}(r) = \frac{dN_{el}}{dV}$, N_{el} being the number of free electrons in the volume V where they are included.

Equation 1.44 can then be rewritten as [19]:

$$E_{out}^{tot}(\Delta k) \propto \boxed{F(\Delta k) = \int_V n_{el}(r) e^{-i\Delta k \cdot r} dV} \tag{1.45}$$

This is the definition of the electronic form factor of an object sample. According to Equation 1.28, this is the Fourier transform of the electronic density.

Thus, ideally, by knowing $E_{out}^{tot}(\Delta k)$ it is possible to extract the electronic density of the target $n_{el}(r)$ (see Equation1.30):

$$n_{el}(\boldsymbol{r}) \propto 1/V_k \int_{V_k} E(\Delta \boldsymbol{k}) e^{i\Delta \boldsymbol{k} \cdot \boldsymbol{r}} d\Delta \boldsymbol{k} \,. \tag{1.46}$$

In other words, in the ideal case it is possible to reconstruct the spatial electronic distribution of a target by knowing the form factor, namely the electric field of the wave emitted when a target is hit by a light wave.

In reality, the measured physical quantity is $I(\Delta \boldsymbol{k})$, the intensity of light (number of photons), which corresponds to the module squared of the electric field,

$$I(\Delta \boldsymbol{k}) \propto |E(\Delta \boldsymbol{k})|^2 \propto |F(\Delta \boldsymbol{k})|^2 \,. \tag{1.47}$$

The inversion of this formula is not trivial, as the information regarding the phase is lost due to the the presence of the module. In order to solve this type of problems phase retrieval algorithms are used [23].

1.6.1 Scattering on crystal

In the last subsection the relation between the Fourier transform and the form factor has been explained. In this section a particular case will be illustrated. It describes what happens when X-rays scatter on a crystal. Crystals are solid materials which present a periodic internal structure, namely, they are composed by the same primitive cell repeated with a regular pattern on a lattice. The mathematical description of the periodic structure of a crystal is given by a the Bravais lattice, [19].

1.6.2 Bravais lattice

The Bravais lattice [19] (in a three dimensional space) is defined as the set of positions described by the equation

$$\boldsymbol{R_n} = n_1 \boldsymbol{a_1} + n_2 \boldsymbol{a_2} + n_3 \boldsymbol{a_3} \,, \tag{1.48}$$

where $\boldsymbol{a_1}, \boldsymbol{a_2}, \boldsymbol{a_3}$ are non-coplanar vectors, named *primitive vectors* of the Bravais lattice; n_1, n_2, n_3 are integer numbers, the notation $\boldsymbol{n}$ indicates the three indexes in a vector representation.

In case of a bi-dimensional lattice, $\boldsymbol{a_3} = 0$ and $\boldsymbol{a_1}, \boldsymbol{a_2}$ are non-parallel vectors. The so-called *primitive* cell is the smallest volume (or surface) unit which can describe any part of the lattice by using only translations.

Assuming that the primitive cell has an electronic density $n_{el}(\boldsymbol{r})$, due to the periodic pattern of the lattice, the electronic density satisfies the equation:

$$n_{el}(\boldsymbol{r}) = n_{el}(\boldsymbol{r} + \boldsymbol{R_n}) \,. \tag{1.49}$$

Due to the periodic pattern of the lattice, the function $n_{el}(\boldsymbol{r})$ can be written as Fourier series, [19]:

$$n_{el}(\boldsymbol{r} + \boldsymbol{R_n}) = \sum_m n_{G_m}^\star e^{iG_m \cdot r} e^{iG_m \cdot R_n} . \tag{1.50}$$

where the coefficients $n_{G_m}^\star$ can be calculated by the Fourier transform

$$n_{G_m}^\star = \mathcal{F}\left[n_{el}(\boldsymbol{r} + \boldsymbol{R_n}) \right] . \tag{1.51}$$

Equation 1.50 holds for each value of R_n, including $R_n = 0$. Putting $R_n = 0$ in the Equation 1.50 and considering Equation 1.49, it follows that:

$$e^{iG_m \cdot R_n} = 1 , \tag{1.52}$$

which is equivalent to [19]

$$\boxed{\boldsymbol{G_m} \cdot \boldsymbol{R_n} = 2\pi N} , \tag{1.53}$$

where N is a positive or negative integer number.

The solutions of Equation 1.53 in a 2D space are,

$$\begin{cases} \boldsymbol{G_m} = m_1 \boldsymbol{b_1} + m_2 \boldsymbol{b_2} \\ \boldsymbol{b_j} \cdot \boldsymbol{a_i} = 2\pi \delta_{ij} \end{cases} , \tag{1.54}$$

$$\begin{cases} \boldsymbol{b_1} = 2\pi \frac{a_2 \times \hat{v}}{|a_1 \times a_2|} \\ \boldsymbol{b_2} = 2\pi \frac{\hat{v} \times a_1}{|a_1 \times a_2|} \end{cases} , \tag{1.55}$$

where $\boldsymbol{R_n} = n_1 \boldsymbol{a_1} + n_2 \boldsymbol{a_2}$, and $\hat{v}$ is a unitary vector perpendicular to the plane defined by the two vectors $\boldsymbol{a}_1$ and $\boldsymbol{a}_2$;

Similarly, the solutions for $\boldsymbol{G_m}$ in a 3D space are, [19]:

$$\begin{cases} \boldsymbol{G_m} = m_1 \boldsymbol{b_1} + m_2 \boldsymbol{b_2} + m_3 \boldsymbol{b_3} \\ \boldsymbol{b_j} \cdot \boldsymbol{a_i} = 2\pi \delta_{ij} \end{cases} , \tag{1.56}$$

which translates into:

$$\begin{cases} \boldsymbol{b_1} = \frac{2\pi}{\Omega} (\boldsymbol{a_2} \times \boldsymbol{a_3}) \\ \boldsymbol{b_2} = \frac{2\pi}{\Omega} (\boldsymbol{a_3} \times \boldsymbol{a_1}) \\ \boldsymbol{b_3} = \frac{2\pi}{\Omega} (\boldsymbol{a_1} \times \boldsymbol{a_2}) \end{cases} , \tag{1.57}$$

where Ω is the volume of the primitive cell:

$$\Omega = \boldsymbol{a_1} \cdot (\boldsymbol{a_2} \times \boldsymbol{a_3}) . \tag{1.58}$$

The ensemble of the $\boldsymbol{G_m}$ vectors composes the *reciprocal lattice*. The Figure 1.14 shows an example of a 2D lattice and the corresponding reciprocal lattice. The primitive vectors

of the direct lattice and the corresponding transformed vectors in the reciprocal lattice are shown. The angle between the vectors a_1 and a_2, θ_a, in the reciprocal lattice becomes $\theta_b = 180 - \theta_a$.

Direct lattice   Reciprocal lattice
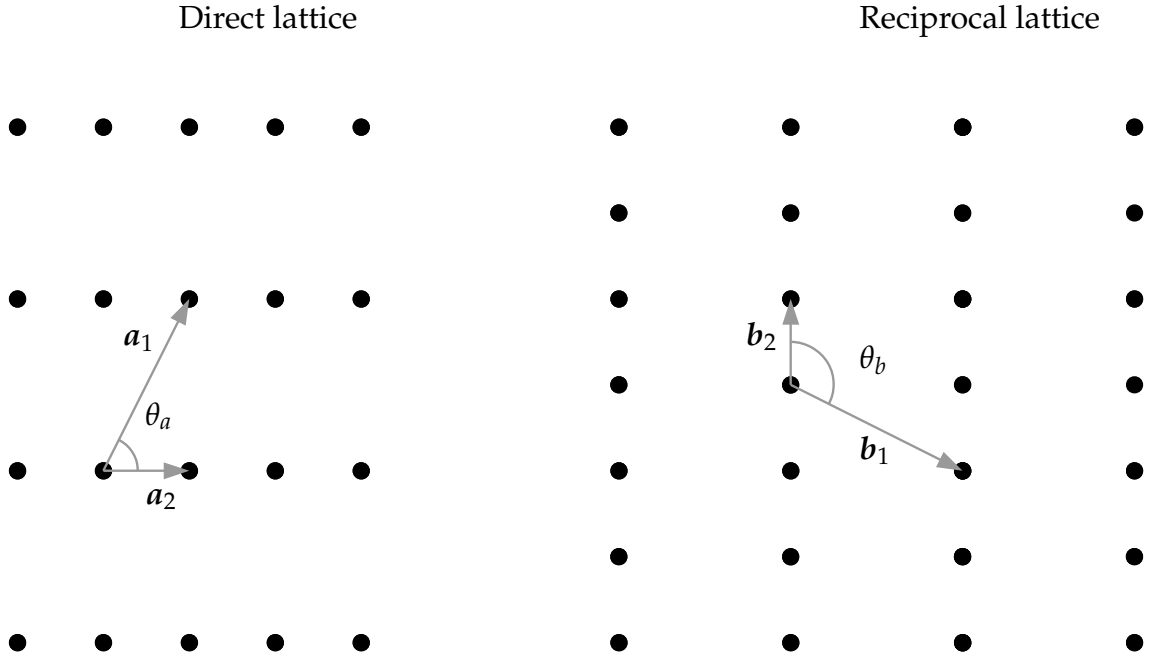
Figure 1.14: An example of how the primitive vector of a direct lattice (on the left) are transformed in the reciprocal lattice (on the right). The angle between the vectors, in the direct lattice, θ_a, in the reciprocal lattice becomes $\theta_b = 180 - \theta_a$.

1.6.3 Laue equations

Assuming a given electronic density $n_{el}(r)$, due to the periodic pattern of the lattice, the electronic density can be decomposed using the Fourier transform, [22],

$$n_{el}(r) = \sum_{G_m} n_{el}^\star(G_m)e^{iG_m \cdot r} . \tag{1.59}$$

Thus, the form factor can be calculated using the definition of Equation 1.45,

$$F(\Delta k) = \int_V n_{el}(r)e^{-i\Delta k \cdot r}dV , \tag{1.60}$$

$$F(\Delta k) = \int_V \sum_{G_m} n_{el}^\star(G_m)e^{iG_m \cdot r}e^{-i\Delta k \cdot r}dV , \tag{1.61}$$

$$F(\Delta k) = \sum_{G_m} n_{el}^\star(G_m) \int_V e^{i(G_m - \Delta k) \cdot r}dV . \tag{1.62}$$

Considering an infinite volume, Equation 1.62 becomes:

$$F(\Delta k) \simeq \sum_{G_m} n_{el}^{\star}(G_m) \delta(G_m - \Delta k). \tag{1.63}$$

The form factor becomes

$$F(\Delta k) = \begin{cases} n_{el}^{\star}(G_m) & if \quad \Delta k = G_m \\ 0 & if \quad \Delta k \neq G_m \end{cases}. \tag{1.64}$$

Therefore, in an ideal case the form factor is different from zero if

$$\boxed{\Delta k = G_m}. \tag{1.65}$$

This equation is the diffraction condition, called also *Laue's condition*, [19].

The indexes m_1, m_2, m_3, of the reciprocal lattice G_m are known as Miller indexes and they are usually denoted by the letters h, l, k. Equation 1.53 becomes

$$G_{hkl} \cdot R_n = 2\pi N, \tag{1.66}$$

which can be decomposed in three equations:

$$\begin{cases} G_{hkl} \cdot a_1 = 2\pi h \\ G_{hkl} \cdot a_2 = 2\pi k \\ G_{hkl} \cdot a_3 = 2\pi l \end{cases}. \tag{1.67}$$

Equations 1.67, using Laue's condition, can be written as

$$\begin{cases} \Delta k \cdot a_1 = 2\pi h \\ \Delta k \cdot a_2 = 2\pi k \\ \Delta k \cdot a_3 = 2\pi l \end{cases}, \tag{1.68}$$

defining the so-called *Laue equations*, [19].

The meaning of Equation 1.65 and 1.68 is the following: for photon scattering on a crystal with a defined lattice, the diffraction pattern, which is equivalent to the crystal form factor, corresponds to the vectors of the reciprocal lattice. In other words, in a coherent scattering on an ideal crystal, constructive interference occurs when the momentum transfered Δk corresponds to a vector of the reciprocal lattice G_m. An example is given in Section 1.6.5.

1.6.4 Bragg's law

The X-ray diffraction process can be further simplified introducing Bragg's law, [19]. Bragg's law, similarly to Laue diffraction, assumes that the photons scattered on the atoms creating spherical wave, which interfere with each other. The simplification of

Bragg's law consists in considering the interaction of photons as the reflection of light waves on the parallel planes of the crystal.
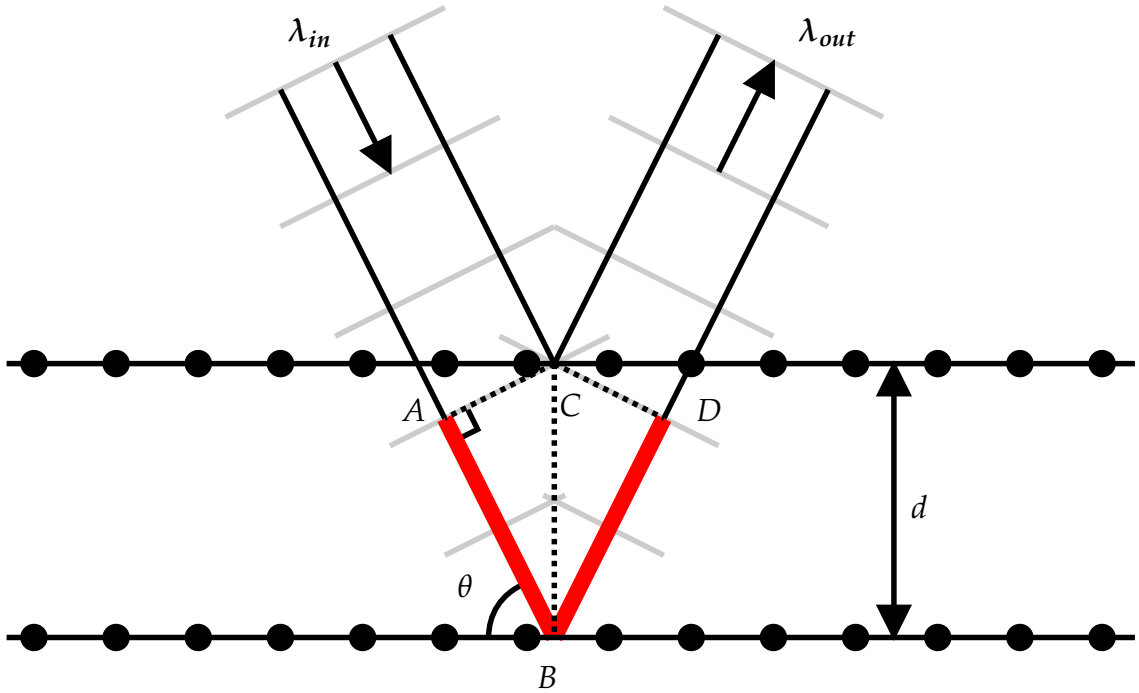
Figure 1.15: A visual representation of Bragg's law. An incoming light wave scatters on two planes of a crystal at an angle θ with respect to the plane. Constructive interference occurs only if the difference between the paths of the two light waves, marked with the red color, is an integer multiple the wavelength.

For a reciprocal lattice defined as

$$G_{hkl} = h\boldsymbol{b_1} + k\boldsymbol{b_2} + mk\boldsymbol{b_3}\,, \tag{1.69}$$

the distance between parallel planes is given by [19]:

$$d = \frac{2\pi N}{|\boldsymbol{G_{hkl}}|}\,, \tag{1.70}$$

where N is an integer number. Taking $N = 1$, Equation 1.70 provides the distance between two consecutive planes of the crystal.

A sketch of a light wave scattering on a crystal is shown in Figure 1.15. The light of wavelength λ_{in} scatters on two planes of the crystal placed at a distance d. The path traveled by the light interacting with the second plane is longer than that of the light interacting with the first plane. Due to the wave nature of the light, constructive interference appears when the difference between the two paths corresponds to an integer multiple of the wavelength.

The length of the segment AB is:

$$L_{AB} = d \cdot sin\theta \, , \tag{1.71}$$

which corresponds to half of the difference between the path lengths. The total difference between the paths is given by

$$L_{AD} = 2d \cdot sin\theta \, . \tag{1.72}$$

The interference between the light waves is constructive if L_{AD} corresponds to an integer multiple of incoming wavelength, λ_{in}. Bragg's law reads then

$$2d \cdot sin\theta = N \cdot \lambda \, , \tag{1.73}$$

where N is an integer number.

Bragg's law can be also directly extracted from Laue's condition.
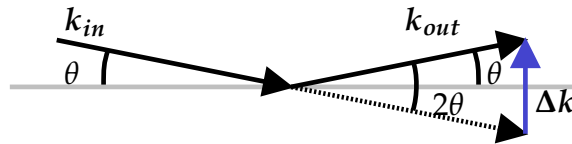
Figure 1.16: Incoming and outgoing wavevector geometry. k_{in} (k_{out}) indicates the wavevector of the incoming (outgoing) light wave.

The momentum transferred Δk is defined as

$$\Delta k \equiv k_{out} - k_{in} \, . \tag{1.74}$$

Due to the assumption of elastic scattering, $k_{in} = k_{out}$, (see Figure 1.16) and due to geometrical considerations, the module Δk can be expressed as

$$\Delta k = 2k sin\theta \, . \tag{1.75}$$

By including the relation between the module k and the wavelength λ,

$$k = \frac{2\pi}{\lambda} \, , \tag{1.76}$$

the condition needed to observe constructive interference (Equation 1.72) can be written as

$$\Delta k = 2\frac{2\pi}{\lambda} sin\theta \, . \tag{1.77}$$

Due Laue's condition, Equation 1.65, constructive interference occurs if

$$\Delta k = G \, . \tag{1.78}$$

where $\mathbf{G}$ is a vector of the reciprocal lattice.

Therefore, expressing Equation 1.78 in terms of modules, Laue's condition can be written as:

$$|\mathbf{G}| = |\mathbf{\Delta k}| . \tag{1.79}$$

So Equation 1.70 can be written as

$$\Delta k = \frac{2\pi N}{d} . \tag{1.80}$$

Considering Equation 1.80 and 1.77, it is obtained:

$$2\frac{2\pi}{\lambda}sin\theta = \frac{2\pi N}{d} , \tag{1.81}$$

which is equal to

$$2d \cdot sin\theta = N \cdot \lambda , \tag{1.82}$$

which is Bragg's law, [19]. An example of an application of this formula is given in the next section.

1.6.5 Examples of diffraction
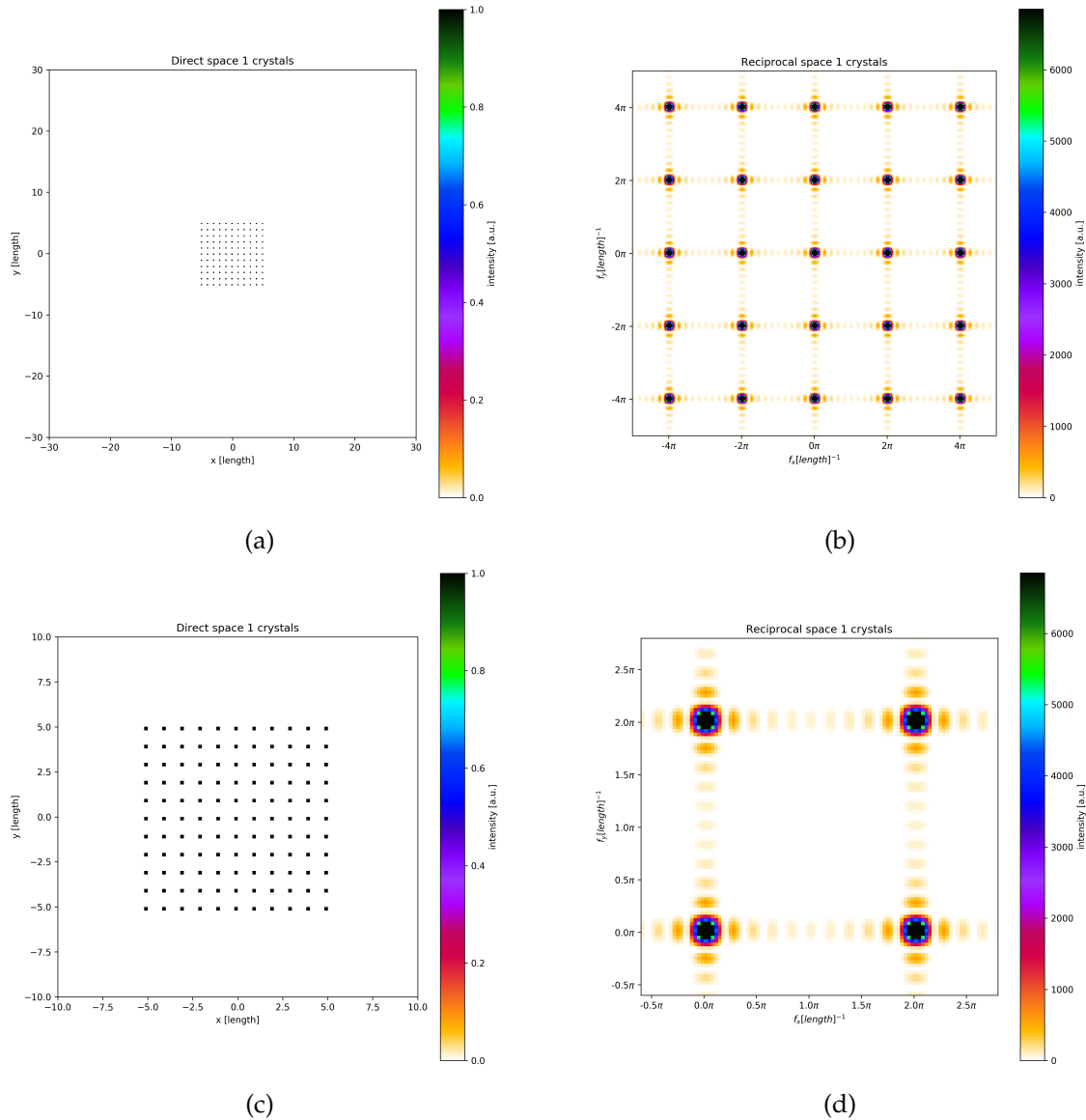
Figure 1.17: Examples of distributions in the real space (left column) and reciprocal space (right column). A simulated lattice with a step of $1a.u.$ and total dimension of $10a.u. \times 10a.u.$ is shown in (a) and (c); the corresponding distributions in the reciprocal space are shown in (b) and (d).

The plots in Figure 1.17, Figure 1.18 and Figure 1.19 show a comparison between direct and reciprocal space. The pattern in the reciprocal space gives the form factor and the diffraction pattern which is observed in a scattering on the distribution given in the direct space. The calculation has been performed by using the numerical Fast Fourier Transform [24] [25] in a 2D space. The plots in the left column show a map, which is the distribution in the real space corresponding to the physical quantity of the electronic density n_{el}. The plots in the right column show the squared module of the form factor, or the intensity of the diffraction pattern, which is the module squared of the Fourier Transform of the

(a)

(b)

(c)

(d)
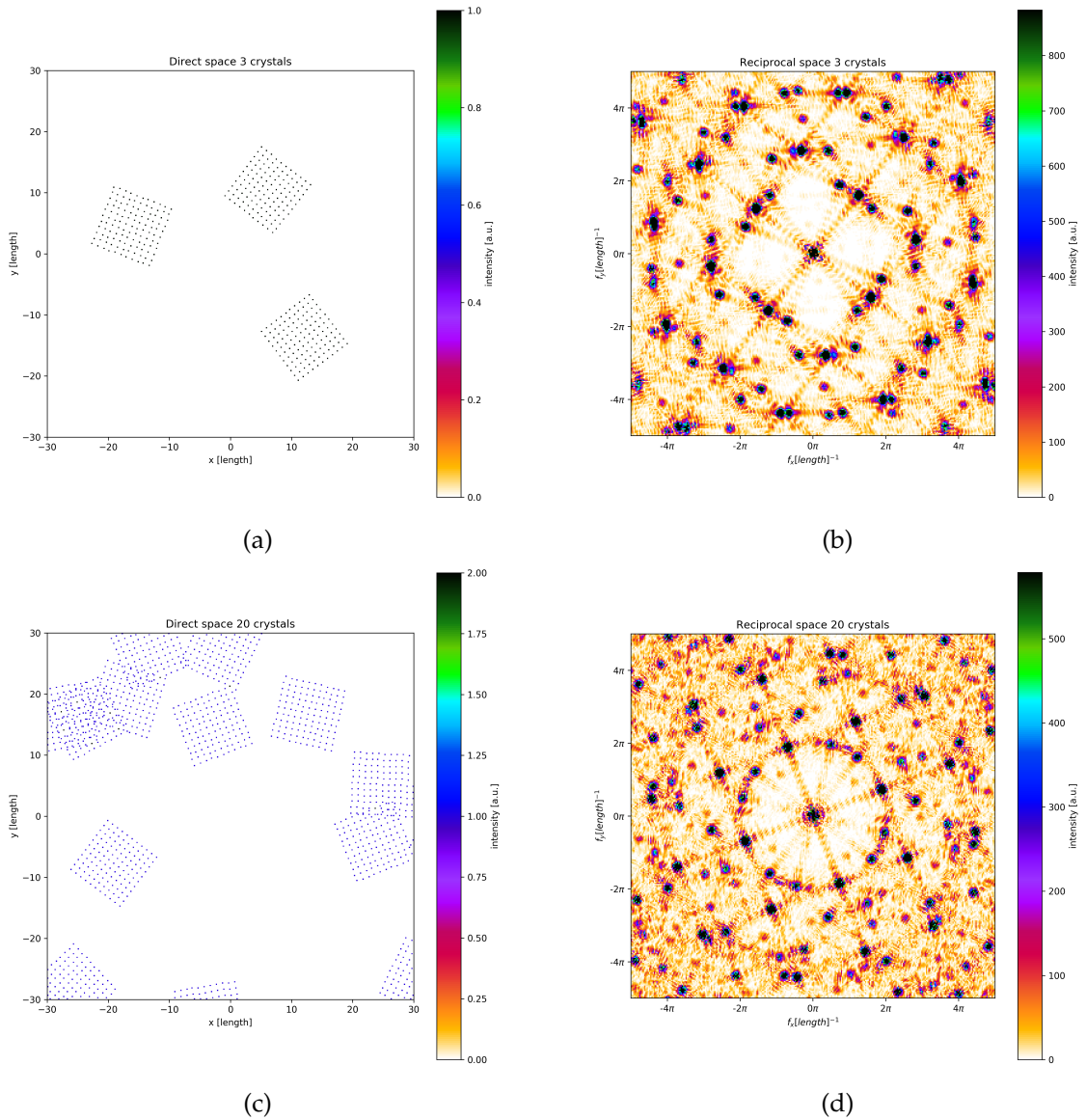
Figure 1.18: Examples of distributions in the real space (left column) and reciprocal space (right column). A simulated lattice has a step of $1a.u.$ and total dimension of $10a.u. \times 10a.u.$. In (a) three crystals randomly positioned and rotated with respect to each other are shown in the real space. The corresponding distribution in the reciprocal space is shown in the (b). In (c), the distribution for 20 crystals in the real space with random position and rotation with respect to each other is shown. In (d), the corresponding distribution in the reciprocal space is shown.

(a)

(b)

(c)
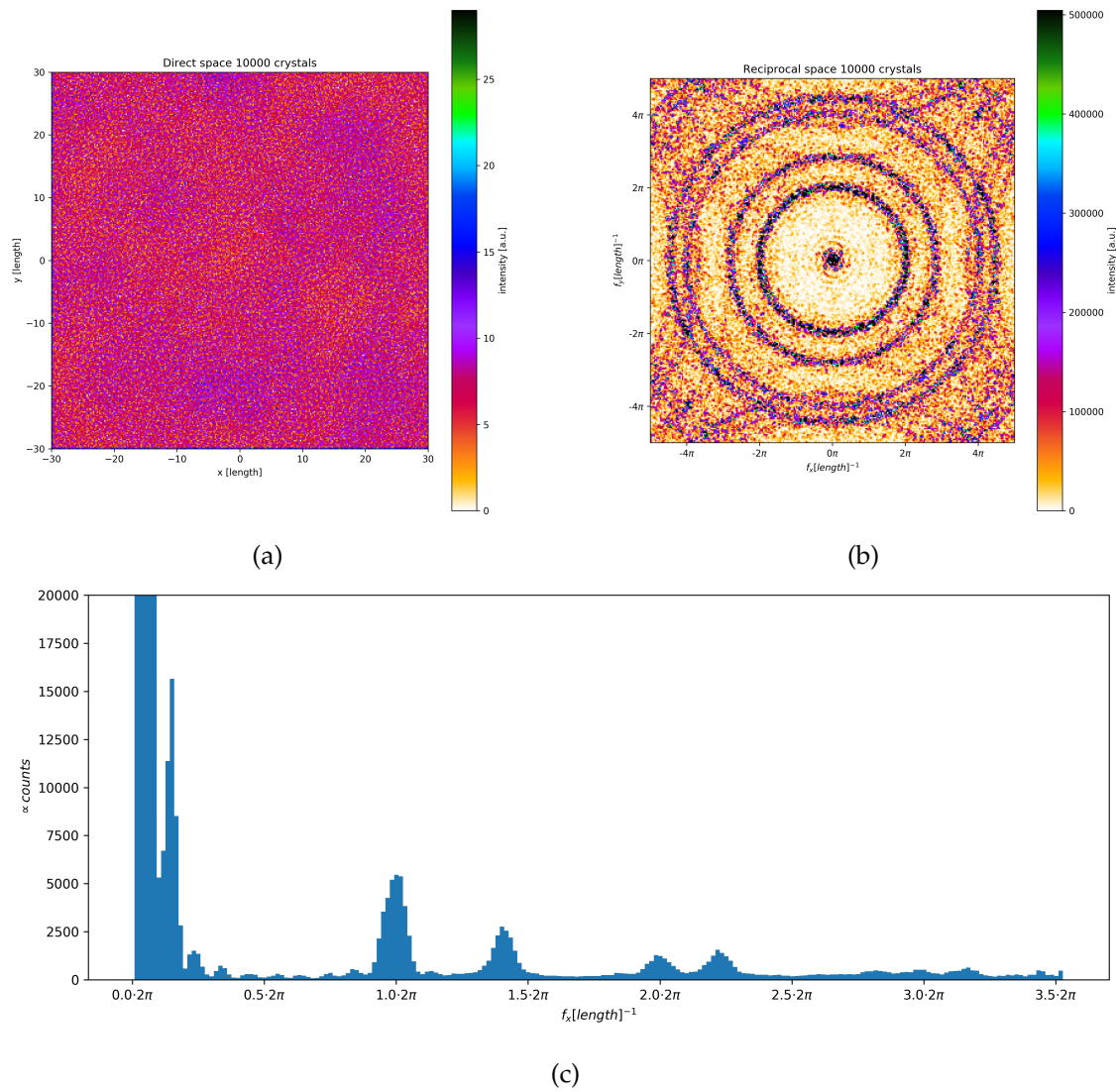
Figure 1.19: Example of distributions in the real space (left column) and in the reciprocal space (right column). In (a), the distribution for 10000 crystal in the real space is shown and in (b) the corresponding distribution in the reciprocal space is shown. The histogram (c) shows the intensity observed in the reciprocal space, in case of diffraction from the pattern shown in (a), as function of the distance from the central spot in (b).

electronic density in the real space. The intensity $I(\Delta k) \propto |F(\Delta k)|^2$ is proportional to the number of scattered photons in the interaction of light with the crystal having the pattern shown in the left plots.

In Figure 1.17(a) a finite lattice is simulated. The lattice constant (the minimum distance between the lattice points) was fixed to 1 arbitrary units (a.u.), and the total size of the simulated crystal was 10 a.u. $\times$ 10 a.u.. Figure 1.17(c) shows a zoom of the same lattice of Figure 1.17(a). The intensity $I(\Delta k)$ is shown in Figure 1.17(b), and zoomed in Figure 1.17(d). The resulting grid in the reciprocal space has a step equal to 2π a.u.$^{-1}$ in agreement with Equation 1.53.

Figures 1.17(d) and 1.17(b), the most intense peaks in intensity correspond to the reciprocal lattice. Moreover, a series of repeated weaker peaks can be observed. The distance between those peaks is $0.2 \cdot \pi$ a.u.$^{-1}$, which in the real space this distance corresponds to $\frac{2\pi}{0.2 \cdot \pi \, \text{a.u.}^{-1}} = 10$ a.u., the total dimension of the simulated crystal.

Figure 1.18(a) shows an example with three crystals at a random position, rotated respect to each other. In Figure 1.18(b) the form factor is shown; the superimposition of three reciprocal lattice rotated with respect to the center can be observed. Figure 1.18(c) and 1.18(d) show an example with 20 crystals; in the reciprocal space it is possible to observe the formation of structures similar to rings.

Figures 1.19(a) and 1.19(b) show the case of 10000 crystals randomly positioned and rotated. In Figure 1.19(b), rings structures are clearly observable. This result is similar to what is usually observed with a diffraction of X-rays on a crystal powder. For a better visualization, Figure 1.19(c) shows the intensity distribution as a function to the distance from the center. It is possible to clearly observe intensity peaks. Excluding the values close to zero, the first peak corresponds to the minimum distance of the peaks in the reciprocal lattice, which is the step of lattice, $hk = 01$ or $hk = 10$, corresponding to $1 \cdot 2\pi$ a.u.$^{-1}$. The second peak corresponds to the first diagonal of the squared lattice, $hk = 11$. The radius is equal to $\sqrt{2} \cdot 2\pi$ a.u.$^{-1}$. The third peak corresponds to $hk = 02$ or $hk = 20$, the correspondent in the reciprocal space is equal to $2 \cdot 2\pi$ a.u.$^{-1}$. The fourth peak corresponds to the diagonal of $hk = 12$ or $hk = 21$, which is equal to $\sqrt{1^2 + 2^2} \cdot 2\pi$ a.u.$^{-1} = \sqrt{5} \cdot 2\pi$ a.u.$^{-1}$ in the reciprocal space.

The weaker peaks appearing between the central spot and the first peak of $1.0 \cdot \pi$ a.u.$^{-1}$ have a distance between each other of $0.2 \cdot \pi$ a.u.$^{-1}$, which corresponds in the real space to 10 a.u., the total dimension of the simulated crystal.

Figure 1.19(b) shows also rings, which seem to be "reflected" by the sides of the map. This effect is caused by the numerical Fourier Transform windowing [26], which is out of the scope of this thesis.

Figure 1.20 shows an image acquired at ESRF with one of the 2D pixel detectors developed for European XFEL, the Large Pixel Detector (see section 2.2.2). The diffraction pattern at 15.5 keV X-rays on silicon powder is shown. Using the Bragg's law, it is possible to calculate the expected radius of the rings, and here below the calculation of the

radius of the first ring is shown.
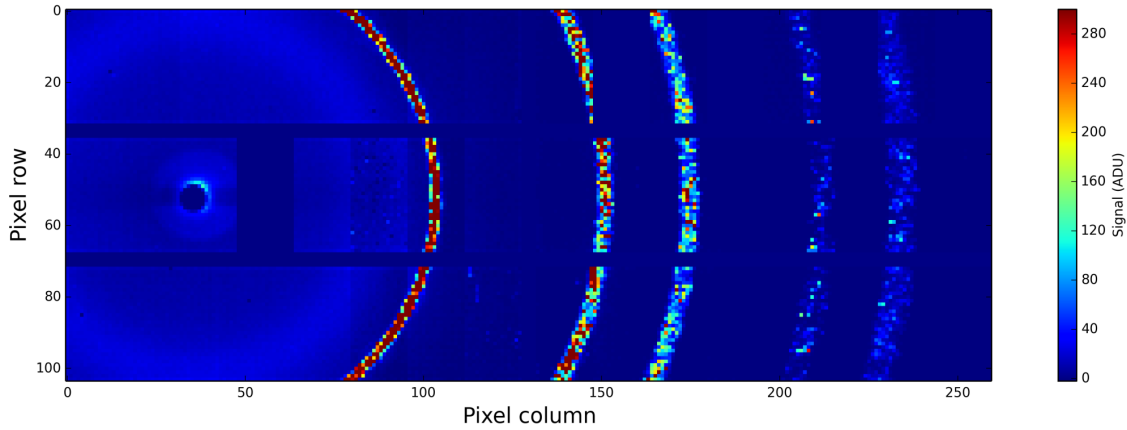
Figure 1.20: An example of X-ray scattering on silicon powder. The X-rays were gener-
ated at the ID09 beamline at ESRF, Grenoble, France. The image was obtained
using the LPD detector. The X-ray energy was 15.2 , keV and the position of
the first ring is estimated to be at $\sim$ 3.3 cm from the center. Courtesy of
P.M.Lang, Detector Group, European XFEL.

The energy of the X-ray beam was $E_{beam} = 15.2$, keV and the distance between the
detector plane and the silicon powder sample was $\sim$ 13 cm. The lattice constant of a
silicon crystal is $a = 5.43$ Å, and due to the Si lattice structure the minimum distance
between two planes [27] is given by $d_{hkl=111} = a/\sqrt{3}$, which corresponds to

$$d_{111} \simeq 3.13 \text{ Å}. \tag{1.83}$$

The wavelength of the X-rays can be calculated from the energy as

$$\lambda = \frac{hc}{E} \simeq \frac{12.4 \text{ ÅkeV}}{E_{beam}[\text{keV}]}, \tag{1.84}$$

For the $E_{beam} = 15.2$ keV gives

$$\lambda = 0.812 \text{ Å} \tag{1.85}$$

According to Bragg's law the first peak is observed at an angle:

$$\theta = arcsin\left(\frac{\lambda}{2d}\right). \tag{1.86}$$

For this case, with $d = d_{111} = 3.31$ Å, θ is

$$\theta \simeq 0.1229 \text{ rad}. \tag{1.87}$$

For a detector positioned at a distance $D \simeq 13cm$ from the sample, the radius of the
first diffraction ring corresponds to

$$r = D \cdot tan\left(2\theta\right) \simeq 3.26cm\,. \tag{1.88}$$

In Figure 1.20, the position of the first ring can be extracted. The pixel size of the LPD is 0.5 mm, so the position of the first peak is $r \simeq 34\,\text{mm}$. This is in good agreement with number expected from Bragg's law.

1.7 Semiconductor X-ray detector

In isolated atoms, the electronic states are discrete, [28]. When two identical atoms come close enough, the original energy levels split in two. In case of n-atoms, each level splits n-times. In case of an extended solid crystal the number atoms is huge. For instance, an amount 28g of silicon, which corresponds to one mole is composed by $\sim 6 \cdot 10^{23}$ atoms (Avogadro's number). When a system contains so many atoms, like a crystal, the electronic levels are so dense that they can be considered a continuum. In Figure 1.21 the concept is shown. This continuum of states is called *band*, [19].
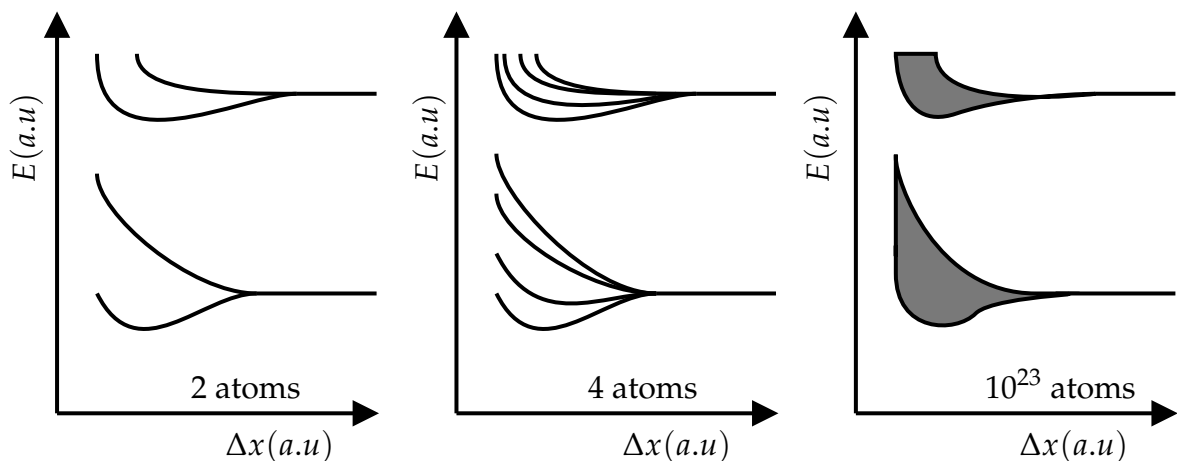
Figure 1.21: A sketch showing the creation of bands. Δx is the interatomic distance; E is the energy.

In a crystal, the possible energy states of the electrons are described by bands. In case of a metal, the conductive and valence bands are overlapping, so the electrons occupy also the conductive band. In case of an insulator, there is a big gap between the conductive and the valence band and, at room temperature, the probability that an electron is in the conduction band is negligible. On the other hand, a semiconductor presents a small band gap. Usually, it is of the order of 1 eV. Due to the electron statistics (Fermi distribution, [19]) semiconductors are weak conductors at room temperature and insulators at absolute zero.

In order to increase the conductivity of semiconductors it is possible to add impurities (doping) in the semiconductor crystal. The doping elements replace an atom on the crystal modifying the electronics structures. Doping is distinguished between n-type and p-type.
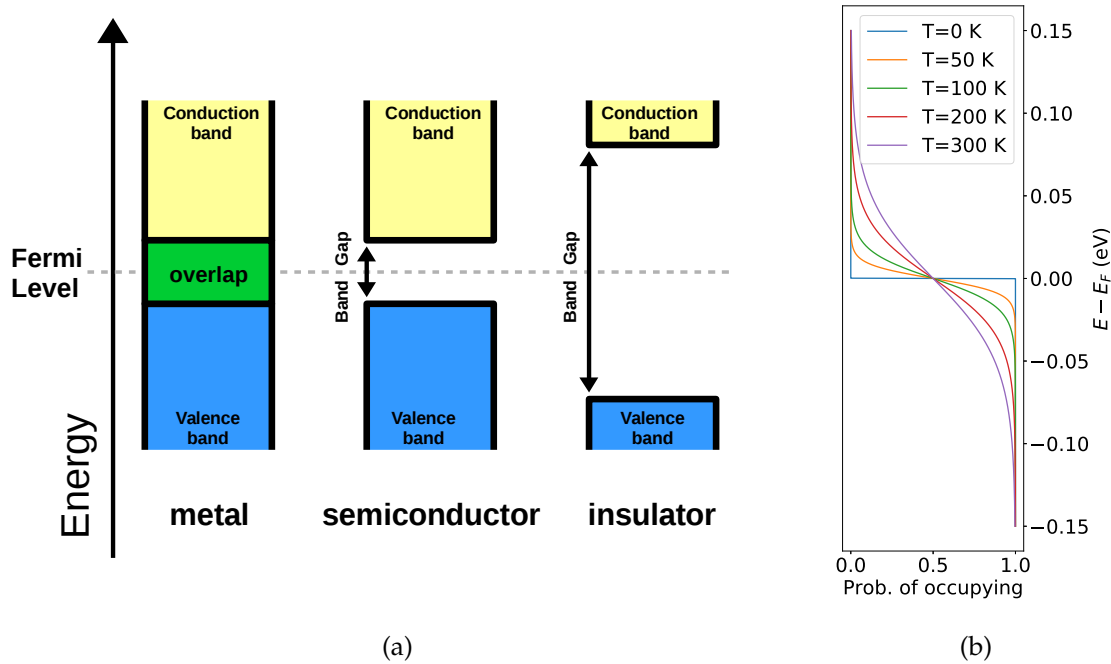
Figure 1.22: A sketch of the bands of metals, semiconductors, insulators (a). In metal the
conduction and valece band are overlapping, in semiconductors the gap is
small ($\sim 1\,\mathrm{eV}$) and in insulator is large ($\gg 1\,\mathrm{eV}$); the Fermi distribution (b)
gives the probability of occupancy of an energy state by an electron at given
temperature.

In the case of silicon (Si), the n-type doping is obtained by replacing in the Si crystal
one atom by an atom of a 5-electron valence element (for example Gallium or Arsenic).
When an atom of the Si crystal is replaced by one of these elements, one electron of the
elements becomes free in the crystal. The n-type impurities are called *donors* because once
in the crystal they release an electron in the conduction band.

The p-type doping is obtained by replacing in the Si crystal one atom by an atom of
a 3-electron valence element (for example Boron or Alluminium). When an atom of the
crystal is replaced by one of these elements, one electron on the covalent bond of the
silicon is captured by the doping atom. For this reason, this type of impurities are called
acceptors; the lack of electrons in the crystal creates a so-called *hole*, which behave like a
positive charge.

In order to explain the working principle of a solid-state diode, here the basic structure
of a semiconductor device, the PN-junction, is described.

The PN-juction is the interface between two regions of a single semiconductor crystal,
p-type doped on one side and n-type on the other side. Due to the opposite charges, the
holes present on the p-side are attracted by the electrons on the n-side, and viceversa,
and they recombine.

In the n-type doped side, the electrons are the majority charge carriers and only a small
amount of holes, generated by thermal excitation, are present. Therefore they are called
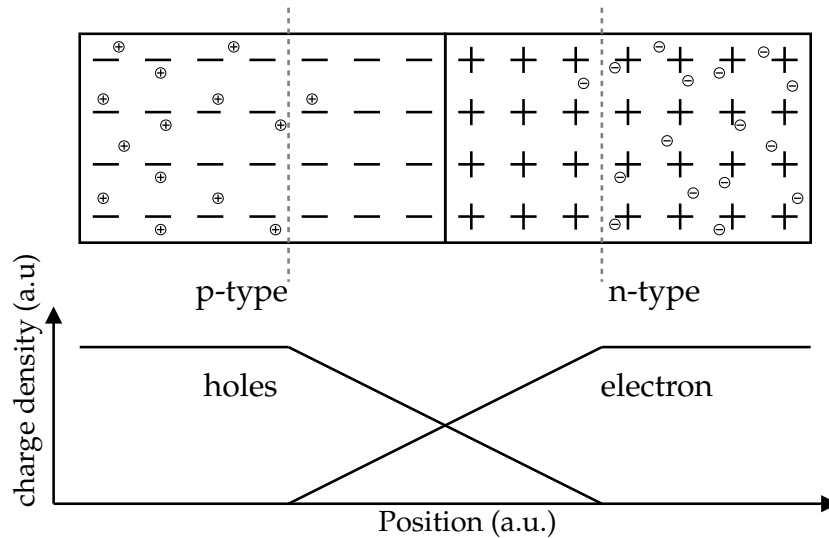
Figure 1.23: On the top, a sketch of the PN-junction: the big signs represent the ions and the small circles represent the free charges; on the bottom, the charge density across the PN-junction.

minority charge carriers.

Viceversa, in the p-type doped part, the holes are the majority carriers, and the electrons are the minority. Electrons can be generated in the p-type side due to thermal excitation. Due to diffusion, the majority charge carriers pass through the PN-junction interface and they recombine by letting behind charged ions in zone adjacent to the junction. The ions generate an electric field which opposes to the diffusion of other charges. Thus, in the zone in proximity of the interface, no free charge carriers are available (*depletion zone*). The static electrical field induces a drift current of minority charge carriers which at equilibrium compensate the diffusion current, so globally at equilibrium no current is present in the PN-junction.
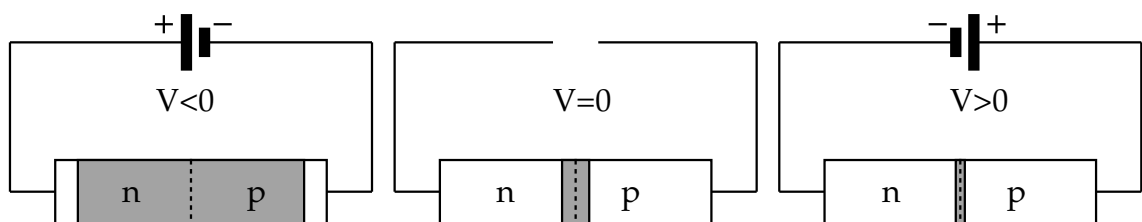
Figure 1.24: A sketch showing the diode in different bias voltage conditions: reverse bias (left), no bias (middle) and forward bias (right). The grey zone inside the diode represent the depletion zone.

If a voltage is applied to the PN-junction as forward bias (positive in the p-side and negative in the n-side), the majority charge carriers (the electrons in the n-side, and holes in the the p-side) are pushed toward the junction. Therefore, they will neutralize the electric field and the depletion zone dimension will be reduced. If the voltage applied increases, the depletion zone can become so thin that the drift current of the minority carriers can not anymore compensate the diffusion current. Therefore, globally a current

given mainly by the diffusion of the majority charges can flow between the two side of the PN-junction. In conclusion the forward-bias PN-junction lets a current flow. In order to avoid to destroy the device, usually an external limiter of current (resistor) is required.

In case of reverse bias (positive voltage applied to the n-side and negative to the p-side), the electrons are pushed away from the junction. This increases the dimension of the depletion zone, therefore the diffusion current is drastically reduced. The main contribution to the global current is given by the drift of the minority charges. In reverse bias the PN-junction lets only a small current flow – called saturation current – not strongly related to the bias but determined by the minority charges concentration in the junction.

The saturation current depends on the number of minority carriers available. The minority carriers (holes in the n-type, and electron in the p-type) are generated when the electrons acquire enough energy to be excited to the conduction band. This can happen due to thermal effects or by external excitations, due e.g. photons. For this reason a solid state diode can be used as a photo-diode.

When X-rays or lower energy photons interact in a semiconductor, the most probable interaction is the photon absorption. The energy is deposited in the material and electron-hole pairs are created. The minimum photon energy required for create a hole-electron pair is given by the energy gap between the valence and the conduction band. In silicon photodiodes, the average energy needed to create an electron-holes pair is by $\sim 3.6\,\text{eV}$, that means 278 electrons/keV.

In case the PN-junction is not biased, the photons interacting in the depletion zone create an electron-hole pairs. Due to the static electrical field, the electrons drift to the n-side and the holes to the p-side. If the PN junction closed with a resistor is illuminated with a flux of photons a current will flow, see the scheme in Figure 1.25. This effect is called photo-voltaic effect.
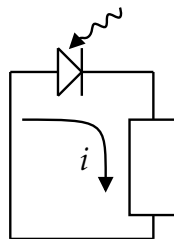
Figure 1.25: A photodiode in the photovoltaic configuration. When the diode is hit by photons, a current flows in the circuit.

As in the previous case, in case the PN-junction is reversely biased, the photons interacting in the depletion zone create charges, and therefore a current. The main advantage of the reverse bias is that the depletion zone is much larger than when the diode is not bias, so the area where the photons can be detected is larger. Moreover, for the same reason, the capacitance of the junction is smaller, allowing a faster signal measurement and lower noise. This is the typical configuration used in photon detectors. A scheme of the photodiode under reverse bias is given in Figure 1.26.
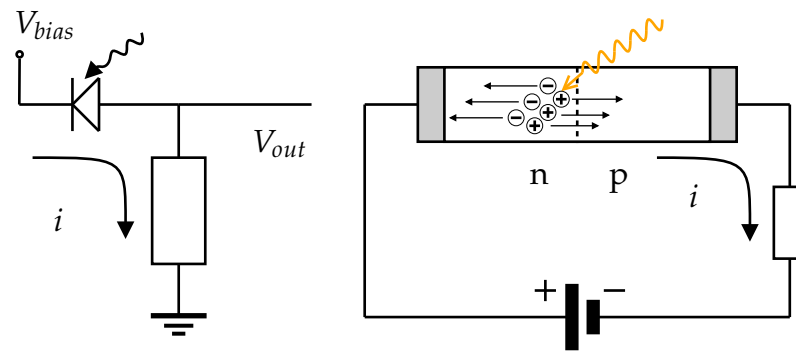
Figure 1.26: A photodiode under the reverse bias voltage. On the left side the schematics, on the right side visual representation of the photon interacting in the depletion zone.

The photodiode is not used in forward bias because the current is mainly driven by the majority charges carrier which are independent on the photons incoming.

The working principle of the PN-diode described is also valid for the so-called PIN-diode, which uses the PIN-junction [29]. This junction is composed by a semiconductor crystal doped P-type on one side, doped N-type on the other side and a central zone let without doping (intrinsic semiconductor, I-type). In the PIN diode, the depletion zone is mainly defined by the intrinsic semiconductor zone, [29]. Increasing the depletion zone, the volume where the photons conversion occurs, increases; improving the performance as photons detection.

For the detection of X-ray photon the silicon sensors takes advantage the basic principle illustrated in this section. Silicon-based detectors used at the European XFEL are described in Chapter 2 and the type of sensors used by the DSSC detector are described in Section 3.1 and 3.2.

2 The European XFEL

The European X-ray Free Electron Laser [4] is a new X-ray facility inaugurated on September 1st, 2017. It is the most powerful and brilliant X-ray source ever built, see Figure 2.1. Comparing with the Linac Coherent Light Source at SLAC (LCLS), the European XFEL covers a wider energy range and has roughly one order of magnitude higher peak brilliance. Other free electron lasers (FELs), such as FLASH, cover a complementary energy range. Free electrons lasers like the XFEL.EU, the LCLS and FLASH have a much higher peak brilliance compared with synchrotron, the number of photons per second is however in some cases comparable.
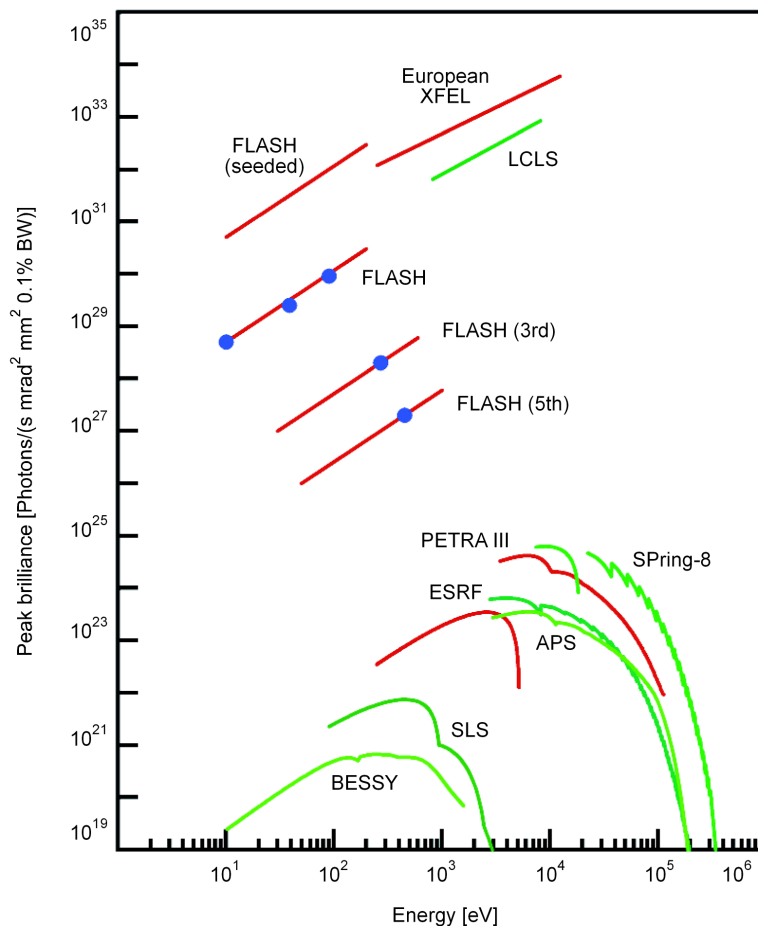
Figure 2.1: Peak brilliance of free electron lasers versus third generation synchrotron light sources, [30].

The European XFEL facility extends for about 3.4 km with an underground tunnel be-

tween the DESY campus (Hamburg) and the XFEL.EU head quarter (Schenefeld, Schleswig-Holstein). The Figure 2.2 shows an aerial photo of the facility.

Figure 2.2: The European XFEL X-ray laser is a 3.4-km-long facility which runs essentially underground. The three sites (framed in red) are located in Hamburg (DESY-Bahrenfeld and Osdorfer Born) as well as in the south of the city of Schenefeld (Pinneberg district, Schleswig-Holstein). - Copyright European XFEL / FHH, Landesbetrieb Geoinf. und Vermessung, [5].
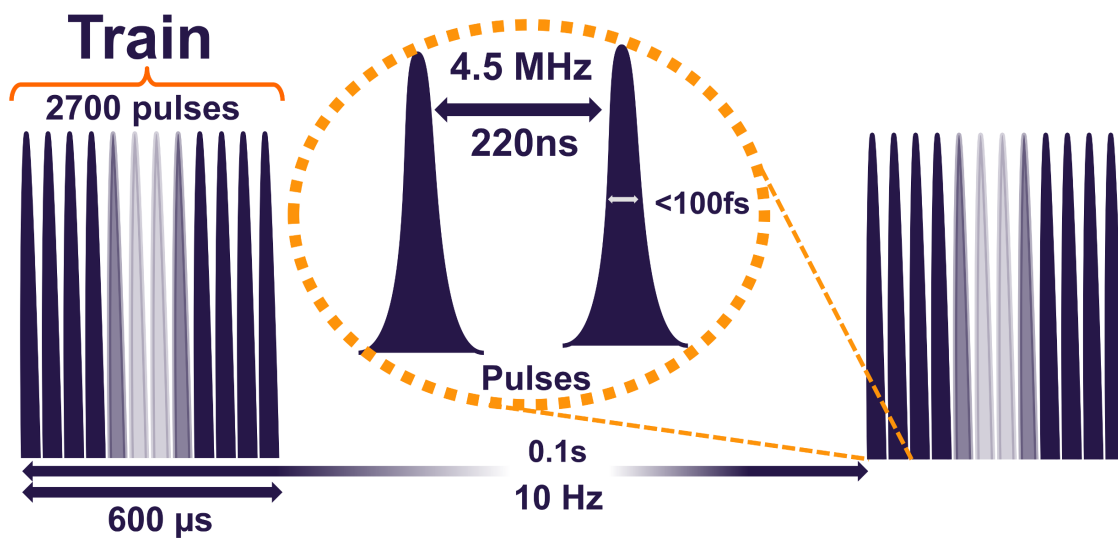
Figure 2.3: A sketch of the XFEL.EU's time-structure as defined in [4]. A train of 2700 pulses is produced every 0.1 s. The distance between the pulses in the train is 222ns and the width of the pulses is < 100 fs.

The XFEL.EU features a unique time structure [4] shown in Figure 2.3. It produces a train of 2700 pulses with a 222 ns (4.5 MHz) separation time from each other. The train is repeated every 0.1 s. The light pulses have a really narrow time shape, with a full width half maximum < 100 fs.

The Figure 2.4 is a block diagram showing the main components of the European XFEL.

The first stage of the machine, the electron injector is located in the DESY [31] campus. The electrons are extracted from a cathode using a pulsed UV-laser which defines the electron bunch timing. The produced electrons are accelerated up to 17.5 GeV by a linear accelerator. The linear accelerator stage is composed of super-conductive resonator cavities kept at 2 K . There are 768 modules, they extend for about 1.7 km between the DESY campus and the Hamburg urban district Osdorfer Born, [5].
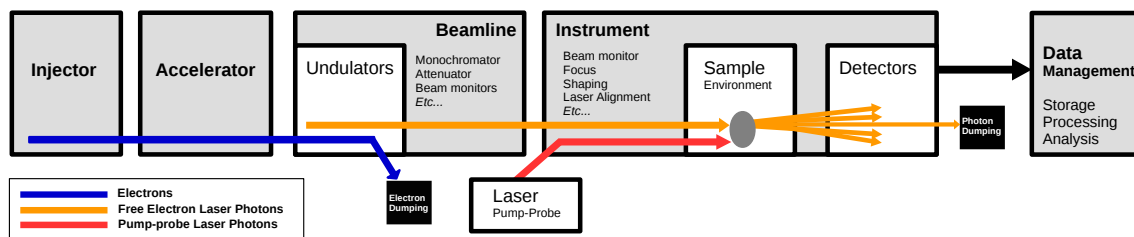
Figure 2.4: A block scheme showing an overview of the main components of the European XFEL.

In order to produce the photons, the accelerated electrons pass through an undulator system named SASE, as the name of the physical process which generates the coherent photons. The basic working principle of undulators and the SASE phenomenon is described in Section 1.4. At the XFEL.EU three beamlines are present at under construction, while five are planned for a later stage. The SASE1 and SASE2 beamlines can produce photons in an energy range between 3 keV to more than 25 keV. The SASE3 beamline generates soft X-rays with an energy between 0.26 keV and 3 keV.

The FEL X-rays reach the XFEL.EU instruments at the end of the SASE tunnels. The instruments foreseen at present are six (two per beamline) and they are shortly described in the next section.

2.1 Instruments and Experiments

To make a wide range of experiments possible, the XFEL.EU facility provides to the users six different end-stations, each with different features. The linear machine as XFEL.EU allows only a limited number of experiments. Therefore six big classes of experiments have been selected to cover the needs of the scientific community. The end-station instruments are designed to allow specific classes of experiments. Despite the diverse type of experiments the basic layout of the instruments is common and includes similar features.

In each instrument it is possible to tune the beam shape and the focus of the X-rays beam by acting on the mirrors and the lenses. The available diagnostic devices allow monitoring continuously the properties of the beam.

An optical laser is also available to the instruments; it can be used for stimulating the sample and characterize the evolution of its properties with time using pump-probe techniques. In them, the optical laser can excite the sample before the arrival of the FEL

shot. This brings the sample to an excited state: by changing the delay between the FEL pulse and the optical laser it is possible to study the temporal evolution of the sample, [32]. Figure 2.5 shows a 3D sketch a pump-probe experiment.
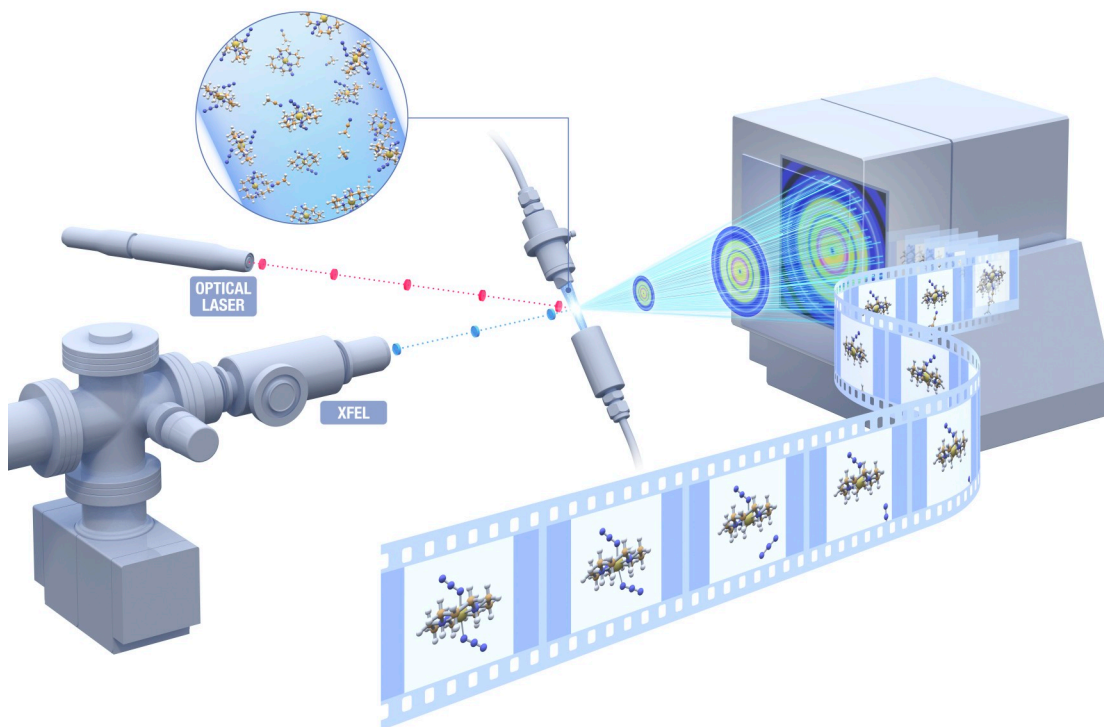
Figure 2.5: The ultrashort, ultrahigh-intensity X-ray laser pulses of the European XFEL enable studies of ultrafast processes in chemistry. Synchronized optical laser pulses (red) active a sample, here shown dissolved in a liquid jet, initiating a chemical reaction. X-ray laser pulses (blue) immediately follow the optical laser, with the resulting scatter recorded by a detector (right). Several of these pulses image different stages of the chemical reaction as it happens, and the data can be arranged sequentially to form a super slow-motion "molecular movie" of the reaction. Copyright European XFEL, [5].

Each end-station has its specific sample environment in which the FEL interacts with the sample. Depending on the type of experiment, the sample environment can be different. For example, in some experiments small samples are injected in ultra high vacuum with a special sample injector; in other experiments a solid target is hold by a special manipulator. In some cases it is possible that pulsed magnetic fields or controlled high temperatures are needed.

The typical types of experiment performed or to be performed at the European XFEL can be divided in two big groups. There are experimental techniques that combine them thus allowing much detail understanding of the materials under investigation.

- The first group includes the spectroscopy, experiments where the FEL excites the electrons of the sample to a higher energy state. The electrons then decay to a lower energy state by emitting photons or electrons. By measuring the energy of

the emitted particles, it is possible to obtain information about the possible energy states of the electrons in the sample. This group of experiments uses spectrometers for measuring the energy of the outgoing photons and time-of-flight devices for measuring the electron and the ion energies.

- The second group of experiments uses coherent scattering of photons on a sample. The produced diffraction pattern gives information on the internal structure of the sample, such as the electron density at a given electronic state. In some cases the high power of the FEL pulse destroys the sample: however studies [33] have demonstrated that the information on the internal structure of the sample is retained in the diffraction image if the pulse is short enough, as the diffraction is produced before the sample looses its structure.

  As explained in Section 1.6, depending on the spatial distribution of the sample, in some experiments really intense Bragg peaks (or circles) are present, for example in case of regular spatial structures (like crystals). In other cases, like for example non-structured materials, the diffraction image shows a more uniform scattering pattern.

  These differences, considering also the different energy ranges and the fast XFEL.EU time structure, drive the requirements for the imaging detectors.

An overview of the XFEL.EU beamlines and end-stations is given in Figure 2.6 and a short description list is given below, [5].

- Beamline: SASE1

  – **SPB/SFX**
    Single Particles, Clusters and Biomolecules and Serial Femtosecond Crystallography.
    Ultrafast coherent diffraction imaging of single particles, clusters and biomolecules: structure determination of single particles (atomic clusters, biomolecules, virus particles, cells), serial femtosecond crystallography.

  – **FXE**
    Femtosecond X-ray experiments.
    Time-resolved investigations of the dynamics of solids, liquids, gases.

- Beamline: SASE2

  – **MID**
    Materials imaging & dynamics.
    Structure determination of nanodevices and dynamics at the nanoscale.

electron tunnel   ⌒   **electron switch**

photon tunnel   ●   **electron bend**

undulator   ▮   **electron dump**

linear accelerator for electrons (10.5, 14.0, 17.5 GeV)	SASE 2 0.05 nm - 0.4 nm	SASE 1 0.05 nm - 0.4 nm	SASE 3 0.4 nm - 4.7 nm

Undulators	SASE1, SASE2		SASE3
Wavelengths	0.4 nm to below 0.05 nm		4.7 nm to 0.4 nm
Photon energy	3 keV to over 25 keV		0.26 keV to 3 keV
Instruments	SPB/SFX, FXE (SASE 1),		SQS, SCS
	MID, HED (SASE 2)		
Magnetic length	175 m		105 m

MID Materials Imaging and Dynamics

HED High Energy Density Science

Optional space for two undulators and four instruments

SPB Single Particles, Clusters, and Biomolecules and
SFX Serial Femtosecond Crystallography

FXE Femtosecond X-ray Experiments

SQS Small Quantum Systems

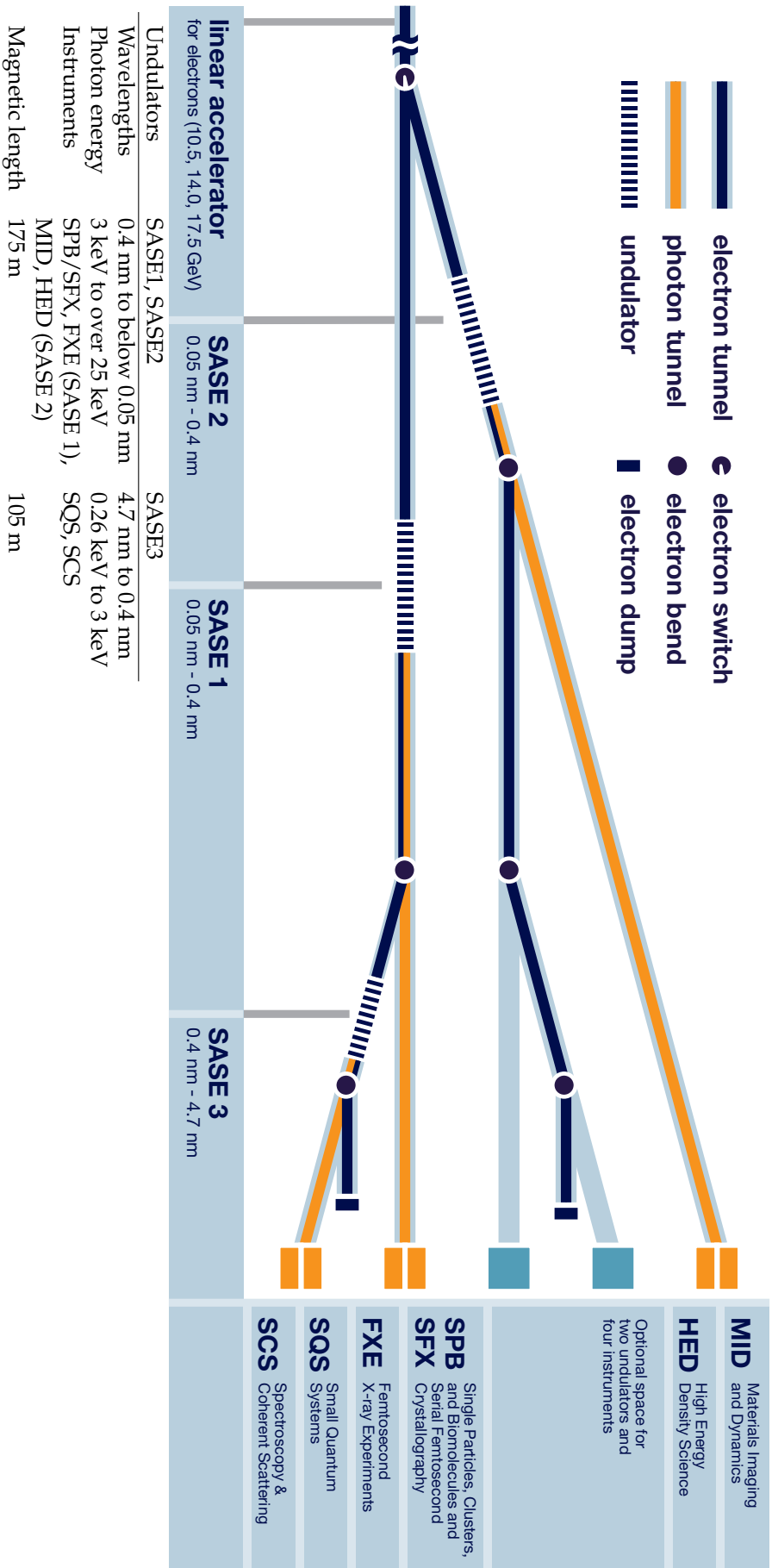**SCS** Spectroscopy & Coherent Scattering

Figure 2.6: The XFEL.EU beamlines layout, [4]. Copyright European XFEL, [5]. In the Tabel under the Figure, the characteristics of the different SASEs (SASE1, 2 and 3), such as wavelength and energy, are described.

    – **HED**

        High energy density matter.

        Investigation of matter under extreme conditions using hard X-ray FEL radiation, e.g. probing dense plasmas.

- Beamline: SASE3

    – **SCS**

        Spectroscopy & coherent scattering.

        See Section 2.1.2.

    – **SQS**

        Small quantum systems.

        See Section 2.1.3.

2.1.1 The SASE3 beamline

A schematic layout of the SASE3 beamline, showing the different beamline elements is shown in Figure 2.7, [34].
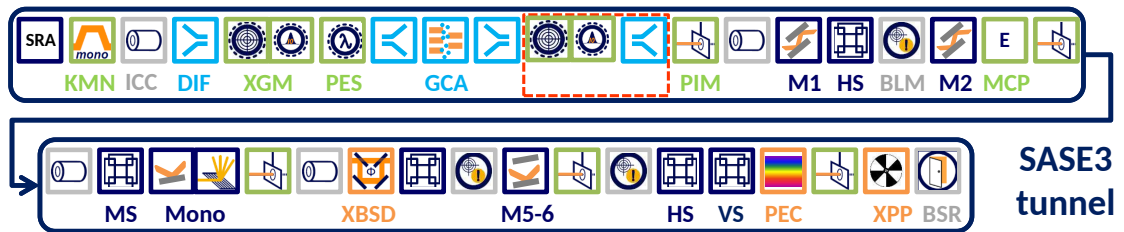
Figure 2.7: The SASE3 schematic layout, [34]

In the FEL community the name "synchrotron radiation" is given to the radiation produced by the electron bunches in the first part of the undulator, namely, when the undulator works in low-gain regime see Section 1.4. The reason of such a naming is the fact that this radiation features a spectrum, which is similar to that of the X-ray radiation produced of synchrotrons, thus the is "synchrotron radiation" features a much broader spatial and spectral distribution (see Section 1.4).

This explains why the first device after the undulator system in a FEL is the Synchrotron Radiation Aperture (SRA). It is essentially an aperture surrounded by a block of boron carbide and tungsten (B_2C/W) which can absorb the synchrotron radiation. Due to the high energy deposited, this device needs to be cooled down. The cooling is made by a water circuit.

After the SRA, the K-Monochromator is present. It is used for tuning the K parameter of the undulators (see Section 1.4) of the undulator, and for optimizing the phase between two segments. The device is a system composed by two separated units: the first is a monochromator made of four crystal of Silicon, used to reduce the X-ray bandwitdh to

a narrow range. The device is kept cold by a water circuit. Due to heating issues this device can be used only in single pulse bunch mode. The second segment includes a scintillator, a mirror and an optical camera. The recorded images give information on the monochromaticity of the beam. This measurement is destructive in the sense that the device is not transparent to X-ray radiation. So this device is used only in order to tune the undulator system.

The next component in the beamline is a X-ray gas monitor (XGM), a gas ionization chamber which contains a noble gas, like Krypton or Xenon. The incoming photons ionize the gas; the produced electrons and ions are accelerated in opposite directions by an electric field. By measuring the deposited charge it is possible to determine the beam intensity (from the amount of charge produced in the gas) and its position from the time the signal takes to reach the detector (delay). A similar concept is also used in the photo electron spectrometer (PES). It sits after the XGM and it has 16 circular segments. The aim of this device is to acquire information about the polarization of the beam. It takes advantage of the fact that in case of linearly polarized light, the electron emission has a privileged direction.

Both the XGM and the PES use the same gas pressure which is higher with respect to the rest of the beamline. For this reason, a differential pumping system is present before and after these elements. The gas used in the XGM and the PES is almost transparent to the FEL pulses due to the low photon-absorption cross-section, so these measurements can run continuously during the XFEL.EU operation.

In order to change the intensity of the FEL beam a Gas Cell Attenuator (GCA) is used. This device is a vacuum system containing a residual gas at a given pressure, which defines the attenuation. The pressure inside this device can be as high as 1 mbar, so a differential pumping system has to be used in order to keep the rest of the beamline under UHV conditions.

The photon optical camera (PIM) is a camera which uses a solid scintillator to obtain shape and intensity information of the beam. This is a non-transparent measurement and absorbs the soft X-rays, so the scintillator is removed when not needed.

Neglecting the collimators, the mirrors and the slits system the next device is the beam loss monitor (BLM). It is mainly a hole surrounded by scintillating material and optical sensors. It is used for monitoring the alignment of the beam. In case of strong misalignment, a stop signal can be sent to the machine in order to avoid damaging other devices. The information on the misalignment can also be used in the VETO mechanism of detectors during data collection, see Section 2.3.3.

At this stage of the beamline it is possible to insert the Micro Channel Plate (MCP) detector to precisely measure the FEL intensity. The measurement of the intensity as a function of the number of undulators used allows to obtain the so-called *FEL gain curve*. It serves to compare the lasing with theoretical simulations.

The beam goes through further collimation stages before passing through a monochro-

mator. A set of mirrors is used to focus the beam on a grating that select the photons within a narrow bandwidth of the incoming beam, and the outgoing beam is then collimated.

If required by the experiment after the monochromator stage, a X-rays splitter delay line (XBSD) can be inserted in the beam. This device splits the beam in two branches. The first branch has a fixed length path instead the second branch has a tunable length. By using a set of mirrors the two beam are merged together. This allows changing the delay between the two split pulses.

The next device in the beamline is the mirror switch (M5-6). It is a set of mirror used for switching between the instrument end-stations SCS, SQS and another possible future end-station. Slits are present after this mirror set for trimming of beam profile.

The last device in the beamline is the Photon Emission Calibration. It is an automatic manipulator equipped with a set of different materials useful to produce reference absorption lines, used for energy calibration purposes. Then, the XPP is a x-ray pulse picker, which is simply a chopper. It is useful during the commissioning phase as it allows selecting some pulses of the incoming bunch train. This helps avoiding damaging detectors or other devices.

Finally, the SASE3 beamline ends with a beam shutter (BSR), leading to the different end stations, SCS and SQS.

2.1.2 Spectroscopy & Coherent Scattering (SCS)

As described in the SCS conceptual design report [34], the SCS instrument provides a platform for different kind of experiments based on soft X-ray spectroscopy and coherent scattering. The schematic layout of the SCS beamline is shown in Figure 2.8.

Figure 2.8: The SCS schematic layout, [34].

The first device of the SCS beamline is the alignment laser (ALAS). It is used to inject into the beam pipe an optical laser used for alignment purposes. This laser is aligned with the FEL beam so it can be used to check the alignment of the other devices.

Then, inside a differential pumping system, a gas monitor device (XGM) is present. This device is similar to that of the SASE3 beamline.

After the gas monitor an X-ray optical cross correlator (XOX) is placed in the beamline. It takes advantage of a particular property of thin films of silicon nitrate. The film is illuminated by an optical laser and by the FEL. The film material has the feature that the reflectivity drops down when the two pulsed sources, the laser and true FEL, are coincident in time and space. Using this feature it is possible to align in time the optical laser used for pump-probing and the FEL pulses.

The solid state attenuator (SAT) can be inserted in the beamline to fine tune the atten-
uation of the incoming beam. It is made of artificial diamond.

The Kirkpatrick-Baez focusing system [35][36] (KBS) is made of bent mirrors used to
focus the FEL beam on the sample inside the environment chamber of the SCS experi-
ment.

The Laser In-Coupling (LIN) is a device used to inject the optical laser beam for pump
probing, and focusing it on the sample.

The sample chamber is the forward-scattering fixed target (FFT) chamber. It features
a slot to include the devices used by sample handling. The chamber has a backward
aperture for interfacing with an imaging detector. The imaging detectors which will be
used are the DSSC (see Chapter 3) or the FastCCD, [37]. In order to be able to measure the
diffraction pattern also very close to the beam in the place peperdicular to it, an additional
detector can be installed more downstream in the beamline.
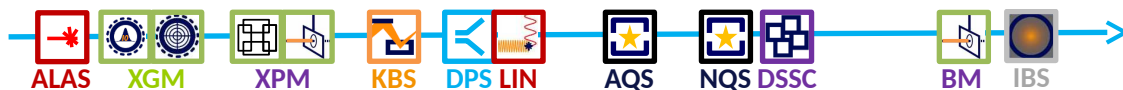
2.1.3 Small Quantum System (SQS)

Figure 2.9: The SQS schematic layout

The SQS instrument aims at the investigation of the electronic and atomic structure
and dynamics of soft matter, biological structures, magnetic materials and structures [38]
[39]. The instrument will allow the study of processes in atoms, ions, small molecules
and clusters occurring in the interaction with very intense X-ray radiation using a variety
of spectroscopy techniques [39].

As for SCS, the SQS instrument the first device is the alignment laser (ALAS) and a gas
monitor used for monitoring the intensity of the beam (XGM). After that, the instrument
features a position monitor (XPM), based on fluorescence light emitted by a crystal, and
an optical camera. The KB-Optics (KBS) is a system of bent mirrors used to focus the
X-ray beam.

The mirrors allow focusing the X-rays beam in two positions:

- the first position (F1) is inside the Atomic Quantum Structure chamber (AQS),

- the second (F2) is inside then Nano Quantum Size chamber (NQS).

The AQS is used to perform experiments on atoms or small molecules. The samples are
injected in liquid-jets into the AQS chamber directly on the FEL beam. The interaction
with the X-rays excites the sample, which becomes highly ionized; electrons, ions and
photons are emitted. The emitted particles are measured with different detectors, such
as an electron-time-of-flight spectrometer (eTOF), a velocity-map-imaging spectrometer

(VMI), a high-resolution XUV fluorescence spectrometer (HRFS) and a magnetic bottle electron spectrometer (MBES).

The NQS chamber is designed to perform experiments with big-clusters, bio-molecules and nano-clusters. The sample (in liquid or aerosol state) is injected directly into the beam. The detectors attached to the chamber and which can be used during the experiments are an electron/ion time-of-flight spectrometer, a Thomson parabola, a reaction microscope spectrometer (REMI) and an imaging detector. The detector used will be DSSC, which is described in Chapter 3.

After the NQS chamber and before the beam dump, other devices are used for diagnostic purposes, such as the measurement of the arrival time, the intensity and position of the FEL beam, [38].

2.1.4 Type of experiments at SCS and SQS

At SCS and SQS various types of experiments can be performed. The main difference between SCS and SQS is that in SCS the target is solid and it is fixed to an holder, while at SQS the environment chamber has been designed to use a sample diluted into a liquid, or in a aerosol form.

The main classes of experiment to be performed at the SCS and SQS beamlines include:

- Coherent X-ray diffraction imaging (CXDI),

- X-ray photon correlation spectroscopy (XPCS),

- Resonant elastic X-ray scattering (REXS),

- Resonant inelastic X-ray scattering (RIXS),

- Nonlinear X-ray spectroscopy (NLXS).

The CXDI is a technique taking advantage of the fact that if a sample is illuminated with a coherent light and the diffracted light is properly sampled by an imaging detector, it is possible to reconstruct uniquely the image of the sample by using phase retrieval algorithms, [23]. The technique can be done at selected resonances of the material under investigation therefore allowing extracting information of electronic and magnetic properties.

The XPCS [40] is a technique used to study the dynamics of a sample. Sequential frames of the diffraction patterns, normally in far field are measured. In this configuration the Bragg diffraction spots have a speckle structure. Recording with a fast imaging detector and information about the dynamics of the sample are extracted by the temporal correlation between the frames.

The REXS [41] is a technique aimed to probe a specific electronic transition in the material. The energy of the incoming photon is tuned to excite a specific state of the electron,

which by falling down in the initial state emits a photon of the same energy. This technique allows obtaining information about the spatial frequency of charge or spin.

The RIXS [42] uses the inelastic scattering techniques. The incoming photons energy is tuned to match a specific resonance, which excites an electron from a deep-inner layer to a higher energy state. The peculiarity of the inelastic scattering is that the electron replacing the vacancy is not the one which was originally excited. For that reason, the outgoing photon has a different energy than the incoming because the final state is not equal to the initial state. This method allows probing the internal electronic states of the matter.

An example of NLXS [34] is the stimulated RIXS, in which the incoming photons excites the electrons to a defined higher energy state. In contrast to the standard RIXS, the decay of the electron to a lower energy state is predominantly non-radiative; only a few percent of the decays go via photon radiation. In the non-radiative process, Augers electrons are emitted; they can be measured with an electron spectrometer.

2.2 The imaging detector

2.2.1 Detector requirements and detector projects at XFEL.EU

Imaging detectors are fundamental to perform diffraction experiments. When the XFEL.EU project was started, no detector existed, which was were able to deal with the requirements sets by the machine [43].

The most critical requirements are related to the unique time structure and the high brilliance of XFEL.EU, see Chapter 2. Moreover, other important detector features, such as single photon sensitivity for 1 keV photons and dynamic range of $\sim 10^4 - 10^6$ keV photons were requested by the scientists to be able to perform experiments [44].

Single photon sensitivity (at a given energy) has the following meaning: the standard deviation of the signal collected when no X-ray illuminate the detector (dark signal) must be much smaller than the signal generated by a single photon of a given energy. The standard deviation of the dark signal is the detector noise. A discussion about the probability of photon misidentification is given in Section 5.5.

An ideal detector for XFEL.EU would be a *universal* imaging detector able to cope with the unique timing of the facility and at the same time cover the wide energy range accessible in the three beamlines, [45]. Moreover, it would provide single photon sensitivity for 1 keV photons and also it would reach a good dynamic range of $10^4 - 10^6$. The detector would be compatible with the end-station experiments environment, which can be either ambient or vacuum. Furthermore, in order to avoid continuous replacements of the components, the detector would need to have a good life time despite of the high radiation dose accumulated during operation.

As mentioned above, one of the main challenges for the XFEL.EU imaging detectors is the timing structure. Many experiments foresee the need to sample images ideally

after every single FEL shot. An ideal detector matching the XFEL.EU time structure must be able to sample at 4.5 MHz 2700 consecutive frames, and to read them out before the following train ($\sim$ 0.1 s). These numbers are challenging not only for the need of fast processing of the signals, but also due to the amount of data-throughput. Assuming a 10^6 pixel camera with a resolution of 16 bits for each pixel, with a simple calculation it turns out that the data-throughput corresponds to 54 GByte/s on average (1 Mpixel $\cdot$ 2700 pulse $\cdot$ 10 Hz $\cdot$ 2 Byte/pixel). This is huge flux of data, not easy to acquire, transfer and store.

The development of a single detector satisfying all requirements at the same time would not be possible in a reasonable amount time and at reasonable costs, [45]. Therefore, three separate detector projects [44] for the XFEL.EU have been founded, each with different approaches and goals.

The three detectors projects are:

1. the Large Pixel Detector (LPD), [46], [47];

2. the Adaptive Gain Integrating Pixel Detector (AGIPD), [48], [49];

3. the DEPFET Sensor with Signal compressor (DSSC), [6], [50].

In order to match the requirements of single photon sensitivity and high dynamic range, the three projects use different approaches. The electronic front-end which amplifies, reads-out and stores the signal from the sensors, is different for the three detector projects. The concept is shown in figure 2.10.
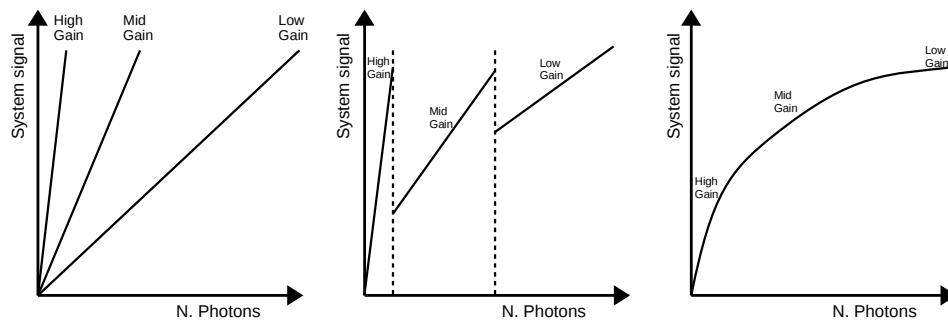
Figure 2.10: A simplified sketch showing three different approaches to reach a high dynamic range. The first approach is that of LPD: the signal from the sensors is amplified in parallel with three different gains. The second approach is that of AGIPD: the signal from the sensors amplified with three different gain automatically switching between each other. The last is the approach of DSSC: the response curve of the sensor is non-linear, and the non-linearities are determined by the sensor design.

The first approach is that of LPD. The signal from a single pixel is processed with three different gain stages in parallel. The second approach is that of AGIPD, among three different gains the appropriate is automatically selected depending on the signal intensity.

The third approach is that of DSSC. A silicon sensor in which the desired nonlinear response depending on the signal intensity is defined during the design and the production of the sensor.

Despite the differences between them, all the detectors must couple to the standard XFEL.EU control system, synchronization clock, VETO interface and data format. This will be described in the Section 2.3.3.

Each detector has its own dedicated readout ASIC (Application Specific Integrated Circuit). All the ASICs for the three projects are realized in the 130 nm IBM technology. Since the ASICs have to readout all the detector channels in parallel, they are bump-bond to the sensors.

The features of the three different detectors are briefly described below.
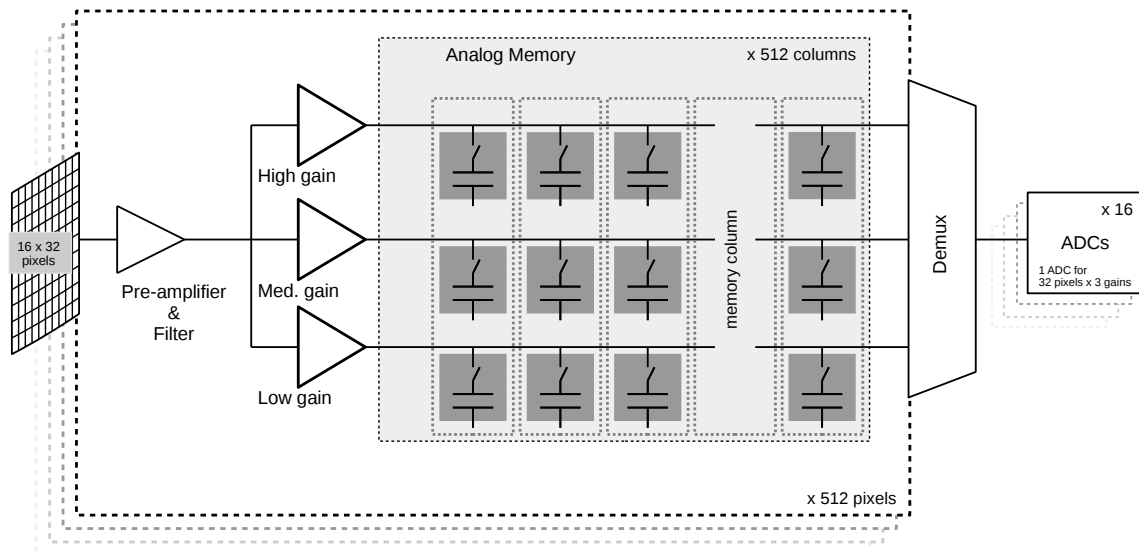
2.2.2 The Large Pixel Detector (LPD)

Figure 2.11: A simplified scheme of the LPD readout. Each ASIC processes the signals coming from 16×32 pixels, applying three different gains and storing the values in an analog memory array. The analog-to-digital conversion is performed outside of the ASICs. Sixteen ADCs are used to digitize the signals coming out of one ASIC.

The Large Pixel Detector is an imaging detector optimized for the detection of hard X-rays, in particular for the energy range between 8 keV and 20 keV. The pixel is squared, with a size of 500 µm. The LPD project is the result of the effort of the Rutherford Appleton Laboratory, the University of Glasgow and the XFEL.EU. The sensors used are 500 µm thick silicon drift detectors featuring a 600 nm thick entrance window, used absorb visible light photons.

The readout of the signals is performed as follows (see Figure 2.11): the charge generated by the X-rays in each pixel is measured by a pre-amplifier, then the signals are amplified with three different gain stages in parallel, as in Figure 2.11, and the voltages

Figure 2.12: The Large Pixel Detector in its final location as part of the FXE instrument. Copyright European XFEL, [5].

are stored in an analog memory pipeline. The control of the memory unit implements also the VETO (as defined in Section 2.3.3) and manages also the read-out done by an ADC. The single ASIC electronic is able to manage 16×32 pixels. Each ASIC contains 16 ADCs and each ADC reads the voltages stored in the analog memory relative to three gains of 32 pixels. The detector is scalable and each monolithic sensor includes 128×64 pixels. Therefore, for the readout of a full sensor 8 ASICs are needed. The system including a single monolithic sensor is called tile. Despite of the fact that the first prototype was the 2-tile system, the basic unit of LPD is the so-called super-module, a system including 8×2 tiles, 256×256 pixels. This is the basic unit for building up the quadrant made of four super-modules and then the megapixel camera. The LPD is a detector built for ambient (not vacuum) environment and uses a liquid cooling system.

The LPD was installed at the FXE beamline in summer 2017 and it is now used for the user program of XFEL.EU. Figure 2.12 shows the LPD detector installed of the FXE beamline at XFEL.EU.

During the work of this thesis, I participated to the measurement performed at the Advanced Photon Source laboratory (Chicago, USA). For me it was an important experience in order to prepare the beam time of DSSC detector.
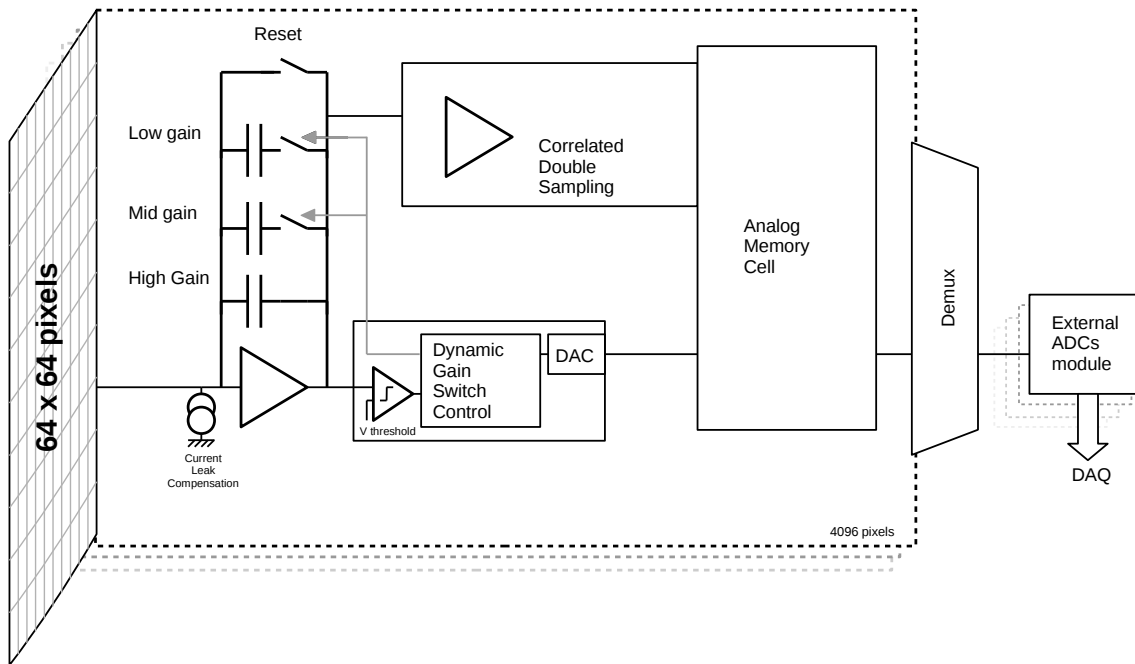
Figure 2.13: A simplified scheme of the AGIPD readout. In order to increase the dynamic range, for each pixel the amplifier switches automatically the gain. The signals are sampled by a correlated double sampling circuit and stored in an analog memory cell. The analog-to-digital conversion is performed by external ADCs.

2.2.3 The Adaptive Gain Integrating Pixel Detector (AGIPD)

The Adaptive Gain Integrating Pixel Detector (AGIPD) is an imaging detector optimized for the detection of hard X-rays. In order to fit the requirements of high gain for low signals together with high dynamic range, the solution adopted by this detector project is the dynamic gain switching, [48]. In the front-end electronics the signal from each pixel passes through a first stage, an amplifier with three different gain settings. The gain is switched automatically after reaching defined thresholds. The mechanism of switching is shown in Figure 2.13. The signal is stored in an analog memory pipeline. The front-end and the analog memory are implemented in a ASIC serving 64×64 pixels. Due to the requirements set by the beamlines, the sensitive part of AGIPD must work in vacuum environment. Therefore the sensors and the ASICs sits in vacuum and they are connected to the external environment by PCBs. The read-out and the analog-to-digital conversion is performed out of the ASIC, outside vacuum, by the electronics, boards operating in ambient conditions.

The AGPID detector is a modular detector, each single module includes 16 ASICs covering one monolithic sensor (512×128 pixels). Four modules together constitute a quadrant, and four quadrants constitute the mega pixel camera.

The AGPID detector was installed at the SPB/SFX beamline in summer 2017 and it is now used for the user program of XFEL.EU. The Figure 2.14 shows AGPID detector
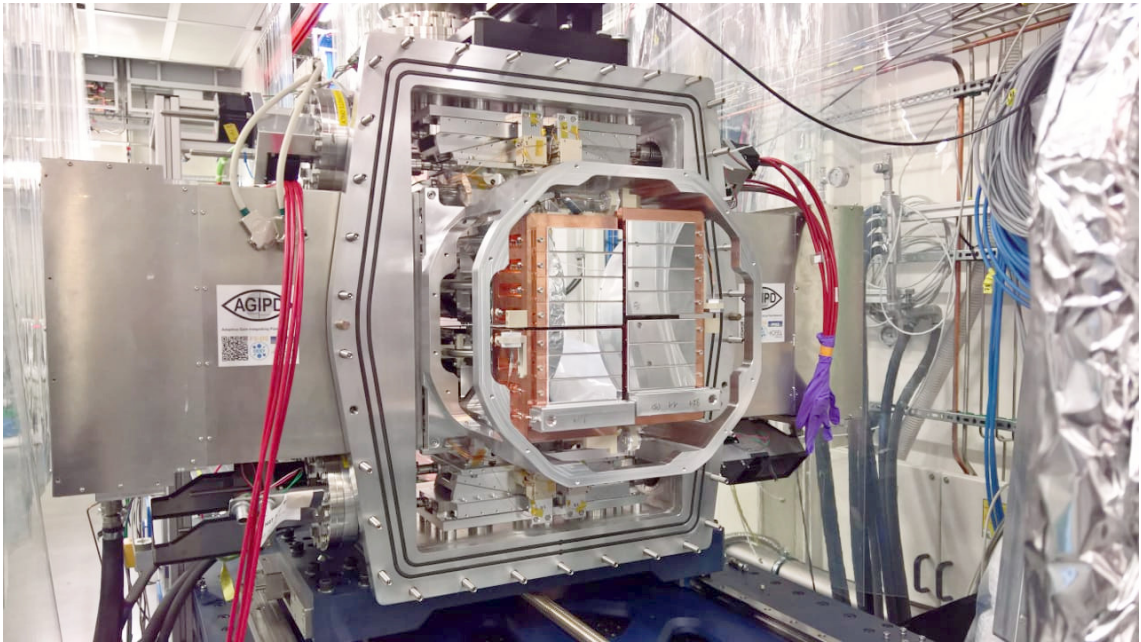
Figure 2.14: The Adaptive Gain Integrating Pixel Detector (AGIPD) in its final location as part of the SPB instrument. Copyright European XFEL, [5].

installed at SFX instrument. A similar one will be installed at MID instrument in 2018 and a 4*M*pixel AGIP in the SFX end-station.

2.2.4 The DEPFET Sensor with Signal Compression (DSSC) detector

The DEPFET Sensor with Signal Compression (DSSC) is an imaging detector optimized for soft X-ray detection. The approach used to reach the high dynamic range and the high gain for low signals is different from the other detector projects. The original project foresaw to use non-linear DEPFET sensors. These sensors feature an extreme low noise and an intrinsic non-linear response to the incoming signal.

Due to the delay in the production of DEPFET sensors, an alternative sensor technology was chosen for the first DSSC camera, featuring pixels based on mini silicon drift detectors (Mini-SDD). The DSSC ASIC readout has been designed with a double front-end, which can read out either type of sensor. In the case of Mini-SDDs, the non-linear response curve is generated in the first amplification stage at the ASIC level.

The read out, the amplification and the analog-to-digital conversion is performed inside the ASIC. Moreover the ASIC provides a digital memory which can store up to 800 frames. Each ASIC reads out 64×64 pixels.

The mini-SDD and DEPFET sensors feature the same geometry; in particular, the interfaces for connection to the electronics are identical. Therefore, it is possible to connect the ASICs to either Mini-SDD or DEPFET sensors.

The basic unit of DSSC camera is DSSC ladder and it has 512×128 pixels. The monolithic sensor of the DSSC has 256×128 pixels, therefore DSSC ladder consists of two

sensors and relative electronics. Four DSSC ladders together constitute a quadrant of the DSSC megapixel camera.

A detailed description of the DSSC detector is given in Chapter 3.

2.3 Common interfaces

In this section, some standards used at the European XFEL are described. The first part is about Karabo, the new control framework developed and used by XFEL.EU; the second part is about the crate used for the timing and synchronization signals generation; the third part is about the idea behind the vetoing system of XFEL.EU; and the last is about the output data format used by the imaging detector project of XFEL.EU.

2.3.1 Karabo
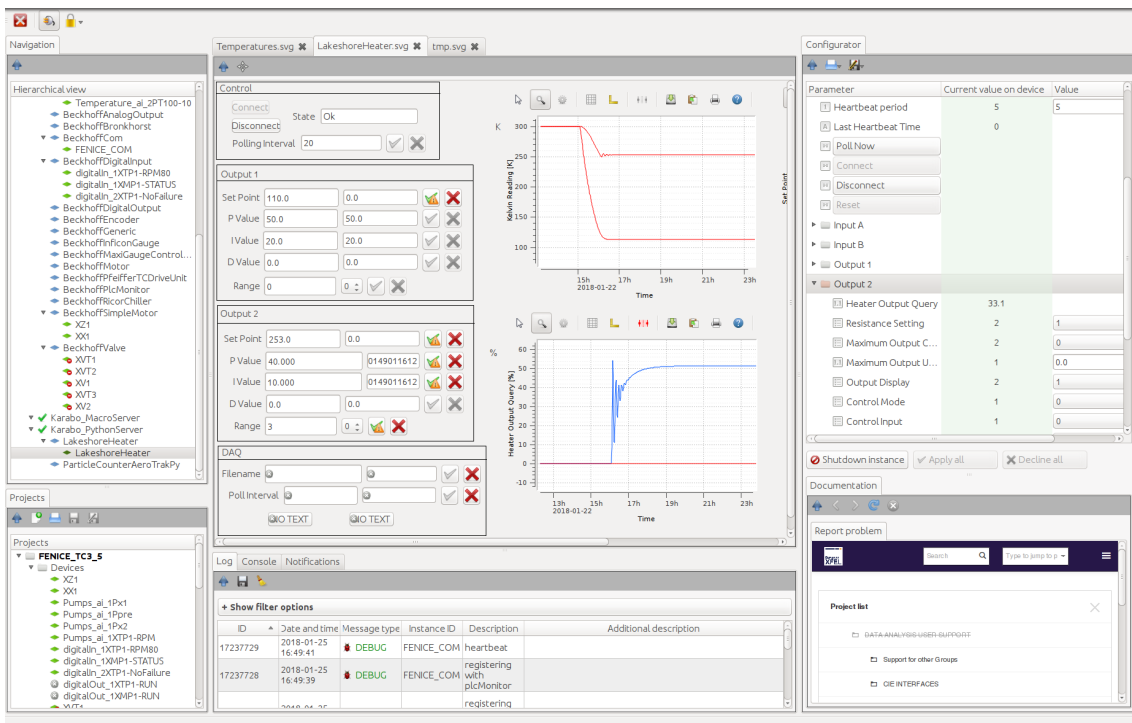
Figure 2.15: A screenshot of the Karabo GUI. In this case Karabo was used for monitoring the temperature controller used in FENICE (see Section 3.5.4).

At the XFEL.EU a new control framework called Karabo was developed, [51]. It is a distributed control system (DCS) which allows for supervisory control and data acquisition (SCADA), [52]. The aim of this project is to integrate under a common platform the controls, the data acquisition, the data management and the scientific computing.

Karabo is based on a client/server architecture and the main components are the Karabo device-server, the Karabo device-client and the Karabo broker. The device-server is a service running on a machine usually physically connected to the hardware to be controlled.
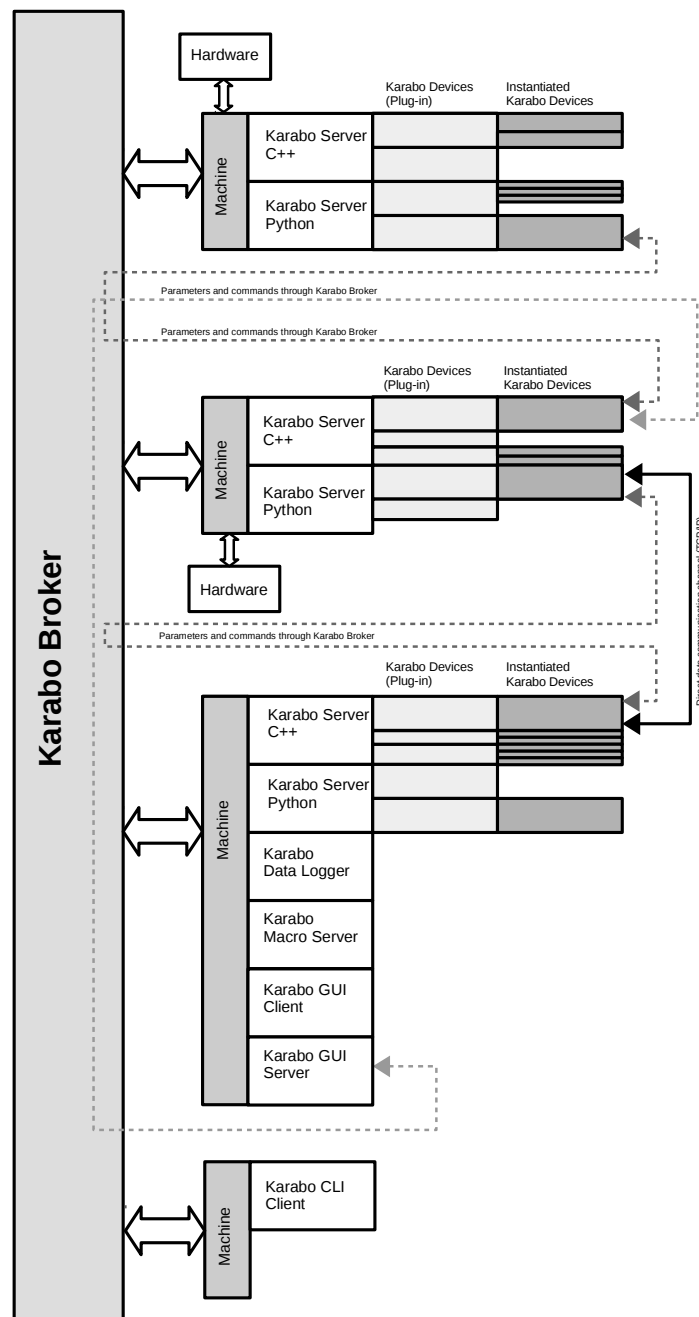
Figure 2.16: A sketch of the Karabo Framework. The system shows the connection of the Karabo servers running on different machines, and running different Karabo devices instantiated. The normal communication (exchange of parameters and commands) between the Karabo devices or client (like the GUI or CLI) passes through the Karabo Broker (dashed arrows). In case a high data rate, a direct TCP/IP channel of communication is also possible (black arrows).

The device-server contains the plug-ins called Karabo devices, which are classes of objects programmed with a defined finite-state machine, parameters, or execution commands. The core of the framework was developed mainly in C++. Many functions are binded also to Python, therefore the Karabo devices can be programmed either Python or C++.

A Karabo device-client can connect to a Karabo device-server for instantiating the plug-ins or controlling instantiated devices. Once a Karabo device is instantiated and running, a client can read or modify the parameters or execute a commands defined in the Karabo device. Karabo foresees a safety level, some parameters or commands can be managed only by authorized users or devices.

A typical device-client for the users is the Karabo Graphical User Interface (GUI) [53], or the Karabo command-line interface (CLI). But a Karabo-device can also behave as Karabo client, so it can control other Karabo devices. The Karabo GUI connects to the servers and features a user-friendly interface. By clicking on a Karabo device is possible to see the parameters and execute commands. The GUI can be used for initializing devices, modifing parameters, and also allows advanced features such as editing and running macros. The user can create an own panels by dragging-and-dropping parameters or commands. Figure 2.15 shows the Karabo GUI with running a scene of a temperature control.

The communication (states, parameters and commands) between the Karabo servers and clients are exchanged via a central Karabo broker.

Karabo is not used only for hardware controlling, but it can be used also for data-processing [54] [55]. In this last case, the communication must not pass through the broker due to the big amount of data to be transferred, as for instance data from the detectors or big data tables. The Karabo broker exchanges only the metadata for opening a direct channel of communication between Karabo devices, based on a protocol which uses direct TCP/IP communication between them. Thanks to this channel it is possible to stream data from a device to another, creating a pipeline of Karabo devices. This can be very useful for data processing. Since a pipeline is composed by many Karabo devices, it has an intrinsically modular design which allows a Karabo developer to take advantage of multi-threading. Each Karabo device can run in a separate thread or even in another machine.

In the context of this thesis, Karabo was used for controlling the detector and its environment, temperature control and monitoring, and control of motion stages. I developed for the first DSSC Ladder prototype a Karabo device able to show the real-time preview of the data, to manage the acquisition and to stora of the data during the peformed tests. The data are stored to HDF5 files [56] as foreseen for the final version of the DAQ system.

2.3.2 MicroTCA crates

In the past, two of the most common crate standards used for measurement, control and automation were the VME (Verso Module Eurocard) and the CAMAC (Computer Automated Measurement And Control); for telecommunication one of the most common is the Advanced Telecommunications Computing Architecture (ATCA, [57]). The MicroTCA [57] standard was orginally developed by the PCI Industrial Computer Manufacturers Group (PICMG, [57]) consortium, for telecommunications as the evolution of the ATCA. Nowadays, the standard MicroTCA.4, *MicroTCA for Physics*, is the most prominent standard for new large experiment facilities such as synchrotrons, colliders or free electron lasers.
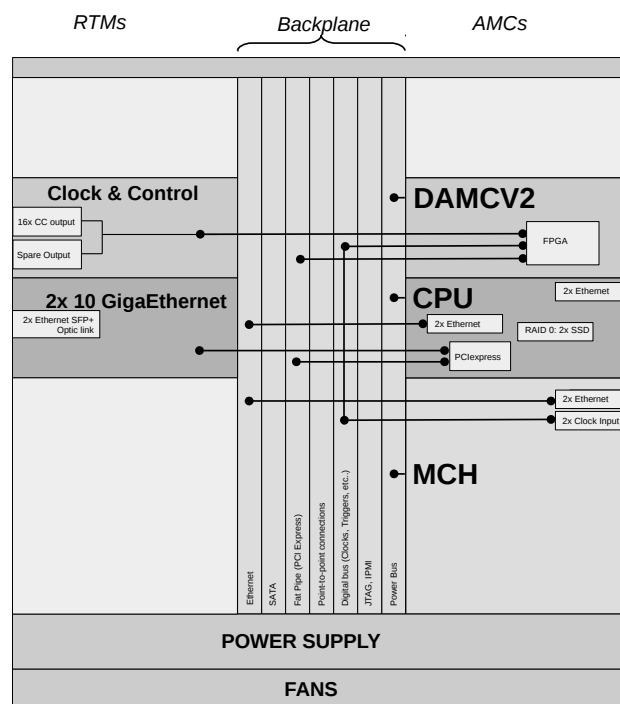
Figure 2.17: Schematic representation of a MicroTCA crate. The different components and modules as described in the text are visible.

A MicroTCA crate allows connecting together different modules which can communicate among each other through the connections on the backplane. There are two types of modules: the front modules (Advance Mezzanine Card, AMC, [57]) and the rear modules (Rear Transition Module, RTM, [57]). The AMC are connected directly to the backplane, instead the RTM are connected to the AMC. This allows the same type of AMC to be used for controlling different types of RTM. The backplane allows the connections between the modules including: a PCI-express fabric; Ethernet connections; SATA connections; point to point signal connection; the power-supply for the modules; and dedicated lines for clocks and triggers.

All devices in the crate, including power supplies and the backplane connections are managed by the MicroTCA Carrier Hub (MCH). The MCH is fully controllable via network, so a crate sitting in a place where the physical access to the device is not possible can be fully managed remotely. In the crate, the boards can be physically replaced when the crate is already running (hot-swap). The MCH allows switching on or off every single boards, and allows rebooting the whole crate. The MicroTCA crates are high reliability system which can implement redundant power supplies and boards including CPU units.

The MicroTCA has become the standard used at XFEL.EU for timing, digitizer and fast controls. The control system for slow control (such motors) is made with Beckhoff devices [58].

In the context of this thesis, I designed and built up the DSSC ladder test-stand which uses a MicroTCA crate as core of the control and time synchronization of the detector.

Clock & Control board

At XFEL.EU, the resonant cavities of the accelerator and all devices which need to be synchronized in phase to the machine use clocks derived from the Master Oscillator clock. The Master Oscillator is a 1.3 GHz clock with an exceptionally good phase noise performance, jitter < 35 fs RMS integrated from 10 Hz to 1 MHz [59]. The signal is generated in a location close to the injector room. The clock is distributed from the injector to the end stations by a dedicated system. The transmitter (injector side) and the receiver (end stations) are coupled by fiber optic, and by using a closed-loop feedback the phase drifts and the noise are compensated by the *timing system*, [60]. The timing system is implemented in MicroTCA boards.

For the imaging detectors, a reference clock at a lower frequency (99 MHz) is used for synchronization. This clock locked-in-phase with the Master Oscillator is generated by the Clock & Control board [61]. This boards generates the reference clock and also other fast commands for the detectors, such as the start and the stop, bunch id and the VETO signals. The signals coming out from this board are three LVDS signals connected to standard RJ45 sockets. One signal is the reference clock at 99MHz, another line is used for the VETO and the third line is the Fast Data. This last line is used for sending the start, stop and the reset commands. The start command includes also information about the train ids and the bunch patterns. The Clock& Control is a RTM module which needs to be coupled with an AMC, the DAMCv2 board, which is a DESY standard multi-purpose FPGA board.

In the normal XFEL.EU operation, the Clock & Control board receives the master clock and other signals from other boards, i.e. Timing System board, through the MicroTCA backplane, and generates the signals (reference clock, fast commands, VETO) based on the 99MHz clock.

The Clock & Control can also work without the Timing System board. It is possible to

set the Clock & Control to use an internal clock generator (stand-alone mode). It is also possible to set the board to receive a clock provided by the backplane of the MicroTCA crate, which can be for example connected to an external clock provided by the SMA connector available in the MCH. In both cases it is possible to set the clock frequency by acting on the internal phase lock-loop (PLL). The multiplication and division factor can be set on the control software. The usage of the Clock & Control board without a timing system is useful to synchronize the detector to an external light source such as a synchrotron with a different timing structure than the XFEL.EU.

The start/stop signals can be generated automatically with a certain repetition rate defined by the user via software.

The Clock & Control board includes also the possibility to use two spare lines for testing purpose. The board can generate a defined pattern of pulses synchronized to the start command based on the reference clock. This is useful for testing the detector with an external pulsed light, but also for checking the synchronization of the detector to an external source. This feature of the board has been used for the measurement in Chapter 4 and 5.

During the work of this thesis the Clock & Control has been used in both modality. The stand-alone mode was used to generate the timing signals for DSSC and also a spare signal used as input to a LED driver. This system was used to test the DSSC detector and its synchronization, see Chapter 4. I integrated the Clock & Control in the DSSC test-stand. I tested and brought it into operation, designing new features when needed.

During the Petra III beam-time (see Chapter 5), the Clock & Control was used in external clock mode and the spare pulse was used as reference only for monitoring the synchronization to the synchrotron. Moreover, in order to emulate the 10 Hz time structure of XFEL.EU, the start/stop signal was generated internally. In order to integrate the DSSC detector in the Petra III, I designed, configured ad realized the concept of synchronization with the synchrotron.

2.3.3 The Veto concept

In contrast to high energy physics, where a trigger systems is used to acquire or analyse only interesting events, rejecting the majority, in photon science the scientists would ideally store all information coming from the 2700 pulses of the XFEL.EU trains. This is not as the XFEL.EU data acquisition system allows to acquire and store only a maximum of 512 images per train. Therefore, the concept of a "VETO" system has been developed. The VETO mechanism consists in flagging in the memory of the detector a frame as non-good. The flag tells the detector that the marked frame can be to overwritten in the memory. The signals which trigger a VETO can be generated by other external system or sensor (for example a beam monitor) or by the detector itself. In this last case, the VETO system can also be used to collect only a fraction of the images when the detector is running at 4.5 MHz, for example in case of planned empty bunches.

2.3.4 The data format

In order to have the same type of data receiver for all the detectors developed for the XFEL.EU the large detector projects use the same transfer protocol and same data format. All detectors use SFP+ 10GB optic link and the Train Transfer Protocol (TTP) [62] is an own XFEL.EU protocol based on plain User Datagram Protocol (UDP) protocol. The UDP protocol is one of the standard protocol used for Internet. It allows to transmits data with a minimal protocol through a network without estabilish a connection. This protocol has a minimal overhead and it assumes that no packet are lost. The reason to use the UDP protocol derives from the fact that in comparison to other protocols, such as the TCP/IP, it is simpler, faster and easily implementable in low level electronics, like FPGA (Field Programmable Gate Array).

In the TTP for data transfer consecutive UDP datagrams are transmitted. Each UDP datagram contains payload of 8129 bytes, a trailer with a progressive packet number and a flag for marking the start or the last datagram. The images and the information from the detector are formatted according to the XFEL Train Data Format (XTDF) [63] and transmitted through the TTP. The data format consists of a sequence of:

- Header: it describes the properties of the train of data (such as data size, version of the protocol, type of detector, encoding, etc...).

- Image: this block is the actual payload of the train. It contains the images stored in the detector memory. The encoding of this block is detector dependent.

- Descriptors: it contains metadata of the image blocks such as pulse id, length of the image payload, and similar.

- Detector specific data: as suggested by the name, are different for each detector. They include all useful information which are not images. For instance, in the case of the DSSC detector this block includes the temperature values recorded from the ASICs and the checksums from the ASICs.

- Trailer: it contains a checksum and a magic-flag used for debugging purposes.

In the context of this thesis, since the official Karabo data receiver (named PCLayer) was not already mature, I developed an independent stand-alone receiver for the XTDF over TTP. It could work either in a stand-alone mode, or controlled by Karabo and it was used for the data preview.

3 DSSC

The DEPFET Sensor with Signal Compression (DSSC) detector [6] is a high speed imaging detector developed by the DSSC Consortium for XFEL.EU. The detector has been designed to meet the requirements set by the SCS and SQS instruments (see Sections 2.1.2 and 2.1.3). It is optimized for the energy range $0.5\,\text{keV} - 6\,\text{keV}$, therefore it needs to operate in high vacuum conditions, 10^{-6} mbar or lower.
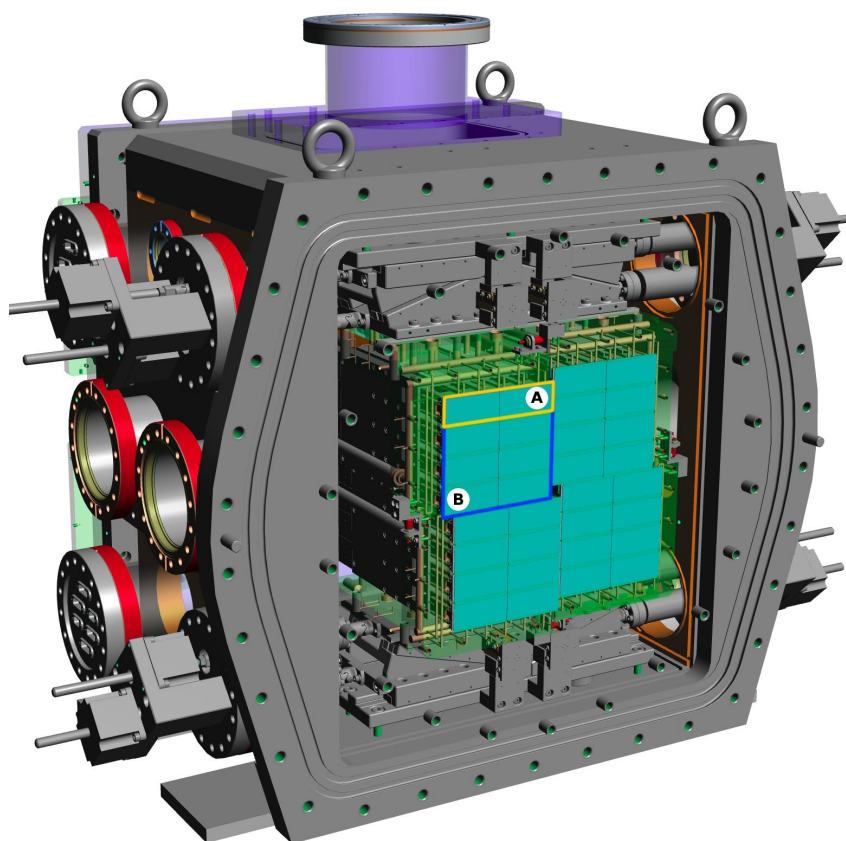

Figure 3.1: The 3D model of the DSSC megapixel camera and in its vacuum chamber. The label A indicates a single ladder and the label B shows the quadrant. Courtesy of the DSSC Consortium [64].

The DSSC detector is a 1 Mpixel [65] camera able to store up to 800 single-pulse images per XFEL.EU train, matching the XFEL.EU pulse rate of 4.5 MHz pulses. The megapixel camera has a sensitive of area approximately $21 \times 21\,\text{cm}^2$ composed of 1024×1024 pixels having hexagonal shape.

Figure 3.1 shows a drawing of the the megapixel camera in its vacuum chamber. The

full mega-pixel camera is composed of 16 ladders, arranged in four quadrants. Each quadrant is composed of four ladders which represents the smallest detector unit including of the full readout chain. As such, each ladder can therefore be tested independently of the others. The results reported in this thesis (Chapter 4 and Chapter 5) are based on the measurement performed with the first prototype of the DSSC ladder.

The original DSSC project foresaw the use of non-linear DEPFET sensors. This type of sensor allows an extreme low noise and a high dynamic range, due to the intrinsic non-linear response of the sensor. Due to delays in the DEPFET production, the consortium has decided to adopt for the first version of the camera a more conventional sensor type, a pixelated sensor composed of silicon-drift detector arrays (Mini-SDD). The full electronics chain is designed to be compatible with both sensor types. The DEPFET sensors are described in Section 3.1 and the Mini-SDD sensors are described in Section 3.2.

The readout ASIC implements a front-end for both type of sensors. The layout of both sensor types is designed to be compatible with the ASIC. Each monolitic sensor contains 256×128 pixels; the DSSC ladder system is composed of two monolitic sensors. Each ASIC can read out 64×64 pixels, a full ladder is readout by 16 ASICs. The description of the ASIC is given in Section 3.3, while Section 3.4 gives a functional description of the DSSC ladder system.

3.1 DEPFET sensors

The Field Effect Transistors (FET) [66] are semiconductor devices where the current between the drain and the source is regulated by the voltage applied to the gate with respect to the source. An example, the pMOSFET is sketched in Figure 3.2.
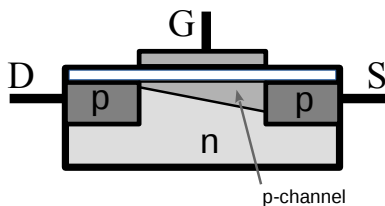

Figure 3.2: Scheme of a p-channel metal-oxide-semiconductor field-effect transistor pMOS-FET. G indicates the gate, S the source, D the drain. The letter p and n indicate the doping of the different parte.

In the p-channel FET, the bulk is n-doped so the majority charge carriers are electrons. When a negative voltage is applied to the gate (G in Figure 3.2), the electrons present in the bulk are pushed away from the zone under the gate, creating a depletion zone. If the voltage increases in magnitude above a certain threshold, the holes are attracted under the gate. In this way, a channel of positive charge carriers (holes) in the zone under the gate is created (p-channel). The channel allows a current flowing between source and drain. This current is modulated by the voltage applied to the gate. For the n-channel

FET, the working principle is similar but with inverted charges and voltages.

The Depletion p-FET (DEPFET) [50] are FET with the source, the drain and the gate located on the front side of a silicon wafer forming a large area diode on the back used to fully deplete the bulk, [6], see Figure 3.3(a). The first DEPFET structure was invented by Lutz und Kemmer [67] in 1985 [68].
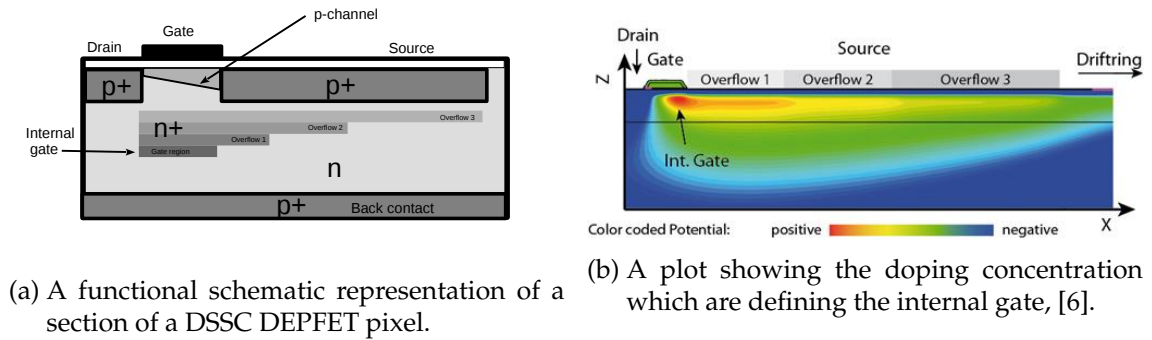

(a) A functional schematic representation of a section of a DSSC DEPFET pixel.

(b) A plot showing the doping concentration which are defining the internal gate, [6].

Figure 3.3: A sketch of the DEPFET sensor.

In the bulk, a deep n-doping (n+) is deposited into an area under the gate. It creates a potential maximum, called *internal gate* where the electrons are attracted into. The bulk is fully depleted by a bias voltage, thus when the radiation interacts with the bulk, free charges (electron-hole pairs) are generated, as described in Section 1.7. Due to the static electric field generated by the doping, the electrons are attracted inside the internal gate and the holes recombine at the extremities of the back-side bulk.

The charges stored in the internal gate induce mirror-charges in the p-channel, which regulate the current flowing between the drain and the source.

The DEPFET allows measuring indirectly the energy deposited in the sensor by measuring the current flowing between the source and the drain.

In comparison to other kind of sensors, such as photodiode, or silicon drift detector, the DEPFETs have peculiarities. In photodiodes or SDD sensors, the energy deposited into the sensors is measured directly as the charge generated inside the sensor and then read out. This is a destructive measurement because the charges are removed from the sensors during the measurement. In the DEPFET, the measurement is performed in a different way. The DEPFET acts an amplifier and the charge stored inside the internal gate can be determined by measuring the current flowing between the source and the drain. Moreover, the charge is not removed from the sensor but it is stored in the internal gate until a reset signal is given.

In order to realize the signal compression, the DSSC project uses special type of DEPFET sensor, the non-linear DEPFET [6]. The internal gate extends also under the source with a gradual lower doping. When radiation interacts with the sensor, free charges are generated in the depletion region and their number is proportional to the deposited energy. In the case of the deposited energy is low, a small number of charge is produced. They accumulate in the region under the gate, giving the maximum contribution to the creation

of mirror charges in the p-channel. This is the case in which the gain (ratio source-drain current vs energy deposited) is maximum. In the case of a larger signal, a fraction of charges spill over into the region below the source, which does not contribute to generate mirror charges in the channel, therefore the gain (ratio source-drain current vs energy deposited) is lower. In the DSSC DEPFET, three regions with different doping concentration are implemented.

The technique used to read-out the current from each single DEPFET pixel sensor is described in the section Section 3.3.

3.2 MiniSDD sensors

The working principle of the silicon drift detectors (SDD) is similar to that of the conventional photodiode. A photodiode typically features an anode and a cathode of similar size. They are used to polarize the diode in reverse polarization, creating a large depletion zone. As explained in the Section 1.7, a photon interacting in the depletion zone generates electron-hole pairs. The charge is collected at the electrodes.

In the SDD, in order to improve the performance, special electrode structures (rings) are implemented. The anode surface is reduced and the control electrodes are used to create a gradient in the electric field which pushes the charges toward the anode. In comparison to a conventional photodiode, the sensitive area does not depend on the size of the anode. The reduced dimension of the anode decreases the capacitance reducing therefore the noise, [69]. The Figure 3.4 shows a comparison between the PIN photodiode and the SDD.

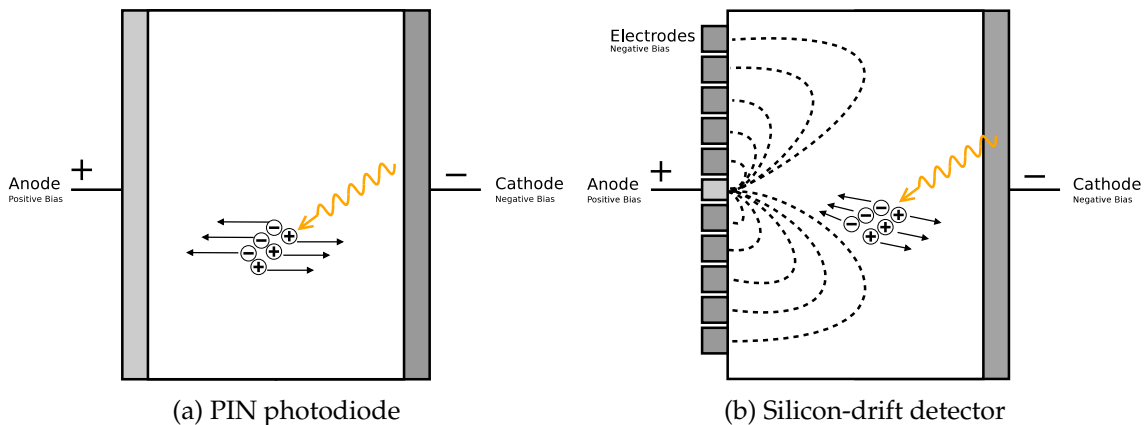(a) PIN photodiode   (b) Silicon-drift detector

Figure 3.4: Comparison between the working principle of a photodiode (a) and a silicon-drift detector (b).

As in the photodiode, the amount of collected charges is proportional to the energy deposited by the photon.

The sensors built for DSSC are arrays of SDD sensor, where each pixel feature a small SDD sensor with only two drift electrodes (Mini-SDD). The front-end electronics implemented in the DSSC ASIC allows using either DEPFET or MiniSDD sensors: for this

reason both type of sensors have the same layout.

Since the Mini-SDD is a linear device, the non-linearity needed to extend the dynamic range are introduced in the first amplification stage of the ASIC, [70]. The front-end used for reading out the Mini-SDD signals is described in the next Section.

3.3 The DSSC ASIC front-end

The DSSC ASIC [71] has 64 x 64 readout channels and it can be coupled with both type of sensors DEPFET and Mini-SDD. The energy deposited by a photon to a single pixel is read out differently in the DEPFET and Mini-SDD cases. For the Mini-SDD, the energy deposited into the sensor is converted into a charge. In case of DEPFET, the energy deposited by the photon into the sensors is converted to a charge internally but in this case the pixel acts as amplifier therefore, the output is a current proportional to the deposited energy.

The front-end of the DSSC readout chip (ASIC) is able to deal with both type of sensors. To measure the charge coming out of a Mini-SDD sensor pixel, an extra ciruit for converting charges into a current is needed. This stage allows introducing the compression of the signal, needed in order to reach the requested high dynamic range.

The DSSC ASIC front-end includes for each single pixel: an input branch (amplification); a filter; an analog to digital converter (ADC) and a memory (SRAM). The single components, part of the ASIC as the ADC, the input stage, the filter and the memory were developed by the different groups of the DSSC Consortium. The global layout of the ASIC was developed by Dr. Florian Erdinger and an extensive description of the features of the front-end electronics can be found in his doctoral thesis [72]. Below is given an overview of these components and the timing of the front-end. A block diagram of the front-end is shown in Figure 3.5.
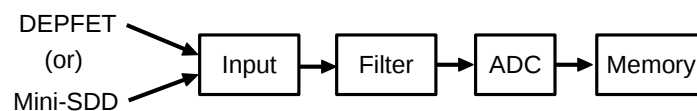

Figure 3.5: A block scheme of the DSSC detector front-end. For both DEPFET and Mini-SDD the same four stages are present. Only the first stage (input branch) is used in a different mode depending on the sensor type.

The input branch

In the case of DEPFET, the output signal from the sensor is a current. The input branch is essentially a cascode (current buffer) and a current sink. The current sink compensates the coarse component of the dark current of the DEPFET; therefore, the current out from this stage is the drain current with a small contribution of dark, which is compensated by the next stage, the filter.

In the case of Mini-SDD, the charges coming out from the sensor are converted into a current and amplified on the ASIC input branch. This stage provides also the possibility to implement a non-linear conversion, to increase the dynamic range.

The main differences between DEPFET and Mini-SDD front-ends is shown in Figure 3.6.
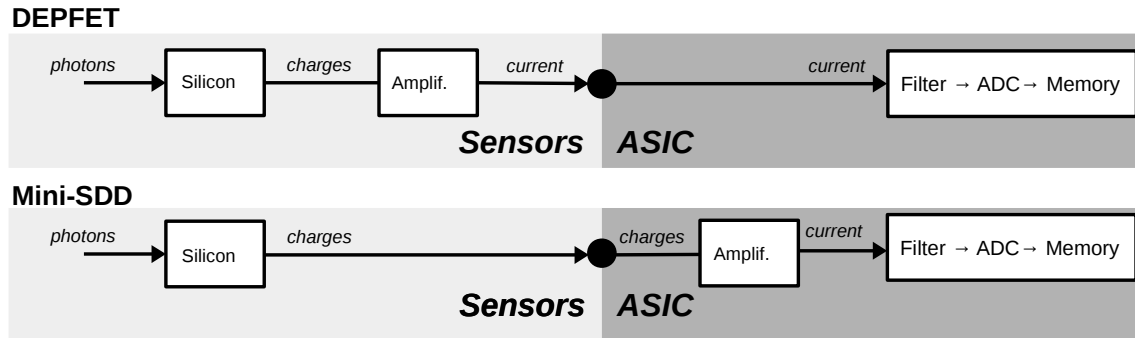

Figure 3.6: A block scheme of the front-end, showing the different approach between the DEPFET and Mini-SDD readout. The filter, the ADC and the digital memory are the same for both type of sensors. The light gray represent the sensors, and the dark gray the ASIC. The black circle between the ASIC and sensors represent the bump used to bond them together.
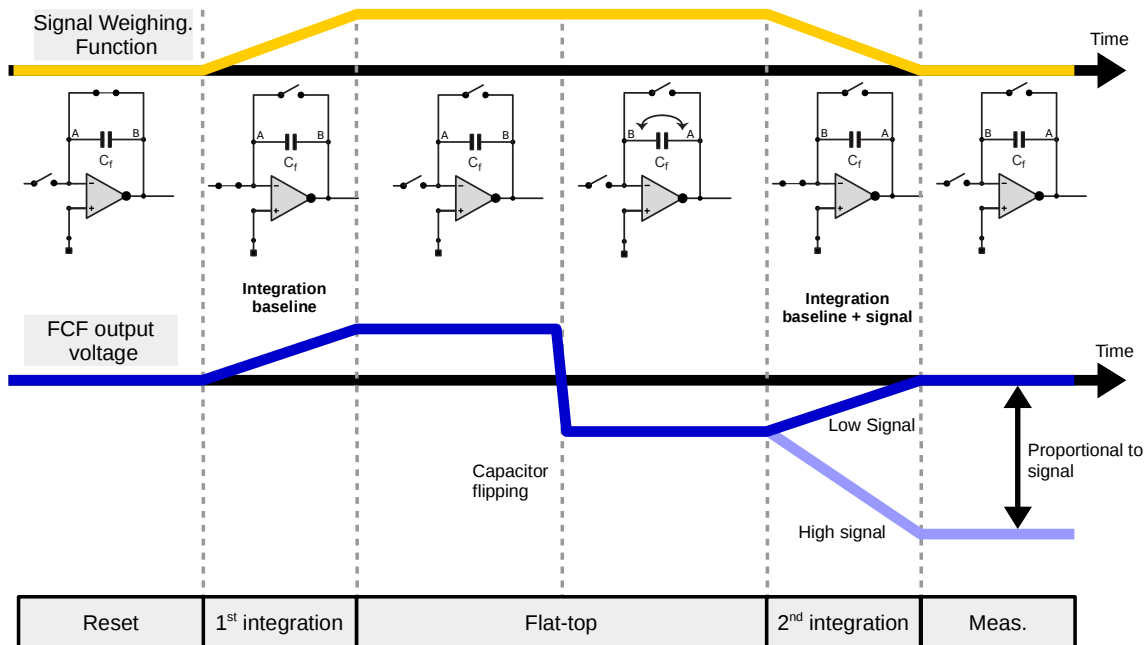

Figure 3.7: A sketch of the FCF filter working principle. The blue line represents the voltage out from the FCF circuit at a given time. The yellow line represent the effect of a signal incoming at a given time(signal weighting function). The input signal (photon) in normal condition arrives during the flat-top phase.

The filter

The Flip Capacitor Filter (FCF) is a stage which perform a double integration and subtraction, for removing the residual dark current contribution. The result is a double-correlated sampling, which reduces the noise contribution, [73]. The different steps of the signal processing are schematically shown in Figure 3.7.

In a first phase, the switch which connects the capacitor plates is close, therefore the capacitor C_F is reset. During the first integration phase the input switch is closed. The current flows into the capacitor plates which starts to integrate the current from the input node (only the baseline current). The voltage between the capacitor is $V(t) = \frac{1}{C_F} \int i_{inp}(t) \mathrm{d}t$, for this reason the gain of the FCF filter is proportional to $1/C_F$. The integration stops when the switch is open. During this phase, called flat-top, the voltage between the plates of the capacitor are keep constant and the capacitor is flipped. It is during this phase that a photon is expected to arrive on sensor. In fact, once the switch is close again, the second integration starts. In this case, not only the baseline is integrated, but the baseline plus the signal. Since the two integration cycle have the same duration the baseline currents are compensated, see Figure 3.7. Once the switch is opened, the charge stored in the capacitor is proportional to the charge deposited into the sensor. The voltage between the capacitor plates is converted to a digital value on the next stage.

The Analog to Digital Converter

The analog to digital converter (ADC) used by DSSC [65] is a single ramp-ADC [74]. The first stage converts the voltage into a time delay and the second stage converts the time information into digital timestamp.

A simplified scheme of the ADC design is given in Figure 3.8. Initially the input switch is closed and the switch to the ramp current source and comparator is opened; therefore the voltage of the ADC input (which is connected to the FCF filter output) is applied to the plates of one capacitor $C_{S\&H}$. In order to convert the voltage stored in the $C_{S\&H}$ to a delay, the input switch is opened and the switch to the ramp current source and comparator is closed. A constant current is injected into the $C_{S\&H}$ and the voltage of the plate of the capacitor $C_{S\&H}$ increases with a constant slope. Once the voltage exceed a certain threshold, the comparator triggers and the latch holds the value of the counter. This digital value can be passed to the digital circuit which manages the SRAM memory. Each pixel implements an ADC. The counter is a Gray-code counter [75] running at 693 MHz in normal operation and used by all pixels of the ASIC.

Timing

The timing of the front-end circuit is managed by a sequencer implemented into the ASIC. The sequencer uses the *fast* clock (693 MHz) derived from the detector reference clock (99 MHz), which in its turn is derived from the bunch clock of the facility (see Sec-
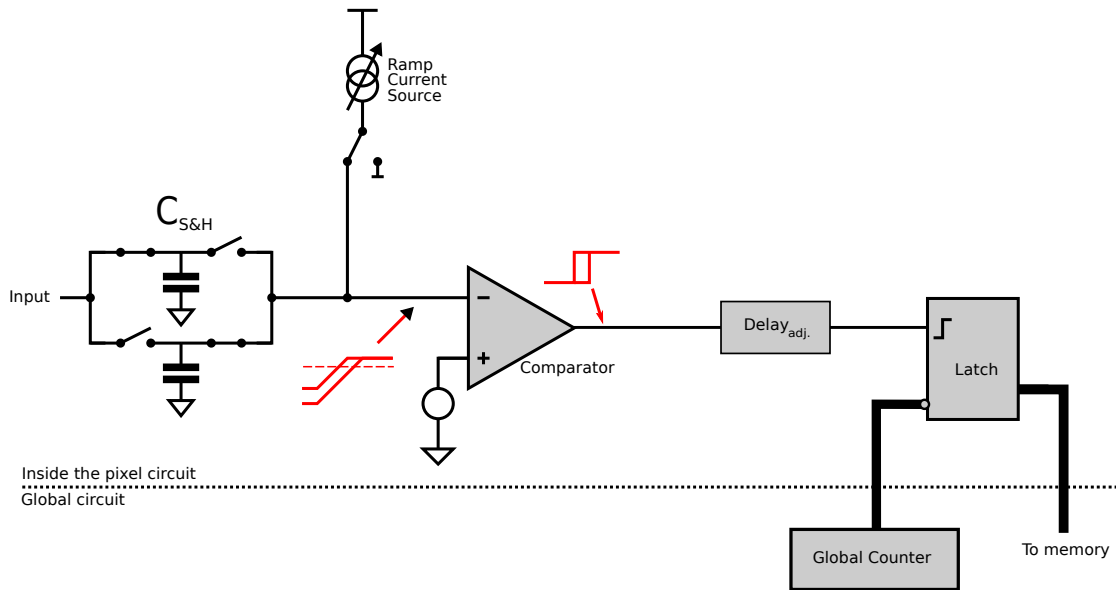
Figure 3.8: A simplified scheme of the working principle of the single-ramp ADC. The input signal converted to a delay triggers a latch connected to a counter. The timestamp is proportional to the input voltage.

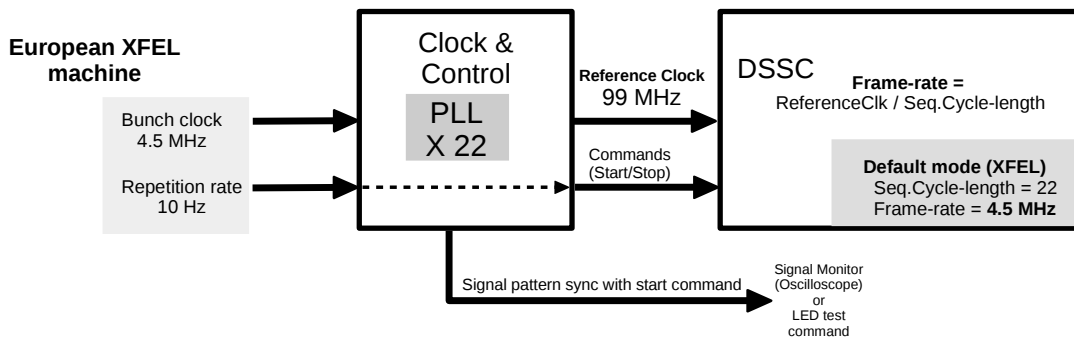Figure 3.9: The scheme of the clock interfaces and timing configuration of the DSSC detector at XFEL.EU. The bunch clock and the repetition rate signals of the XFEL.EU are handled by the Clock & Control system (see Section 2.3.2). The frame rate is defined by the sequencer-length and the 99 MHz clock coming from the Clock & Control system. The time alignment to the XFEL trains is given by the start/stop commands.

tion 2.3.2). The global counter used by the ADC is based on the *fast* clock.

The frame-rate of the detector is defined by the cycle-length configured on the sequencer as

$$\text{FrameRate} = \text{ReferenceClock} / \text{CycleLength} = 99 \text{ MHz} / \text{CycleLength} .$$

The typical timing configuration to be used for the normal operation of the DSSC detector at XFEL.EU is shown in Figure 3.9.

The European XFEL has a 10 Hz train repetition rate. A unique feature of the DSSC detector is the fact that the components of the ASIC, with the exception of the digital parts, are switched on for the arrival of the train, and off when no train arrives. This allow a drastic reduction of the power requirement, and a consequent reduction of the heat generated by the read-out electronics. In order to switch on all necessary components, the detector needs to receive a start command at least 20 µs before the European XFEL train arrives. In this way the system has enough time to turn on the local power supply (see Section 3.4) and to settle. The detector can then sample and store up to 800 frames (burst) per train. After the burst, the power lines used for the analog circuits of the ASIC are switched off and the system reads out the memory, transferring the data to an external device. This operation takes about 90 ms, short enough for the detector to enter in idle mode, waiting for the next start command. Figure 3.10 shows the phases of the detector data acquisition as configured for the XFEL.EU timing structure.

Gain and parameter trimming

The effective gain of a pixel depends on many ASIC parameters. As the ASIC is not an ideal circuit, each pixel can have different features. For each pixel, several parameters can be tuned at the ASIC level to compensate the pixel-by-pixel gain differences. If the detector is perfectly tuned to detect single photons of energy E_γ, the energy of the single photon (E_γ) generates a signal in the center of the first ADC bin; the energy of two photons ($2E_\gamma$) corresponds to a signal in the center of the second ADC bin and so on. Figure 3.11 shows graphically the concept. Since the detector has an electronic noise defined as the standard deviation of the signal measured when no photon hits the detector a dark signal can be misidentified as a photon (false photon detection). The probability of such an event depends on the level of electronics noise and it is discussed in Section 5.5.

The so-called ASIC trimming is performed by an automatic procedure determining the parameters, which optimize the uniformity of the pixels response to a given signal. This algorithm was developed by Manfred Kirchgessner and is described extensively in his doctoral thesis [76].

3.4 The DSSC ladder readout

The basic module of the DSSC detector is the DSSC ladder [65]. The DSSC ladder system includes all the components needed for acquiring the data from a single DSSC ladder,
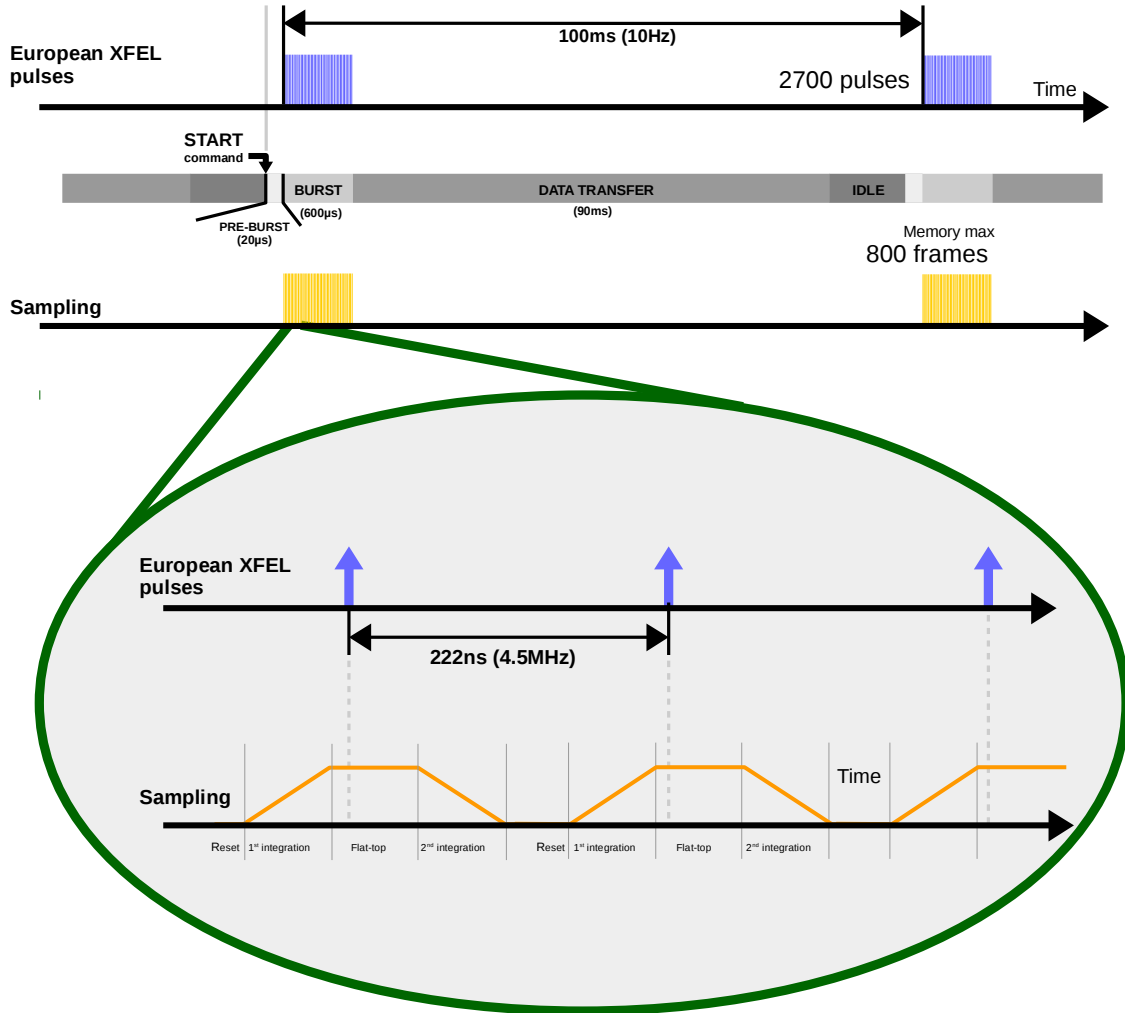
Figure 3.10: The DSSC detector signal acquisition timing, as configured for European XFEL timing. In the first sketch, the timing structure at the XFEL.EU, with its trains coming at 10 Hz repetition rate, and featuring 2700 pulses at 222ns distance from each other, is shown. The DSSC detector receives the START command at least 20 μs before the arrival of the train. The second line indicates the DSSC detector phases (start command, pre-burst, burst, data transfer idle). A total of 800 frames can be stored into the detector memory per train. The zoom in the lower part indicates the expected time alignment between the XFEL.EU pulses and the detector sampling. The XFEL pulse arrives during the *flat-top* phase of the detector.
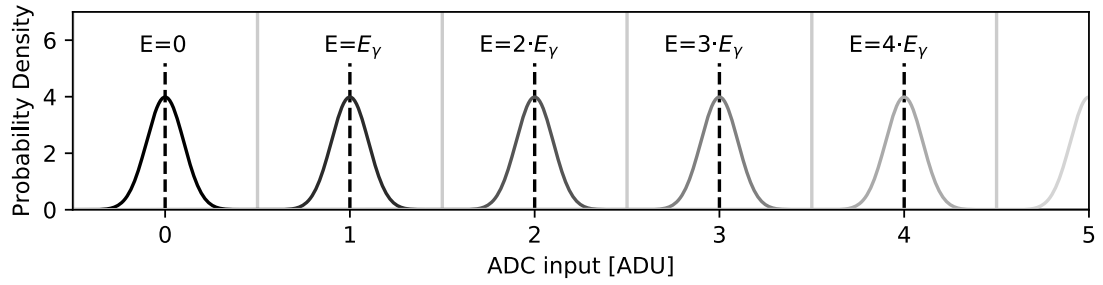
Figure 3.11: In the case of perfectly tuned detector, the energy of the single photon (E_γ) generates a signal ending in the center of the first ADC bin; the energy of two photons ($2E_\gamma$) generates a signal in the center of the second ADC bin and so on. The effect of the compression plays no role in the first bins. The sigma of the Gaussian distribution of the detector signal is due to the electronic noise of the detector. The gray vertical lines represents the border of the ADC bins.

i.e. 512×128 pixels. In this sense, the ladder can be used as an independent detector system. An overview of the DSSC ladder system is given in Figure 3.12.

The first part of the ladder is the focal-plane. It includes the two monolitic sensors (for a total of 512×128 pixels) bump-bonded to 16 readout ASICs, which in turn are wire-bonded to the mainboard.

The mainboard is a ceramic PCB featuring commercial high-density connectors for the connection to the other boards. It is connected to the input/output board (IOB), to a flex cable (FC) and to the four regulator boards (RBs).

The RBs are special local power supplies, which are used for providing the power to the ASICs. The ASICs power cycle is given by the regulator boards managed by the IOB. In the case of DEPFET, the strong current pulses used for removing the charge stored in the internal gate of the sensor is provided by the gate drivers located on the RBs. In the case of Mini-SDD, the gate drivers are not used.

The IOB is a FPGA-based board used mainly for reading out the data [77] from the ASICs memory and repack them in the Xilinx Aurora protocol [78] and transmit them to the Patch Panel Transceiver (PPT). Moreover, this device is used to manage the regulator boards and so the power-supply timing.

The FC is used to supply the high voltages used for the sensors bias voltage and also it used to connect the JTAG chain between the mainboard (thus the ASIC) and the outside components.

The module interconnection board connects these devices together to the patch panel flex cable. All the boards of the ladder are included in a mechanical container and are meant to be operated in vacuum. The patch panel is placed in ambient, the connection at the vacuum interface is given by a vacuum feedthrough in which the connector of the patch panel flex cable is glued. The patch panel provides the sockets for the power-supply cables and the slot for the patch panel transceiver (PPT).

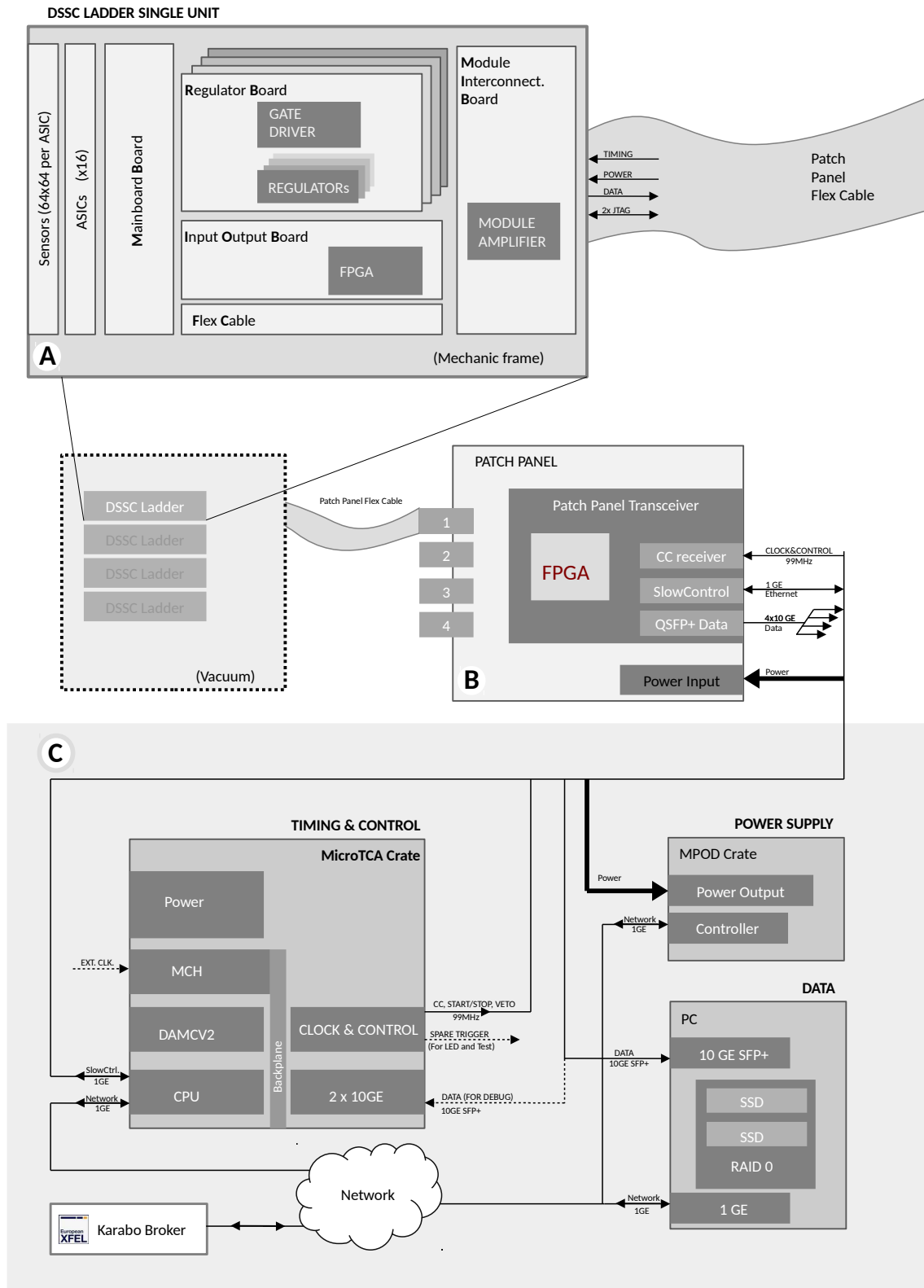Figure 3.12: DSSC Ladder system, a simplified block scheme. The label A indicates all the components part of the DSSC ladder. These devices are sitting in vacuum. The label B indicates patch panel trasceiver (PPT). It supports up-to four DSSC ladder, forming a quadrant. The label C indicates the power supply and the standard XFEL components used for controlling and for storing the data from the detector.

The PPT [79] is a Xilinx FPGA-based board with a MicroBlaze soft processor [80], running a Linux server accessible via Ethernet. This board programs the register of the ASICs, configures the IOBs, synchronizes the read-out to the standard XFEL CC such as the reference clock, the veto, the bunch id. The PPT reads out the ASICs data output through the IOB, it converts them in the standard XFEL train data format and sent them through the optic link to the XFEL.EU data acquisition system. The data output connection is a Quad Small Form-factor Pluggable (QSFP+) corresponding to four independent 10 GBit/s Ethernet (SFP+) optic lines. The PPT supports up to four ladders and each 10GE line is assigned to a single ladder.

The power-supplies are MPOD-based crate. The MPOD [81] are universal multi-channel low voltage (LV) and high voltage (HV) computer controlled power-supply system produced by Wiener [81]. A MPOD crate is composed of modules which can be dedicated to HV or LV. The MPOD controller module allows controlling the system by TCP/IP network, USB or CAN (Controller Area Network, [82]) interfaces. Each channel can be switched on and off, and in the HV modules it is possible also to ramp up or to ramp down the channels. Many safety features like interlock and overcurrent protection are present. For the single DSSC ladder, only a MPOD-Mini power supply is required, while for a quadrant a full MPOD crate is needed.

The Clock & Control signals [61] as well the PC Layer used for the data acquisition will be provided at the XFEL.EU beamlines. For testing purposes the DSSC ladder systems uses its own stand-alone solutions. A MicroTCA crate configured with a Clock & Control board was set up for synchronization purposes. It features also a dual 10GE optic board which allows testing also the data acquisition.

The data acquisition system was a fast machine (Intel Xeon(R) CPU E5-2680 v2) equipped with 64 GByte of RAM, a 10Gbit/s Ethernet optic board, a dual fast solid state disks (SSD) configured in RAID 0 (stripe) array.

During the work of this thesis, in a first phase, I built a semi-automatic tests for the Regulator Boards, and I tested the functionalities of the IOB and the PPT and the integration between the components. I designed the and build the DSSC ladder MicroTCA system. When the sensors were mounted on the DSSC ladder electronics, I brought into operation the detector and measured its performance. The tests and characterization were performed with two different types of DSSC ladder systems.

The first system is a small version of the DSSC ladder. It includes all the standard devices of the DSSC ladder system but uses a replacement board instead of the standard mainboard (MB). This replacement MB was built to allow the use of a single ASIC and it was used with a DEPFET sensor. This system was design to be used in ambient to perform tests in the laboratory. It was used to debug the electronics, to work on the integration and to determine with a pulsed LED light the preliminary performances of the detector, see Chapter 4.

The second system is a full DSSC ladder system connected to the Mini-SDD sensors.
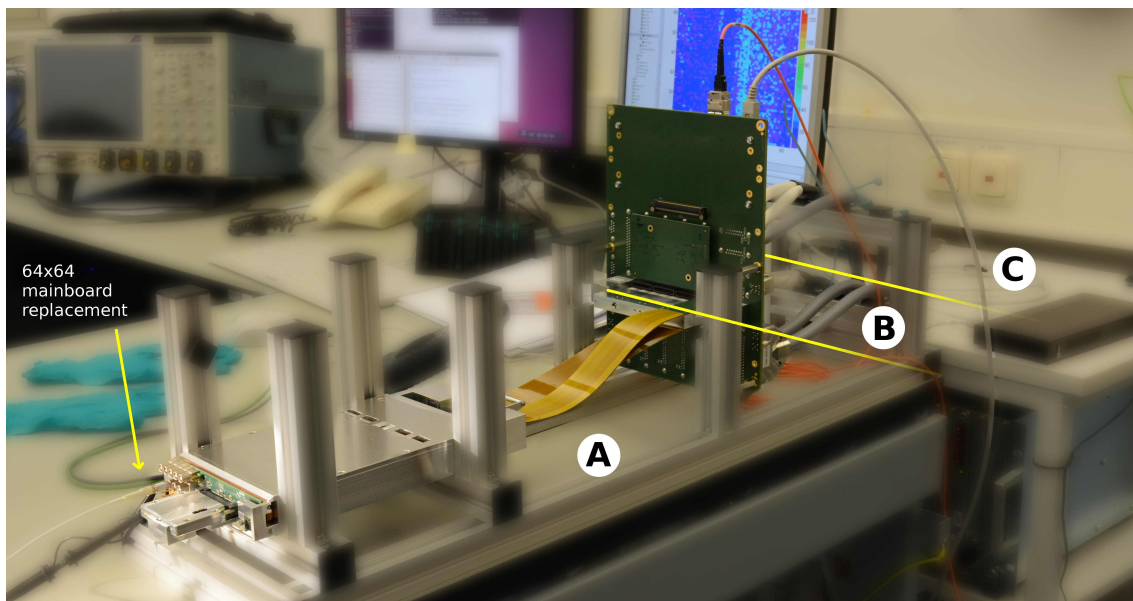
Figure 3.13: DSSC ladder in clean room, equipped with a single ASIC. The zone A in-
             cludes the components prepared for vacuum, such as the mechanic frame
             of the ladder holding sensors, ASICs and other components. The zone B
             corresponds to the patch panel and its links, these devices works in ambi-
             ent environment. The zone C includes the power supplies and the external
             components, [83].

This system was designed to work in vacuum. Therefore, it requires a special vacuum
test stand, that is described in the next Section.

3.5 Vacuum environment and FENICE

At the XFEL.EU instruments, the DSSC detector must work in a UHV environment. This
requirement complicates many aspects of the project. Each device which requires to be
operated in vacuum, needs to be qualified for it. When operated in vacuum, each material
releases a certain amount of gas, called residual gas. Each components of the DSSC ladder
was therefore tested separately in a dedicated setup, and the residual gas analysis (RGA
[84]) was performed. The Figure 3.14 shows residual gas analysis of the DSSC ladder
including all components.

   In this context, I built a test-stand (BigPipe) which was used for the vacuum qualifica-
tion of the components.

   The vacuum requirements means also that special care must be taken during the pro-
duction and the electronics test phase. The boards were handled in a clean room environ-
ment and in order to avoid to contaminate with grease or other substances, the boards
were always handled with gloves. Some PCB boards needed a special cleaning process
after the production in order to remove the possible residuals from the production pro-
cess.

   The fact that boards have to be operated in vacuum puts some constraints on the design

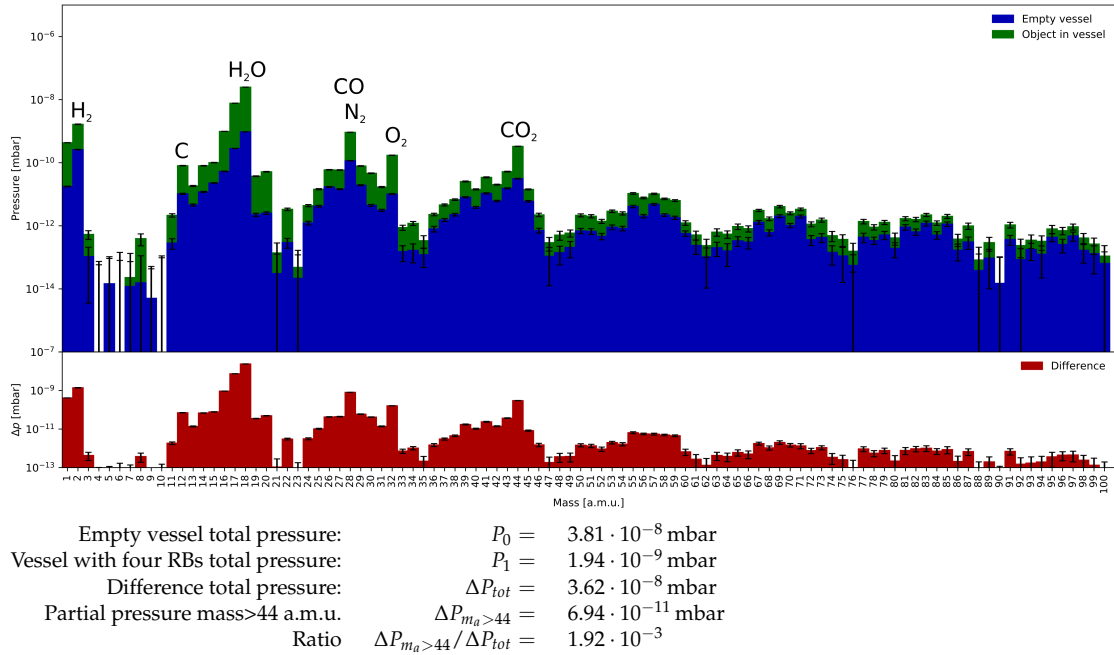|		
Empty vessel total pressure:	$P_0 =$	$3.81 \cdot 10^{-8}$ mbar
Vessel with four RBs total pressure:	$P_1 =$	$1.94 \cdot 10^{-9}$ mbar
Difference total pressure:	$\Delta P_{tot} =$	$3.62 \cdot 10^{-8}$ mbar
Partial pressure mass>44 a.m.u.	$\Delta P_{m_a>44} =$	$6.94 \cdot 10^{-11}$ mbar
Ratio	$\Delta P_{m_a>44} / \Delta P_{tot} =$	$1.92 \cdot 10^{-3}$

Figure 3.14: The residual gas analysis (RGA) of the DSSC ladder after baking. The y-axis shows the partial pressure and the x-axis shows the mass of the measured ions. The first measurement (green) was performed after having vacuum pumped an empty vessel for four days. The second measurement (blue) was performed after vacuum pumping, for a similar amount of time, the DSSC ladder insert into vessel. The nett contribution of DSSC ladder to the pressure is given by the difference of the two measurement (red). The DSSC ladder reaches pressure $< 10^{-7}$ mbar and $\Delta P_{m_a>44}/\Delta P \sim 10^{-3}$, which is enough for high vacuum according to the criteria [85] defined by the Vacuum Group of European XFEL.

also due to thermal conductivity. In normal ambient condition, electronic devices can dissipate a certain amount of heat by natural air convection. In a vacuum environment, the heat is dissipated mostly via irradiation which is a much less efficient process than convection. Thus, a physical contact between the devices to be cooled and the cooling system is required. This aspect was taken into account in the board design. In some cases in order to establish a good thermal contact between components, specials metal foil were used.

In order to test the full DSSC ladder system in vacuum a dedicated vacuum test stand was designed and produced. It is described in the next Section.

3.5.1 The vessel

The Flexible Experimental iNfrastructure In Controlled Environment (FENICE) is a multipurpose vacuum chamber designed and built to operate the DSSC ladder system in vacuum.
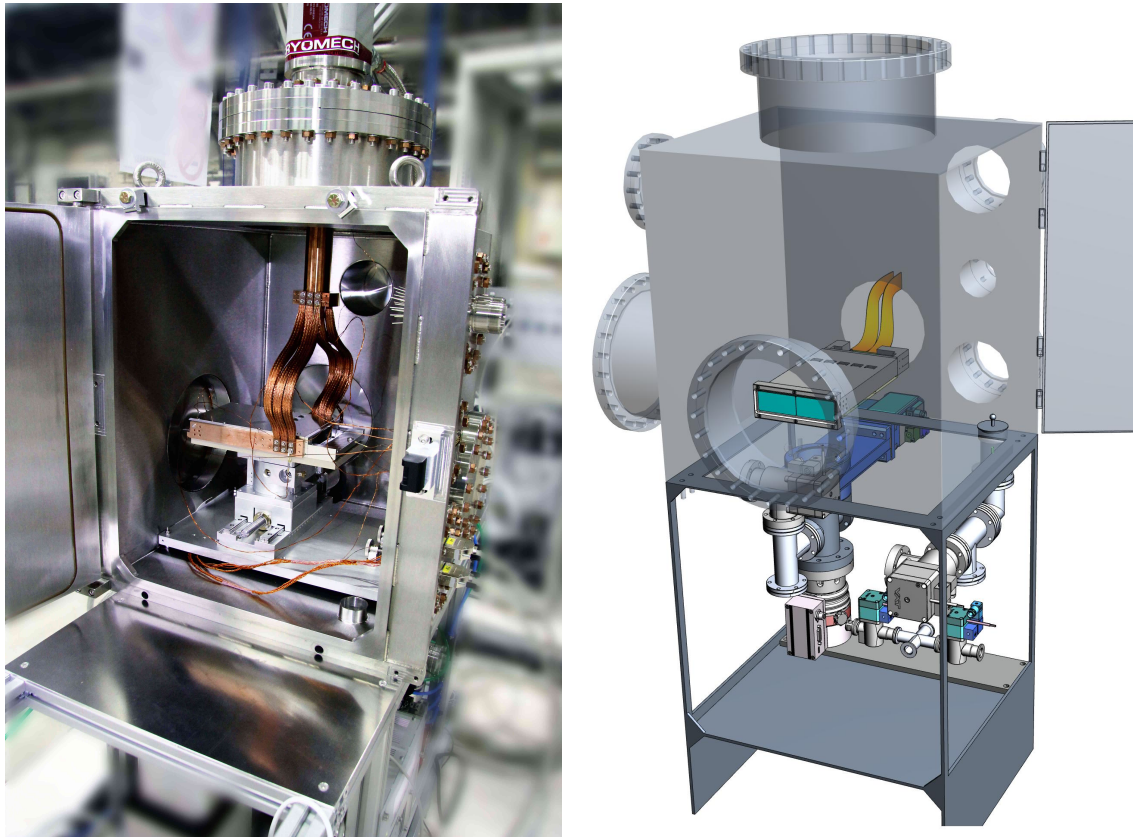
(a) A photo of FENICE with the ladder mechanics mounted.

(b) A 3D model of the system. In the lower part, parts of the vacuum component are visible.

Figure 3.15: The FENICE vacuum vessel.

The chamber was internal dimension of $45\,\text{cm} \times 39\,\text{cm} \times 50\,\text{cm}$ and it is equipped with two axis motion stages, a cooling and a temperature control system. The FENICE vessel provides many flanges and feed-throughs with different purposes described be-

low. A picture of FENICE is shown in Figure 3.15.

The big flange on the top is used to insert in the chamber the cold head of the chiller. One of the two flanges on the bottom is used for the connection to the pumping system (described in the next Section). The other flange on the bottom is used for venting the vessel with dry nitrogen (N_2) and for pressure measurement via a pressure gauge.

On the front, a flange with an inner diameter of 200 mm (DN200CF) was designed for connecting the vessel to X-ray sources. In the opposite wall (back), a large flange is used to connect the feed-through for Patch Panel Flex Cables. Three other feed-throughs allow the connection of the motion stages to the PLC system used to control them; the connection of the PT100 [86] temperature sensors to the same PLC; and the connection to a temperature control system based on a PID [87] feedback system. These system are described in detail below. Also other different flanges and feed-throughs are present, at the measurement used as spares.

In this context, I collaborated to FENICE design and in particular its pumping system of FENICE.

3.5.2 The pumping system

A scheme of the pumping system of FENICE is shown in Figure 3.16.
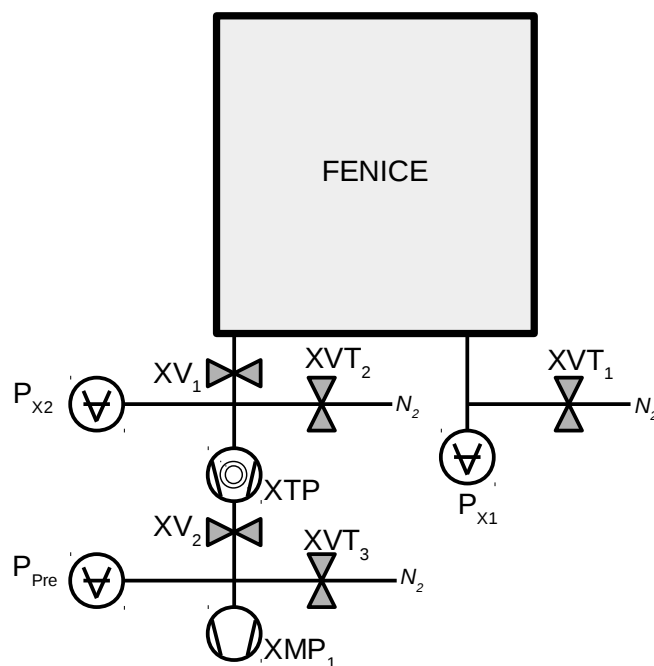

Figure 3.16: FENICE vacuum pumping scheme. The description of the label is given in Section 3.5.2.

The bottom of the vessel has two flanges. The first one is connected to a pressure gauge

(P_{X1}) and to a venting valve (XVT_1). The other flange is connected a shutter valve (XV_1). It is used for insulating the the vessel from the turbo-pump (XTP). Between the shutter valve and the turbo pump a venting valve (XVT_2) and a pressure gauge (P_{X2}) is installed. The turbo pump used is the High Pace 80 [86] which has as nominal pumping speed 80 l/s. The turbo pump can run only under the pressure of ~ 1 mbar; a membrane rough pump (XMP_1) is used to obtain this the level of pre-vacuum. Between the turbopump and the rough pump, a valve (XV_2) is installed. Here a pressure gauge (P_{Pre}) and a venting valve (XVT_3) are also installed. A oil-free membrane pump is used to be compliant both with the vacuum requirements and with the need to run the pump in a clean room.

3.5.3 The monitor system and the pressure measurement

The FENICE has been designed to use a dedicated Programmable Logic Controller (PLC) system. It is made using Beckhoff [58] elements and it is integrated in the Karabo Framework. The aim of the PLC system is to control the valves, the turbo pump, the pressure and temperature monitoring, and the motion stages.

The motion stages allow moving the DSSC ladder along two axis: one direction is along the vertical direction; and the other direction parallel to the front flange used for X-ray illumination. It was decided to not include a third axis in order to avoid possible collision of the detector sensors on the vessel wall during the testing phase. Within the range of the movement stages, it is physically impossible that the ladder hits the vessel.

During the measurements performed at the beamline P04 at Petra III, the PLC system was used to control the movement of the stages. The control of the vacuum system components was done manually; the value of the pressure inside the vessel was however constantly monitored.

The pressure gauges were connected to a Pfeiffer MaxiGauge [86], which allowed to reading out by a serial port the pressure measured by the sensors. In this context, I developed a data-logger. The monitoring was performed using scripts running on a Linux based small single-board computer, the Raspberry PI [88]. The script recorded the pressure values measured by the gauges and wrote them to a text file. The values could be plotted in realtime on any PC.

Another script running on the Raspberry PI which I developed was extra safety system. The script included a safety temperature threshold. In case the temparature of the ladder was measured to be above this threshold, the script would have switched off the MPOD power supply of the ladder, and would have prevent switching it on again, until the temperature value would have been again back to a normal. Moreover, the script would have sent an email to the responsible person, warning that a problem appeard on the temperatures.

In the final version of DSSC 1 Mpixel detector, a hardware board connected directly to the Patch Panel, the Safety Interlock Board (SIB) [89] is used to provide the detector hardware interlock. The SIB checks many parameters in order to avoid damage to the

detector during the working phase and it gives also the signal allowing switching the detector on. The SIB checks continuously the environment parameters (pressure, temperature and humidity), and it checks if all cables are correctly connected. In case of error, the SIB can prevent the switching on of the detector or force an emergency switch off, and sends an error signal to the beamline.

3.5.4 The chiller and the temperature control system

In order to remove the heat generated by the DSSC ladder, a PT60 Cryorefrigerator by Cryomech [90] was used. The cooling system of FENICE is composed of an external chiller and a cold head. The first is a compressor which exchanges the heat between an external cooling water system – provided by the facility – and the helium pipes connected to the cold head. The helium pipes are connected to the cold head mounted on the top flange of FENICE vessel. Internally, the cold head has a cold finger which can be connected thermally to the devices which need to be cool down.

To establish a thermal connection between the detector and the cold finger, the copper braids are fixed to the cold finger and connected on the side of the mechanics of the DSSC ladder, see Figure 3.15.

The chiller can pump out from the cold head up to 60 W at 80 K.

As the power generated by the DSSC ladder is roughly 10 W, the ladder could reach cryogenic temperatures also during operation. In order to stabilize the temperature and avoid too low temperatures which can damage the DSSC ladder components, the LakeShore Temperature Controlled 336 [87] was connected to the ladder. The device uses two PT-100 temperature sensors for measuring the temperature and to control two resistors which can release heat up to 100 W. The temperature sensors are connected in vacuum; one to the cold finger, and one to the mechanical box of the ladder, in an area close to the detector silicon sensors. An example of transition from ambient temperature down to $-20°C$ is shown in Figure 2.15. The temperature controller tests showed that the temperature could be set between $-40°C$ to $30°C$ degrees with a stability of $0.1°C$.

4 DSSC Ladder with a single ASIC. First tests with non-linear DEPFET.

This chapter illustrates the methods and the results of the first tests performed with the full DSSC readout chain. The system used is a fraction of the whole 1 Mpixel detector as it will be finally built, but it contains all representative components of the complete system. The prototype used was the DSSC ladder, in which the main-board was replaced with a single ASIC board.

The goal of these tests was to verify that the whole detector system was working. This was the first real measurement in the laboratory involving the whole DSSC readout chain and a light source. These tests allowed to define a detector configuration appropriate for the collection of a light signal and to verify that the synchronization between an external light source and the detector readout was working. Moreover, during these tests it was possible to record data to perform a first characterization of the detector.

The content of this chapter has been in part already published in the peer-reviewed Journal of Instrumentations (JNIST) as proceeding of the International Workshops on Radiation Imaging Detectors 2016 (iWoRiD) conference in Barcelona [83].

4.1 The test-stand

As mentioned above, the detector prototype used for performing the tests was the DSSC Ladder (see Chapter 3). The full ladder system in its final setup features 16 ASICs, but in this case it was equipped with a replacement board holding just a single ASIC.

The sensor used is a non-linear DEPFET sensor with 128×64 pixels. Since a single ASIC was connected, only 64×64 pixels were used for the measurements.

Visible light was used for these first test. The DSSC ladder system was used in ambient with passive cooling, as the single-ASIC replacement board produces less than 1W of heat, which can be dissipated by normal air convention; therefore the detector does not need to be actively cooled to work a room temperature.

The test stand was set up as shown in Figure 3.13 (page 80). The DSSC ladder was sitting on a laboratory desk and connected to the whole DSSC readout electronics described in Section 3.4. In contrast to the scheme in Figure 3.12 (page 78), the data were directly acquired via the MicroTCA crate, without using an extra PC. Due to the writing speed and the available disk space, a burst (800 consecutive frames) every about five seconds was acquired, the other bursts were discarded.

The detector system was connected to the Clock & Control (CC, see section 2.3.2) which was configured in stand-alone mode. The CC generates the reference clock at 99 MHz and, in order to emulate the 10 Hz cycle of the European XFEL repetition rate, the board was configured to generate a start/stop cycle of a duration of 0.1 s. Furthermore, the CC board was configured to produce a pulse synchronized to the start command, which was used to drive a LED, see Figure 3.9. The LED was in turn used to illuminate the ladder, as it will be described below.
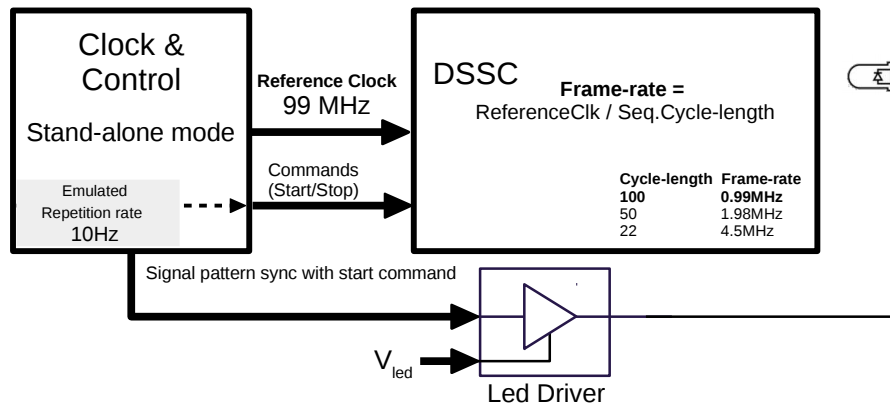

Figure 4.1: A scheme showing the timing configuration of the detector, the LED used for the ladder illumination and the Clock & Control in stand-alone mode.

The signals coming out from the Clock & Control are low voltage differential signals (LVDS), therefore the power is not high enough to drive a LED. For this reason, a small LED driver was built. The driver had a pre-amplifier stage which converted LVDS (from the Clock & Control board) to TTL signals (FIN1002), followed by a TTL multiple buffer (AC541) which finally drove a fast MOSFET (FDG8850NZ). The final stage could drive up to $\sim$ 2 A. The LED light intensity depends on the current flowing into the LED, defined by the voltage (VLed) provided by the power supply. The device suppling the voltage is a programmable power supply, controllable externally via a serial port. During the measurement the voltage applied was in the range between 0 and 29 V.

The resistor limiting the maximum current flowing into the LED was chosen in order to maximize the current while avoiding to burn the LED. The nominal maximum current of the used LED was 20mA, according to the LED specifications for short pulses, the maximum current limit could have been 10 times higher without causing any damage. The LED used was a high power visible light (red) LED.

4.2 Synchronization test

The first tests were done to check that the detector was correctly synchronized to the Clock & Control. This was obtained by illuminating the sensor with the LED triggered by the Clock & Control. This test also allowed to check for if the data receiver software was correctly interpreting the data.

In order to perform these tests the DSSC ladder system was set to operate with an ASIC readout cycle 100 units long. As the reference clock runs at 99 MHz, this sequencer length corresponds to $100/99$ MHz $\simeq 1010$ ns, so a frame rate of ~ 1MHz.

The front-end was configured with the following parameters:

- sequencer cycle-length set to 100 (frame-rate 0.99 MHz, 1010.1 ns/cycle);

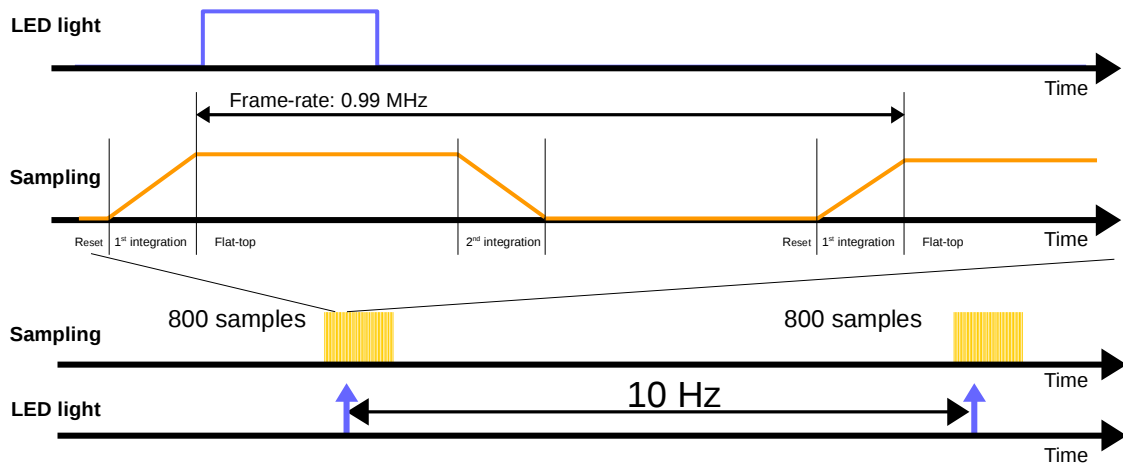- integration length set to 100.8 ns

- flat-top length set to 403 ns.

Figure 4.2: A sketch showing the timing configuration of the LED light and the DSSC detector. The LED was producing a light pulse every 0.1s, the detector was synchronized to collect the data of this pulse always in the same memory cell.
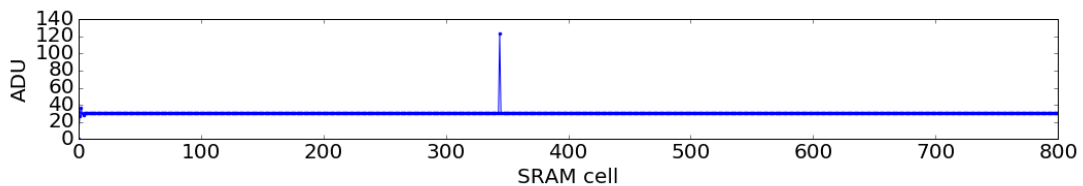

Figure 4.3: The memory cell content of a single pixel of the DSSC ladder during the illumination with the LED pulse.

The mechanics box - protecting and holding the board where the sensor and ASIC are mounted - had a slot where the LED could be inserted and blocked.

In a first phase, the Clock & Control, set in stand-alone mode with a 10 Hz repetition rate, was configured to produce a single LED pulse synchronized with start command sent to the detector. Figure 4.2 shows the timing configuration of the LED light and the DSSC detector. The LED was producing a light pulse every 0.1s, the detector was synchronized to collect the data of this pulse always in the same memory cell. Figure 4.3 shows the content of the 800 memory cells (one burst) of a single pixel illuminated by the

LED. In Figure 4.3 the LED pulse is clearly visible. By tuning the Clock & Control, it was possible to move the timing of the LED signal with a granularity of $\sim$ 10ns. By setting different increasing time delays, we observed lower (down to the baseline) signals on the detector. This occured when the LED pulse fall outside the detector integration window (flat-top). The best synchronization between the LED and the detector was determined by identifying the point in time when the intensity of the signal on the detector was maximal. By repeating this test, as expected, the light pulse was observed always in a single and fixed memory cell, and with a stable signal output. This first result showed that the detector was correctly synchronized to the Clock & Control signals.

Together with this measurement, it was possible for the first time to verify that the data from the DSSC ladder were transmitted, received and interpreted correctly. Figure 4.4 shows a single frame collected by the DSSC detector, as illuminated by the LED placed at a few millimeters distance from the sensor. Figure 4.5 shows a single image collected with the DSSC detector illuminated through a paper mask with the LED placed at $\sim$ 4cm of distance from the sensor. In both images the baseline was subtracted, calculated as the mean of 800 frames with LED light off.

The image shows that the data are correctly packed by the DSSC readout chain and correctly reordered in the PC receiver.
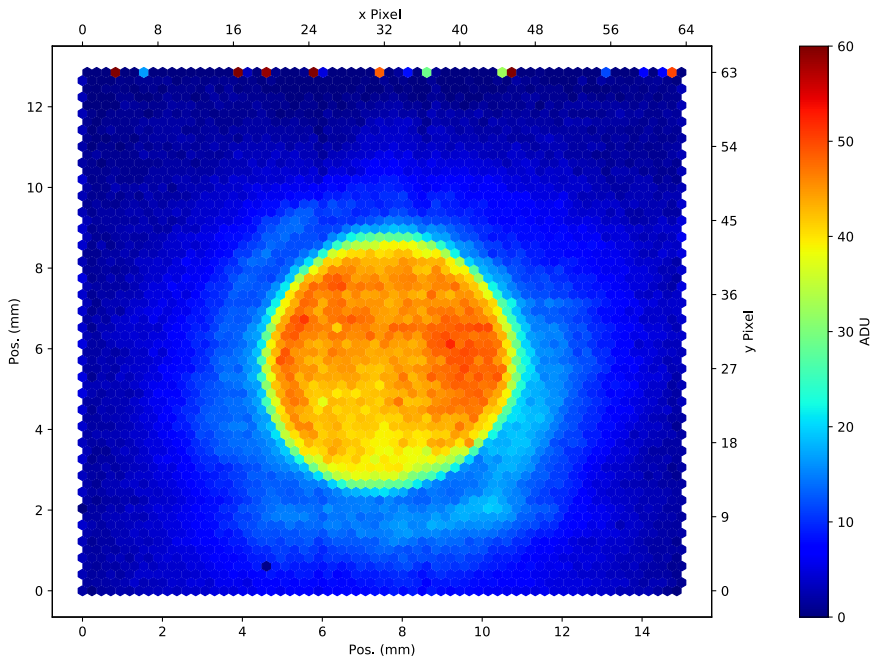

Figure 4.4: An image obtained by the DSSC detector illuminated by the LED positioned at a few millimeters distance from the sensor.
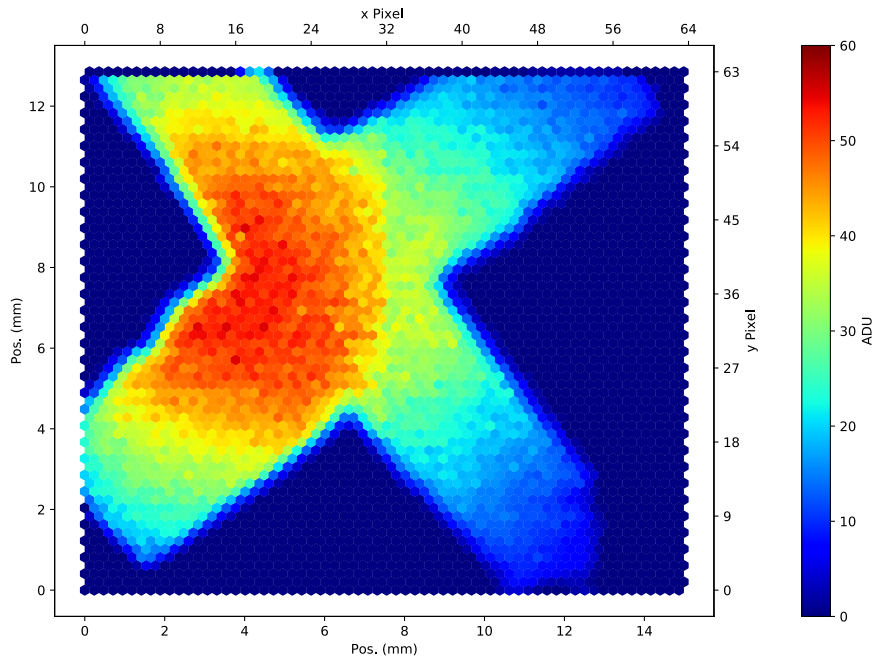
Figure 4.5: An image of an illuminated paper-mask located between the detector and the light source. The distance between the sensor and the mask was ~ 4 cm.

4.2.1 Non-linear sensor characteristic

The second phase of the tests consisted of a preliminary characterization of the detector using visible light.

Since the intensity of the light produced by the LED is not directly proportional to the voltage applied, to evaluate the intensity of the light generated by the LED as function of the power supply voltage, a calibrated amplified silicon-photodiode from ThorLabs (DET10A) was used. The LED calibration consists in associating each different input voltage (VLed) to the relative light intensity seen by the reference detector.

The light intensity is not measured in absolute units, but a value proportional to the real one is given. The idea is to calibrate a *relative light intensity* of the LED system (LED connected to its driver) with the silicon photodiode. Once this calibration is performed, it is possible to move the LED into the holder in front of the DEPFET sensors for measuring the characteristic non-linear response curve of the DEPFET. The reasons why the *relative light intensity* is used instead of an absolute measurement is explained below.

The light intensity measured by the reference photodiode does not correspond to the intensity measured by a single DSSC pixel, as the LED illuminates many pixels (see Figure 4.4) as a whole. Moreover, even in the hypothetical case, in which the absolute light intensity hitting the single pixel of DSSC was known, the ratio between the number of visible light photons hitting the detector and the energy deposited is not known because the quantum efficiency of the DSSC detector for visible light is not known a priori. A

proper detector calibration would need an X-ray source. As this was not possible at the time of these tests, the measurement took advantage of the non-linear response curve at the sensor, which was known previously, allow a preliminary calibration (see below).

The characteristic compression curve of the sensor was previously measured [91] by the sensors producers using a stand-alone system, independent of DSSC. They measured the current coming out from the single sensor pixel as function of the deposited energy. A multi-pulsed laser injecting was used to inject photons into a single pixel. The absolute energy calibration was obtained by a cross calibration with radioactive sources, [91]. For this measurement, we consider the curve provided by the sensor producer as a reference (see Figure 4.6).
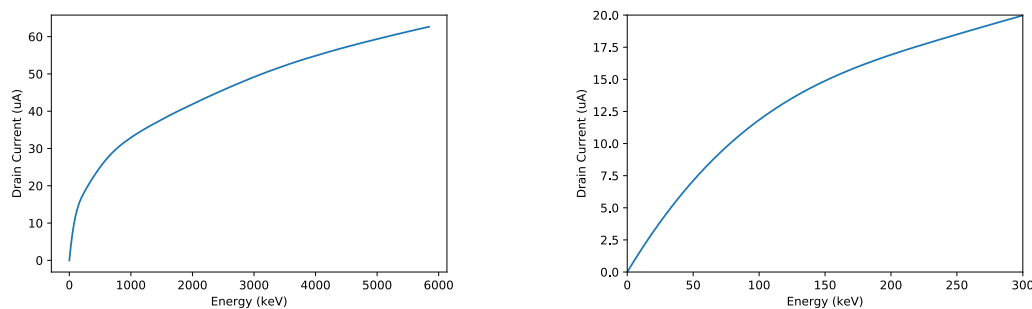

Figure 4.6: The characteristic curve of the non-linear DEPFET provided by the sensor producer, [91]. On the left the complete curve; on the right a zoom on a range similar to that measured during the measurement described in this chapter.

The LED system calibration was performed as follow. The signals from the photodiode were measured using an oscilloscope closed to a $50\,\Omega$ resistor, to match the impedance of the photodiode. An example of a typical signal is given in Figure 4.7. It shows the signal produced by the silicon photodiode and sampled by the oscilloscope. The integral of the pulse is proportional to the charge generated in the photodiode, which in its turn is proportional to the number of photons absorbed. The oscilloscope allowed sampling the data and transmitting them to a PC. For this reason, the integration of the pulse was performed numerically afterwards after the sampling.

The reproducibility of the pulse was extremly high. It means that by setting the same VLed, the difference between the integrals of two acquired pulses is negligible with respect to the electronic noise. The numerical integration of the signal of the photodiode took into account the following features. As shown in Figure 4.7, the blue part is considered as the baseline. The black part of the curve is the signal. It has a temporal-length of $\sim 400\,\mathrm{ns}$, which corresponds to the time window used in the configuration of the DSSC detector. The red part of the curve is the tail. In order to estimate the light intensity, first the baseline is subtracted to the curve assuming a constant value over the whole time width; then, the curve is integrated in the region corresponding to the black curve in the plot. The tail is considered negligible as it contributes less than 2 % to the pulse and it is outside the integration time window of DSSC.
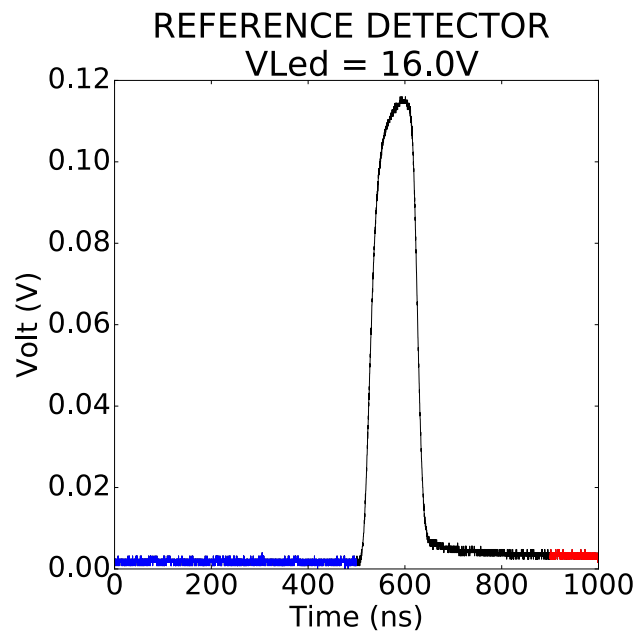
Figure 4.7: A typical LED-light pulse seen by the reference photodiode and measured with the oscilloscope. The integral of the curve is proportional to the energy of the photons absorbed by the photodiode. The integral is calculated, considering the blue color as the baseline, the black color as the light pulse, and the red as color the tail, [83].
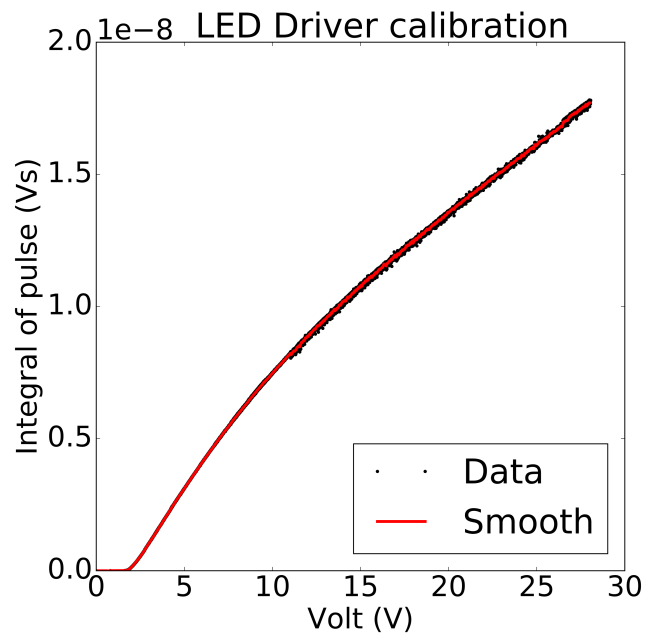

Figure 4.8: The integral of the pulse as a function of the input voltage to the LED drivers, [83].

The characteristic curve of the LED system is obtained by varying VLed from 0 V to 29 V, and by calculating the integral of the pulse recorded by the silicon photodiode; the results are is shown in Figure 4.8.

By systematically changing the light intensity it is possible to measure the characteristic response curve of the DSSC system under test with the LED light. In this way, a relative calibration of the pixels is obtained. This can serve as a basis for an absolute calibration by complementing it with the signals measured by the detector when illuminating it with one or more well-known X-ray sources, as described in more detail in [92].
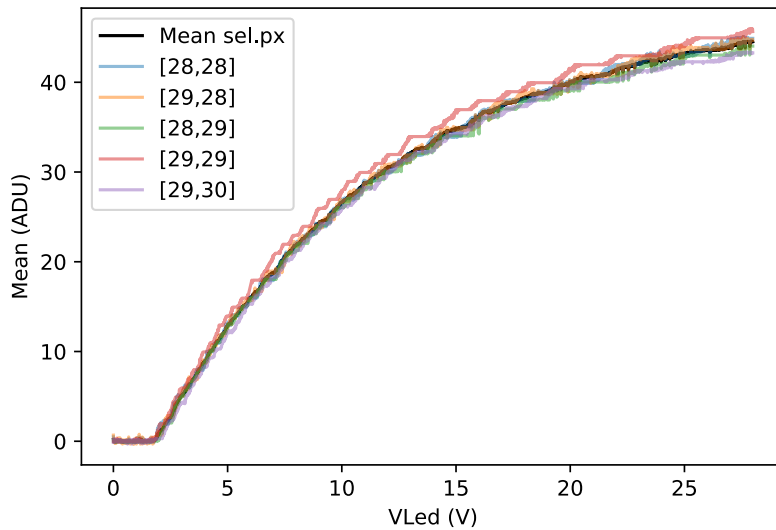

Figure 4.9: The mean values of the light intensity of the selected pixel read by the DSSC detector as a function of the VLed. Each point is the mean value of 10 consecutive LED pulses. The black line is the mean value of the data from the five selected pixels. On the x-axis the VLed.

To perform the measurements, the steps are the following: first, the LED is positioned on the holder of the silicon photodiode and the LED system is calibrated as explained above. In short, each VLed voltage is associated to a relative light intesity value, L [$a.u.$].

Then, the LED is moved to the holder placed in front of the DSSC detector and VLed is varied systematically in the same range used during the calibration. The ADC values (I_{ADC}) read on the DSSC pixels corresponding to each VLed value are recorded. In order to increase the statistics, 10 consecutive LED pulses are used. The characteristic curve for a few selected pixels is shown in Figure 4.9. The selected pixels were chosen as a group of neighboring pixels, among the mostly illuminated, which present similar ADC values for the same VLed.

Finally, VLed is converted into a relative light intensity L [$a.u.$] using the relative light intensity calibration curve previously obtained (Figure 4.8). The result is shown in Figure 4.10.

The DEPFET reference curve provided by the sensor producer features on the x-axis
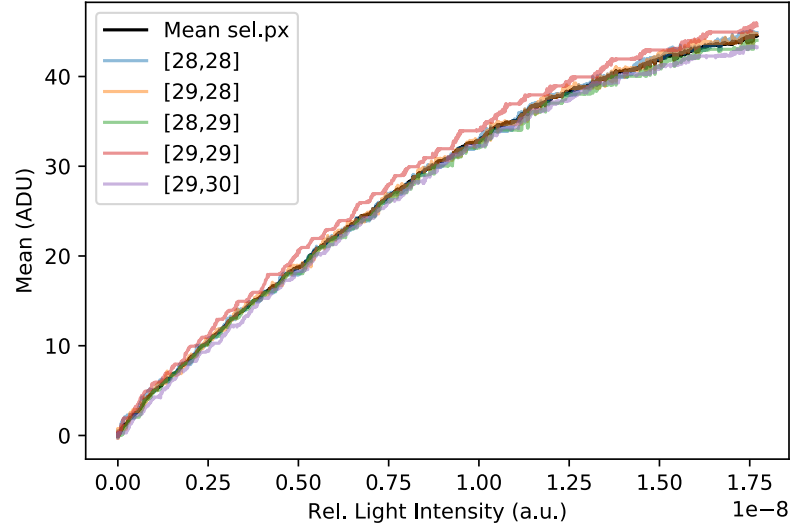
Figure 4.10: The mean values of the light intensity measured on the selected pixel read by the DSSC detector as function of the relative light intensity of the LED, Figure 4.8. Each point is the mean value of 10 consecutive LED pulse. The black line is the mean value of the data from the five selected pixel.

the energy deposited, E_{dep} [keV], and on the y-axis the drain current, i_{drain} [µA], see Figure 4.6. In our case, the experimental data use a light source calibrated in relative units L [$a.u.$], so the conversion function between the relative light intensity and the equivalent energy deposited into the pixel is unknown. The conversion function is assumed to be linear. Assuming the detector front-end to be working correctly, the drain current coming out from the sensor is proportional to I_{ADC} [ADU].

The non-linear characteristic curve allows performing a best-fit between the experimental curve (in units I_{ADC} [ADU] vs relative light intensity L [$a.u.$]) and the reference curve (in units µA vs keV) by looking for the best coefficients matching the two curves.

The goal is to find the the best parameters α and β, which allows the conversion:

$$\begin{cases} I_{ADC} \, [\text{ADU}] = \alpha \cdot i_{drain} \, [\text{µA}] \\ L \, [a.u.] = \beta \cdot E_{dep} \, [\text{keV}] \end{cases} . \tag{4.1}$$

In other words, the best-fit function determines the best parameters (α and β) of the linear transformation, which superimposes the experimental data (Figure 4.10) to the reference data (Figure 4.6). A χ^2 minimization method is used to perform the fit.

In order to increase the statistics, the mean value and the standard deviation of the signals measured by the selected pixels were evaluated for 10 consecutive LED pulses. Figure 4.11 shows in black the mean value of the measured ADU values I_{ADC} [ADU] as function of the relative light intensity L [$a.u.$]; in green the standard deviation is shown. The red curve is the reference curve provided by the sensors producer (drain current

i_{drain} [μA] vs energy deposited E_{dep} [keV]). The two curves are superimposed by using as conversion values the results of the fit, α and β.

The residual shown in Figure 4.11 is defined as:

$$residual[\sigma] = (I_{ADC} - I_{expected})/\sigma_{I_{ADC}}\,. \qquad (4.2)$$

while the relative residual is defined as:

$$residual[rel.] = (I_{ADC} - I_{expected})/I_{ADC}\,. \qquad (4.3)$$

The uncertainty associated to the ADU measurement was estimated by using the standard deviation of the distribution of the relative residuals. It results to be 6%.

The gain as the number of ADC counts per 1 keV of energy deposited. It can therefore be extracted from the slope of the curve in Figure 4.11. The slope of the reference curve is:

$$g[keV/μA] = \frac{\mathrm{d}E_{dep}}{\mathrm{d}i_{drain}}\,.$$

Therefore, the initial slope of the reference curve is

$$g_0 = 0.17\,μA\,/keV \qquad (4.4)$$

which can be converted in $[ADU]$

$$g_0 = \alpha \cdot 0.17μA/keV = (0.49 \pm 0.03)\,ADU/keV\,. \qquad (4.5)$$

Since the uncertainty on the reference curve is much lower than the uncertainties associated to this measurement, the relative uncertainty associated to the gain and the inverse gain corresponds to the relative uncertainty on the ADC counts, which has been estimated above, as 6%.

The inverse of the gain g^{-1}, in [keV/ADU] corresponds to the ADC bin-size. Figure 4.12 shows the ADC bin-size as a function of the energy deposited on DEPFET. The initial ADC bin-size corresponds to

$$g_0^{-1} = (2.04 \pm 0.12)\,keV/ADU\,. \qquad (4.6)$$

For the noise analysis, 150 bursts were recorded with LED off. The noise was estimated as the standard deviation of the gaussian distribution which better fit the experimental histogram obtained. The method used was maximization of the binned likelihood.

The noise [ADU] and its associated uncertainty are the results of the fit. The noise in [keV] is obtained by multiplying by g_0^{-1} and the uncertainty associated to it includes also the 6% estimated before:

$$noise\,[keV] = g_0^{-1} \cdot \sigma_{noise[ADU]} \pm \delta\,, \qquad (4.7)$$
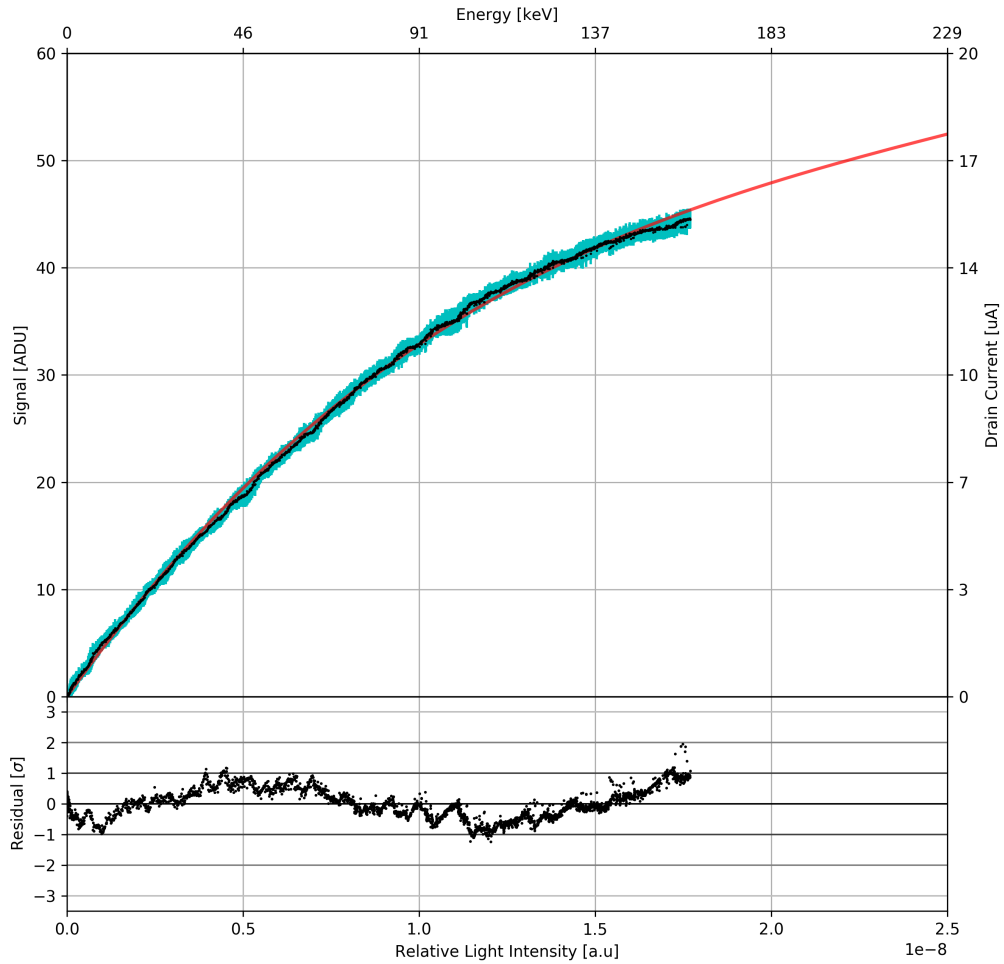
$$\chi^2 = 629.88 \; ndof = (2777 - 2 - 1)$$

Param.	Value	Parab Error
$\alpha \, [\mathrm{ADU}/\mu\mathrm{A}]$	2.9	0.0073
$\beta \, [a.u./\mathrm{keV}]$	1.097e-10	4.5e-13

Figure 4.11: The experimental data points (black), namely, the mean value of 10 consecutive LED pulses, on five selected pixels; the standard deviation (cyan). The reference curve provided by the sensor producer (red). The *residual [σ]* is evaluated according to Equation 4.2.
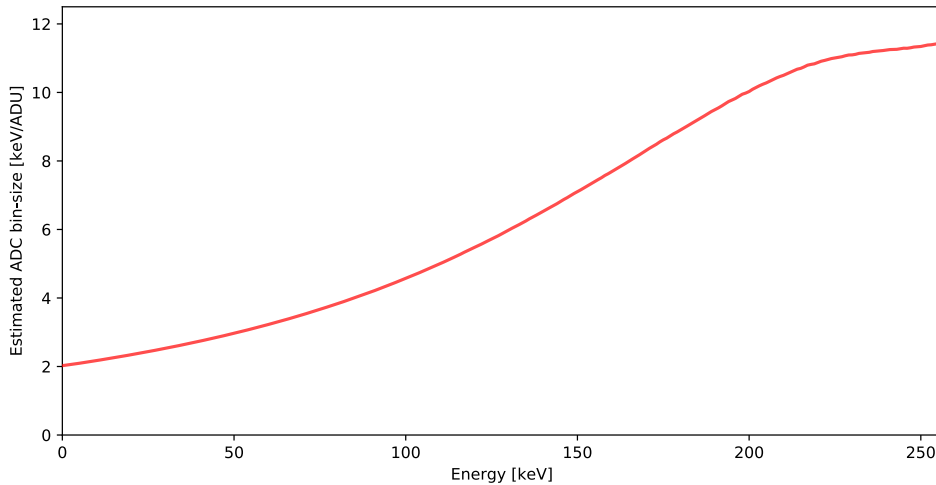
Figure 4.12: The ADC bin-size as a function of the energy. It is given by the gradient of the reference curve times the α parameter.

$$\delta = g_0^{-1} \cdot \sigma_{noise[ADU]} \sqrt{\left(\frac{\sigma noise\,[\text{ADU}]}{noise\,[\text{ADU}]} \right)^2 + (6\%)^2}\,. \tag{4.8}$$

The table below shows the results of the noise estimation.

y	x	*noise* [ADU]	*noise* [keV]
28	28	0.380 ± 0.001	0.78 ± 0.05
28	29	0.295 ± 0.001	0.60 ± 0.04
29	28	0.362 ± 0.002	0.74 ± 0.04
29	29	0.372 ± 0.001	0.76 ± 0.05
30	29	0.572 ± 0.002	1.17 ± 0.07

Globally, for the five selected pixel, the mean of the noise

$$noise = (0.374 \pm 0.001)\ \text{ADU}\,, \tag{4.9}$$

which converted in energy becomes

$$noise = (0.76 \pm 0.05)\ \text{keV}\,. \tag{4.10}$$

The present results confirm what already obtained with the DSSC detector and the first generation of ASIC, with different setups and different conditions. They confirm that the full system is working as a whole and the performance are similar to those obtained with smaller prototype and not using the full DSSC electronics, running also at lower rates.

5 First calibration of full DSSC Ladder with Mini-SDD sensors at beamline

This chapter illustrates the first measurements performed at a beamline with the DSSC ladder featuring a full-size focal plane equipped with Mini-SDD sensors. For the first time the DSSC ladder system together with its vacuum test stand (FENICE) was operated in an external facility, the Petra III synchrotron at DESY. The measurements were performed to verify the system functionality and the stability of the DSSC readout system, and also to determine important parameters such as noise and gain for a single pixel and for a fraction of the detector area.

Some results of this chapter have been published as proceeding of the conference 2017 IEEE Nuclear Science Symposium and Medical Imaging Conference in Atalanta [93].
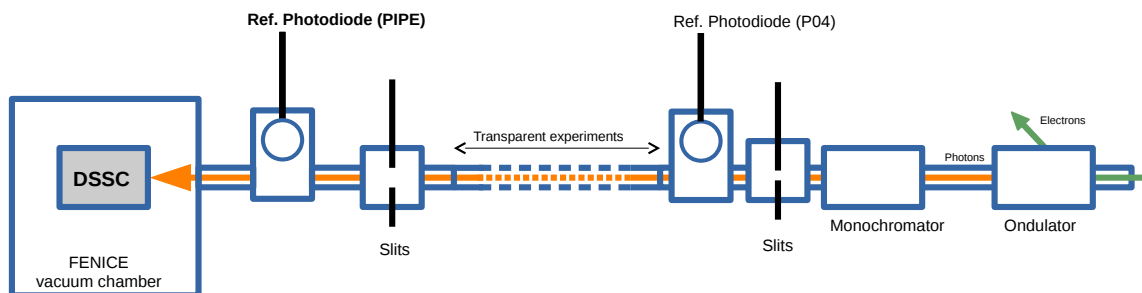
5.1 The beamline P04 at Petra III

Figure 5.1: A sketch of the DSSC ladder test setup at the P04 beamline at Petra III, DESY.

The P04 beamline at Petra III is a soft X-ray beamline with an energy range between 250 eV and 3 keV located at DESY, Hamburg. In this section, some information of the beamline, useful for the experiments, is given; detailed information about the Petra III synchrotron and the P04 beam line can be found at [94] [95].

The Petra III synchrotron provides an electron bunch every 192 ns, equivalent to a repetition rate of 5.2 MHz. In order to produce photons at the beamline, the electrons pass through an undulator system (see Section 1.4), which is tuned to generate X-rays. The photons going out from the undulators have a broad energy spectrum and in order to obtain a monoenergetic photons beam, a monocromator is used.

Using the beamline control system, it is possible to select easily the mean energy of the photons generated by the undulator, and futhermore it is also possible to tune the central

frequency of the monochromator. During our measurements (except for a few cases) the monochromator energy was set to a fixed value of 1 keV. By detuning the undulator system it is possible to change the photon flux, keeping the photon energy constant.

Figure 5.1 shows a simplified scheme of the beamline configuration during the DSSC tests. The FENICE test-stand (described in section 3.5) was installed at the very end of the beamline due to space limitations and also because other X-ray experimental systems were mounted upstream in the beamline. These experimental instruments used only a small fraction of the X-ray photons of the beam for their experiment, thus they can be considered *transparent* for our measurements. The experimental infrastructure installed just upstream of FENICE was equipped with a photodiode to measure the photon flux and with slits to reduce the beam size. The photodiode (indicated as *PIPE diode* in figure 5.1) was placed downstream of the slits and was moved in and out of the beam using a manual vacuum manipulator. When the diode was used for measuring, it acted as a beam-stop, so it was not possible to measure the photon flux and at the same time take data with the DSSC detector.

5.1.1 Timing

As mentioned in Section 5.1, the Petra III synchrotron has a electrons-bunch rate of 5.2 MHz, namely the X-ray pulse arrives continuously every 192 ns.

The maximum nominal rate of the DSSC detector is 4.5 MHz (see Chapter 3). Although the detector could in principle work also at the 5.2 MHz, it was decided not to put the system under too much stress for these measurements and to operate at half of the Petra III rate, namely 2.6 MHz. The parameters of the detector front-end electronics were set as follow:

- Sequencer cycle-length set to 38,
  (corresponding to a frame rate of 2.6 MHz, 383.83 ns/frame);

- Integration time set to 57 ns

- Flat-top length set to 61 ns;

- VETO ignored;

In order to be able to operate the detector with this timing, the PLL system of the Clock & Control was configured as in Figure 5.4. As the bunch clock were multiplied 19 times the reference clock was ~ 99 MHz. Setting the front-end cycle-length to 38 units allowed to operate the detector at the frame-rate $5.2\,\text{MHz} * 19/38 = 2.6\,\text{MHz}$. The Clock & Control was also used to provide the start and the stop command to the detector with a 10 Hz cycle, emulating the European XFEL train repetition rate.

5.2 Alignment

5.2.1 Synchronization

The first step to be done in order to perform the measurements is to synchronize the DSSC detector readout to the Petra III bunch clock, so that the photon pulse arrives in the time window during which DSSC signal readout.

In order to tune the synchronization of the detector to the X-ray pulse arrival time, an automatic "delay scan" was performed. This procedure changes in step the *pre-burst* delay. As shown in Figure 3.10 (page 76), the *pre-burst* delay corresponds to the period between the START command - received by the detector from the Clock & Control - and the first sample acquired by the detector, which corresponds to first flat-top. This delay can be tuned with a granularity corresponding to the length of the reference clock cycle ($1/99\,\mathrm{MHz} \simeq 10\,\mathrm{ns}$).

The result of the delay scan is shown in Figure 5.2. According to this result, the detector delay was set such as the bunch arrived to the detector at the beginning of the flat-top, corresponding to a delay value of 10 clock-cycles in the plot.

Figure 5.4 shows schematically the concept of the synchronization of the DSSC detector to the Petra III pulses. The system was set up such that the Petra III pulse, shown in the top line, arrives at the beginning of the flat-top.

The Figure 5.5 shows one of the first images obtained at Petra III with DSSC detector after the synchronization. The illuminated area is visible and the edges of such area are defined by the slits position at the beamline.
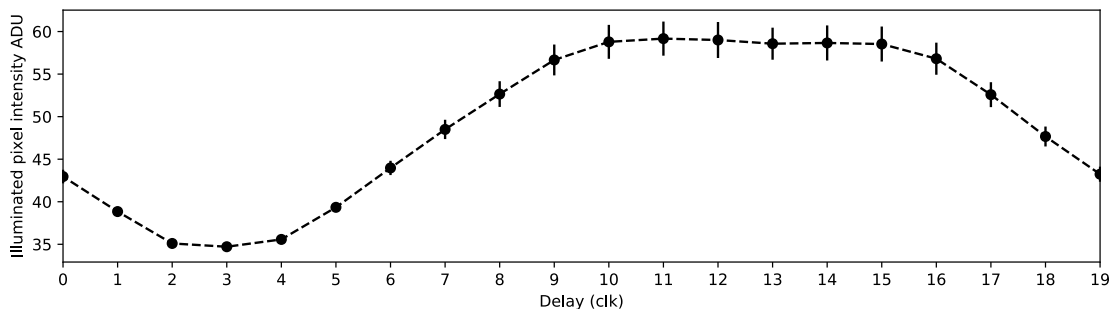

Figure 5.2: Results of the delay scan, aimed to synchronize the DSSC detector to the Petra III. On the y-axis the intensity of the signal seen by an illuminated pixel as a function of the *pre-burst* delay corresponding to the period between the START command and the first sample acquired.

5.2.2 Beam positioning

In order to be able to perform calibration measurement on a simple pixel, the slits placed on the experimental setup upstream of FENICE were used. This allowed to collimate the beam on a single pixel of the DSSC detector. By using the *PIPE diode*, the beam intensity
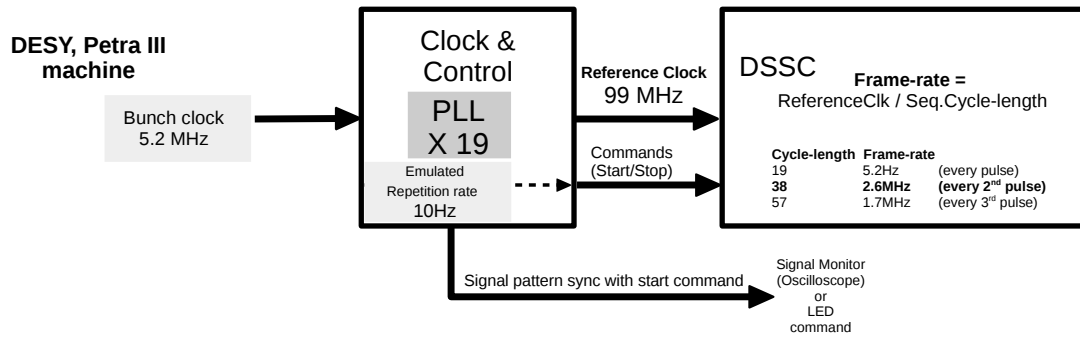
Figure 5.3: A scheme showing the way DSSC detector was synchronized to the Petra III pulses. The Clock & Control provided also the start and stop signals to the detector, with a repetition rate of 10 Hz locked-in-phase to the Petra bunch clock, emulating the European XFEL.
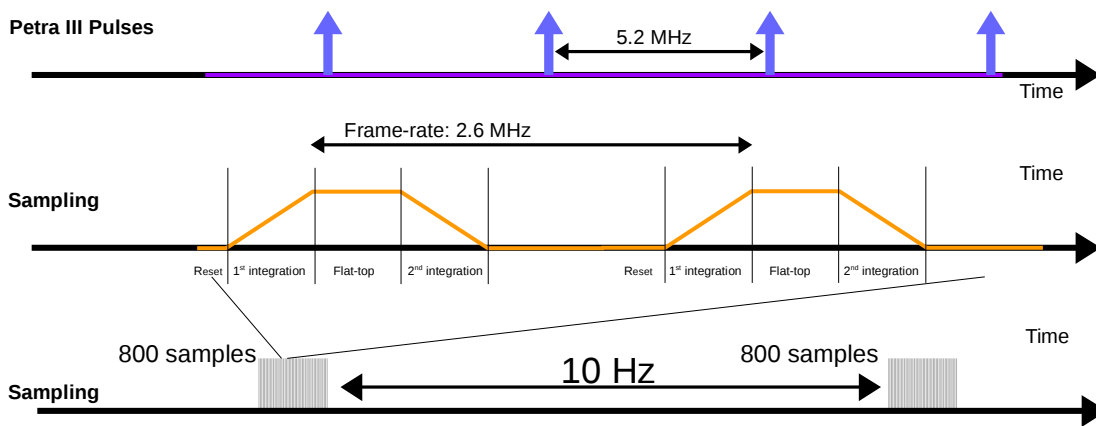
Figure 5.4: A scheme showing the synchronization between the DSSC detector and the Petra III pulses. The system was set up such that the Petra III pulse, shown in the top line, arrives at the beginning of the flat-top. In the last line, it is shown how 800 frames (burst) were collected at the rate of 10 Hz, in a scheme similar to that one used at European XFEL.

Figure 5.5: One of the first images obtained at Petra III with the DSSC detector. In this image the offset has been subtracted. The illuminated frame and the dark frame result from the mean values of a single burst (800 samples). Two ASICs are not correctly initialized and they have more noise than the other ones. The white box is a zoom of the area illuminated by the beam.

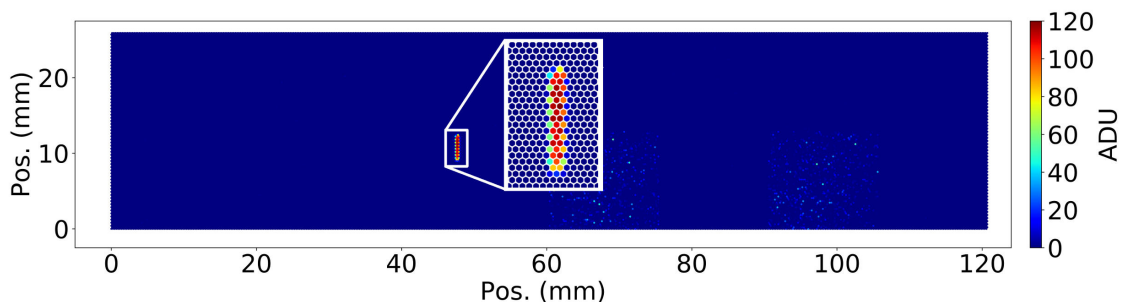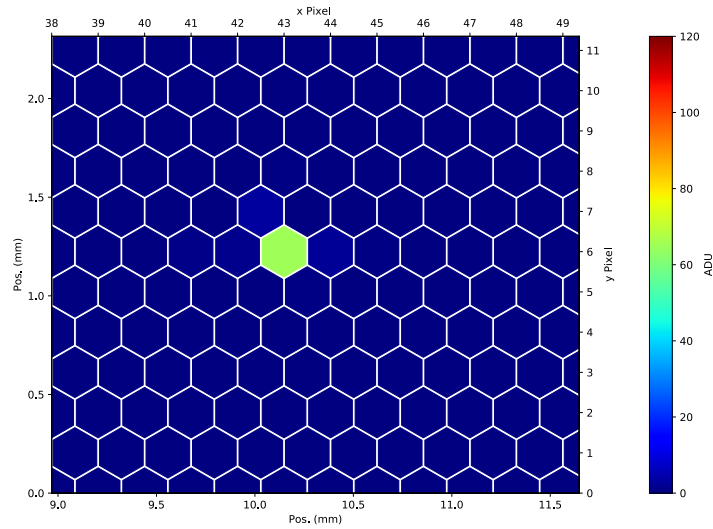Figure 5.6: An image of the detector illuminated when the beam was cut by the slits such as to illumate a single pixel.

hitting on this single pixel could be measured (see Section 5.1). Therefore, the number of photons hitting the pixel was known. Figure 5.6 shows an image collected when the slits where used to illuminate a single pixel, showing that the procedure was successful.

5.2.3 Measurement

The measurements at the P04 beamline were performed during two night shifts. The main goal of measurements of the first night was to obtain a *gain scan*, corresponding to the measurement of the response curve of the detector for different gain settings. The response curve is the detector signal output in ADU units vs the energy deposited, which is measured with a reference detector (the *PIPE diode*), see below.

The second night, the goal was to perform an area scan to obtain the gain of an extended area of one ASIC.

The reference measurement of the total flux of photons on the selected pixel(s) were performed with a photodiode, *PIPE diode*, see Figure 5.1. In order to avoid to waste beam time, the measurement of the total flux of photons for different undulator configurations was performed only at the beginning and at the end of the DSSC measurements set. That means that before starting the data acquisition with the DSSC detector, we performed a scan of the various beamline settings (undulator tunings) versus flux measured by the photodiode. The used settings and the corresponding results are shown in Table 5.1. The photon flux could be varied by using the parameters V_{gap} and $E_{undulator}$. As mentioned the $E_{undulator}$ was used to detune the undulator system with respect to the energy set by the monochromator.

The maximum flux could be obtained for $E_{undulator} = E_{monochromator} = 1\,\text{keV}$; this max-

V_{gap}	$E_{undulator}$	PhotoDiode [photon/pulse]
4.34	880	1.1
4.24	880	2.8
4.14	880	4.6
3.64	880	13.8
2.04	880	33.8
2.04	885	38.2
2.04	890	53.8
2.04	895	55.1
2.04	900	79.1
2.04	905	87.6
2.04	910	112.0
2.04	915	125.3
2.04	925	184.9
2.04	930	197.3
2.04	935	307.1
2.04	940	340.0
2.04	950	482.2
2.04	955	668.9
2.04	960	1226.7
2.04	970	2044.4
2.04	975	3333.3

Table 5.1: Beam intensity measured with the reference photodiode used for the gain scan (first night) as function of the beamline parameters V_{gap} and $E_{undulator}$, used to vary the flux. The monochromator was fixed to the value $E_{monochromator} = 1000\,\text{eV}$

imum value was however never used as corresponding flux was too high for a single DSSC pixel. Therefore, only values $E_{undulator} < E_{monochromator}$ were used. V_{gap} allowed to regulate the aperture of some slit placed much upstream in the beamline. The impact on the variation of this parameter on the flux was determined empirically at the beamline.

The photon energy was defined by the monochromator and fixed at 1 keV, thus the number of photons per pulse corresponds to the energy deposited per pulse inside the pixel, expressed in [keV].

5.3 The gain scan

The aim of this set of measurements was to obtain the response curve of the DSSC detector for a set of different gain settings. The gain of the detector, defined as number of ADU units measured per unit of deposited energy, can be changed by a set of detector parameter. In this case all set of parameters was keep constant except for the C_F parameter, which corresponds to the value of the feedback capacitor at the front-end of the detector, see Section 3.3. The Table 5.2 shows the different values of C_F used during the measurement, and the corresponding capacity.

For each gain setting, the beamline was set up to have different photon flux intensities. For each intensity at least 50 *bursts* were acquired, each burst containing 800 frames.

Therefore, each acquired set of measurement consists of $800 \times 50 = 40000$ frames. The analysis of the measurements performed takes into account only the single illuminated

C_F	Capacitance
1	1 pF
2	1.5 pF
3	2.5 pF
5	4.4 pF
8	7.9 pF
15	13.8 pF

Table 5.2: Values of the C_F used in the measurement and corresponding value of the front-end feedback capacitor.

pixel. In Figure 5.7, the memory content of a single burst for 5 different measurements, corresponding to five different photon intensity is shown. Figure 5.8 shows the memory content of 50 bursts of the same 5 measurement.
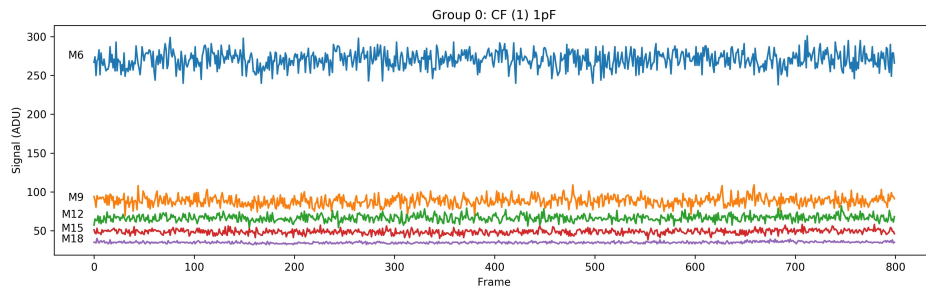

Figure 5.7: Memory content of the illuminated pixel in ADU. Each different color correspond to a different measurement.
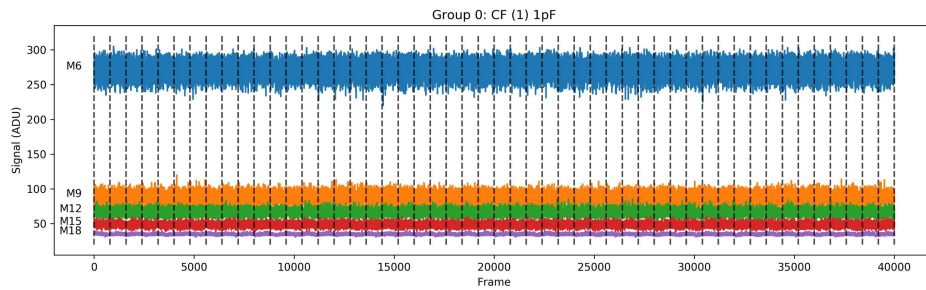
Figure 5.8: Memory content of 50 bursts. Each different color correspond to a different measurement.

The expected distribution of the number of photons N_γ seen by the DSSC detector is the Poisson one. A Poisson distribution can be approximated by a Gaussian distribution with a negligible effect for $N_\gamma \gtrsim 10$, [96].

For each measurement, histogram of the ADC values was produced. The obtained spectrum was fitted to a gaussian distribution by using a χ^2 minimization methods.

The histograms presents a strong visible alternate pattern caused by differential non-linearity (DNL) of the ADC. In particular, the bin size appears to have a periodic pattern with a 2-bins step. This unwanted effect on the ADC was measured in similar config-

urations by the ADC developers. The DNL estimated by the ADC developers in such configuration was $\sigma_{DNL} = 0.3$.

In order to extract the mean μ and the standard deviation σ from the histograms, two strategies were used. The first one consists to create a histogram by merging two ADC-bins into a single bin. In this way the differential non linearities are reduced; in particular the strong effect between even and odd ADC-bins is compensated. The parameters μ and σ are extracted by a standard χ^2 minimization. The result are shown in Figure 5.10.

The other strategy consists to consider the histogram as is, namely using the ADC bins. The extraction of the parameters μ and σ is performed with a χ^2 minimization but in this case, in order to take into account the DNL effect, the χ^2 function is modified as explained below.

The χ^2 is defined as

$$\chi^2 = \sum_i \left(\frac{E_i - O_i}{\sigma_i} \right)^2 \tag{5.1}$$

where E_i is the content of the i-th bin as expected from a Gaussian distribution; the O_i is the measured value in the same bin; σ is the uncertainty on the value E_i. The statistical uncertainty on E_i is $\sqrt{E_i}$; another important contribution to this uncertainty is coming from the detector ADC binning. In case of the used configuration, the ADC binning is affected by non-linearities, which affect the bin sizes, such that the bin sizes are not equal to each other. In order to take into account the contribution of this effect the total σ is expressed as:

$$\sigma_i^2 = \sigma_{counts}^2 + \sigma_{ADC}^2 , \tag{5.2}$$

where

$$\sigma_{ADC} = \sigma_{DNL} \cdot E_i . \tag{5.3}$$

The χ^2 function becomes

$$\chi^2 = \sum_i \frac{(E_i - O_i)^2}{E_i \cdot (1 + E_i \cdot \sigma_{DNL}^2)} . \tag{5.4}$$

The output values of the fit function are μ, σ with their uncertainties and the χ^2 of the fit. The results of the fit with modified χ^2 is shown in Figure 5.9. The results are summarized in Table 5.3. The estimated of μ and σ in comparison to the fit performed with the rebinning has a difference lower than the 1%. For this reason, the rest of the analysis has been performed by using the result of fits calculated with the modified χ^2.

For each gain setting, the detector response expressed as the mean (in ADU units) of the gaussian of the acquired distribution was extracted. Correlating this to the energy information given by the photodiode, the detector response curve can be extracted. The energy measured by the photodiode is an estimation of the deposited energy on the DSSC detector under the following assumptions: the photons hitting the active area of the DSSC
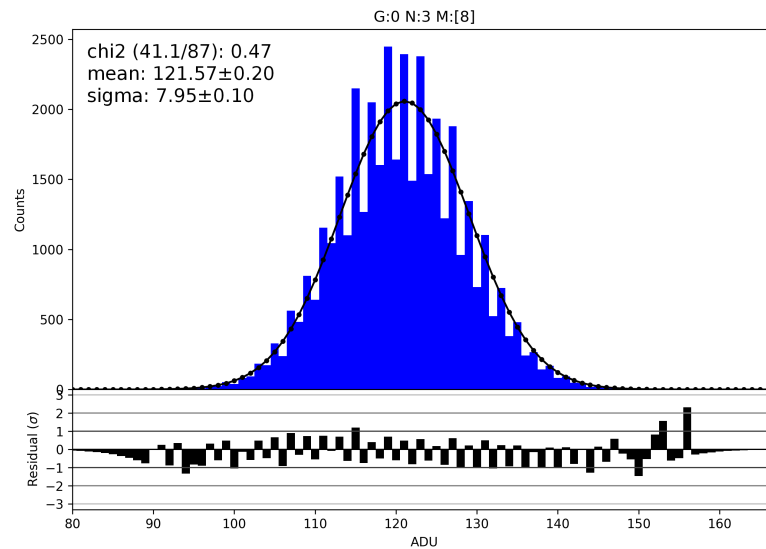
Figure 5.9: An example of histogram of data acquired with the highest gain, C_F=1 (1pF). The binning corresponds to the ADC binning. The residual and the χ^2 take into account the $\sigma_{DNL} = 0.3$ as explained in the section 5.3.
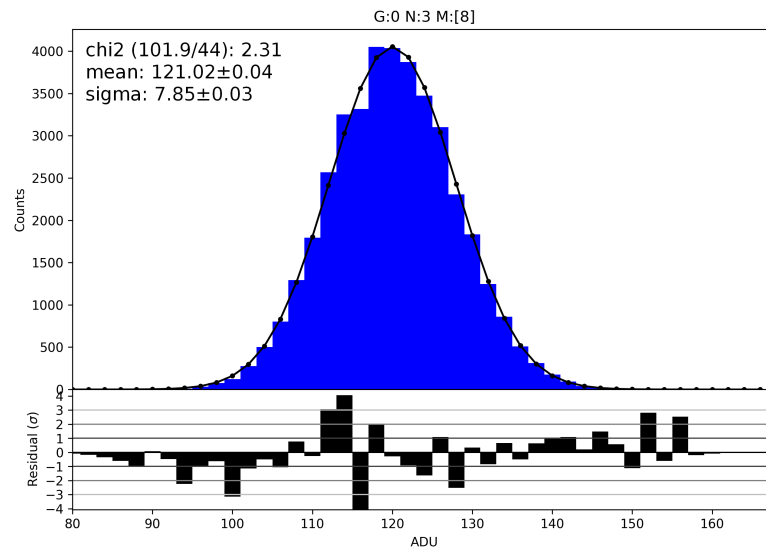

Figure 5.10: An example of histogram of data acquired with the highest gain, C_F=1 (1pF). The histogram has been rebinned: each bin corresponds to 2 consecutive ADC bins. The residual and the χ^2 in normal way, which corresponds to assume $\sigma_{DNL} = 0$, see section 5.3.

Binning	σ_{DNL}	μ	σ	χ^2	$ndof$	$\chi^2/ndof$
2 ADU	0	121.02 ± 0.04	7.85 ± 0.03	101.9	44	2.31
1 ADU	0.3	121.57 ± 0.20	7.95 ± 0.10	41.12	87	0.47

Table 5.3: The results of the fit on the same data assuming different σ_{DNL} and histogram binning.

detector are fully absorbed by the selected pixel; the photons hitting into the photodiode are fully absorbed. The uncertainty assumed of the estimation of the deposited energy corresponds to 10% of the photon flux, [97], due the stability of the beamline P04.

Figure 5.11 shows the results obtained with C_F set to 1 (configuration with a C_F capacitor of 1pF) which corresponds to the maximum gain. Because of the high statistics ($800 \times 50 = 40000$ samples), the statistical uncertainty of the mean ADC value is negligible and for this reason it is not visible in the plot; instead, an uncertainty of the 10% has been associated to the energy measured by the photodiode.

Figure 5.11 shows that, as expected, a linear relation between lines the measured ADU values and the energy deposited on the pixel. The extracted parameter m and q express the energy as function of the ADU counts as:

$$E = m \cdot I_{ADU} + q, \tag{5.5}$$

Therefore m is a measurement at the inverse of the gain (ADC bin-size) in this configuration, expressed [keV/ADU], and q is the energy offset expressed in [keV]. The stamp negative value of q is due to the fact that no dark image has been subtracted from the signal before performing the fit of the histograms, so zero ADU does not correspond to no energy deposited.

The response curves for different gain settings are shown in Figure 5.12. The x-axis shows the energy measured by the photodiode. The y-axis shows the mean value in ADU extracted by the fit of the histograms. In Figure 5.13, a detail of the first part of the response curves for different gain settings is shown. The dashed lines are linear fits in the region $E < 400\,\text{keV}$. By decreasing the gain, the curves become non linear anymore in the high-energy region, as the compression effects of the front-end electronics come into place (Figure 5.12). However, as it can be seen in 5.13, the first region of the curve always shows a linear relation between the energy and the detector input.

The extracted gains are summarized in Figure 5.14. The gain is shown as a function of the capacitance C_F. The gain and the feedback capacitor show, as expected, a linear relation.

In order to estimate the noise of the detector, 50 bursts without X-rays were acquired for each gain configuration. Under the assumption of Gaussian noise, $\sigma_{dark}[\text{ADU}]$ was extracted using a gaussian fit on the histograms of the dark values acquired. The uncertainty associated to σ consider the 0.3 ADU of the DNL. The estimated noise in ADU

Figure 5.11: Mean value of the ADU values measured on the illuminated pixel of the DSSC detector as a function of the energy measured with the photodiode. The detector was configured with C_F=1. The residual divided by sigma are shown under the plot. The line shows the function, *energy* $= m \cdot mean + q$, where *m* corresponds to the inverse gain [keV/ADU], and *q* to the energy offset [keV]. The results of the fit parameters and the errors estimation are shown in the plot.

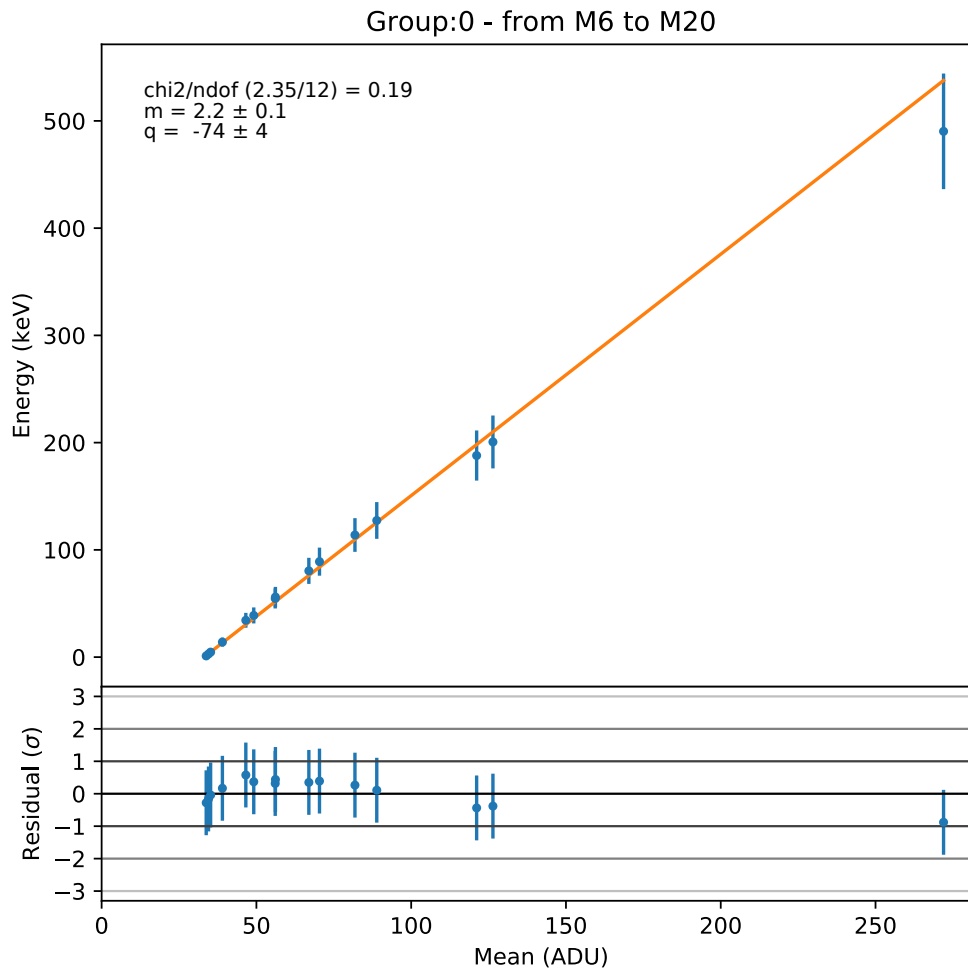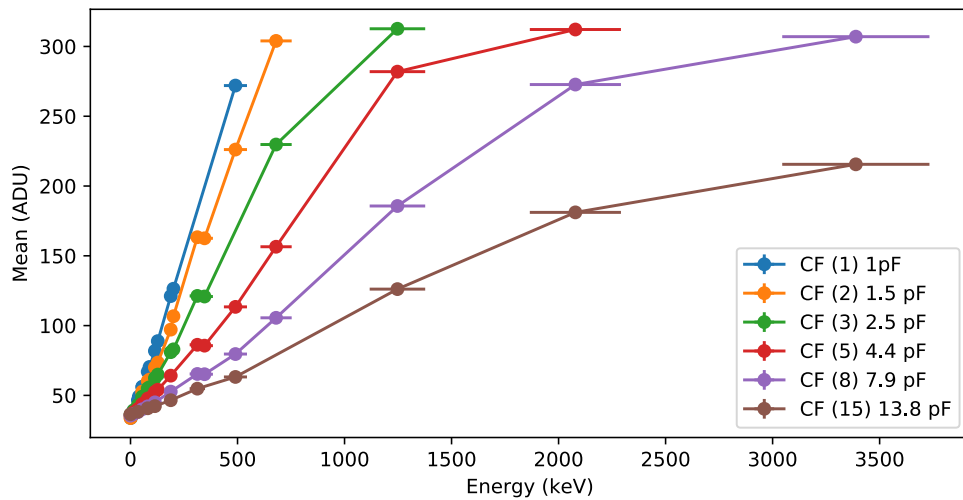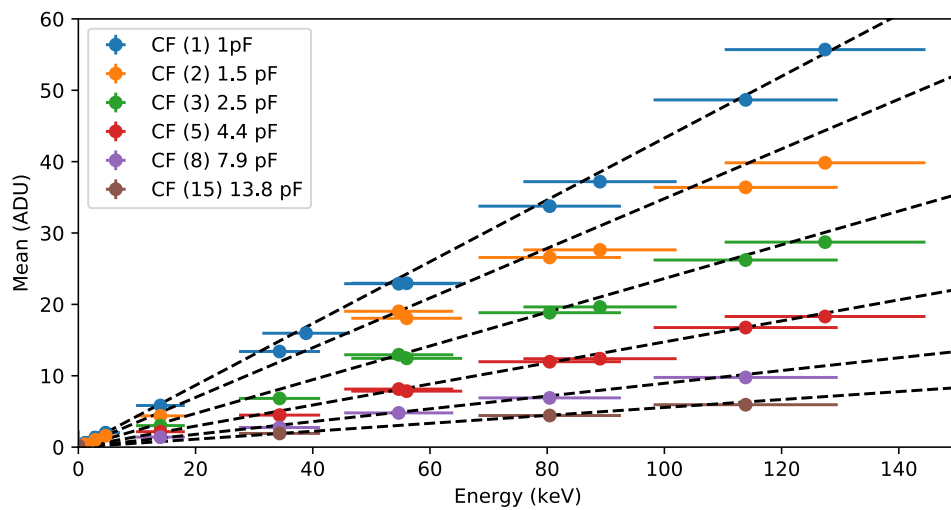Figure 5.12: The detector response for different gain configurations. The mean value of the ADU values measured on the single illuminated pixel of the DSSC detector is plotted as a function of the energy measured with the photodiode. The dark image subtraction has not been performed for this plot.

C_F	Cap. [pF]	$Gain$[ADU/keV]	$\Delta Gain$[ADU/keV]	$Offset$[ADU]	$\Delta Offset$[ADU]	χ^2	NDOF	χ^2_ν
1	1	0.433	0.022	33.183	0.466	1.375	11	0.123
2	1.5	0.347	0.015	33.768	0.003	5.262	12	0.439
3	2.5	0.236	0.010	36.237	0.002	3.121	10	0.312
5	4.4	0.147	0.008	35.751	0.352	1.408	9	0.157
8	7.9	0.089	0.006	35.253	0.354	1.220	6	0.203
15	13.8	0.056	0.005	36.336	0.400	0.555	3	0.185

Figure 5.13: A zoom of the detector response curves for different gain configurations. indicated in the legend. In these curves the dark value has been subtracted from the mean value. The dashed lines corresponds to the linear fits performed for energy $\leq 400\,\mathrm{keV}$.
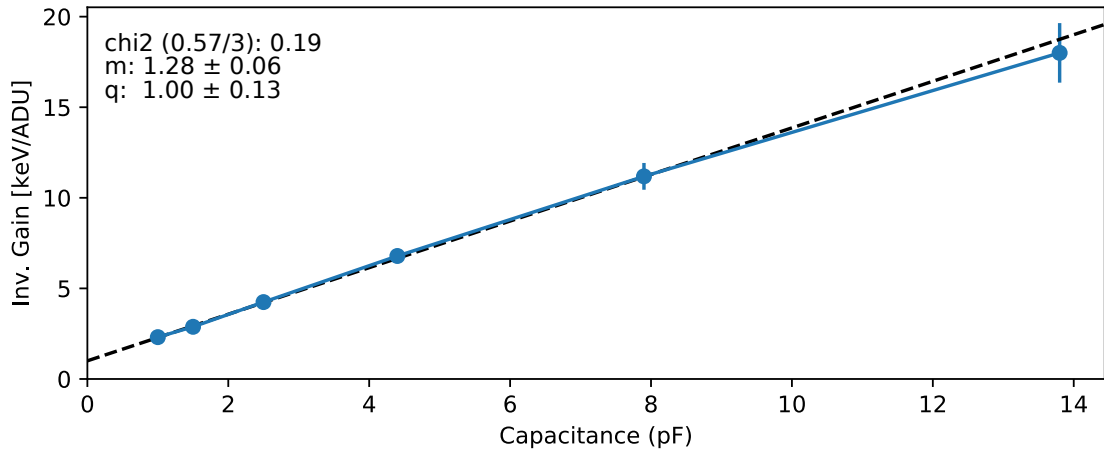
Figure 5.14: The inverse gain (in [keV/ADU]) vs the value of the feedback capacitor. The experimental data point are the gains estimated in Figure 5.13. The line represents a linear fit to the data, the results of the fit are shown in the plot.
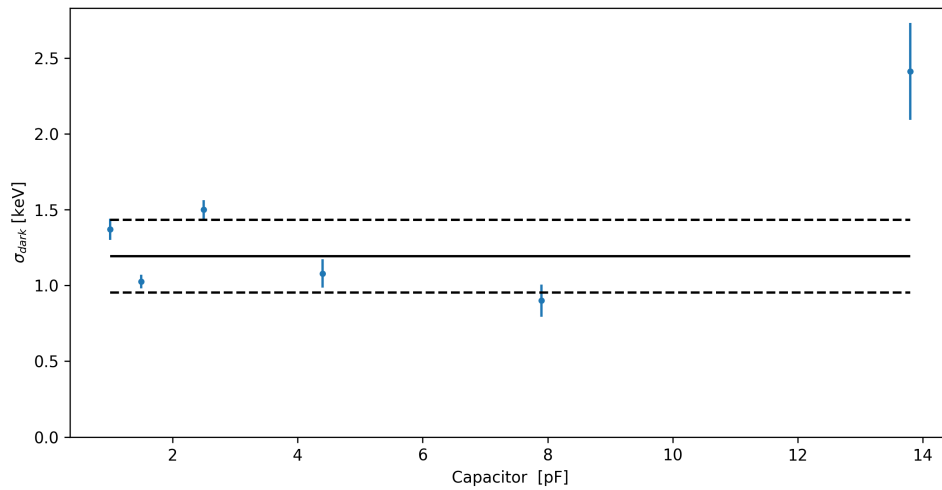
$$\mu_{\sigma_{dark}} = 1.19\text{keV} \quad \sigma_{\sigma_{dark}} = 0.24\text{keV} \quad \sigma_{\mu_{\sigma_{dark}}} = 0.03\text{keV}$$

Figure 5.15: The noise σ_{dark} [keV] vs the front-end capacitor value. The mean μ_σ, the standard deviation σ_σ are the weighted mean and the standard deviation of the values in the plot, while σ_μ is the statistical uncertainty of the weighted mean.

units can be converted into noise expressed in keV by using the gain estimation obtained above. The main contributions to the noise come from the sensors and the first amplifier, thus the noise ideally should not depend on the gain configuration. Figure 5.15 shows the noise estimation for the different gain configuration. No dependence on the gain is observed, as expected.

5.4 The Area Scan

The so called *area-scan measurement* was taken during the second night shift. The aim of this measurement was to acquire data to study the behavior of an extended area of a single ASIC of the detector. In order to perform the area scan, the beamline was set to a fixed configuration; to have in average the same number of photons per pulse. The monochromator was configured to provide a photon energy of $E_\gamma = 1\,\text{keV}$. In a first phase, by acting on the slits the beam was centered and shrunk as much as possible on a single pixel. Then, an automatic script controlling the motion stage placed inside FENICE (see Section 3.5.3) was used to move the DSSC ladder inside FENICE and to control the data acquisition.

The scanned area covered a surface of $\sim 3 \times 12\,\text{mm}^2$ and corresponds to 17×57 pixels. For each position in which the stages were stopped, five bursts were acquired then the ladder was moved again. The full automatic acquisition procedure took about two hours.

A sketch showing the movement steps of the beam is given in Figure 5.16(a). The Figure shows where the beam would have hit the ladder in case of perfect alignment of the ladder surface with respect to the beam, namely, beam orthogonal to the sensors surface and the ladder positioned in exact horizontal direction inside FENICE.

Figure 5.16(b) shows a more realistic case, in which a rotation of 0.5° around the lower left pixel is introduced. This might had been caused, for example, by a non perfect horizontal mounting of the ladder inside FENICE.

Figure 5.17 shows a few examples of the acquired measurements. The plots on the right show four frames taken at different positions of the motion stage. The localization of the beam on a single pixel is visible on the plot. The plot shows just the ASIC where the beam was pointing. The table on the left in Figure 5.17 shows a set of the steps performed during the measurement and the corresponding position of the motion stage. The data were collected on ASIC number 12 and the scanned area, corresponding to 15×57 pixels, covered roughly one fifth of the ASIC (64×64 pixels). It was decided to perform the scan covering almost the full vertical extension of the ASIC. This is because the fact that, due to the electronic architecture, this is the direction in which the largest pixel-to-pixel variations are expected, [98].

5.4.1 The photodiode-independent method

Before and after the area scan, the beam intensity was estimated using the beamline photodiode, see 5.1. After the end of the area scan, it was found out that the value of the total estimated photon flux was not constant during this measurement. The number of photons per pulse measured before the start of the procedure was 168 ± 17 photons/pulse. After the end of the scan it was reduced to 80 ± 8 photon/pulse. For this reason it is not possible to assume a constant photon flux during the area scan. Thus, it is not possible to evaluate the photon beam intensity during the area scan using the value estimated with

the photodiode, except for the first and last steps of the motion stage, namely, close in time to the measurements.

Therefore, an alternative approach is used. This method takes advantage of the information provided by the distribution of the number of photons measured by the detector. In literature, for example in [99] [100], a similar approach has been used successfully for the characterization of detector based on silicon photon multiplier.

Since the detector is counting photons, the statistical distribution associated to counting events is a Poissonian distribution. The parameters of such distribution are:

$$\mu = N, \tag{5.6}$$

$$\sigma_N^2 = N, \tag{5.7}$$

$$\sigma_N = \sqrt{N}, \tag{5.8}$$

where N is the number of photons.

The method is based on the following assumptions:

1. the detector output shows a linear response as function of the deposited photons in the region where the singal is not too high namely, in the region where the compression mechanism of the ASIC plays no role;

2. the noise contribution of the detector (electronic noise) is negligible compared to fluctuations in the number of measured photons;

3. the numbers of photons is $N > 10$, so the Poisson distribution can be approximated by a Gaussian distribution.

The first assumption allows expressing each signal recorded by a single pixel of the detector as

$$ADU(E_{dep.}) = g \cdot E_{dep.} + ADU_{dark}, \tag{5.9}$$

where ADU_{dark} is the signal output provided by the detector when no photon hits the pixel; $ADU(E_{dep.})$ is detector output when a certain energy ($E_{dep.}$ in [keV]) is deposited on the pixel; g is the gain of the pixel expressed in [ADU/keV].

In case of a monochromatic photon beam, assuming a quantum efficiency equal to one, the deposited energy can be written as

$$E_{dep.} = E_\gamma \cdot N, \tag{5.10}$$

where E_γ is the single photon energy and N is the number of photons. Equation 5.9 then becomes

$$ADU(N) = \alpha N + ADU_{dark}, \tag{5.11}$$

where the N is the number of incoming photons; $\alpha = g \cdot E_\gamma$ is the gain expressed in [ADU/$photons$] and can be calculated as

$$\alpha = \frac{ADU(N) - ADU_{dark}}{N} \,.$$

(5.12)

By considering a set of frames acquired at a constant photon flux, the expected distribution of the number of photons is a Poissonian. It can be approximated by a Gaussian defined by the parameters mean μ_N and sigma σ_N. Assuming that ADU_{dark} features a gaussian distribution, the distribution of $ADU(N)$ is a gaussian defined by the followings parameters

$$\mu_{ADU(N)} = \alpha\mu_N + \mu_{ADU_{dark}} \,,$$

(5.13)

$$\sigma^2_{ADU(N)} = (\alpha\sigma_N + \sigma_{ADU_{dark}})^2 \,.$$

(5.14)

As the electronic noise of the detector is expected to be negligible compared to the fluctuations on the number of measured photons (assumption above), $\sigma_{ADU_{dark}} \ll \alpha\sigma_N$. Considering Equation 5.7, Equation 5.14 becomes

$$\sigma^2_{ADU(N)} = \alpha^2\sigma^2_N = \alpha^2 N \,,$$

(5.15)

and therefore

$$N = \frac{\sigma^2_{ADU(N)}}{\alpha^2} \,.$$

(5.16)

Inserting Formula 5.15 in 5.12 gives:

$$\boxed{\alpha = \frac{\sigma^2_{ADU(N)}}{ADU(N) - ADU_{dark}}} \,,$$

(5.17)

and inserting Formula 5.17 into 5.16, gives

$$\boxed{N = \frac{(ADU(N) - ADU_{dark})^2}{\sigma^2_{ADU(N)}}} \,.$$

(5.18)

The two last formulas show that, under the assumptions above, it is possible to estimate the gain and the number of photons hitting the detector without the need to know a priori the photon flux.

(a) Ideal
alligment

(b) Misalligment of 0.5 degree
around the first pixel (lower-left pixel).

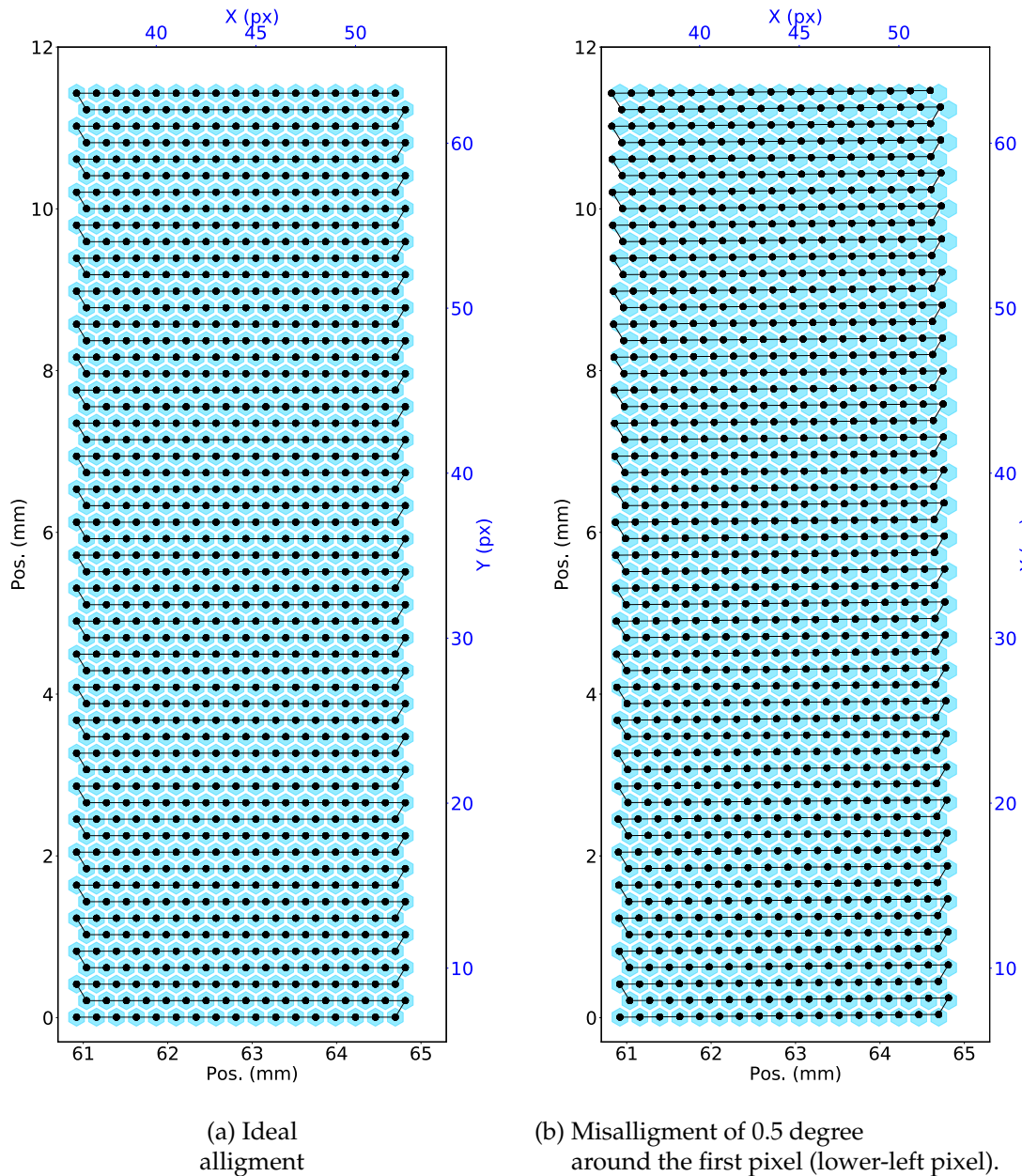Figure 5.16: Motion path during the area scan (in black) showing the beam position on the ladder. In cyan, the pixel sensors position. The area scan started from the lower left pixel. In the left plot, perfect alignment is assumed: beam orthogonal to the sensors surface and the ladder positioned in exactly horizontal. In the right plot, a misalignment corresponding to a rotation of 0.5 degree around the lower left pixel is assumed.

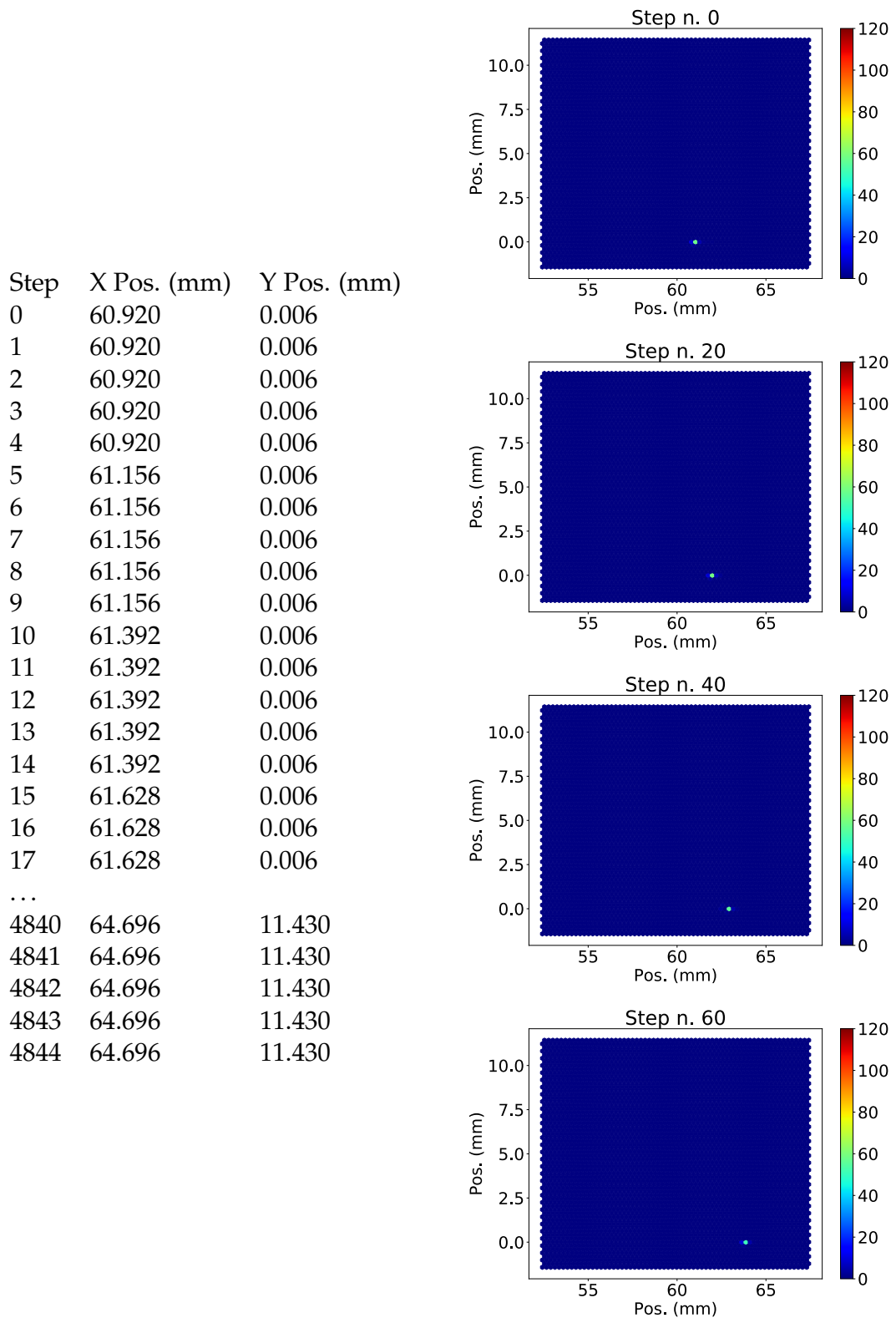| Step	X Pos. (mm)	Y Pos. (mm)
0	60.920	0.006
1	60.920	0.006
2	60.920	0.006
3	60.920	0.006
4	60.920	0.006
5	61.156	0.006
6	61.156	0.006
7	61.156	0.006
8	61.156	0.006
9	61.156	0.006
10	61.392	0.006
11	61.392	0.006
12	61.392	0.006
13	61.392	0.006
14	61.392	0.006
15	61.628	0.006
16	61.628	0.006
17	61.628	0.006
...		
4840	64.696	11.430
4841	64.696	11.430
4842	64.696	11.430
4843	64.696	11.430
4844	64.696	11.430

Figure 5.17: On the left a table showing the first and last motor steps coordinates; on the right the images acquired with the ASIC illuminated by the beam, with the detector in different positions corresponding to the step number indicated on top of the plots.

5.4.2 Data analysis: the pixel maps

Table 5.4 summarizes the results produced with the area scan measurement. The figures listed in the table are pixel maps in which each hexagon corresponds to a single pixel, and the color of each hexagon represents the quantity written in the label of the plot (for example SIGNAL, STD.SIGNAL, *etc.*). Further details and comments are given in the text below.

Name	Units		
DARK	[ADU]	is the output the detector when the sensor is not illuminated	Figure 5.18(a), pag. 124
RAWSIGNAL	[ADU]	is the output the detector when the sensor is illuminated	Figure 5.19(a), pag. 125
SIGNAL	[ADU]	$= \text{RAWSIGNAL} - mean(\text{DARK})$	Figure 5.21(a), pag. 127
STD.RAWSIGNAL	[ADU]	$= st.dev.(\text{RAWSIGNAL})$	Figure 5.22(a), pag. 128
STD.DARK	[ADU]	$= st.dev.(\text{DARK})$	Figure 5.20(a), pag. 126
STD.SIGNAL	[ADU]	$= \sqrt{st.dev.(\text{RAWSIGNAL})^2 - st.dev.(\text{STD.DARK})^2}$	Figure 5.23(a), pag. 129
EST.PHOTONS.	[#]	$= \text{SIGNAL}^2/\text{STD.DARK}^2$	Figure 5.24(a), pag. 130
EST.GAIN	[ADU/keV]	$= \text{STD.SIGNAL}^2/\text{SIGNAL}$	Figure 5.25(a), pag. 131
EST.INV.GAIN	[keV/ADU]	$= 1/\text{EST.GAIN}$	Figure 5.26(a), pag. 132
NOISE	[keV]	$= \text{STD.DARK} \times \text{EST.INV.GAIN}$	Figure 5.27(a), pag. 133

Table 5.4: The list of the pixel maps obtained from the area scan measurement.

In all the pixel maps, the pixels sitting on the column x=43 and featuring an odd row number were defect. Therefore they were removed from the plot and from the analysis. In particular, the read out from these pixels show a non-stable behavior, with values jumping between saturation and zero and vice-versa. The reason was identified in a non perfect connection between these pixels and the ASIC in this electronic prototype.

The explanation of the various measured quantities listed in Table 5.4 and shown as Figure in the following of this Chapter is given below.

- DARK [ADU]

  The dark frame acquisition consists of 70 bursts, which corresponds to a total of $70 \times 800 = 56000$ frames acquired when the beam was not hitting the detector. The map in Figure 5.18(a) shows the mean value of the dark signal for each pixel. This measurement is needed because it determines the offset, which must be subtracted from readout obatined when the bin hits the detectors, to get the amplitude of the signal. The plot 5.18(a) shows that the mean value of the dark is higher for the pixel in the upper side of the plot. This is due to the features of this ASIC generation and it is confirmed by measurements done with other setup [101]. The histogram 5.18(b) shows the distribution of the dark. The mean value is 51.3 ADU and the standard deviation results 4.8 ADU. The mean of the dark value and its standard deviation depends from the ASIC feature and from its configuration.

- **STD.DARK** [ADU]

  The STD.DARK is the standard deviation of the dark frames:

  $$\text{STD.DARK} \equiv st.dev.(\text{DARK}). \tag{5.19}$$

  This quantity corresponds to the noise of the detector expressed in [ADU]. The map of STD.DARK is shown in Figure 5.20(a) and the histogram calculated over all considered pixels is shown Figure 5.20(b). The mean value of the standard deviation of the dark is 0.72 ADU. It represents the noise of expressed in [ADU] units and it is discussed in the next section.

- **RAWSIGNAL** [ADU]

  As mentioned above, during the area-scan measurement, five bursts (corresponding to a total of $5 \times 800 = 4000$ frames) were acquired for each position of the motion stage.

  The plot in Figure 5.19(a) shows the raw signal acquired when the beam was hitting the detector on a given pixel. No signal subtraction was performed. On the plot, each hexagon represents the mean value of detector output of the corresponding pixel. The value shown is calculated as the mean of five consecutive bursts with the beam in the same position. In Figure 5.19(a), it is possible to observe a decrease of intensity between the lower part and the higher part. This is opposite to what observed in 5.18(a) the dark offset map, where the mean values are higher in the upper part of the plot. In the case of raw signal, this decrease is determine due to physical effects, which will be explained following. Figure 5.19(b) shows the histogram of RAWSIGNAL evaluated over all considered pixels.

- **SIGNAL** [ADU]

  In order to determine the signal intensity in [ADU], the offset, namely, the mean value of the dark frames, has to be subtracted from the raw signal:

  $$\text{SIGNAL} = \text{RAWSIGNAL} - mean(\text{DARK}). \tag{5.20}$$

  The pixel map in Figure 5.21(a) shows the SIGNAL. The color of each hexagon represents the mean value. In comparison to RAWSIGNAL, SIGNAL appears more smooth. Also in this case, the plot features an intensity gradient, the top side shows higher values and the bottom side shows lower values of the detector output signal. For this reason the histogram evaluated over all the pixels, shown in Figure 5.21(b) has a broad distribution. The intensity gradient is due to physical effect which will be explained following.

- **STD.SIGNAL** [ADU] and **STD.RAWSIGNAL** [ADU]

  According to Equation 5.18 the number of photons hitting the detector can be determined by using the standard deviation of the signal. The standard deviation of the SIGNAL is given by

$$\text{STD.SIGNAL} \equiv st.dev.(\text{SIGNAL}). \tag{5.21}$$

  Due to presence of the offset of the electronics (dark signal), the detector output when the photons are detected (raw signal) is given by

$$\text{RAWSIGNAL} = \text{DARK} + \text{SIGNAL}. \tag{5.22}$$

  Since the measurement of the dark and the signal are independent, it is possible to assume that there is no direct correlation between the two quantities. For that the standard deviation of the raw signal can be written as

$$st.dev.(\text{RAWSIGNAL})^2 = st.dev.(\text{SIGNAL})^2 + st.dev.(\text{DARK})^2. \tag{5.23}$$

  From the last equation is possible to calculate the standard deviation of the signal as

$$\text{STD.SIGNAL} = st.dev.(\text{SIGNAL}) = \sqrt{st.dev.(\text{RAWSIGNAL})^2 - st.dev.(\text{DARK})^2}. \tag{5.24}$$

  Figure 5.23(a) shows the map of STD.SIGNAL. The plot features an intensity gradient: the top part has lower intensity in comparison to the higher part. This is a characteristic of the ASIC and from configuration used.

  Since $st.dev.(\text{RAWSIGNAL})^2 \gg st.dev.(\text{DARK})^2$, the Formula 5.22 can be approximated as

$$\text{STD.SIGNAL} \simeq \text{STD.RAWSIGNAL}. \tag{5.25}$$

  The STD.RAWSIGNAL pixel map is shown in Figure 5.22(a). As expected, it looks very similar to the STD.SIGNAL map. The mean values of STD.RAWSIGNAL and STD.SIGNAL have a differences $< 2\%$.

- **EST.PHOTONS** [#]

  The number of photons can be estimated by Equation 5.18, which can be rewritten as

$$\text{EST.PHOTONS} = mean(\text{SIGNAL})^2/\text{STD.SIGNAL}^2. \tag{5.26}$$

Since the photon energy was fixed by the monochromator to $E_\gamma = 1\,\text{keV}$, the EST.PHOTONS is equivalent to the deposited energy into the pixel in [keV] units.

The result is shown in Figure 5.24(a). This pixel map shows a strong gradient. On the bottom part, the estimated number of photons per pulse is about 110 and in the top part it reduces down to 35. This reduction can be explained by the contribution of two effects. The first is a the detector-beam misalignment and the second effect is a slow decay of the photon beam intensity due to a slow drift of the beam trajectory in the beamline. These effects are discussed in detail above.

- **EST.GAIN** [ADU/keV]

The gain estimation is calculated using Equation 5.17. According to this formula the estimation of the gain is not affected by the misalignment and the beam intensity decrease. Equation 5.17 can be rewritten as

$$\text{EST.GAIN} = \text{STD.SIGNAL}^2/mean(\text{SIGNAL})\,. \tag{5.27}$$

Figure 5.25(a) shows the map of the estimated gain, and Figure 5.25(b) shows the histogram of the gains. The estimated mean gain is $0.43\,[\text{ADU/keV}]$ with a statistical uncertainty of 1%. This result is discussed in the next Section.

- **INV.EST.GAIN** [keV/ADU]
The inverse of the gain corresponds to the estimated ADC bin-size expressed in energy units [keV]. It is calculated as

$$\text{INV.EST.GAIN} = 1/\text{EST.GAIN}\,. \tag{5.28}$$

Figure 5.26(a) shows the pixel maps of the estimated ADC bin-size and Figure 5.26(b) its distribution. The mean bin-size is $2.43\,\text{keV/ADU}$ with a standard deviation of $0.25\,\text{keV/ADU}$. This result is discussed in the next section.

- **NOISE** [keV]
The noise can be estimated from the standard deviation of the dark signal (Figure 5.20(a)) converted in keV using the gain.

$$\text{NOISE}\,[\text{keV}] = \text{INV.EST.GAIN}\,[\text{keV/ADU}] \times \text{STD.DARK}\,[\text{ADU}]\,. \tag{5.29}$$

The noise map is shown in Figure 5.27(a). The Figure 5.27(b) shows the histogram of the estimated noise in energy. The mean value of noise in the measured area is $1.6\,\text{keV} \pm 0.3\,\text{keV}$. This result is discussed in the next section.
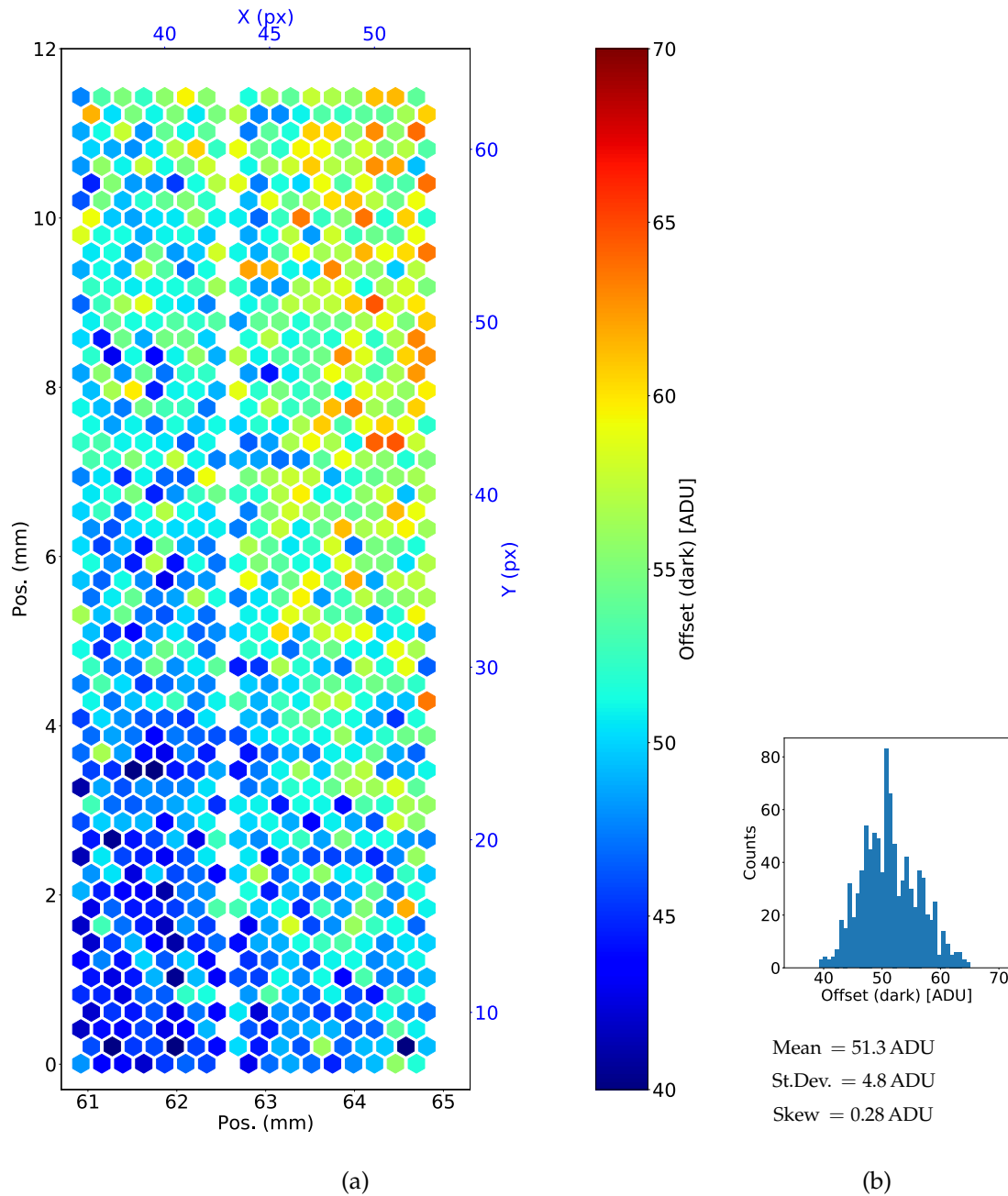
(a)

(b)

Figure 5.18: The **DARK** offset map. In the plot (a) each hexagon corresponds to a pixel. The color of each hexagon represents the mean value of the detector output calculated over 70 consecutive bursts (56000 frames) when the beam was not hitting the detector. The histogram (b) shows the distribution of the dark offset values. The pixels in column x=43 and featuring odd row-number were removed as they are defect.

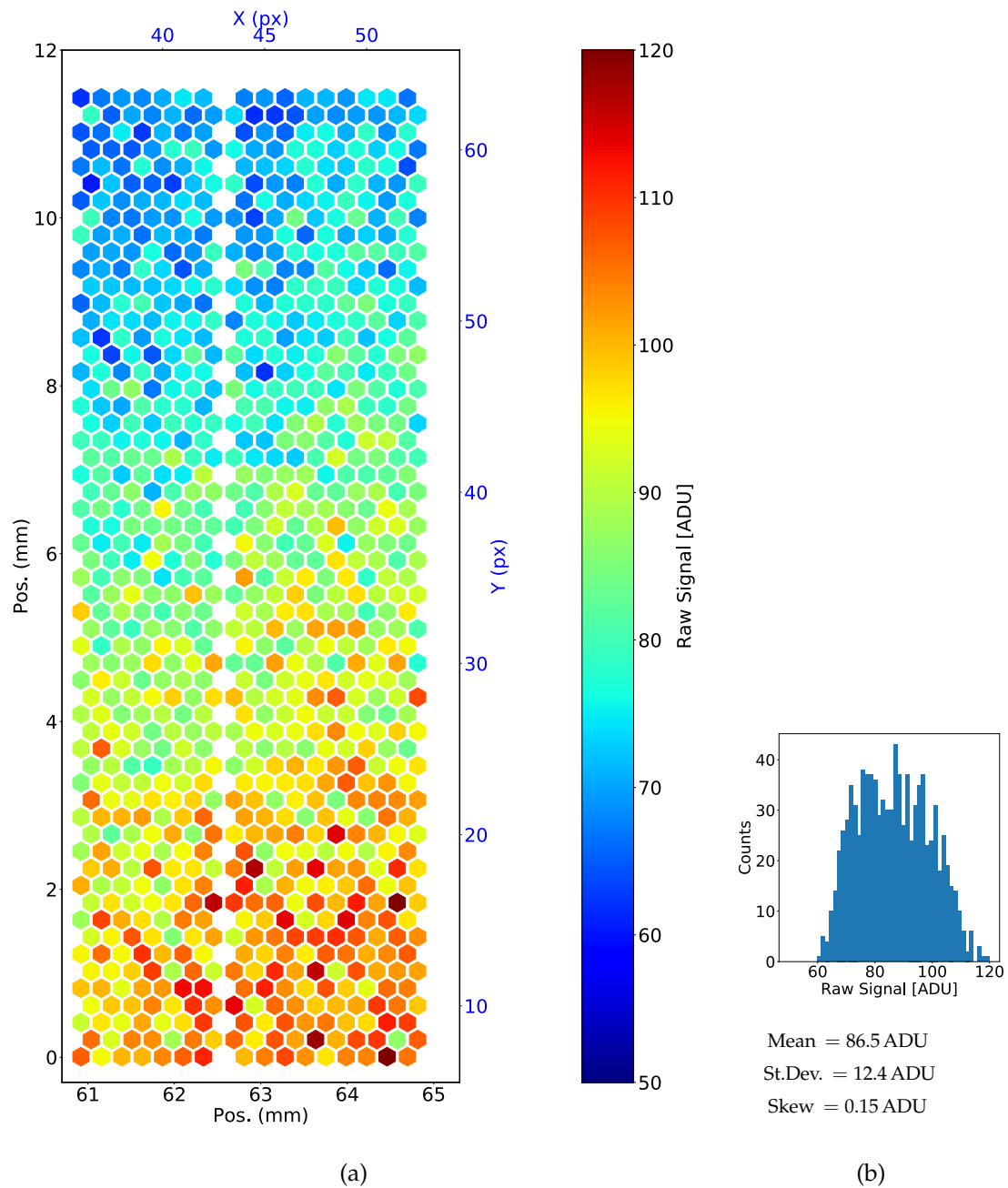(a)   (b)

Figure 5.19: The **RawSignal** map. In the plot (a) each hexagon corresponds to a pixel.
The color of each hexagon represents the mean value of the detector output
for the pixel hit by the beam in the corresponding step of the area scan. The
mean value is calculated over five bursts (4000 frames) acquired when the
beam was hitting the detector. The histogram (b) shows the distribution of
the raw signal over all the considered pixels. The pixels in column x=43 and
featuring odd row-number were removed as they are defect.
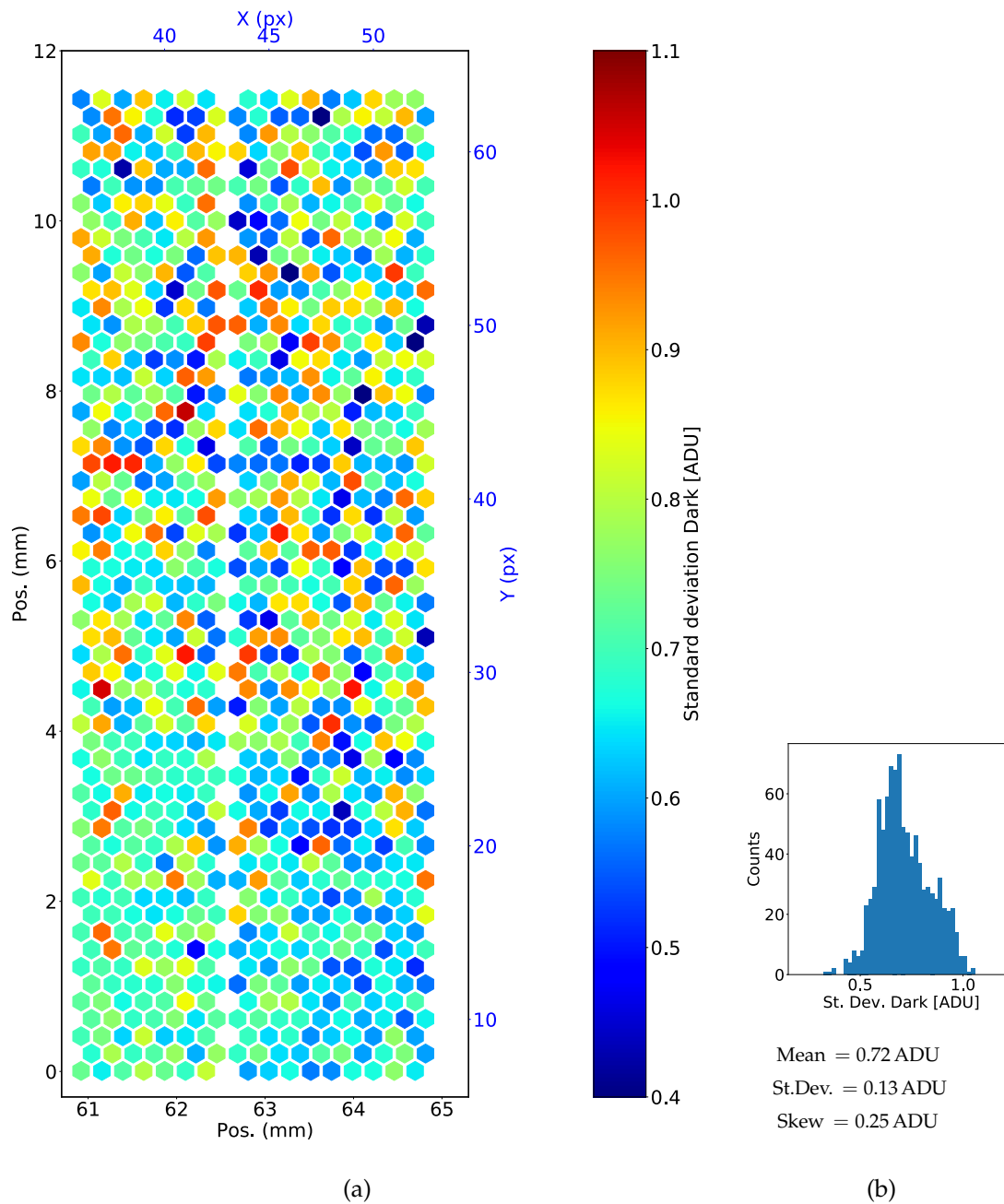
(a)

(b)

Figure 5.20: The **STDDARK** map. In the plot (a) each hexagon corresponds to a pixel. The color represents the standard deviation of the detector output on the given pixel when the beam was not hitting the detector. For each pixel the standard deviation was calculated over the data acquired in of 70 consecutive bursts corresponding to 56000 frames. The histogram (b) shows the distribution of the standard deviation of the dark frames over all pixels. The pixels in column x=43 and featuring odd row-number were removed as they are defect.

(a)   (b)
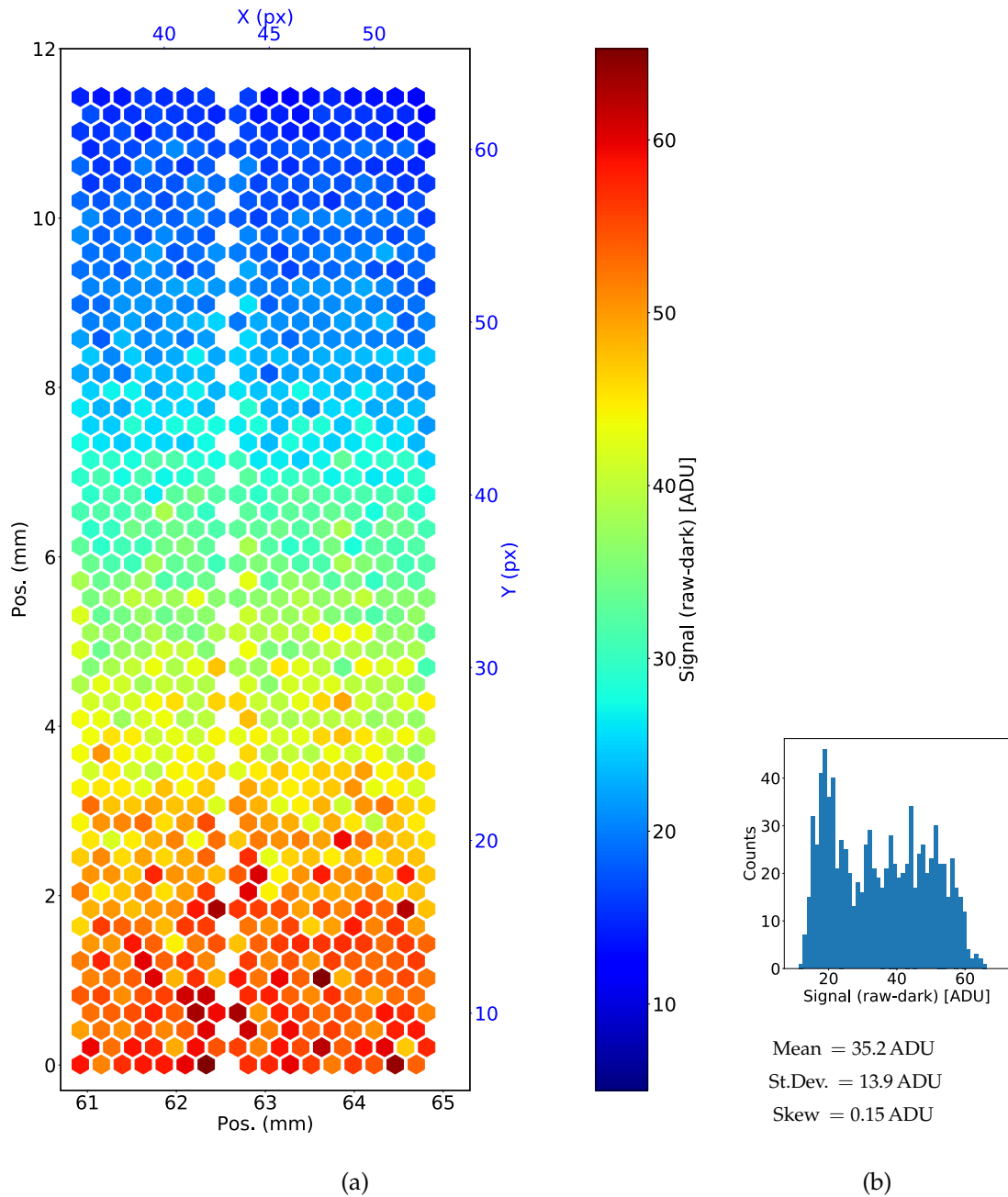
Figure 5.21: The **Signal** map. In the plot (a) each hexagon corresponds to a pixel. The color of each hexagon represents the mean value of the detector photon-response for the pixel hit by the beam in the corresponding step of the area scan. The mean value is calculated over five bursts (4000 frames) acquired when the beam was hitting the detector. The histogram (b) shows the distribution of the signal evaluated over all pixels. The pixels in column x=43 and featuring odd row-number were removed as they are defect.
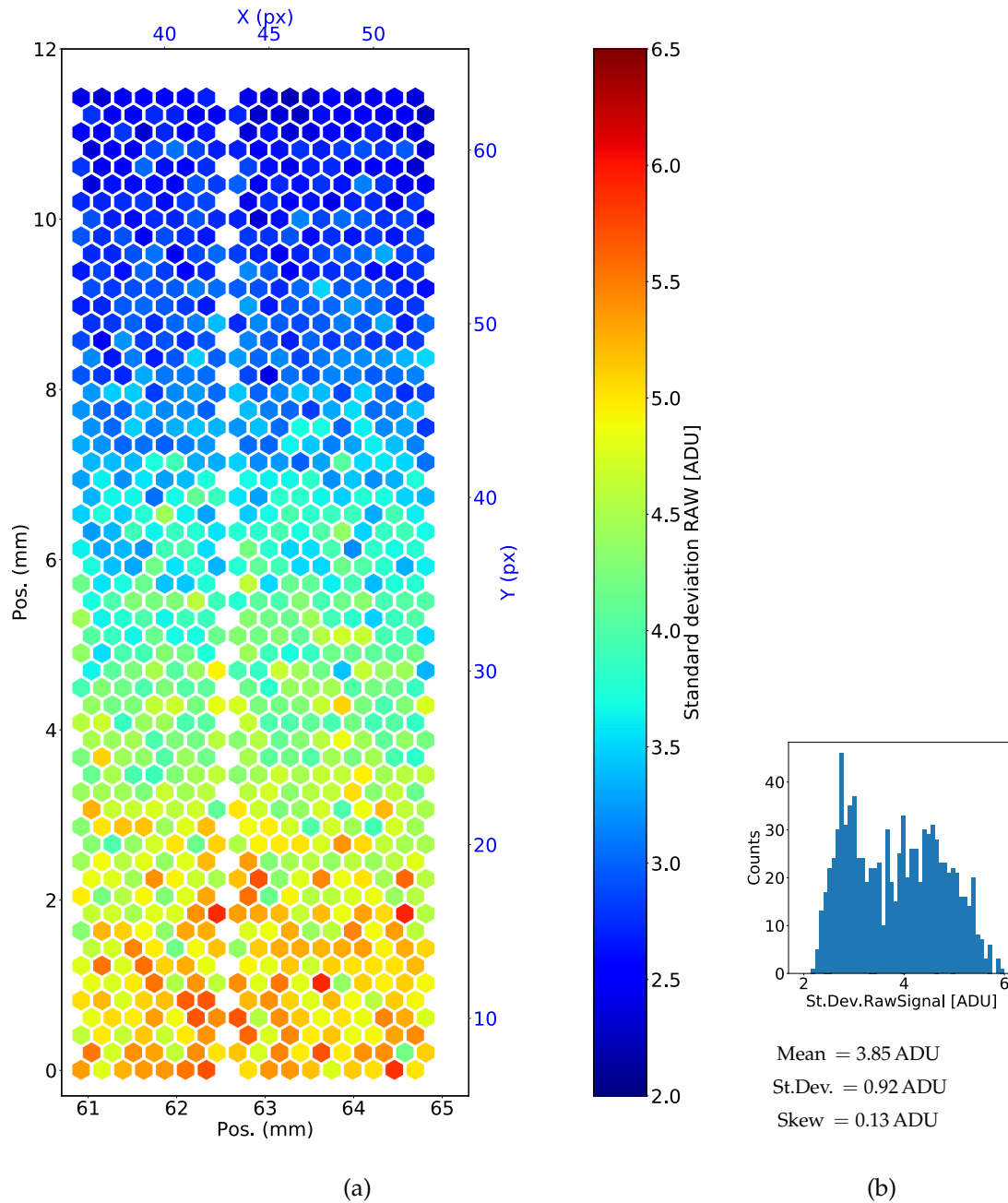
(a)

(b)

Figure 5.22: The **STD.RAWSIGNAL** pixel map. In the plot (a) each hexagon corresponds to a pixel. The color of each hexagon represents the standard deviation of the detector output for the pixel hit by the beam in the corresponding step of the area scan. The standard deviation value is calculated over five bursts (4000 frames) acquired. The histogram (b) shows the distribution of the signal calculated over all pixels. The pixels in column x=43 and featuring odd row-number were removed as they are defect.
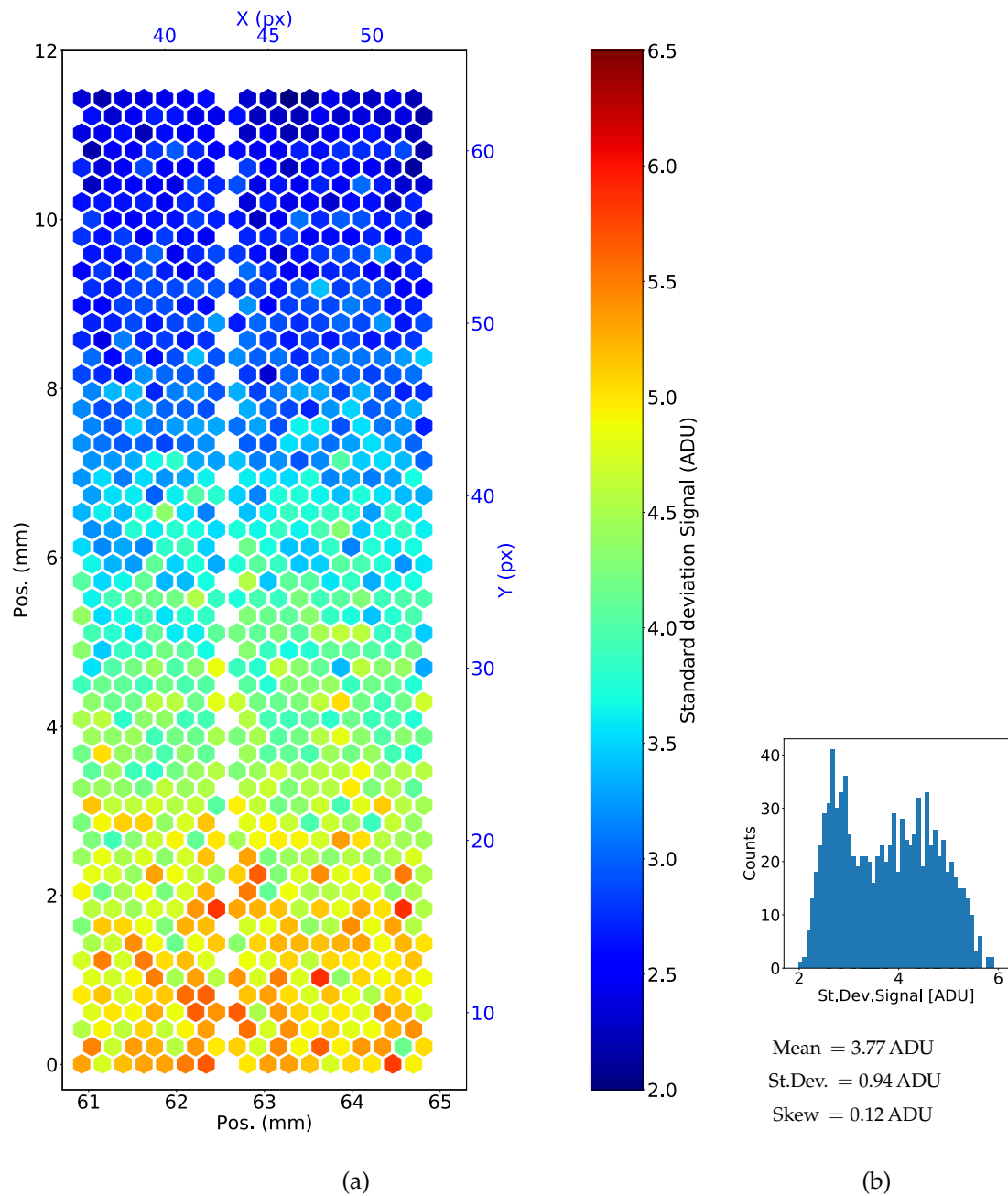
(a)

(b)

Figure 5.23: The **STD.SIGNAL** pixel map. In the plot (a) each hexagon corresponds to a pixel. The color of each hexagon represents an estimation of the standard deviation of the detector photon-response, calculated as described in the text. The histogram (b) shows the distribution of standard deviation of the estimated detector photon-response calculated over all pixels. The pixels in column x=43 and featuring odd row-number were removed as they are defect.
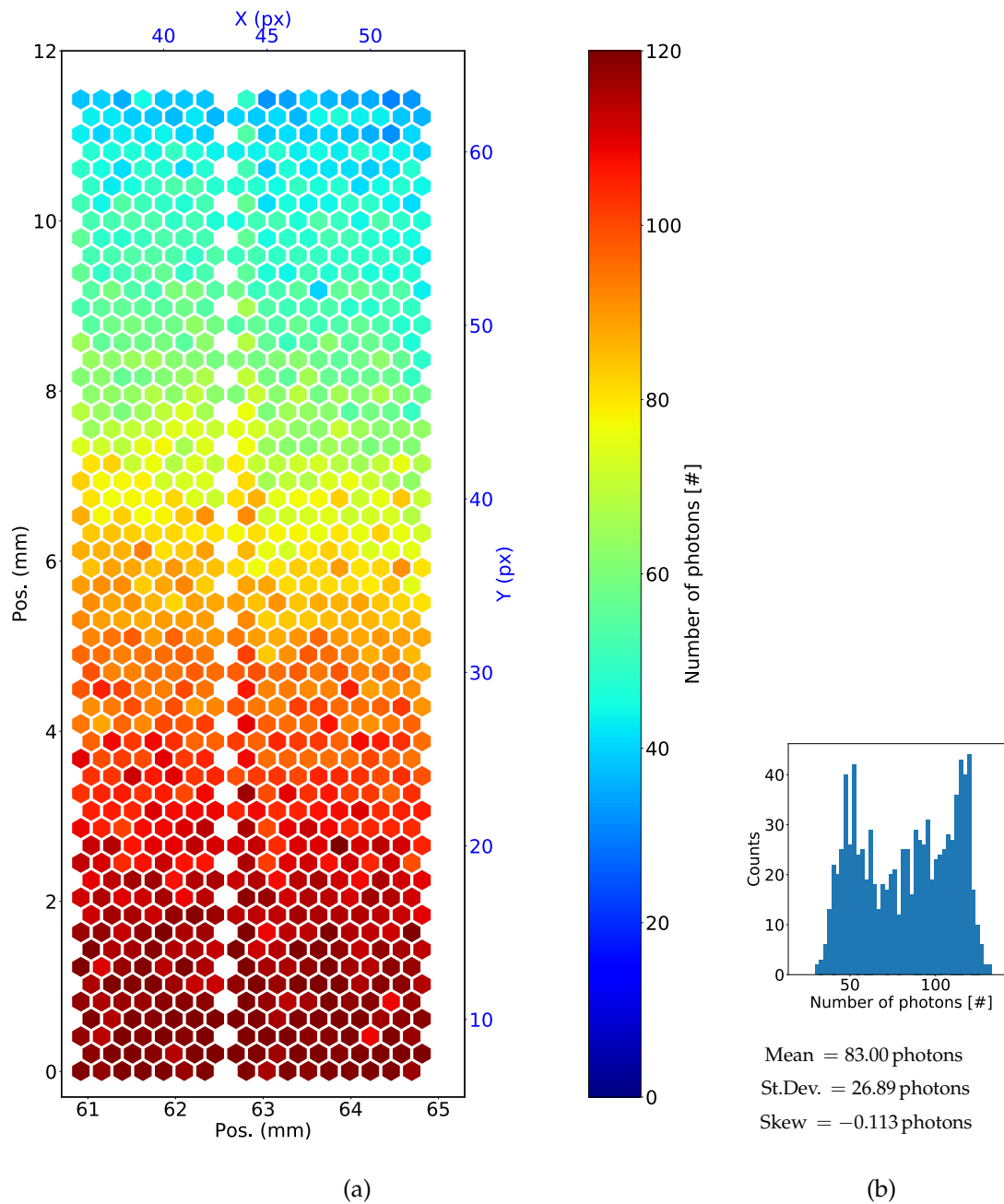
(a)

(b)

Figure 5.24: The **Est.Photons** pixel map. In the plot (a) each hexagon corresponds to a pixel. The color of each hexagon represents the estimated number of photons hitting the pixel evaluated as explained in the text. The histogram (b) shows the distribution of the estimated number of photons calculated over all pixels. The pixels in column x=43 and featuring odd row-number were removed as they are defect.
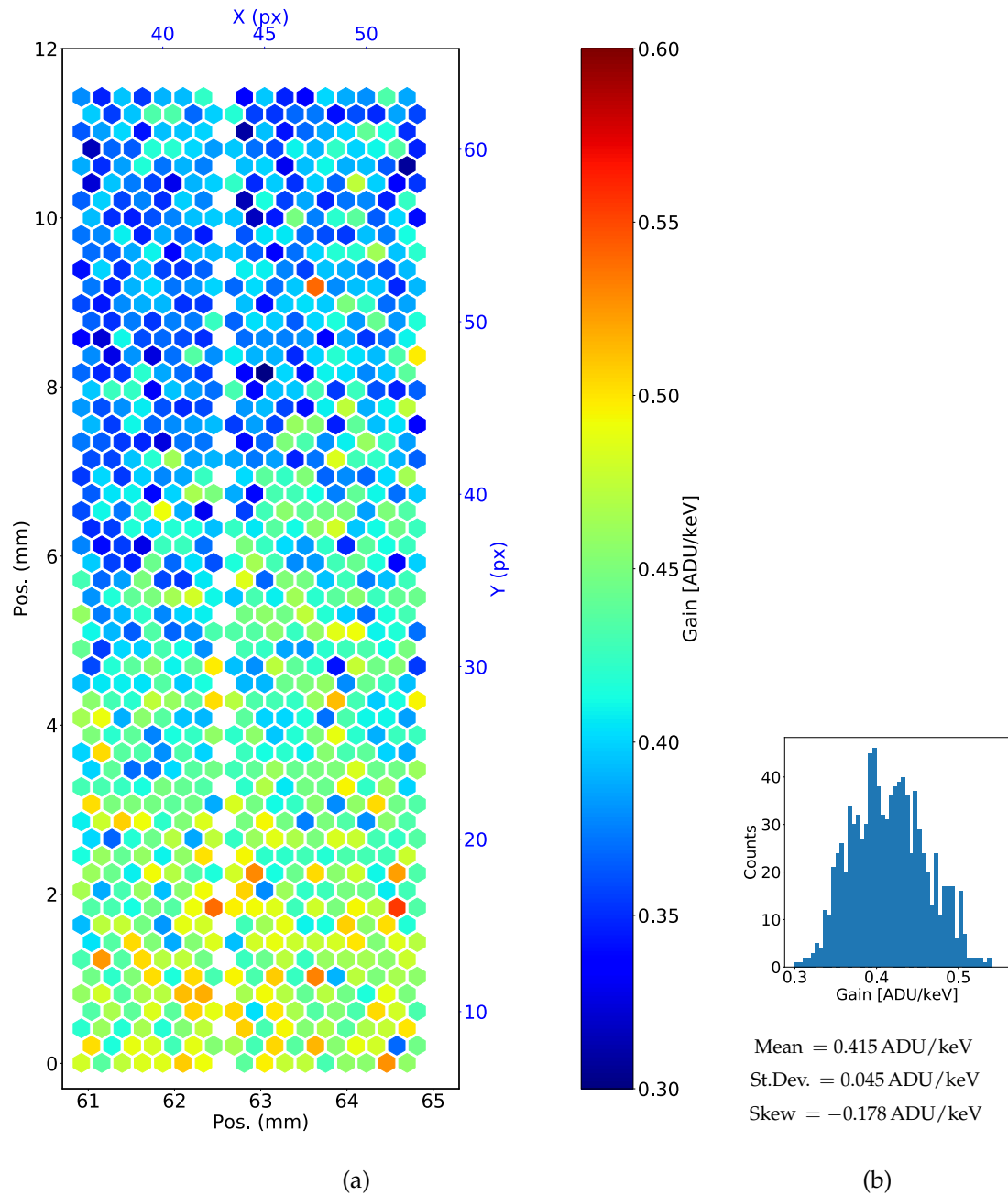
(a)   (b)

Figure 5.25: The **EST.GAIN** pixel map. In the plot (a) each hexagon corresponds to a pixel. The color of each hexagon represents the estimated gain of the pixel evaluated as explained in the text. The histogram (b) shows the estimated gain distribution calculated over all pixels. The pixels in column x=43 and featuring odd row-number were removed as they are defect.
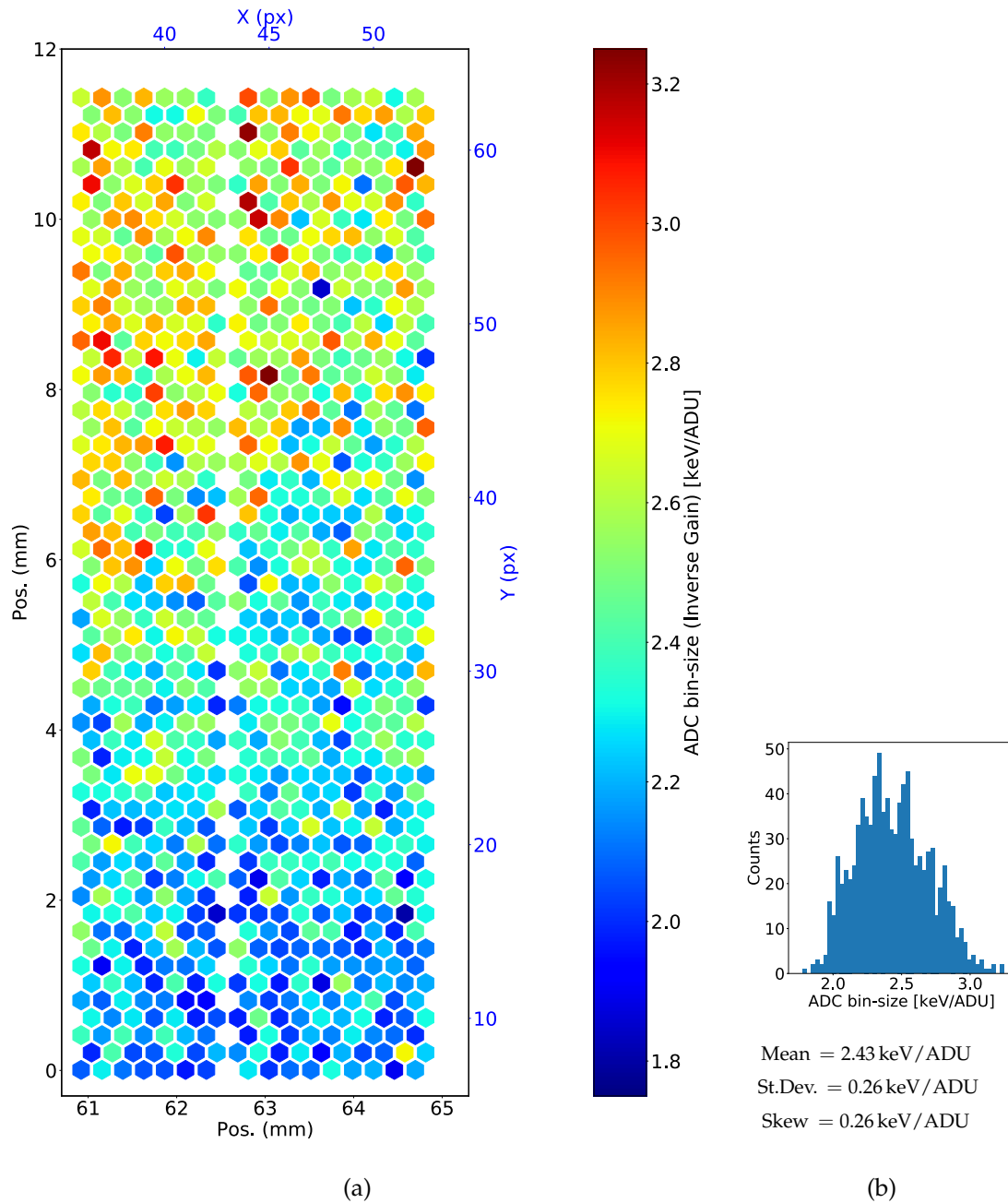
(a)   (b)

Figure 5.26: The **Est.Inv.Gain** pixel map. In the plot (a) each hexagon corresponds to a pixel. The color of each hexagon represents the inverse gain of the pixel evaluated as explained in the text. The inverse gain corresponds to the ADC-bin size. The histogram (b) shows the inverse gain distribution calculated over all pixels. The pixels in column x=43 and featuring odd row-number were removed as they are defect.
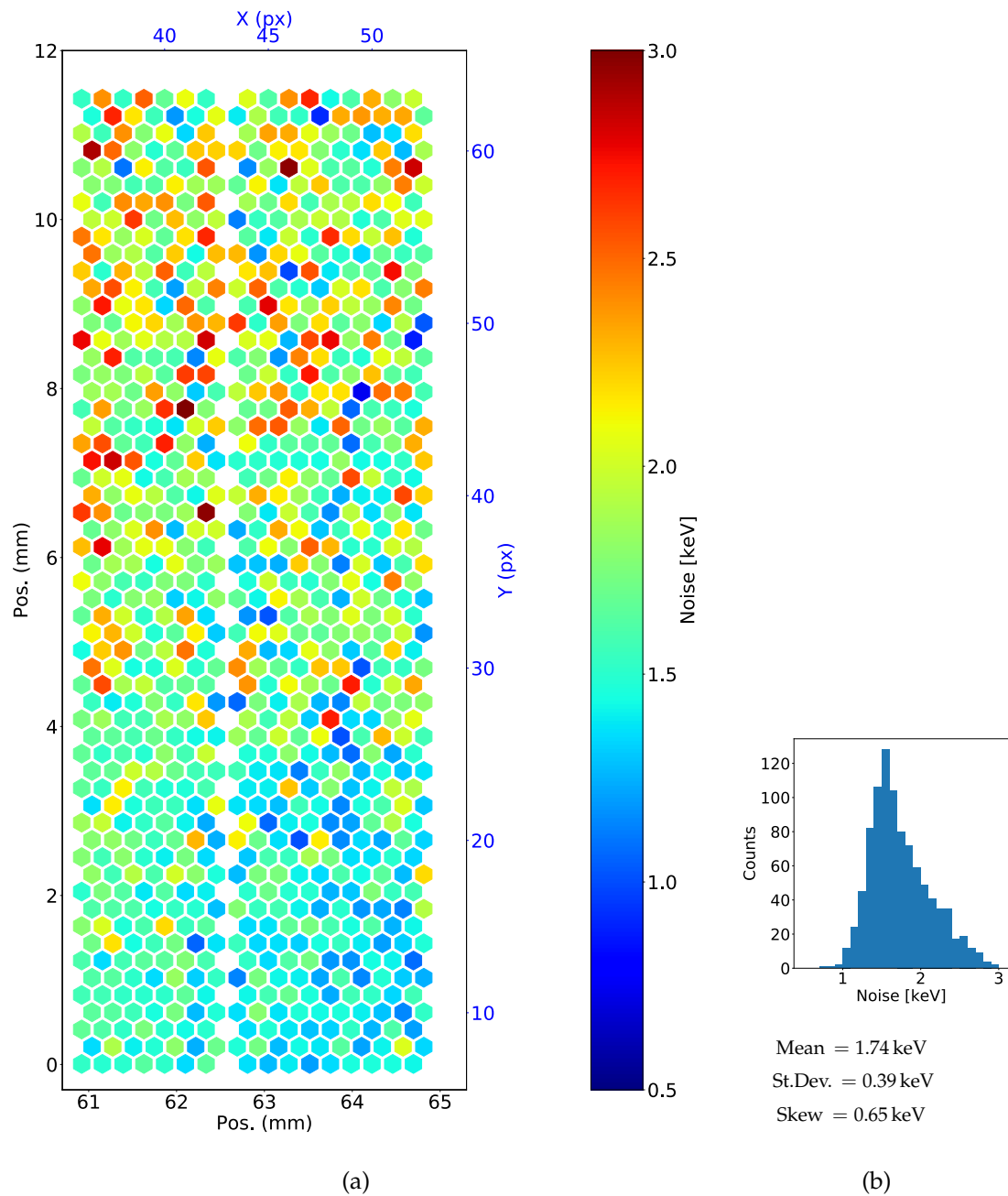
Figure 5.27: The **Noise** pixel map. In the plot (a) each hexagon corresponds to a pixel. The color of each hexagon represents the noise of the pixel evaluated as explained in the text. The histogram (b) shows the noise distribution calculated over all pixels. The pixels in column x=43 and featuring odd row-number were removed as they are defect.

5.4.3 Discussion of the results

After the measurement was performed, it was discovered that the alignment between the beam and the selected pixel was not perfect. As a consequence, in the last acquisitions the beam was illuminating more than one pixel. This was probably due to the not perfect positioning of the DSSC ladder in the FENICE vessel with respect to the beam. An example of misalignment was already shown in Figure 5.16(b). It shows that even a very small misalignment of 0.5° with respect to the horizontal direction causes a misalignment of half a pixel in the region, which is the farthest from the starting point.

The hint for the second effect was given by the photon flux measurement. The photodiode was used to measure the estimated number of photons hitting the sensor for every pulse. Since the beamline monochromator was set to 1 keV, the number of photons per pulse corresponds also to the energy deposited per pulse expressed in keV. The photodiode measurements were performed before and after the area scan, which lasted about two hours. The comparison between the number of photons estimated with the photodiode and the number estimated with the DSSC detector (Equation 5.18) is shown in Table 5.5.

In the case of the DSSC detector, only the pixel in which the beam should have hit the detector in case of perfect alignment is considered for the estimation of the numbers given in Table 5.5.

	Photodiode (photons/pulse)	DSSC selected pixel (photons/pulse)
Begin of the area scan (A)	168 ± 17	110 ± 24
End of the area scan (B)	80 ± 8	35 ± 8
Ratio (B)/(A)	48%	32%

Table 5.5: The comparison between the number of photons hitting the DSSC detector estimated with the photodiode and the number of photons estimated with the DSSC detector itself. In case of the DSSC, only the Central pixel (defined in the text) is considered.

Both the number of photons estimated with the DSSC detector and measured by the photodiode show clearly a decrease of the photon flux. But the discrepancy between the photodiode values and the number of photons estimated with DSSC is remarkable. It can be explained in two ways: either the photodiode-independent method for the calibration gives wrong results, or a misalignment effect as explained above is also present and the beam was shared between more than one pixel towards the end of the area scan. In order to investigate better this fact the plot in Figure 5.29 was produced. This plot shows on the x-axis the acquisition time; on the y-axis the estimated number of photons hitting the pixel. The pixel marked as **Central Px.** corresponds to the single pixel ideally hit by
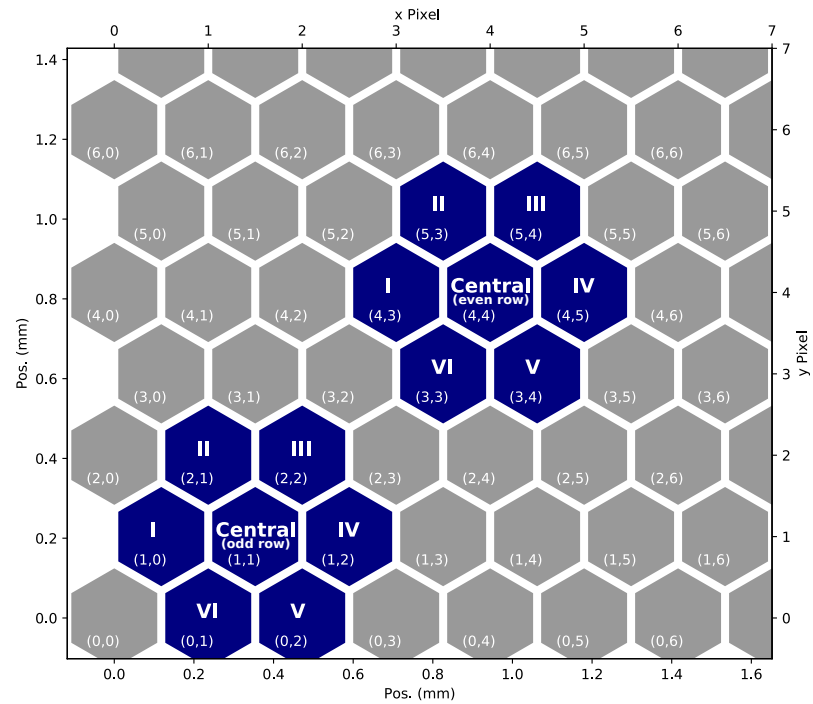
Figure 5.28: The definition and numbering of neighbor pixels around a given pixel.

Pixel	Coordinates			
	with Y_0 odd		with Y_0 even	
Central	Y_0	X_0	Y_0	X_0
I	Y_0	$X_0 - 1$	Y_0	$X_0 - 1$
II	$Y_0 + 1$	X_0	$Y_0 + 1$	$X_0 - 1$
III	$Y_0 + 1$	$X_0 + 1$	$Y_0 + 1$	X_0
IV	Y_0	$X_0 + 1$	Y_0	$X_0 + 1$
V	$Y_0 - 1$	$X_0 + 1$	$Y_0 - 1$	X_0
VI	$Y_0 - 1$	X_0	$Y_0 - 1$	$X_0 - 1$

Table 5.6: The definition and numbering of neighbor pixels around a given pixel.

the beam during the area scan centered pixel; the other pixels are the *first neighbor pixels* defined as in Figure 5.28 and in Table 5.6.

For instance, the **I Px.** corresponds to the first pixel on the left with respect to the centered pixel. In the plot at Figure 5.29, the number of photons measured by the **Central Px.** pixel decreases with time. On the other hand, the pixel **I Px.** shows an increasing number of photons with time. Already in the first minutes of acquisition it is possible to see that the beam was shared by two pixels. At the beginning of the scan the ratio between the number of photons hitting the pixel **Central Px.** and **I Px.** was about six. Then, in the last minutes of the area scan the two pixels **Central Px.** and the **I Px.** featured similar values of the measured photons. This gives a good indication that the hypothesis of misalignment is correct. Moreover, the number of photons estimated in the **Central Px.** pixel, as mentioned before, is lower than that measurement performed by the photodiode.

This mismatch can be understood by including (summing) also the photons measured from the *first neighbor pixels*. It means to sum the number of photons of the **Central px** together with the number of photons of the pixels around it. The black line in Figure 5.29 shows the sum of the estimated numbers of photons including the **Central Px.** and the first neighbor. The resulting values at the beginning and at the end of the area scan are shown in the Table 5.7.

	Photodiode (photons/pulse)	DSSC sum over neighbor pixels (photons/pulse)
Begin of the area scan (A)	168 ± 17	152 ± 24
End of the area scan (B)	80 ± 8	72 ± 8
Ratio (B)/(A)	48%	47%

Table 5.7: The comparison between the number of photons estimated with the photodiode and the number of photons estimated with the DSSC detector. In the case of the DSSC detector the number of photons is estimated as sum over first neighbor pixels (defined in the text) and Central Px.

The result shows that including the first neighbor pixels the estimated number of photons is within the uncertainty compatible with the measurement performed using the photodiode. This gives a strong indication that the method used is correct; moreover it demonstrates that the misalignment effect can be considered and included in the analysis.
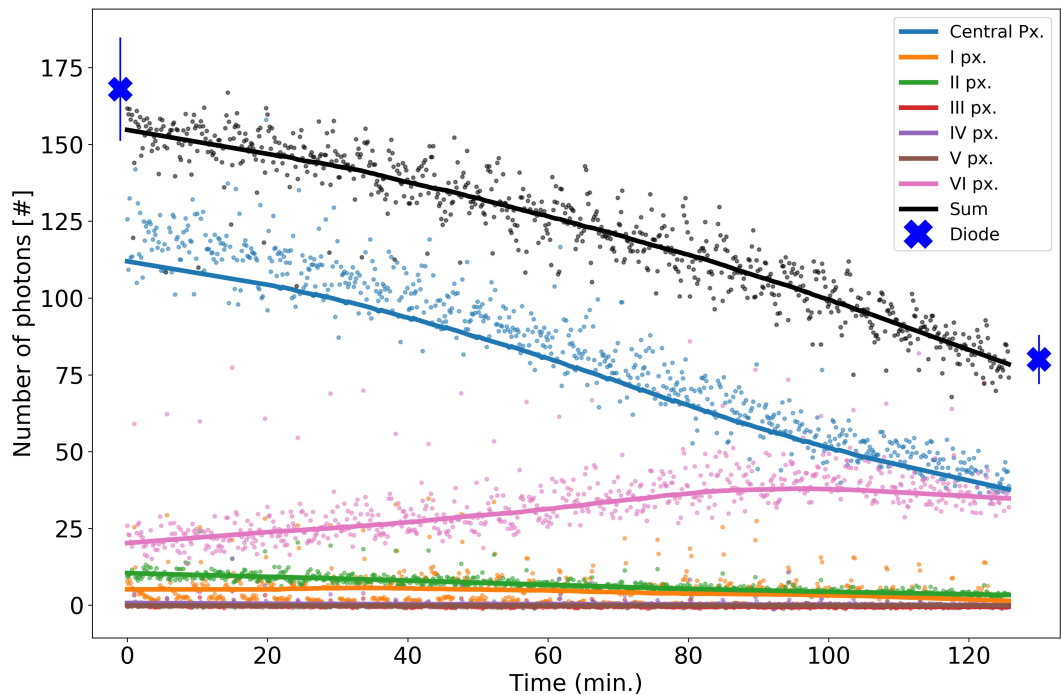
Figure 5.29: Estimated number of photons for the central pixel, its first neighbors and their sum. The **Central Px.** is the pixel where the beam hit the detector in case of perfect alignment between the beam and the ladder. The other pixels are the neighbors as defined in the Figure 5.28. The sum of the number of photons hitting all the considered pixels (central and neighbors) is shown in black. The smooth lines are used just for better illustration of the data.

5.5 Discussion of the results and comparison between the two prototypes

In order to understand the meaning of the measured detector noise, some words regarding photon misidentification. In the ideal case the energy of a single photon corresponds to 1 ADC counts. In this case, the photon produces a signal in the ADC input which is peaked in the middle of the first ADC bin, as shown in Figure 3.11 at Page 3.11. For each single pixel the standard deviation of the dark, σ_{dark} (electronic noise) is assumed to have a Gaussian distribution. The probability density function is a normalized Gaussian defined as

$$G_{\mu,\sigma}(x) = \frac{1}{\sqrt{2\pi\sigma^2}} e^{-\frac{1}{2}\left(\frac{x-\mu}{\sigma}\right)^2}, \tag{5.30}$$

where μ is the mean, σ is the Gaussian sigma, corresponding to the standard deviation, x is the variable corresponds to the input value of the ADC, in ADU units. The ADC input x is a continuous value while the ADC output is a binned discrete value. Here an ideal binning is assumed: BIN0 corresponds to x=[-0.5,0.5]; BIN1 to x=[0.5,1.5] and BINn to x=[n-0.5,n+0.5].

Since G is a probability density function, it is normalized such that

$$\int_{-\infty}^{+\infty} G(x)\mathrm{d}x = 1. \tag{5.31}$$

When the detector is not illuminated, the probability of detecting a false signal equivalent to one or more photons (*false photons*) is shown in Figure 5.30(a) and corresponds to the integral of the probability density function between 0.5 and $+\infty$:

$$P(BIN \geq 1|\mu = 0) = \int_{0.5}^{+\infty} G_{\mu=0,\sigma=\sigma_{dark}}^{noise}(x)\mathrm{d}x. \tag{5.32}$$
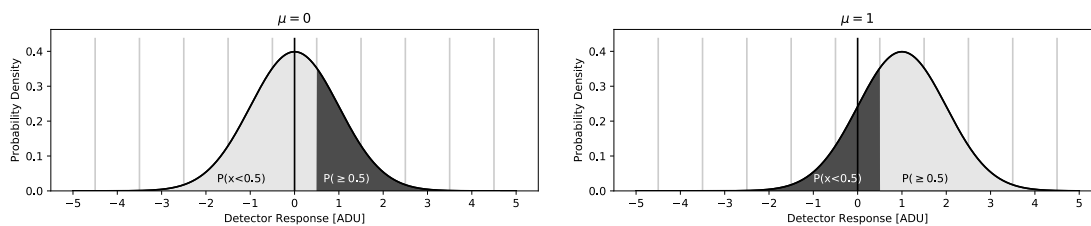
(a) The signal distribution in case of no photons. (b) The signal distribution in case of a single photon has been absorbed by the sensor.

Figure 5.30: The equivalence between the probability of false-photon detection and the probability of no-photon detection when a single photon is absorbed by the sensor. In both cases an ideal calibration was assumed, 1 ADU equal to the energy of a single photon; the used σ is very large just for illustration purposes.

The probability to detect no photon when actually one photon has hit the sensor is

$$P(BIN \leq 0|\mu = 1) = \int_{-\infty}^{0.5} G_{\mu=1,\sigma=\sigma_{dark}}^{noise}(x)\mathrm{d}x \,, \tag{5.33}$$

which is identical to the probability of detecting false photon(s):

$$P(BIN \geq 1|\mu = 0) = P(BIN \leq 0|\mu = 1) \,. \tag{5.34}$$

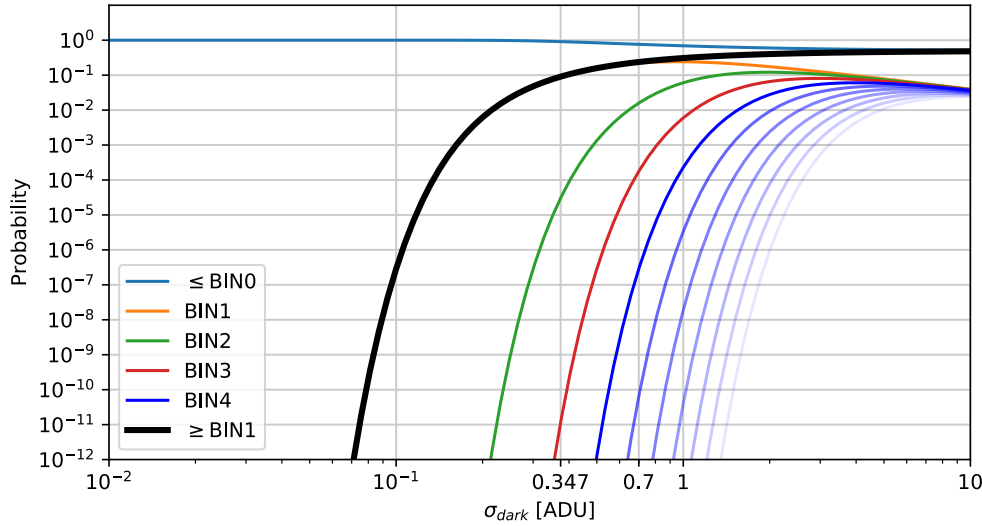Figure 5.30 illustrates the meaning of the last equation.

Figure 5.31: The probability that the detector measures a signal on a given ADC bin (illustrated by the different colors) when only electronic noise is present, as function of the noise (σ_{dark}). The black line shows the probability of false-photon(s) detection ($\geq$BIN1).

ADC BIN:	0 ADU	1 ADU	2 ADU	≤ 0 ADU	≥ 1 ADU
Interval:	[-.5,.5]	[.5,1.5]	[1.5,2.5]	$(-\infty,0.5]$	$[0.5,\infty)$
$\sigma_{dark} = 1$ ADU	$3.8 \cdot 10^{-1}$	$2.4 \cdot 10^{-1}$	$6.1 \cdot 10^{-2}$	$6.9 \cdot 10^{-1}$	$3.1 \cdot 10^{-1}$
$\sigma_{dark} = $ **0.7 ADU**	$5.2 \cdot 10^{-1}$	$2.2 \cdot 10^{-1}$	$1.6 \cdot 10^{-2}$	$7.6 \cdot 10^{-1}$	$\mathbf{2.4 \cdot 10^{-1}}$
$\sigma_{dark} = 0.5$ ADU	$6.8 \cdot 10^{-1}$	$1.6 \cdot 10^{-1}$	$1.4 \cdot 10^{-3}$	$8.4 \cdot 10^{-1}$	$1.6 \cdot 10^{-1}$
$\sigma_{dark} = $ **0.374 ADU**	$8.2 \cdot 10^{-1}$	$9.1 \cdot 10^{-2}$	$3.0 \cdot 10^{-5}$	$9.1 \cdot 10^{-1}$	$\mathbf{9.1 \cdot 10^{-2}}$
$\sigma_{dark} = 0.3$ ADU	$9.0 \cdot 10^{-1}$	$4.8 \cdot 10^{-2}$	$2.9 \cdot 10^{-7}$	$9.5 \cdot 10^{-1}$	$4.8 \cdot 10^{-2}$
$\sigma_{dark} = 0.2$ ADU	$9.9 \cdot 10^{-1}$	$6.2 \cdot 10^{-3}$	$3.2 \cdot 10^{-14}$	$9.9 \cdot 10^{-1}$	$6.2 \cdot 10^{-3}$
$\sigma_{dark} = 0.15$ ADU	~ 1	$4.3 \cdot 10^{-4}$	$7.6 \cdot 10^{-24}$	~ 1	$4.3 \cdot 10^{-4}$
$\sigma_{dark} = 0.10$ ADU	~ 1	$2.9 \cdot 10^{-7}$	$2.7 \cdot 10^{-51}$	~ 1	$2.9 \cdot 10^{-7}$
$\sigma_{dark} = 0.05$ ADU	~ 1	$7.6 \cdot 10^{-24}$	~ 0	~ 1	$7.6 \cdot 10^{-24}$

Table 5.8: The probability that the detector measures signal at a given ADC bin when only electronic noise is present. The values in the table are calculated assuming a distribution $G(\sigma_{dark}, \mu = 0)$. In the first row the bins used in the integration; in second row the integration intervals of a given bin(s).

Figure 5.31 shows the probability that electronic noise is detect in a given ADC bin. The probability of detecting a fake photons or more, $P(BIN \geq 1|\mu = 0)$, is represented by the

black line ($\geq$BIN1). The Table 5.8 shows numerically some interesting cases. In order to have a reasonable low probability ($< 10^{-4}$) of photon misidentification the detector needs to have a noise $< 0.15\,\text{ADU}$. In case of a noise of 0.1 ADU the probability of fake photon detection is $\sim 10^{-7}$.

The configurations used for the two DSSC ladder systems, one equipped with DEPFET (64 x 64) and the other equipped with Mini-SDD (512 x 128) show a similar initial gain. This allows to compare the estimation of the noise of both systems. Table 5.9 below summarize the results obtained for both prototypes.

Type of sensor	DEPFET	Mini-SDD
Frame-rate [MHz]	1	2.6
C_F	1	1
Pixels included in the analysis	5	855
Gain* [ADU/keV]	0.49 ± 0.03	0.42 ± 0.05
ADU bin-size* [keV/ADU]	2.04 ± 0.12	2.43 ± 0.26
Noise [ADU]	0.374 ± 0.001	0.7 ± 0.1
Noise [keV]	0.76 ± 0.05	1.7 ± 0.6
Noise [e^-]	211 ± 14	473 ± 167

* in the first ADC bins, with no signal compression.

Table 5.9: The comparison of the results obtained with the ladder system implementing the DEPFET (left column) and Mini-SDD (right column).
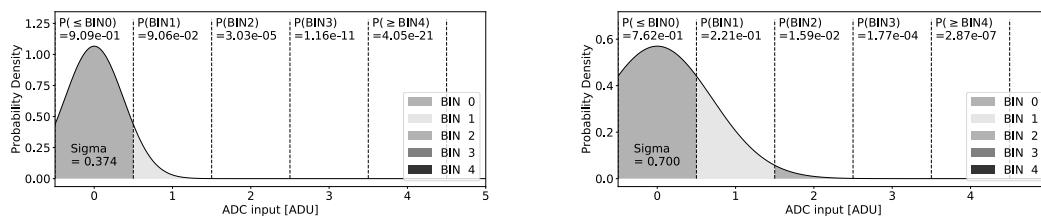
(a) The sigma used in this plot is the average standard deviation of the dark measured on the DEPFET prototype. The bin size is 2.04 keV.

(b) The sigma used in this plot is the average standard deviation of the dark measured on the Mini-SDD prototype. The bin size = 2.43 keV.

Figure 5.32: The probability density function of the average measured electronic noise. Figure (a) is refers to the DEPFET prototype and Figure (b) refers to the Mini-SDD prototype. In this plot has been assumed that the incoming photon has an energy equal to the center of the first bin.

The comparison between the DEPFET and the Mini-SDD systems shows that the Mini-SDD system has a noise about two times higher the DEPFET noise. Figure 5.32 shows

the electronic noise of both prototypes and the probability that a fake signal is detected in a given bin. The resulting noise does not allow single photon detection. In the Mini-SDD case the probability of false photon detection is 24% and in case of DEPFET the probability is 9%. In both cases, the ASIC configurations was chosen such the maximum possible gain could be reached. The target gain of 1 keV/ADU was not reached.

As mentioned in Section 3, the DEPFET is an active sensor and it is acting as amplifier; instead in the case of Mini-SDD, the amplification is performed inside the ASIC. The results shown above together with the tests performed by the ASIC delevopers show that the current version has issues as strong DNL and shows problem in the front-end and the Mini-SDD front-end is more affected by these issues. For these reasons, the ASIC has been redesign and produced. The new version will be used for the 1Mpixel DSSC camera.

Conclusions

The European X-Ray Free Electron Laser started operation in September 2017. The facility provides to the scientific community the possibility to use the most brilliant coherent X-ray source ever built with a unique time structure. The free electron laser produces, every 0.1 s, a train of 2700 pulses with a 222 ns (4.5 MHz) time separation between each other. In the first years of operation, three beamlines will provide to XFEL.EU a wide photon-energy range: two beamlines are dedicated to hard X-rays (from 3 keV to 25 keV) and one beamline to soft X-ray (from 0.25 keV to 3 keV). For each beamline the facility provides two end-stations, called instruments, which include the ensemble of apparatus and tools needed for performing a specific class of experiments. Although each instrument has different goals, the common basic layout includes tools for shaping focusing and monitoring the beam, the pump-probe laser, the sample environment and the detectors.

A big class of experiments uses the diffraction process to investigate different types of phenomena: for example it is possible to study the electronic density of a sample by measuring the diffraction pattern generated by scattering of coherent X-rays on the sample. In this type of experiments, the imaging detectors play a fundamental role. The quality of the measurement of a diffraction pattern is strictly correlated to the quality of the imaging detector used. Some experiments at XFEL.EU require to the detectors to have a sensitivity of a single photon per pulse together with a high dynamic range ($\sim 10^5$). Moreover to take advantage from the XFEL.EU fast repetition rate, the detectors must be able to take image with a frame-rate of 4.5 MHz. When the European XFEL project started no detector existed in the market which was able to fit these requirements. For this reason, XFEL.EU commissioned three new detector projects, based on the state-of-arts technology. The three projects are dedicated to the detection of X-ray photons of different energies. Each detector uses its own approach for this aim. In this thesis, the DSSC project has been presented and a DSSC detector prototype has been tested and characterized. The prototype investigated is the DSSC ladder, the smallest unit which includes all electronics components representative of the final 1 Mpixel DSSC camera.

At the beginning of this thesis, the work was initially oriented to the testing and integration of the components, in order to bring into operation the detector. When the sensors became available, the measurements on the full prototype became possible and the detector characterization could be performed.

In a first phase, I worked in the DESY FEC (Electronics Development Group C) laboratory to build a test stand used for electronics tests of the components of DSSC. Initially, I built a semi-automatic test stand for electronics tests of the Regulators Boards. This included also the tests of the MPOD power supplies and the development of the interface to control them. After this phase, the main goal of my work was to create a test-stand for the DSSC ladder operation in ambient. This test-stand consisted, among the others, of the DSSC ladder, the power supplies, a fast data receiver, a timing generator (MicroTCAc rate equipped with CC board). During this phase I built a LED driver which could be synchronized to the detector and which could emulate the XFEL.EU time structure.

Before the sensors were mounted on the electronics, the DSSC ladder test-stand was used to test the electronics components. During this phase I intensively tested the PPT and IOB, and I collaborated to the ASIC testing with its designers. This phase allowed to find the working point of the detector, namely, the configurations allowing the detector to work properly. During this phase a first data-receiver (HDF5 writer) and a first Karabo interface was developed. When finally the DEPFET sensors were mounted on the electronics, it was possible to test the detector with visible light (pulsed LED) and realize the first characterization of the system.

The DSSC ladder system was replicated: two ladders were located at DESY FeC for ambient tests and one ladder was tested in vacuum.

The vacuum test stands were built inside the clean tent in the detector group laboratory at the HERA South hall (DESY). There, the XFEL.EU laboratory infrastructure for detector calibration and characterization is located. I collaborated to the development of the laboratory and in particular I worked on the outgassing test-stand and I collaborated to the definition of the requirements and to the commissioning of FENICE, the chamber designed for testing the DSSC ladder in vacuum. In order to perform the vacuum qualification of the DSSC components, I build a small vacuum test-stand (BigPipe). It was needed to vacuum-qualify the components, to define cleaning procedures helping in the design the FENICE chamber. During this phase, I designed and built small data-loggers based on single-board computers which allowed storing the values of the pressure and the temperature measured in the vacuum setups. They were used initially the BigPipe, and later in FENICE.

After a test phase of FENICE, a DSSC ladder was mounted inside the vacuum chamber and operated for the first time in vacuum and with an active cooling system. This system allowed to bring into operation the detector in conditions compatible with those of soft X-rays beamline. When finally the sensors were mounted on the ladder, it was possible to move the system to the P04 beamline at Petra III allowing for the first time the characterization of the DSSC ladder prototype.

During this work, two different DSSC prototypes were investigated:

- The first prototype was equipped with a 64×64 pixels DEPFET sensor, connected to a single ASIC. The detector was used in ambient conditions; for the first time,

the whole system was tested with a pulsed external visible light source (LED). This allowed performing a first detector characterization giving as result the response curve of the detector as function of the light intensity. To perform a preliminary detector calibration, the detector response curve was measured with visible light and cross calibrated using a reference curve provided by the sensor producer.

- The second prototype was the DSSC ladder equipped with 16 ASICs and two full-size Mini-SDD sensors, for a total of 512 × 128 pixels. It was tested with a X-ray source, in vacuum. In particular, the detector was tested at the P04 beamline at the Petra III synchrotron. The detector originally developed for the XFEL.EU time structure was correctly synchronized to the synchrotron. This allowed performing a gain-scan for a single pixel and a characterization of an extended part of the detector sensitive area (area-scan). During the area-scan the beam featured a slow reduction of intensity, confirmed by the measurements performed with the DSSC and a reference diode. In this case, a statistical method was used to be able to characterize the detector without knowing a-priori the number of photons hitting the detector.

In both cases, the DSSC ladder was brought successfully into operation. The measurements confirmed that it was possible to synchronize it to the light sources, and that the detector could be operated with the XFEL.EU time structure. Both the prototypes were calibrated, gain and noise were determined and compared. The prototypes were configured to had a similar gain. In both cases a strong differential non-linearity (DNL) on the analog-to-digital converter was observed. The average noise measured was 0.7 ADU for the Mini-SDD system and 0.3 ADU for the DEPFET system which corresponds to 1.7 keV and 0.76 keV, respectively. According to these values, the detector noise is too high to allow single photon detection. The probability of false-photon detection is 24% for the Mini-SDD system and 9% for the DEPFET. The gain of the two prototypes was set to the maximum possible and it was not reaching the target of 1 keV / ADU.

The above mentioned features, together with other testing of the ASIC chip, triggered a redesign of the ASIC, aimed to improve the detector performance. A new version of the ASIC is now available and will be used for the assembly of the 1M pixel DSSC camera. The test and characterization of the new chip need to be performed but it is out of the scope of this thesis.

Bibliography

[1] *Wilhelm Conrad Röntgen - Biographical*, Nobelprize.org. Nobel Media AB 2014,
URL: http://www.nobelprize.org/nobel_prizes/physics/laureates/1901/rontgen-bio.html (visited on 10/04/2017)

[2] Alexi Assmus: "Early history of X rays", Beam Line **25**, 10–24 (1995)

[3] *Nobel Prize in Physics 1914 - Presentation*, Nobelprize.org. Nobel Media AB 2014,
URL: http://www.nobelprize.org/nobel_prizes/physics/laureates/1914/present.html (visited on 10/04/2017)

[4] M. Altarelli et al.: *Technical Design Report: The European X-Ray Free-Electron Laser*,
DESY Report 2006-097 (2006)
ISBN: 978-3-935702-17-1

[5] European XFEL GmbH: *Official Web-site*,
URL: http://www.xfel.eu (visited on 04/25/2013)

[6] M. Porro et al.: "Development of the DEPFET Sensor With Signal Compression: A Large Format X-Ray Imager With Mega-Frame Readout Capability for the European XFEL", IEEE Transactions on Nuclear Science **59**, 3339–3351 (2012)
DOI: 10.1109/tns.2012.2217755

[7] Michael F. L'Annunziata: *Radioactivity: Introduction and History, From the Quantum to Quarks* (Elsevier 2016)
ISBN: 9780444634962

[8] N. Raab et al.: "Status of the laboratory infrastructure for detector calibration and characterization at the European XFEL", Journal of Instrumentation **11**, C12051 (2016)
DOI: 10.1088/1748-0221/11/12/c12051

[9] O. W. Richardson: *Thermionic Emission From Hot Bodies* (Wexford College Press 2003)
ISBN: 1929148100

[10] Günter H. Zschornack: *Handbook of X-Ray Data* (Springer Berlin Heidelberg 2007)
ISBN: 3540286187

[11] J.D. Jackson: *Classical Electrodynamics, 2nd Edition* (John Wiley & Sons, New York 1975)
ISBN: 0-471-43132-X

[12] L. Courvoisier Thierry J.: *High Energy Astrophysics. An Introduction* (Springer-Verlag Berlin Heidelberg 2013)
ISBN: 978-3-642-30969-4

[13]   Peter Schmüser et al.: *Free-Electron Lasers in the Ultraviolet and X-Ray Regime* (Springer International Publishing 2014)
       ISBN: 3319040804

[14]   Uwe Bergmann: *X-Ray Free Electron Lasers* (Royal Society Of Chemistry 2017)
       ISBN: 1849731004

[15]   HASYLAB DESY: "High-Gain FEL by Microbunching" (2017)
       URL: http://photon-science.desy.de/facilities/flash/the_free_electron_laser/how_it_works/high_gain_fel/index_eng.html

[16]   Glenn F. Knoll: *Radiation Detection and Measurement* (John Wiley & Sons Inc. 2010)
       ISBN: 0470131489

[17]   NIST: *X-Ray Form Factor, Attenuation, and Scattering Tables*,
       URL: https://physics.nist.gov/PhysRefData/FFast/html/form.html (visited on 08/29/2017)

[18]   NIST: *XCOM: Photon Cross Sections Database*,
       URL: https://physics.nist.gov/PhysRefData/Xcom/html/xcom1.html (visited on 08/29/2017)

[19]   Charles Kittel: *Introduction to Solid State Physics* (TBS 1995)
       ISBN: 9788126510450

[20]   Devraj Singh: *Fundamentals of Optics* (Prentice-Hall of India Pvt.Ltd 2015)
       ISBN: 8120351460

[21]   Paolo Russo: *Handbook of X-ray imaging : physics and technology* (CRC Press, Boca Raton, FL 2018)
       ISBN: 9781498741521

[22]   Elias M. Stein: *Fourier Analysis* (Princeton University Press 2011)
       ISBN: 9781400831234

[23]   Rick P. Millane: "Phase retrieval in crystallography and optics", Journal of the Optical Society of America A **7**, 394–411 (1990)

[24]   William H. Press et al.: *Numerical Recipes* (Cambridge University Pr. 2007)
       ISBN: 0521880688

[25]   SciPy.org: *Discrete Fourier Transform*,
       URL: https://docs.scipy.org/doc/numpy-1.13.0/reference/routines.fft.html

[26]   Vojin G. Oklobdzija: *Computer Engineering Handbook* (CRC Press 2001)
       ISBN: 9781420041545

[27]   CR Hubbard, HE Swanson, FA Mauer: "A silicon powder diffraction standard reference material", Journal of Applied Crystallography **8**, 45–48 (1975)

[28]   Alan Durrant: *Quantum physics of matter* (Institute of Physics in association with the Open University, Bristol Philadelphia 2000)
       ISBN: 0750307218

[29]   Jerry C. Whitaker: *The Electronics Handbook* (CRC Press 1996)
       ISBN: 9780849383458

[30] Massimo Altarelli: *Status of the European X-ray Free-Electron Laser, MID Workshop, Grenoble, European XFEL*,
URL: https://www.xfel.eu/sites/sites_custom/site_xfel/content/e35165/e46561/e46883/e59447/e62217/e62218/e59450/xfel_file59451/mid-workshop-2009-altarelli_eng.pdf (visited on 01/23/2018)

[31] *Deutsches Elektronen-Synchrotron (DESY), Hamburg, Germany*
URL: www.desy.de

[32] M. J. Lederer et al.: "Pump-probe laser development for the European X-Ray Free-Electron Laser Facility", X-Ray Free-Electron Lasers: Beam Diagnostics, Beamline Instrumentation, and Applications, San Diego, California, Aug. 12, 2012, Proc. SPIE 8504, 85040L (2012)
DOI: 10.1117/12.928961

[33] H. N. Chapman, C. Caleman, N. Timneanu: "Diffraction before destruction", Philosophical Transactions of the Royal Society B: Biological Sciences **369**, 20130313–20130313 (2014)
DOI: 10.1098/rstb.2013.0313

[34] A. Scherz et al.: "Conceptual Design Report: Scientific Instrument Spectroscopy and Coherent Scattering (SCS)" (2013)
DOI: 10.3204/xfel.eu/tr-2013-006

[35] Paul Kirkpatrick, A. V. Baez: "Formation of Optical Images by X-Rays", J. Opt. Soc. Am. **38**, 766–774 (1948)
DOI: 10.1364/JOSA.38.000766

[36] Hirokatsu Yumoto et al.: "Focusing of X-ray free-electron laser pulses with reflective optics", Nature Photonics **7**, 43–47 (2012)
DOI: 10.1038/nphoton.2012.306

[37] Friederike Januschek et al.: *Performance of the LBNL FastCCD for the European XFEL*, 2016

[38] M. Meyer: "Technical Design Report: Scientific Instrument SQS" (2012)
DOI: 10.3204/xfel.eu/tr-2012-007

[39] M. Meyer: "Conceptual Design Report: Scientific Instrument SQS" (2011)
DOI: 10.3204/xfel.eu/tr-2011-003

[40] G Grübel et al.: "XPCS at the European X-ray free electron laser facility", Nuclear Instruments and Methods in Physics Research Section B: Beam Interactions with Materials and Atoms **262**, 357–367 (2007)

[41] Jörg Fink et al.: "Resonant elastic soft x-ray scattering", Reports on Progress in Physics **76**, 056502 (2013)

[42] Akio Kotani, Shik Shin: "Resonant inelastic x-ray scattering spectra for electrons in solids", Reviews of Modern Physics **73**, 203 (2001)

[43] Andreas Koch et al.: "Detector Development for the European XFEL: Require-
      ments and Status", Journal of Physics: Conference Series **425**, 062013 (2013)
      DOI: 10.1088/1742-6596/425/6/062013

[44] M. Kuster et al.: "Detectors and Calibration Concept for the European XFEL",
      Synchrotron Radiation News **27**, 35–38 (2014)
      DOI: 10.1080/08940886.2014.930809

[45] Markus Kuster: "Detector for European XFEL", 4th EIROforum School on Instru-
      mentation, ESO & EUROfusion (15-19 June 2015) (2015)
      URL: https://indico.cern.ch/event/368852/contributions/1785539/attachments/
      733586/1006506/20150618-XFELDetectors-Kuster.pdf (visited on 01/24/2018)

[46] Mathew Hart et al.: "Development of the LPD, a high dynamic range pixel detec-
      tor for the European XFEL", 2012 IEEE Nuclear Science Symposium and Medical
      Imaging Conference Record (NSS/MIC) (IEEE 2012)
      DOI: 10.1109/nssmic.2012.6551165

[47] A Koch et al.: "Performance of an LPD prototype detector at MHz frame rates un-
      der Synchrotron and FEL radiation", Journal of Instrumentation **8**, C11001 (2013)
      DOI: 10.1088/1748-0221/8/11/C11001

[48] A. Allahgholi et al.: "The adaptive gain integrating pixel detector", Journal of In-
      strumentation **11**, C02066 (2016)
      DOI: 10.1088/1748-0221/11/02/C02066

[49] Ulrich Trunk et al.: "AGIPD: a multi megapixel, multi megahertz X-ray camera
      for the European XFEL", Selected Papers from the 31st International Congress on
      High-Speed Imaging and Photonics, ed. by T. Goji Etoh, Hiroyuki Shiraga (SPIE
      2017)
      DOI: 10.1117/12.2269153

[50] G. Lutz et al.: "DEPFET sensor with intrinsic signal compression developed for
      use at the XFEL free electron laser radiation source", Nuclear Instruments and
      Methods in Physics Research Section A: Accelerators, Spectrometers, Detectors
      and Associated Equipment **624**, 528–532 (2010)
      DOI: 10.1016/j.nima.2010.03.002

[51] Burkhard Heisen et al.: "Karabo: An Integrated Software Framework Combining
      Control, Data Management, and Scientific Computing Tasks", 14th International
      Conference on Accelerator & Large Experimental Physics Control Systems, San
      Francisco (USA), 6 Oct 2013 - 11 Oct 2013 (2013)

[52] European XFEL (ed.): *Karabo 2.0.8 documentation*, ed. by European XFEL
      URL: https://in.xfel.eu/readthedocs/docs/karabo/en/latest/concepts/
      introduction.html (visited on 01/13/2018)

[53] Martin Teichmann et al.: "Karabo-GUI: A Multi-Purpose Graphical Front-End for
      the Karabo Framework", Proceedings, 15th International Conference on Accel-
      erator and Large Experimental Physics Control Systems (ICALEPCS 2015): Mel-

bourne, Australia, October 17-23, 2015, WEPGF153 (2015)
DOI: 10.18429/JACoW-ICALEPCS2015-WEPGF153

[54] Steffen Hauf et al.: "Calibration processing at the European XFEL Implementation and concepts", 2015 IEEE Nuclear Science Symposium and Medical Imaging Conference (NSS/MIC) (IEEE 2015)
DOI: 10.1109/nssmic.2015.7581928

[55] Astrid Muennich et al.: "Integrated Detector Control and Calibration Processing at the European XFEL", International Conference on Accelerator and Large Experimental Control Systems, Melbourne (Australia), 18 Oct 2015 - 23 Oct 2015, WEPGF050 (2015) arXiv: 1601.01794

[56] The HDF Group: *Hierarchical Data Format, version 5*, 2018,
URL: http://www.hdfgroup.org/HDF5

[57] PICMG: *PCI Industrial Computer Manufacturers Group*,
URL: https://www.picmg.org/ (visited on 12/12/2017)

[58] *Beckhoff Automation GmbH & Co. KG*,
URL: http://www.beckhoff.com/ (visited on 12/15/2017)

[59] Lukasz Zembala et al.: "Master Oscillator for the European XFEL", 5th International Particle Accelerator Conference, Dresden (Germany), 15 Jun 2014 - 20 Jun 2014 (2014)

[60] Patrick Gessler: "Synchronization and Sequencing of Data Acquisition and Control Electronics at the European X-Ray Free Electron Laser", Technische Universität Hamburg-Harburg, Diss., 2015, Dr. (Technische Universität Hamburg-Harburg, Hamburg 2015), p. 120
DOI: 10.3204/DESY-THESIS-2015-049

[61] E Motuk et al.: "Design and development of electronics for the EuXFEL clock and control system", Journal of Instrumentation **7**, C01062 (2012)
DOI: 10.1088/1748-0221/7/01/C01062

[62] D. Boukhelef R. Halsall: *Train Transfer Protocol*, ed. by European XFEL GmbH, Internal XFEL.EU, 2017

[63] K. Wrona et al.: *XFEL Train Data Format*, ed. by European XFEL GmbH, Internal XFEL.EU, 2017

[64] Cornelia Wunderer, Heinz Graafsma, Frank Okrent: *DSSC megapixel camera with vessel 3D PDF, Internal Report*, 2018,
URL: https://docs.xfel.eu/share/page/site/dssc/document-details?nodeRef= workspace://SpacesStore/02477f66-fdfb-4a01-912c-eb2c5efd1583

[65] Karsten Hansen, Helmut Klar, Dirk Muntefering: "Camera head of the DSSC X-ray imager", 2011 IEEE Nuclear Science Symposium Conference Record (IEEE 2011)
DOI: 10.1109/nssmic.2011.6154666

[66] Christo Papadopoulos: *Solid-state electronic devices : an introduction* (Springer, New York, NY 2014)
ISBN: 9781461488354

[67] Gerhard Lutz et al.: "The DEPFET Sensor-Amplifier Structure: A Method to Beat 1/f Noise and Reach Sub-Electron Noise in Pixel Detectors", Sensors **16**, 608 (2016)
DOI: 10.3390/s16050608

[68] J. Kemmer, G. Lutz: "New detector concepts", Nuclear Instruments and Methods in Physics Research Section A: Accelerators, Spectrometers, Detectors and Associated Equipment **253**, 365–377 (1987)
DOI: 10.1016/0168-9002(87)90518-3

[69] Amptek Inc.: *A comparison of Silicon Drift (SDD) and Si-PIN detectors*,
URL: https://amptek.com/pdf/drift%20vs%20pin.pdf (visited on 01/12/2018)

[70] A. Grande et al.: "An open-loop front-end stage with signal compression capability and improved PSRR for mini-SDD pixel detectors", Journal of Instrumentation **12**, T12008 (2017)
DOI: 10.1088/1748-0221/12/12/t12008

[71] Florian Erdinger et al.: "The DSSC pixel readout ASIC with amplitude digitization and local storage for DEPFET sensor matrices at the European XFEL", 2012 IEEE Nuclear Science Symposium and Medical Imaging Conference Record (NSS/MIC) (IEEE 2012)
DOI: 10.1109/nssmic.2012.6551176

[72] Florian Erdinger: "Design of Front End Electronics and a Full Scale 4k Pixel Readout ASIC for the DSSC X-ray Detector at the European XFEL"
DOI: 10.11588/heidok.00022273

[73] Stefano Facchinetti et al.: "Characterization of the Flip Capacitor Filter for the XFEL-DSSC Project", IEEE Transactions on Nuclear Science **58**, 2032–2038 (2011)
DOI: 10.1109/tns.2011.2159994

[74] C. Reckleben et al.: "8-bit 5-MS/s per-pixel ADC in an 8-by-8 Matrix", 2011 IEEE Nuclear Science Symposium Conference Record (IEEE 2011)
DOI: 10.1109/nssmic.2011.6153987

[75] F. Gray: "Pulse code communication", U.S. Patent 2632058, 1953

[76] Manfred Kirchgessner: "Control, Readout and Commissioning of the Ultra-High Speed 1 Megapixel DSSC X-Ray Camera for the European XFEL", PhD thesis (Ruperto-Carola University of Heidelberg 2018)
DOI: 10.11588/heidok.00023870

[77] M Kirchgessner et al.: "The high performance readout chain for the DSSC 1Megapixel detector, designed for high throughput during pulsed operation mode", Journal of Instrumentation **10**, C01011 (2015)
DOI: 10.1088/1748-0221/10/01/c01011

[78]   *Xilinx Aurora Protocol*,
       URL: https://www.xilinx.com/aurora (visited on 01/30/2018)

[79]   A. Kugel et al.: "The PPT-module: High-performance readout for the DSSC detector at XFEL", 2013 IEEE Nuclear Science Symposium and Medical Imaging Conference (2013 NSS/MIC), 1–6 (2013)
       DOI: 10.1109/NSSMIC.2013.6829518

[80]   *Xilinx MicroBlaze Soft Processor Core*,
       URL: https://www.xilinx.com/products/design-tools/microblaze.html (visited on 01/30/2018)

[81]   W-IE-NE-R Power Electronics GmbH (ed.): *MPOD Universal Low and High Voltage Power Supply System*, ed. by W-IE-NE-R Power Electronics GmbH,
       URL: http://www.wiener-d.com/sc/power-supplies/mpod--lvhv/ (visited on 12/12/2017)

[82]   BOSCH: "CAN Specification, Version 2.0" (1991) (visited on 12/12/2017)

[83]   M. Donato et al.: "First functionality tests of a 64 x 64 pixel DSSC sensor module connected to the complete ladder readout", Journal of Instrumentation **12**, C03025 (2017)
       DOI: 10.1088/1748-0221/12/03/C03025

[84]   Pfeiffer Vacuum AG (ed.): *Vacuum Technology Book, Volume II*, ed. by Pfeiffer Vacuum AG,
       URL: https://www.pfeiffer-vacuum.com/en/info-center/vacuum-technology-book/ (visited on 01/30/2018)

[85]   M Dommach: "UHV Guidelines for X-Ray Beam Transport Systems", XFEL.EU TN-2011-004 (2013)
       URL: http://bib-pubdb1.desy.de/record/88939/files/XFEL_EU_TN-2011-001.pdf (visited on 01/31/2018)

[86]   *Components or device from Pfeiffer Vacuum.*
       URL: https://www.pfeiffer-vacuum.com/ (visited on 01/30/2018)

[87]   Lakeshore,
       URL: http://www.lakeshore.com (visited on 12/15/2017)

[88]   Raspberry Pi Foundation,
       URL: http://www.raspberrypi.org/ (visited on 12/15/2017)

[89]   Sneha Nidhi et al.: "Safety-Interlock System of the DSSC X-Ray Imager" (2016)
       DOI: 10.3204/pubdb-2016-06099

[90]   Cryomech,
       URL: http://www.cryomech.com/ (visited on 12/15/2017)

[91]   Stefan Aschauer: *Private Communication*, PNSensor

[92]   G. Weidenspointner et al.: "Strategy for calibrating the non-linear gain of the DSSC detector for the European XFEL", 2011 IEEE Nuclear Science Symposium

Conference Record (IEEE 2011)

DOI: 10.1109/nssmic.2011.6153648

[93] Georg Weidenspointner et al.: "DSSC Prototype Ladder Operation and Performance Study at PETRA III / P04" (2017)

DOI: 10.1109/nssmic.2017.8532810

[94] Jens Viefhaus et al.: "The Variable Polarization XUV Beamline P04 at PETRA III: Optics, mechanics and their performance", Nuclear Instruments and Methods in Physics Research Section A: Accelerators, Spectrometers, Detectors and Associated Equipment **710**, 151–154 (2013)

DOI: 10.1016/j.nima.2012.10.110

[95] Deutsches Elektronen-Synchrotron DESY: *P04 Variable Polarization XUV Beamline*

URL: http://photon-science.desy.de/facilities/petra_iii/beamlines/p04_xuv_beamline/index_eng.html (visited on 12/27/2017)

[96] John Peacock: *Lecture notes: Astronomical Statistics (October 15, 2012)*,

URL: http://www.roe.ac.uk/~jap/teaching/astrostats/ (visited on 01/29/2018)

[97] Jens Viefhaus: *Private Communication*, P04 beamline (DESY, Petra III)

[98] *DSSC internal reports prepared for the meeting of the European XFEL Detector Advisory Commitee, May and November 2016*, Internal Reports

[99] M. Gauga et al.: "Calibration of the MAGIC Telescope", Proceedings of the 29th International Cosmic Ray Conference. August 3-10, 2005, Pune, India. 101–106 (2005)

[100] V. Chmill et al.: "On the characterisation of SiPMs from pulse-height spectra", Nuclear Instruments and Methods in Physics Research Section A: Accelerators, Spectrometers, Detectors and Associated Equipment **854**, 70–81 (2017)

DOI: 10.1016/j.nima.2017.02.049

[101] Jan Soldat: "Characterization, Operation and Wafer-level Testing of an ultra-fast 4k Pixel Readout ASIC for the DSSC X-ray Detector at the European XFEL", PhD thesis (Ruperto-Carola University of Heidelberg 2018)

DOI: 10.11588/heidok.00024041

Acknowledgements

This thesis would not have been possible without the support of many people.

First and foremost, I would like to warmly thank and to express all my gratitude to **Dr. Monica Turcato**. Our collaboration at work was great. I think without her persistence to push to bring the detector at the beamline, I would not be able take any data for this thesis. Her advices, the continuous reviews and her constant support were extremely important for me and for my thesis. *Grazie di tutto Monica!*.

Secondly, I would like to warmly thank **Dr. Markus Kuster** who offered me a position at the Detector Development group of European XFEL GmbH where I worked four year. I would like also to warmly thank **Prof. Dr. Erika Garutti** for accepting this thesis project. I really appreciate her constructive comments, the suggestions, the review and the ability to transmit me enthusiasm and motivation.

I am grateful also to the leader of the DSSC Consortium, **Dr. Matteo Porro**, for his support, corrections and his explanations.

During the first years of work, I worked mainly together with the DESY Electronic Development group (FeC). The nice atmosphere of the group and the competences of this team represented for me a great place where to learn and to begin to work on the DSSC detector. For that, I would like to warmly thank **Dr. Karsten Hansen** for having *adopted* me in his group and for the many constructive discussions and exchange of ideas.

I would like to warmly thank the other members of DESY FeC group. In particular, I am grateful to **Christian Reckleben, Pradeep Kalavakuru** and **Dr. Helmut Klär** for their constant support, collaboration and for teaching me many things about electronics and about the core of DSSC. I can not forget to thank Eric Wüstenhagen and Alexander Venzmer for their fast and complete support about IT, electronics and mechanics at DESY FeC.

The preparatory work and the shifts for measurements at Petra III involved many people. First of all, I would warmly thank the responsible of the P04 beamline Dr. Jens Viefhaus for having given us the possibility to bring into operation the DSSC ladder at the beamline.

Then, I would warmly thank my XFEL.EU colleagues. I would start with the engineer, Marko Ekmedžić, for the mechanics design he prepared for us, and the two technicians, Rüdriger Schmitt and Thomas Dietze, who prepared, unmounted, moved, adapted and

Now, I would write something more personal. If I made the decision to begin this adventure is thanks to Luz. You know that without you, this German adventure would never begin. For this, I would like to say you a huge thank you. Even if our roads have been split many years ago already, I would like to say that I will be always grateful to you, also for this.

The years in Hamburg were for me until now the most intense, complicate and hard years of my life. But in the other hand, I am really happy for having met friends there as Sneha, Giuseppe, Idoia, Mayank, Dawid, Andreas, Marlene, Fransec, Catherine, Ilka, Alessio, Giovanna, and especially, Gabriele and Christoph. I would never forget our dinners, beers, the random tours and the time spent together. People, you really make my life better there!

Last but not least, Ambra: in the most dark days you were always there for me, trying push me out from my desperation. Since I met you, your presence has been my motivation in Hamburg. Sometimes, I think you saved literally my life there, and with it also my career. *Grazie di tutto! Anche se un "grazie" non sarà mai abbastanza!!*. Good luck for everything, I hope you can complete very soon and submit your thesis as well! I wish you all the bests!

Finally, I am thankful to my parents who always supported me. I am grateful them especially for having helped me economically during my (long) undergraduate studies in Genoa (Italy), and for having sustained my *crazy* choices, like the two consecutive experiences as exchange student in Uppsala (Sweden). And I thank them for being always proud to have a son far away, working in Hamburg.

With my family, I would like to also mention my younger brother Dr. Silvio, who – because of the passion for technology and science transmitted by our father – is the other physicist of the family. I will never forget when we were young teenagers, how much we were proud to be able to build at home a flying plastic bag, filled with hydrogen homemade by hydrolysis... At the end, if I started this path and now I am writing the last words of a doctoral thesis is also thank to our "experiments" and games played together too many years ago in the our "laboratory", the *Soffitta*.

Declaration of Authorship

I hereby declare, on oath, that I have written the present dissertation by my own and have not used other than the acknowledged resources and aids.

Genoa, Italy, 20.12.2018,   *Mattia Donato*